

Experimental Generation and Modeling of Vortical Gusts and Their Interactions with an Airfoil

Thesis by
Esteban Antonio Lemus Hufstedler

In Partial Fulfillment of the Requirements for the
degree of
Doctor of Philosophy in Aeronautics

The logo for the California Institute of Technology (Caltech), featuring the word "Caltech" in a bold, orange, sans-serif font.

CALIFORNIA INSTITUTE OF TECHNOLOGY
Pasadena, California

2017
Defended May 2, 2017

© 2017

Esteban Antonio Lemus Hufstedler
ORCID: 0000-0001-7162-920X

All rights reserved

ACKNOWLEDGEMENTS

I would like to thank my advisor, Professor Beverley McKeon, for her advice, teaching, and support throughout the years and projects. With her help, I have learned to be a better scientist, presenter, writer, and figure-maker. It has been a privilege to work with her. I would also like to thank my thesis committee members, Professors Tim Colonius, Anthony Leonard, and Morteza Gharib, for productive discussions about my research and for reviewing this thesis.

The friendly atmosphere of the McKeon group has been very helpful throughout the years. Our research discussions, presentation critiques, and social events have helped me stay informed and happy. I'd like to particularly thank Reeve Dunne, as our discussions of unsteady aerodynamics, analysis techniques, and experimental methods have worked their way into this thesis at fundamental levels.

I would never have made it to Caltech without the support of my family. None of this would have been possible without the generations of my family that invested so much time and energy into me. This is a debt that cannot be repaid.

My friends made helped make my doctoral studies enjoyable. I would like to especially thank the incoming class of 2010, as we struggled through the challenges of first year and beyond together. The hikes, road trips, ultimate frisbee, and other fun helped keep my world balanced.

I would like thank my wife, Artemis Ailianou, for her love and support, and for justifying one of my reasons for coming to Caltech.

This research was funded by the Gordon and Betty Moore Foundation through Grant GBMF#2645 to the California Institute of Technology.

ABSTRACT

This thesis examines two methods of vortical gust generation and the interaction between these gusts and an airfoil. These flows were studied with both experiments at $Re = 20,000$ and potential-flow based simulations.

The standard method of generating a vortical gust has been to rapidly pitch an airfoil. A novel approach is presented: heaving a plate across the tunnel, and changing direction rapidly to release a vortex. This method is motivated by the desire to limit a test article's exposure to the wake of the gust generator by moving it to the side of the tunnel.

A series of potential flow models were used to examine these flows: steady and unsteady thin airfoil theory, an extension of Tchieu and Leonard's [65] unsteady airfoil model, and an unsteady vortex panel method.

Experiments characterized the generated gusts and verified that the strength of the shed vortices approximately matched the theoretical predictions. The inviscid simulations were unable to predict viscous effects like the wakes of the generators. The pitching airfoil resulted in a persistent wake in the test section, whereas the wake of the heaving plate only temporarily disturbed the flow.

The vortex-wing interaction was examined using both mechanisms. When the wake of the generator was far from the wing, the unsteady simulations provided reasonable estimates for the early variation in lift. This demonstrated that the initial lift peak is due to inviscid effects. Each of the potential flow methods with wake models provided reasonable estimates of this lift. The simplicity of the unsteady thin airfoil theory model recommends its use for examining early vortex-wing interactions.

With the test article mounted at the midline of the tunnel, the wakes had substantial effects when the pitching generator was near the midline of the tunnel, or when the heaving plate passed the midline. The simulations were not able to capture the effects of the wakes or predict the effects of the airfoil's angle of attack. This had the largest effect on the timescale of the post-gust approach to the final forces. With the airfoil at $\alpha = 0^\circ$, this was 5-10 t_c , which is characteristic of attached flows. The airfoil at $\alpha = 10^\circ$ needed double the time to approach its final state after perturbations due to its separated flow. The heaving plate's withdrawal allowed for measurement of the resumption of vortex shedding, which was impossible with the pitching airfoil's persistent wake.

PUBLISHED CONTENT AND CONTRIBUTIONS

Hufstedler, EAL and McKeon, BJ. "Isolated Gust Generation for the Investigation of Airfoil-Gust Interaction", 46th AIAA Fluid Dynamics Conference, AIAA AVIATION Forum, (AIAA 2016-4257). DOI: <http://dx.doi.org/10.2514/6.2016-4257>

EAL Hufstedler performed the experiments, analyzed the data, and collaborated in the conception of the research and in the writing of the article with BJ McKeon.

TABLE OF CONTENTS

Acknowledgements	iii
Abstract	iv
Published Content and Contributions	v
Table of Contents	vi
List of Illustrations	x
List of Tables	xiii
Nomenclature	xiv
Chapter I: Introduction and Background	1
1.1 Introduction	1
1.2 Gusts in the Wild	1
1.3 Theoretical Unsteady Aerodynamics	2
1.4 Studies of Gusts and Unsteady Aerodynamics	4
1.4.1 Modeling Freestream Unsteadiness with Body Motion	4
1.4.2 Classical Unsteadiness	4
1.4.3 Gust Response and Control	6
1.4.4 Vortex Interaction	7
1.5 Summary	8
Chapter II: Analytical Models and Simulations	10
2.1 Introduction	10
2.2 Thin airfoil theory models	10
2.2.1 Pitching Airfoil	10
2.2.2 Heaving Plate	14
2.2.3 Point Vortex Model of Airfoil-Vortex Interaction	17
2.3 Extension of Tchieu-Leonard unsteady airfoil model	19
2.3.1 Tchieu-Leonard unsteady airfoil model	19
2.3.2 Extended Tchieu-Leonard model	19
2.4 Unsteady Panel Methods	21
2.4.1 Background	21
2.4.2 Equations of the Vortex Panel Method	22
2.4.2.1 Vortex Panels	22
2.4.2.2 Determination of Panel Strengths	23
2.4.3 Panel Method Simulations	24
2.4.3.1 Pitching Airfoil	25
2.4.3.2 Heaving Plate	25
2.4.3.3 Airfoil-Vortex Interaction	27
2.5 Comparison of Analytical Models and Simulations	27
2.5.1 Pitching Airfoil	29
2.5.2 Heaving Plate	31
2.5.3 Airfoil-Vortex Interaction	33

2.6 Summary	35
Chapter III: Experimental Equipment	38
3.1 Introduction	38
3.2 NOAH Water Tunnel	38
3.3 Particle Image Velocimetry	38
3.4 Static Airfoil	39
3.5 Dynamic Airfoil	41
3.6 Heaving Plate Apparatus	42
3.7 Gantry System	44
3.8 Summary of Experiments	44
Chapter IV: Gust Generation	47
4.1 Introduction	47
4.2 Analysis Techniques	47
4.2.1 Gust Unwrapping	47
4.2.2 Vortex Identification	48
4.3 Experimental Generation of Gusts via Pitching Airfoil	50
4.3.1 Perturbation of Freestream	50
4.3.2 Characterization of Gusts	51
4.3.3 Three-dimensionality of Gusts	52
4.3.4 Discussion	55
4.4 Experimental Generation of Gusts via Heaving Plate	58
4.4.1 Perturbation of Freestream	58
4.4.2 Passing Plate	60
4.4.3 Flow around the Heaving Plate	60
4.4.4 Effects of Re_c and S	63
4.4.5 Effects of c_p	65
4.4.6 Effects of H and T	67
4.4.7 Three-dimensionality of Gusts	70
4.4.8 Discussion	72
4.5 Comparison of Gust Generation Methods	79
4.6 Summary	80
Chapter V: Gust-Wing Interaction	83
5.1 Introduction	83
5.2 Experimental Apparatus	83
5.3 Baseline Forces	85
5.3.1 Static Gust Generators	85
5.3.2 Forces due to a passing plate	86
5.3.3 Discussion	89
5.4 Interaction with Pitching Airfoil Gusts	92
5.4.1 Experimental Results	92
5.4.2 Comparison with Theory	96
5.4.3 Discussion	96
5.5 Interaction with heaving plate gusts	101
5.5.1 Experimental Results	101
5.5.2 Comparison with Theory	104

5.5.3 Discussion	105
5.6 Summary	110
Chapter VI: Conclusion	114
6.1 Summary	114
6.2 Future Work	116
Bibliography	118
Appendix A: Descriptions of experiments	125
A.1 Introduction	125
A.2 Static Airfoil (SA) Experiments	125
A.2.1 Experiment SA-1	126
A.2.2 Experiment SA-2	126
A.2.3 Experiment SA-3	126
A.2.4 Experiment SA-4	126
A.2.5 Experiment SA-5	126
A.3 Pitching Gust Generator (PGG) Experiments	127
A.3.1 Experiment PGG-1	127
A.3.2 Experiment PGG-2	127
A.3.3 Experiment PGG-3	128
A.4 Heaving Gust Generator (HGG) Experiments	128
A.4.1 Experiment HGG-1	128
A.4.2 Experiment HGG-2	129
A.4.3 Experiment HGG-3	129
A.4.4 Experiment HGG-4	129
A.4.5 Experiment HGG-5	130
A.4.6 Experiment HGG-6	130
A.4.7 Experiment HGG-7	130
A.4.8 Experiment HGG-8	130
A.4.9 Experiment HGG-9	130
A.4.10 Experiment HGG-10	131
A.4.11 Experiment HGG-11	131
Appendix B: Derivation of Extended Tchieu-Leonard Unsteady Airfoil Model	140
B.1 Introduction	140
B.2 Conformal Mapping	140
B.3 Vorticity Distributions	141
B.3.1 Lifting Cylinder at Angle α	141
B.3.2 Rotating flat plate	142
B.3.3 External vortex	143
B.3.3.1 Wake vortices	145
B.4 Review and Extension of the TL model	145
B.4.1 Lift on plate	145
B.4.2 Moment on plate	146
Appendix C: Additional Figures	148
C.1 Simulations	148
C.2 Heaving plate	148
C.3 Forces on static airfoil	148

C.4 Interaction with pitching airfoil gusts 149
C.5 Interaction with heaving plate gusts 149

LIST OF ILLUSTRATIONS

<i>Number</i>	<i>Page</i>
1.1 Plot of the Wagner function.	4
2.1 Schematics of theoretical models	11
2.2 Examples of pitching trajectory.	12
2.3 Examples of heaving trajectory.	15
2.4 Schematic of the UPM	22
2.5 Diagram of a vortex panel in its local coordinate system.	24
2.6 Simulated wakes of pitching airfoil.	26
2.7 Simulated wakes of heaving plates.	28
2.8 C_L of the simulated pitching airfoil.	30
2.9 Comparison of estimated pitching gust circulations.	32
2.10 C_L of the simulated heaving plates.	33
2.11 Comparison of estimated heaving gust circulations.	34
2.12 C_L and vortex paths from vortex interaction simulations	36
3.1 Diagram of the NOAH tunnel.	39
3.2 Calibration and characterization of the NOAH tunnel	40
3.3 Cross-section of a NACA 0018	41
3.4 Diagram of the wing's mount	41
3.5 Diagram of free-surface plate.	42
3.6 Diagram of pitching airfoil system.	43
3.7 Diagram of heaving plates	43
3.8 Diagram of heaving plate system.	44
3.9 Heaving plate mechanisms.	45
3.10 Image of the gantry system	46
4.1 Example of gust unwrapping	48
4.2 Flow behind static airfoil	51
4.3 Unwrapped vorticity downstream of the pitching airfoil	53
4.4 Speed and y-position of vortices from pitching airfoil	54
4.5 Vortical gust circulation downstream of the pitching airfoil.	55
4.6 Fit of vortical gust circulation downstream of the pitching airfoil.	56
4.7 Velocity profiles of vortices downstream of the pitched airfoil.	57
4.8 Unwrapped x -velocity downstream of the airfoil, cross-plane	57

4.9	Flow modification by static plate.	59
4.10	Flow behind 5 cm passing plate	61
4.11	Flow behind 10 cm passing plate	62
4.12	Sketches of flow around the heaving plate.	63
4.13	Vorticity around heaving plate.	64
4.14	Vortical gust circulation behind plate.	65
4.15	Fit of vortical gust circulation behind plate.	66
4.16	Reynolds number variation of heaving plate.	67
4.17	Unwrapped gusts downstream of the plate	68
4.18	Vortical gust circulation downstream of the plate.	69
4.19	Fit of vortical gust circulation downstream of the plate.	70
4.20	Speed and y -position of vortices	71
4.21	Unwrapped gusts downstream of the plate	72
4.22	Unwrapped gusts downstream of the plate	73
4.23	Velocity profiles of vortices downstream of the plate.	74
4.24	Vortical gust circulation downstream of the plate.	75
4.25	Fit of vortical gust circulation downstream of the plate.	76
4.26	Unwrapped gusts downstream of the plate, cross-plane	77
4.27	Parameter space of gust generator	78
4.28	Behavior of flow around heaving gust generator	81
4.29	Comparison of gust generators	82
5.1	Example of force processing	84
5.2	Diagram of baseline force experiments	86
5.3	Baseline forces on the test article	87
5.4	Baseline drag polars of the test article	88
5.5	Forces due to passing plate's wake	90
5.6	Envelope of forces due to passing plate's wake	91
5.7	Example of pitching gust interaction	93
5.8	C_L of gust interaction from pitching airfoil	95
5.9	Mean-subtracted C_L from the pitching airfoil gusts, $\alpha = 0$	97
5.10	Mean-subtracted C_L from the pitching airfoil gusts, $\alpha = 5^\circ$	98
5.11	Mean-subtracted C_L from the pitching airfoil gusts, $\alpha = 5^\circ$	99
5.12	Example of heaving gust interaction	102
5.13	C_L of gust interaction from heaving plate	103
5.14	C_L from the heaving plate: recovery times	105
5.15	Scaled C_L from the heaving plate: $\alpha = 0, S = 0.1$	106

5.16	Scaled C_L from the heaving plate: $\alpha = 5, S = 0.1$	107
5.17	Scaled C_L from the heaving plate: $\alpha = 5, S = 0.25$	108
5.18	Scaled C_L from the heaving plate: $\alpha = 10, S = 0.1$	109
5.19	Suggestions for best use of generators	111
C.1	Simulated $C_L(t)$ of vortex-wing interaction for $\alpha = 0^\circ$	150
C.2	Simulated $C_L(t)$ of vortex-wing interaction for $\alpha = 5^\circ$	151
C.3	Simulated $C_L(t)$ of vortex-wing interaction for $\alpha = 10^\circ$	152
C.4	Flow around heaving plate with Reynolds number variation.	153
C.5	Paths of vortices from pitching: t-x	154
C.6	Paths of vortices from pitching: t-y	155
C.7	Baseline forces on the test article	156
C.8	C_D of pitching gust interaction	157
C.9	C_L of pitching gust interaction	158
C.10	C_M of pitching gust interaction	159
C.11	C_D envelope of pitching gust interaction	160
C.12	C_L envelope of pitching gust interaction	161
C.13	C_M envelope of pitching gust interaction	162
C.14	C_D of heaving gust interaction	163
C.15	C_L of heaving gust interaction	164
C.16	C_M of heaving gust interaction	165
C.17	C_D envelope of heaving gust interaction	166
C.18	C_L envelope of heaving gust interaction	167
C.19	C_M envelope of heaving gust interaction	168

LIST OF TABLES

<i>Number</i>	<i>Page</i>
2.1 List of aerodynamic models.	27
2.2 Execution time for each model, normalized by that of the analytic equations.	29
4.1 Circulation of the vortices compared in Figure 4.29. The pitching airfoil has $c_a = 10$ cm, and the heaving plate has $c_p = 5$ cm.	79
A.1 Parameters of Experiment SA-1.	132
A.2 Parameters of Experiment PGG-2.	133
A.3 Parameters for Experiment HGG-1	133
A.4 Parameters for Experiment HGG-2	134
A.5 Parameters for Experiment HGG-3	134
A.6 Parameters for Experiment HGG-4	135
A.7 Parameters for Experiment HGG-6	135
A.8 Parameters for Experiment HGG-7	136
A.9 Parameters for Experiment HGG-8	137
A.10 Parameters for Experiment HGG-9	138
A.11 Parameters for Experiment HGG-10	139

NOMENCLATURE

- α . Angle of attack of airfoil.
- α_1 . Initial angle of the pitching airfoil.
- α_2 . Final angle of the pitching airfoil.
- α_{eff} . Effective angle of attack of moving plate: $\arctan(S)$.
- $\alpha_{upstream}$. Angle of attack of the upstream airfoil.
- Δx . Streamwise distance between plate and airfoil.
- Γ_v . Circulation of the shed vortex.
- $\Gamma_{airfoil}$. Bound circulation of the airfoil.
- Γ_{plate} . Bound circulation of the plate.
- ν . Kinematic viscosity of the fluid.
- ω . Vorticity.
- ϕ . Wagner's function.
- ρ . Density of the fluid.
- τ . Dimensionless time: t/t_c .
- τ_a . Dimensionless time, with airfoil's convection time.
- τ_c . Dimensionless time, with plate's convection time.
- b . Wetted span of wing or plate.
- c_a . Airfoil chord length.
- C_D . Drag coefficient.
- C_L . Lift coefficient.
- c_p . Plate chord length.
- $C_{D,est}$. Drag coefficient estimated from the measured moment due to lift.
- $C_{L,est}$. Lift coefficient estimated from the measured moment due to lift.
- $C_{L,qs}$. Quasi-steady lift coefficient.
- $C_{L,wag}$. Lift coefficient calculated using the Wagner function.

- H . Heaving distance ratio: h/c .
- h . Plate heave distance.
- h_0 . Initial plate offset from wall.
- L . Lift.
- Re_c . Reynolds number with respect to length c : Uc/ν .
- S . Heaving speed ratio: V_{heave}/U .
- T . Heaving time ratio: t_{heave}/t_c .
- t . Time.
- t_c . Chordwise convective time: c/U .
- t_p . Normalized pitching time: t_{pitch}/t_c .
- t_{accel} . Plate acceleration time.
- t_a . Normalized plate acceleration time: t_{accel}/t_c .
- t_{heave} . Heaving time: h/V_{heave} .
- t_{pitch} . Time needed to pitch 95% of the way from the initial to final angle.
- U . Freestream speed.
- u . Velocity in the x direction.
- v . Velocity in the y direction.
- V_{heave} . Plate heave speed: SU .
- $w_{3/4}$. Downwash at the 3/4-chord point.
- x' . Distance computed from unwrapping.
- x_r . Distance from the leading edge to point of rotation.
- y_a . Vertical position of the airfoil.
- y_v . Vertical position of the incoming vortex.
- y_{peak} . Position of maximum displacement of the heaving plate.
- y_{plate} . Vertical position of the upstream plate.
- $y_{upstream}$. Position of the pitching airfoil.
- E-TL**. Extended Tchieu-Leonard model of unsteady aerodynamics.

PIV. Particle image velocimetry.

QS-TAT. Quasi-steady thin airfoil theory.

S-TAT. Steady thin airfoil theory.

TAT. Thin airfoil theory.

TL. Tchieu-Leonard model of unsteady aerodynamics.

UPM. Unsteady panel method.

W-TAT. Wagner function in thin airfoil theory.

Chapter 1

INTRODUCTION AND BACKGROUND

1.1 Introduction

Aircraft and creatures with wings agree: gusts are important. Were the world simpler, creatures and craft could fly through a world without variations in the wind's velocity, and without the complicated structural and aerodynamic effects that such variations incur. Unfortunately, unsteadiness is a fact of the high Reynolds number flows around us. To better cope with such unsteadiness, research is necessary to examine the aerodynamic response of wings to gusts, as well as to create analogues of those gusts for further research. Significant research has been performed investigating transverse and lateral gusts, but there has been less emphasis on gusts with a single dominant vortex-like structure, particularly experimentally. The exception is rotorcraft research, where blades periodically interact with the wake of their forerunners. Vortical gusts are also potentially significant when an aircraft passes the wake of another. Improved knowledge of the interaction between an airfoil and a vortical gust can lead to better models of such interaction, and potentially safer aircraft.

This thesis describes the theoretical and experimental generation of vortical gusts, and how such gusts interact with an airfoil. The comparison of theory to experiments is vital, as it validates or invalidates the applicability of theory to a physical system.

1.2 Gusts in the Wild

There is a range of different types of gusts, both natural and man-made. One type of gust is natural unsteadiness in the atmosphere. Donely [16] wrote an early review of the topic which showed that atmospheric gusts are roughly independent of direction. The velocity profiles of these gusts were well modeled as sinusoidal or triangular functions. Etele [20] classified different scales of unsteady wind as part of a modeling effort: geostrophic, atmospheric boundary layer, and small-scale random turbulence. Two commonly used models of continuous gusts are the Dryden [17] and von Kármán [70] wind turbulence models. These used the power spectral densities of measured atmospheric turbulence to specify stochastically variable velocities in three dimensions. In contrast to continuous gusts, the Federal Aviation Administration [1] has defined a discrete gust as a change in the flow's velocity

scaled with one period of a one-minus-cosine function:

$$v = \begin{cases} 0, & x < 0, \\ \frac{V_m}{2} \left(1 - \cos \frac{\pi x}{d}\right), & 0 \leq x \leq d, \\ V_m, & x > d. \end{cases} \quad (1.1)$$

Here, V_m is the final velocity, and d is the length over which the flow accelerates.

Other gusts are due to man-made structures and vehicles, such as the unsteady flows around large buildings [26] or the wakes of aircraft [61] or their rotors [59]. This thesis focuses on vortical gusts, which are discussed in section 1.4.4.

1.3 Theoretical Unsteady Aerodynamics

Typically, research on gusts has focused on mitigating the effects of undesired unsteadiness in the flow around bodies. Through a change in the reference frame, certain types of unsteadiness in the flow can be modeled instead as motion of the body. Thus, studies of desired body motions can be used to better understand the effects of external flow unsteadiness.

Early studies of unsteady aerodynamics were extensions of steady two-dimensional thin airfoil theory [22]. As with steady thin airfoil theory, these works had the same limitations: thin airfoils; attached, inviscid, incompressible flow on the body; small angles of attack; a zero-thickness wake that leaves the body at a sharp trailing edge and proceeds downstream with no vertical deflection; and irrotational flow outside of the body and wake. This model incorporates knowledge of the physical flow in two ways: viscosity is the physical cause of flow smoothly leaving the sharp trailing edge of an airfoil, as well as the cause of the wake.

Steady thin airfoil theory estimates the lift coefficient as a function of the linearized downwash at the 3/4-chord point, $w_{3/4}$:

$$\begin{aligned} w_{3/4} &\approx U \sin(\alpha), \\ &= U\alpha, \end{aligned} \quad (1.2)$$

$$\begin{aligned} C_{L,steady} &= \frac{2\pi}{U} w_{3/4}, \\ &= 2\pi\alpha. \end{aligned} \quad (1.3)$$

Here, U is the freestream velocity and α is the airfoil's angle of attack.

For unsteady maneuvers or flows, the downwash must be extended to include the effects of varying the angle of attack and vertical position of the plate:

$$w_{3/4,unsteady}(t) = U\alpha(t) - \frac{dy_a(t)}{dt}y'_a(t) + \left(\frac{3}{4}c_a - x_r\right)\alpha'(t). \quad (1.4)$$

Here, y_a is the vertical position of the airfoil, and the prime, $()'$, is used to denote differentiation with respect to time. The chord length of the airfoil is c_a , and x_r is the distance from the plate's leading edge to its axis of rotation. The quasi-steady estimate of the lift using this downwash is:

$$\begin{aligned} C_{L,qs}(t) &= \frac{2\pi}{U}w_{3/4,unsteady}(t), \\ &= 2\pi\alpha(t) - 2\pi\frac{y'_a(t)}{U} + 2\pi\frac{\alpha'(t)}{U}\left(\frac{3}{4}c_a - x_r\right). \end{aligned} \quad (1.5)$$

This is reasonable if the dynamics are sufficiently slow, but it neglects the conservation of circulation [67], and in doing so, the effect of the changing wake on the airfoil.

Wagner [72] approached this problem by initially addressing the case of an airfoil instantaneously changing its horizontal speed or angle of attack. His work led to what is now known as the Wagner function, approximated by Jones [40] as

$$\phi(\tau) \approx \begin{cases} 0, & t < 0, \\ 1 - 0.165e^{-0.091\tau_a} - 0.335e^{-0.6\tau_a}, & t \geq 0. \end{cases} \quad (1.6)$$

This describes how the lift on the airfoil changes over time due to such an acceleration at $\tau_a = 0$. In this equation, $\tau_a = t/(c_a/U)$ is the time nondimensionalized by the convection time along the airfoil's chord. As can be seen in Figure 1.1, half of the final lift is gained instantaneously, and the remainder is attained asymptotically.

Since this solution relies on the linearity of the flow's response to the dynamics, the Wagner function can be used, via convolution in Duhamel's integral [16], to compute the airfoil's reaction to more complex motions:

$$C_{L,wag}(t) = \frac{2\pi}{U}\left(w_{3/4}(t)\phi(0) + \int_0^\infty w_{3/4}(t-s)\phi'(s)ds\right). \quad (1.7)$$

Later work by Theodorsen [66] described the forces on a wing due to harmonic oscillation. In conjunction with an estimate of the added mass of fluid entrained by the

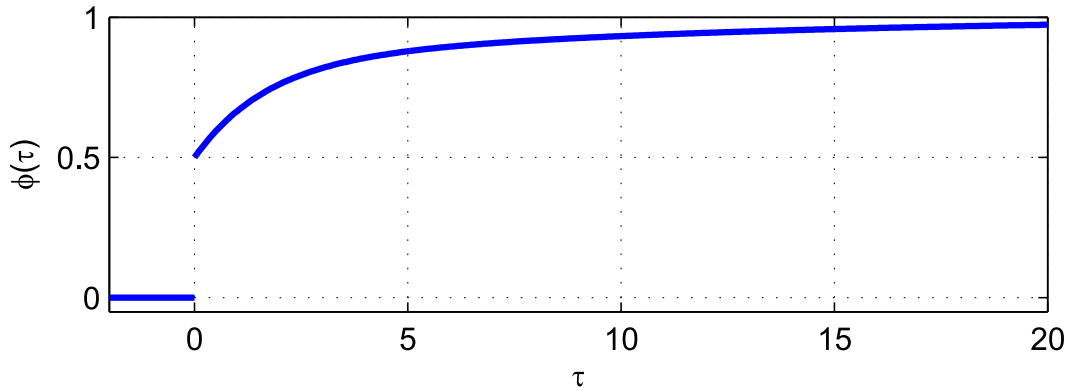


Figure 1.1: Plot of the Wagner function.

motion and a model of the wing's structural properties, this led to a powerful means of predicting flutter behavior. Jones [40] and Garrick [23] provided useful approximations of the Theodorsen and Wagner functions, expanding their use significantly. The related problem of a sharp-edged transverse gust was studied by Küssner [45]. Sears and von Kármán [71] then analyzed the response of an airfoil to a harmonic vertical gust. Isaacs [35, 36] and Greenberg [31] extended Theodorsen's analysis to oscillating flows and airfoils. Together, these analyses formed the basis for future work on unsteady flows. A recent extension of the unsteady airfoil problem by Tchieu [64] and Leonard [65] successfully used a conservation of impulse approach to computationally model the evolution of the airfoil's wake, discretized into point vortices.

1.4 Studies of Gusts and Unsteady Aerodynamics

1.4.1 Modeling Freestream Unsteadiness with Body Motion

A number of studies have compared the effects of an unsteady freestream against analogous airfoil motions. Granlund et al [29] directly compared an unsteady freestream with corresponding airfoil motions, and found that gust response can be properly studied in a steady freestream. Perrotta and Jones [54] also compared the response of an airfoil to a transverse gust to equivalent airfoil motion, and found some agreement, though future work was deemed necessary.

1.4.2 Classical Unsteadiness

The impulsively started flat plate problem has been investigated in depth, often in efforts to improve understanding of flapping flight. Beckwith, Pitt Ford, and Babinsky [5, 56] examined this at different angles of attack and at final Reynolds numbers of 30,000 and 60,000. These studies showed that the lift on the plate,

and the bound circulation, matched the Wagner function when the steady-state flow around the plate was unstalled. When the plate was stalled, the lift grew much more quickly. Ford and Babinsky [55,57] also studied the lift on accelerated flat plates at non-zero angles of attack, particularly focusing on the growth of the leading edge vortex. At $\alpha = 45^\circ$, the acceleration profile had a strong effect on the lift's rate of increase. At lower $\alpha = 15^\circ$, the wake circulation was found to reasonably match Wagner's function, though the lift also contained non-circulatory effects. Mancini et al [47] studied this problem with flat plates of aspect ratio 4, and confirmed that Wagner's function (modified to account for the finite aspect ratio) did hold for low angles of attack, after an initial transient caused by the leading edge vortex.

The effects of unsteady freestream velocities and airfoil motions have been examined extensively at the Illinois Institute of Technology's unsteady flow wind tunnel by Williams, Kerstens, and others. By opening and closing shutters downstream of the test section [74,75], harmonic variation of the freestream velocity could be imposed. The airfoil was also actuated in pitch and plunge. In this facility, Granlund et al [29] examined the response of a thin airfoil to such sinusoidal gusts and found good agreement with Greenberg's formula when the flow was attached. At higher angles of attack, the airfoil statically stalled, resulting in lift fluctuation amplitudes that were significantly higher than theory predicted. In a separate facility, Strangfeld et al [62] found a good match with Greenberg's formula for high amplitudes of freestream fluctuations at small angles of attack.

The transverse sharp-edged gust problem has been examined for decades. One of the earliest means was a NACA gust tunnel constructed in 1937, which launched model aircraft with a catapult over a vertical blower [15] to simulate transverse gusts. This was succeeded in 1945 by a larger version of the system [16]. These early studies found reasonable matches between theory and experiments. Similarly, Perrotta and Jones [54], used a set of jets mounted on the bottom of a tow tank to provide a limited region of transverse velocity.

The problem of the harmonic transverse gust has also been examined experimentally and numerically. The typical approach [8] to create such gusts is to harmonically pitch vanes upstream of the test section. A small number of such vanes [6,33] created distinct vortices, which yielded a transverse velocity far from the vortices. Golubev et al [25] numerically modeled two-dimensional sharp-edge and harmonic variations in the oncoming flow interacting with an airfoil at $Re_c = 10,000$. For low wing loading, the responses to oscillating streamwise and transverse flows matched

inviscid predictions, apart from the low-frequency oscillations which appeared to create a large dynamic-stall effect. Baik et al found a good match with theory [3,4] for pitching and plunging airfoils, rather than in oscillating flows. The exception was for leading-edge separated flows, which were found to almost entirely avoid the Wagner function's slow growth.

A large field of literature has grown studying flapping wings, often motivated by power extraction or generation of thrust. Triantafyllou's review [68] of experimental work on biomimetic foil motions described the general state of the art for sinusoidal pitching and heaving. Rival et al [58] related the LEV formation on such a heaving airfoil to Dabiri's [13] optimal vortex formation time concept. The pattern of shed vortices from a flapping airfoil can be quite interesting, as shown in the soap film experiments by Schnipper et al [60]. Eldredge et al's study [19] of a pitch up, pitch-down motion provided a discrete alternative to harmonic pitching. A related motion was used by Granlund et al [30] to examine the effect of different pitching rates on a flat plate. Dunne et al [18] examined experimentally, in a linear frame, the flow around an analogue of a vertical axis wind turbine. Tsai [69] numerically studied a similar, though rotating, system at lower Reynolds numbers. Choi [10] numerically examined the evolving flow around a heaving wing, and applied control techniques to maximize lift by tailoring its pitching.

The field of flapping wings is not limited to two dimensions. Jones et al [38,39,48], examined the behavior of the leading edge vortex on rotating wings with finite aspect ratios. Yu et al [76] extended study of the pitch up-down to a finite aspect ratio wing with different planform shapes.

1.4.3 Gust Response and Control

As would be expected, unsteady aerodynamics researchers have studied how to model the response of aircraft to gusts, as well as how to counter the effects of gusts. The one-minus cosine approximation of a gust has been used by Etele [20] and Moulin [51], among others, in a number of computational models of gust response. Brunton et al [7] measured the response of airfoils to an unsteady freestream, and generated a model of the system dynamics. Though the Theodorsen model was a reasonable approximation, the formally identified dynamics gave a more accurate representation of the system's behavior. Williams, Colonius, et al [43,73] used system-identification techniques to find a model of the system dynamics for an airfoil in an unsteady freestream with control of surface blowing. This model was

then used to reduce the forces on the wing in response to the unsteady freestream. An additional means of extracting energy from flows is the use of gust soaring, where small aircraft gain kinetic and potential energy from unsteadiness in the wind. Langelaan [46] and Patel et al [52] created simulated systems in which small aircraft could fly for more time by extracting energy from such unsteadiness.

1.4.4 Vortex Interaction

With regard to vortices interacting with a body, Rockwell's [59] review of the topic is an excellent primer. He reviewed the basic types of encounters between an extended body and a line vortex: parallel, perpendicular, and normal to the body. These can be thought of as, respectively, a two-dimensional point vortex passing over an airfoil, a trailing vortex from an airplane interacting with a following aircraft, and a wing cutting through a vortex shed from a tall tower. This thesis focuses on the first class of vortex interactions, though there is a rich field of experimental and numerical data for the other classes of interactions. In the parallel interaction, the size of the vortex, with respect to the body, is quite important. If the vortex is much larger than the body, the body can still significantly disrupt the structure of the vortex. If the vortex is much smaller than the chord length of the body, it will likely remain fairly undisturbed if it is farther than one half chord from the surface. Closer in, the vortex will be sheared and possibly break apart, as well as disrupt the boundary layer of the body. Though this is ideally a two-dimensional encounter, small three-dimensional variations in the vorticity will be enhanced by vortex stretching, potentially resulting in significant three-dimensionality.

The study of interactions with wing-parallel vortices is often motivated by rotorcraft, as each blade is typically in the wake of its forerunner. The vortex chopping causes significant noise, which would ideally be reduced. Recently, Morvant et al [50] and Falissard et al [21] examined compressible blade-vortex interactions with novel numerical schemes. Related transonic experiments have been carried out by Kalkhoran et al [41], where a single vortex was created upstream of the test article by pitching an airfoil.

Experimentally, the typical method of generating vortical gusts has been to either have an upstream body shedding von Kármán vortices, or to pitch an airfoil upstream of the test article. Straus et al [63] used the pitching method to test such interactions at a Reynolds number of 375,000 for the downstream airfoil, and 210,000 for the pitching airfoil, which was three chord-lengths upstream. The phase-averaged

pressures on the test article sometimes matched the results of an unsteady panel method with discrete vortices, except for cases where the flow appeared to separate, and where the vortex had clockwise rotation. Golubev et al [24–26] simulated vortex interactions at Reynolds numbers of 10,000 and 60,000, where the size of the vortex was comparable to that of the airfoil. These again found that larger, stronger, closer vortices resulted in larger resulting forces on the airfoil, even up to creating stall-like flow around the airfoil. At the higher Reynolds number, the inclusion of three-dimensionality in the simulations reduced some of the oscillations in the forces, but the overall force history was quite similar to the two-dimensional simulation.

The current state of the art is well summarized in a paper by Peng and Gregory [53], which also used the pitching airfoil method for vortex generation with a downstream airfoil at $Re_c \approx 100,000$. They divided the area around the airfoil into regions depending on how deformed the incoming vortex becomes, and measured the decay of the vortex. When very close to the airfoil, the vortex strongly interacted with the boundary layer. Farther away, the interaction was less viscosity-driven. Overall, they found that the separation distance had the strongest impact on the behavior of the vortex.

Experimental studies on vortex interactions with airfoils in high-lift configurations by Klein et al [44] and Hahn et al [32] also used the pitching-plate method of gust generation. They found that these vortices could cause flow separation at the trailing edge, and a slow return to the pre-disturbance pressure distribution. The effect of finite aspect ratio on the wing-vortex interaction was numerically studied by Gordnier and Visbal [27], particularly focusing on head-on collisions and transitional flow at $Re_c = 200,000$. The collision split the vortex, disturbing both the upper and lower boundary layers. The typical flow around the airfoil reasserted itself over roughly eight convective time units.

1.5 Summary

This thesis describes the use of a new kind of vortex generator: rather than pitching an airfoil that is otherwise fixed, a transversely moving flat plate changes direction to release a vortex. The pitching system has the disadvantage that the flow around the vortex generator continues to interact with the test article. By releasing a vortex and moving away, the novel vortex generator investigated in this thesis moves its wake to the side of the tunnel, rather than continuously releasing it in front of the

test article. Along with the expected differences in the positions of their wakes, these two methods have significantly different means of vortex generation, and so must be rigorously examined.

The research described in this thesis aims to better understand the generation of vortical gusts, using the pitching and heaving gust generators, and to study their effects on a wing. The primary focus of this thesis is experimental work at a chordwise Reynolds number of 20,000. This is a high enough Reynolds number that simulations across a wide range of parameters would be prohibitively expensive, whereas similar experiments can be completed relatively quickly.

With these goals in mind, the thesis is organized in the following manner. Chapter 2 applies the tools of theoretical and numerical unsteady aerodynamics to examine the behavior of the pitching airfoil, heaving plate, and the interaction between an airfoil and an oncoming vortex. Chapter 3 describes the equipment used for experimental investigations of these problems, and Appendix A details the executed experiments. Chapter 4 examines the results of experimental vortex generation, and compares the two systems. Chapter 5 describes the response of a downstream airfoil to these vortices. Conclusions and suggestions for future work are discussed in Chapter 6.

Chapter 2

ANALYTICAL MODELS AND SIMULATIONS

2.1 Introduction

This chapter investigates simplified potential-flow based models of the pitching airfoil, the heaving plate, and a vortex passing an airfoil. Schematics of these scenarios are shown in Figure 2.1. These models aim to predict the circulation of the vortical gusts generated by the pitching airfoil and heaving plate, as well as the effect of such a gust on a wing.

Potential flow models were chosen for their ease of execution, as full simulations or experiments are costly in terms of time and equipment. Three classes of models are described: analytic thin airfoil theory, a numerical model with simplified wake evolution, and unsteady panel method simulations with dynamic wakes. As these are inviscid models, the streamwise force is neglected in these analyses. In reality, an unsteady wake region with reduced average speed would develop behind the generators.

This chapter will introduce each modeling approach and conclude with comparisons of their application to the pitching airfoil, heaving plate, and airfoil-vortex interaction scenarios.

2.2 Thin airfoil theory models

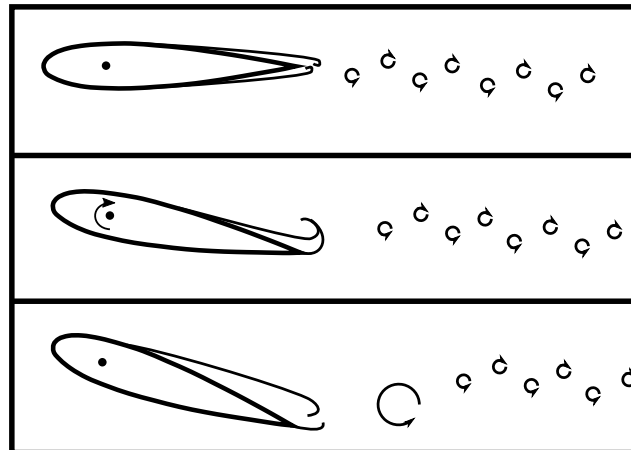
In this section, the gust generators and gust-wing interaction are examined through the lens of thin airfoil theory (TAT). The circulation bound to the aerodynamic body is used to determine the circulation that is shed when the airfoil pitches or the plate changes directions. The vortex-airfoil interaction provides estimates of the variation in lift on the airfoil.

2.2.1 Pitching Airfoil

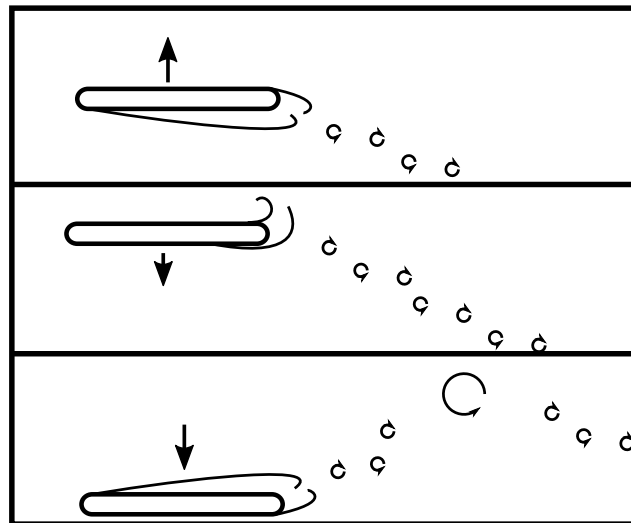
A simple, smooth trajectory for the angle of attack of a pitching airfoil is described by the arctangent function. This trajectory and its parameters are as follows:

$$t_c = c_a/U, \tag{2.1a}$$

$$t_p = t_{pitch}/t_c, \tag{2.1b}$$



(a) Sequential sketches of the generation of a vortical gust by pitching an airfoil. At top is the airfoil before pitching, with regular vortex shedding behind it. In the center, the airfoil is in the middle of pitching, with a vortex rolling up near the trailing edge. In the final frame, the vortex is convecting downstream, as the flow around the airfoil establishes itself.

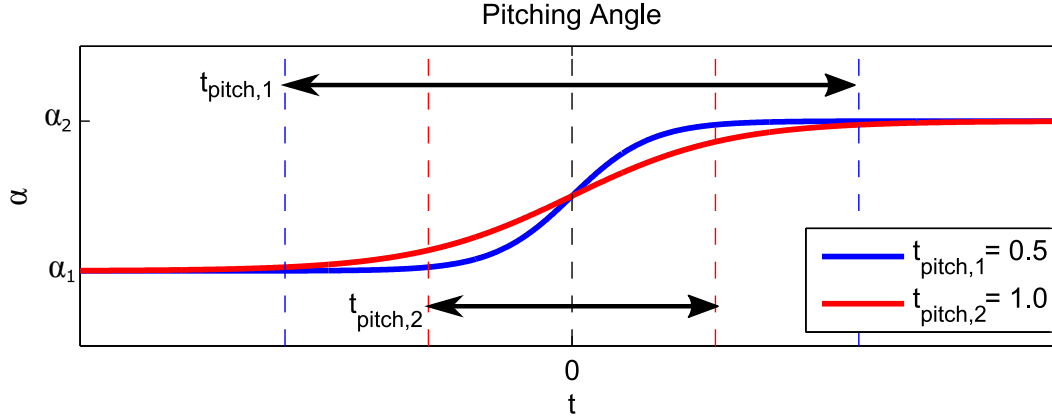


(b) Sequential sketches of the generation of a vortical gust by heaving a flat plate. In the top frame, the plate is moving upward, with a wake of regularly shed vortices. In the second, the plate has just reversed direction, and is forming a vortex on the upper surface. In the third frame, the plate continues moving downward as the primary vortex convects downstream.

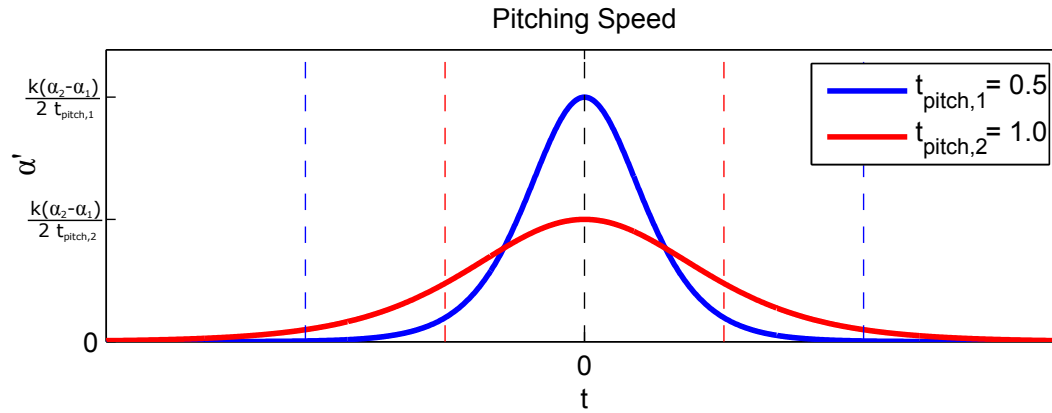


(c) Interaction between an airfoil and a vortex. The dotted line is the path of the vortex as it moves past the airfoil.

Figure 2.1: Schematics of the studied flows. Panels *a* and *b* show the methods of generating vortical gusts. Panel *c* shows a vortex passing an airfoil.



(a) Two trajectories of the pitching airfoil's angle.



(b) Angular speeds of the two trajectories.

Figure 2.2: Examples of the pitching trajectory and speed of the airfoil. Two pitching times are illustrated.

$$\tau = t/t_c, \quad (2.1c)$$

$$k = 2 \operatorname{arctanh}(19/20), \quad (2.1d)$$

$$\alpha = \alpha_1 + \frac{1}{2}(\alpha_2 - \alpha_1) \left(1 + \tanh \left(\frac{k\tau}{t_p} \right) \right). \quad (2.1e)$$

Here, the freestream velocity is U , the chord length of the airfoil is c_a , the initial and final angles of attack are α_1 and α_2 , and the airfoil completes 95% of its motion over time t_{pitch} . Two examples of this motion, with different pitching times, are in Figure 2.2.

Through the removal of vertical motion from Equation 1.4, the quasi-steady lift of the airfoil can be modeled as

$$C_{L,qs}(t) = 2\pi\alpha + \frac{2\pi}{U} \frac{d\alpha(t)}{dt} \left(\frac{3}{4}c_a - x_r \right). \quad (2.2)$$

As it is quasi-steady, this estimate neglects the effect of the wake. An exact solution of Equation 1.7, including the Wagner function's estimate of the wake's effects, has proven elusive for this trajectory. If the airfoil pitches quickly, that is if $t_{pitch} < t_c$, and if the change in angle of attack is small, then an accurate approximation is

$$C_{L,wag}(t) \approx \begin{cases} \frac{1}{2} (2\pi\alpha_1 + C_{L,q_s}), & t < -t_{pitch}/2, \\ 2\pi\alpha_1 + (C_{L,q_s} - 2\pi\alpha_1)\phi(t + t_{pitch}/2), & t \geq -t_{pitch}/2. \end{cases} \quad (2.3)$$

This retains the effect of the pitching speed, resulting in a sharp peak in the lift while the airfoil is in motion.

If the pitching is assumed to be instantaneous at $t = 0$, and the pitching velocity is neglected, the lift coefficient may be approximated as a simple function of the Wagner function:

$$C_{L,inst,wag}(t) \approx \begin{cases} 2\pi\alpha_1, & t < 0, \\ 2\pi(\alpha_1 + (\alpha_2 - \alpha_1)\phi(t)), & t \geq 0. \end{cases} \quad (2.4)$$

The bound circulation of the airfoil, $\Gamma_{airfoil}$, is determined from the Kutta-Joukowski theorem as in Equation 2.5, where b is the span of the airfoil.

$$\begin{aligned} \Gamma_{airfoil} &= -L / (\rho U b), \\ &= -C_L \frac{c_a U}{2}. \end{aligned} \quad (2.5)$$

By Kelvin's theorem of conservation of circulation, the circulation of the shed vortex, Γ_v , is approximated as the negative of the change in bound circulation over the airfoil's motion. Using either the instantaneous or smooth pitching approximation, with the noted assumptions, yields

$$\begin{aligned} \Gamma_v &\approx - \left(\Gamma_{airfoil}(t_{pitch}/2) - \Gamma_{airfoil}(-t_{pitch}/2) \right), \\ &\approx \frac{1}{2} \pi (\alpha_2 - \alpha_1) c_a U. \end{aligned} \quad (2.6)$$

This simple relation suggests that the circulation of a shed vortex should scale linearly with the change in angle of attack and chord length of the airfoil. The freestream speed, airfoil length, and change in angle of attack can thus be used to tailor the circulation of the shed vortex.

2.2.2 Heaving Plate

The trajectory of the heaving plate in this thesis is specified by a version of Eldredge's smooth motion equation [19]. This allows for constant speed over most of the motion, but is smoothed in the corners to reduce the magnitude of acceleration. The plate's motion and speed are defined in Equation 2.7:

$$t_c = c_p/U, \quad (2.7a)$$

$$t_a = t_{accel}/t_c, \quad (2.7b)$$

$$T = t_{heave}/t_c, \quad (2.7c)$$

$$S = V_{heave}/U, \quad (2.7d)$$

$$\tau = t/t_c, \quad (2.7e)$$

$$k = 2 \operatorname{arctanh}(19/20), \quad (2.7f)$$

$$y_p(t) = h_0 + \frac{c_p t_a S}{2k} \log \left(1 + \sinh \left(\frac{kT}{t_a} \right)^2 \cosh \left(\frac{k\tau}{t_a} \right)^{-2} \right), \quad (2.7g)$$

$$y'_p(t) = \frac{1}{2} S U \left(\tanh \left(\frac{k(\tau + T)}{t_a} \right) + \tanh \left(\frac{k(\tau - T)}{t_a} \right) - 2 \tanh \left(\frac{k\tau}{t_a} \right) \right). \quad (2.7h)$$

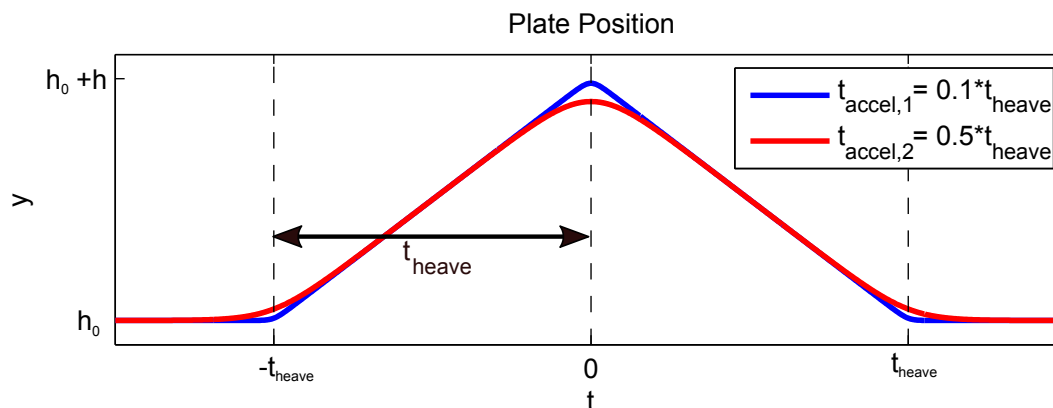
Here, the chord length of the plate is c_p and three parameters are used: the dimensionless heaving time T , the dimensionless heaving velocity S , and dimensionless acceleration time t_a . The parameter k was defined such that 95% of the velocity change occurs over the acceleration time t_{accel} . The initial and final position of the plate is h_0 .

The trajectory can alternatively be parameterized in terms of the dimensionless heaving distance H , rather than T , where $H = h/c_p = TS$. Examples of this trajectory with different values of t_a are shown in Figure 2.3.

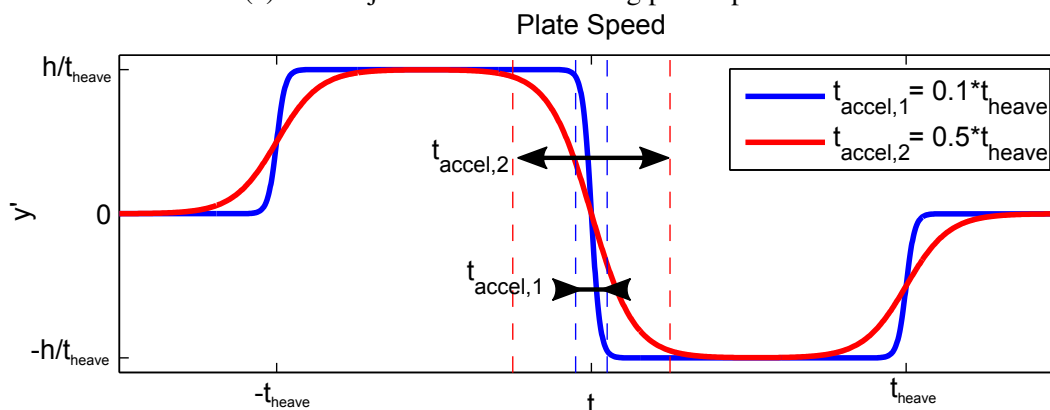
As long as $t_a < 1 \ll T$, and the details of the change in direction are unnecessary, then the velocity and position of the plate can be approximated as

$$y_p(t) \approx \begin{cases} h_0 - c_p S (|\tau| - T), & |t| < t_{heave}, \\ h_0, & \text{otherwise,} \end{cases} \quad (2.8)$$

and



(a) Two trajectories of the heaving plate's position.



(b) Speeds of the two trajectories.

Figure 2.3: Examples of the heaving trajectory and speed of the plate. Two acceleration times are illustrated, for the same heaving time.

$$y'_p(t) \approx \begin{cases} US, & -t_{heave} < t < 0, \\ -US, & 0 < t < t_{heave}, \\ 0, & \text{otherwise.} \end{cases} \quad (2.9)$$

When the heaving plate accelerates, it changes its circulation and must shed a corresponding amount into its wake. The primary vortex is shed when the plate reverses direction at $t = 0$, and additional starting and stopping vortices are shed near $t = \pm t_{heave}$. The following analysis relies on the assumptions of unsteady thin airfoil theory as described in the previous chapter, including that S is small. The general form of the downwash, $w_{3/4}$ (Equation 1.4), is simplified to reflect the constant zero geometric angle of attack. Using the approximate trajectory, the

quasi-steady lift coefficient can be approximated as

$$C_{L,qs,approx}(t) \approx \begin{cases} -2\pi S, & -t_{heave} < t < 0, \\ 2\pi S, & 0 < t < t_{heave}, \\ 0, & \text{otherwise.} \end{cases} \quad (2.10)$$

Since this is an unsteady problem, use of the Wagner function should improve estimation of the lift over time. Equation 2.11 is an accurate approximation of the integral with the Wagner function in Equation 1.7, again while $t_a < 1 \ll T$:

$$C_{L,wag}(t) \approx \begin{cases} 0, & t < -t_{heave}, \\ -2\pi S \phi(t + t_{heave}), & -t_{heave} \leq t < 0, \\ 2\pi S (1 + 2\phi(t_{heave}) (\phi(t) - 1)), & 0 \leq t < t_{heave}, \\ -2\pi S (1 - 2\phi(t_{heave}))^2 (\phi(t - t_{heave}) - 1), & t_{heave} \leq t. \end{cases} \quad (2.11)$$

The case where $T \lesssim 1$ is more complicated, as the different phases of motion significantly interfere with each other.

The bound circulation of the plate, Γ_{plate} , and the circulation of the shed vortex, Γ_v , may be estimated analogously to the pitching airfoil. Using either the quasi-steady or unsteady approximation yields the same results:

$$\Gamma_{plate}(t) = -C_L(t) \frac{c_p U}{2}, \quad (2.12)$$

$$\begin{aligned} \Gamma_v &\approx \Gamma_{plate}(0^-) - \Gamma_{plate}(0^+), \\ &\approx \pi c_p S U. \end{aligned} \quad (2.13)$$

This indicates that the circulation of the shed vortex should scale linearly with the heaving speed and chord length of the plate. Similarly, the vortices shed at the start and end of motion should have half of that absolute circulation, but of opposite sign. The freestream speed, plate length, and heaving speed can thus be used to tailor the circulation of the shed vortex.

2.2.3 Point Vortex Model of Airfoil-Vortex Interaction

The simplest model of an airfoil-gust interaction involves a 2D point vortex passing over a point, the origin, chosen to represent the leading edge of an airfoil of chord length c_a . We assume that the vortex, at instantaneous position x_v , moves only with the freestream velocity, and is parameterized by its constant vertical position, y_v , and circulation, Γ_v . Given the airfoil's angle of attack, α , the quasi-steady downwash at the 3/4-chord point of the airfoil can be modified to include the effect of the oncoming vortex:

$$x_v = Ut, \quad (2.14a)$$

$$v_{v,3/4} = \frac{(3c_a/4 - x_v)\Gamma_v}{2\pi((3c_a/4 - x_v)^2 + y_v^2)}, \quad (2.14b)$$

$$w_{3/4} = U\alpha + v_{v,3/4}. \quad (2.14c)$$

The quasi-steady lift on the airfoil can then be computed as:

$$C_{L,qs}(t) = \frac{2\pi}{U} w_{3/4}(t). \quad (2.15)$$

Simple differentiation yields the times and values of the quasi-steady lift's extrema:

$$C_{L,qs,extrema} \left(\frac{3c_a \mp 4y_v}{4U} \right) = 2\pi\alpha \pm \frac{\Gamma_v}{2Uy_v}. \quad (2.16)$$

This shows that the farther away the vortex is (large $|y_v|$), the earlier, wider, and weaker the lift peak is. The lift reaches its extrema when the vortex is at a 45° angle from the horizontal with respect to the 3/4-chord point.

Inclusion of the Wagner function yields an integral equation that models the effect of the wake:

$$C_{L,wag}(t) = \frac{2\pi}{U} \left(w_{3/4}(t)\phi(0) + \int_0^\infty w_{3/4}(t-s)\phi'(s)ds \right). \quad (2.17)$$

An approximation of the Wagner function can be used to arrive at a closed-form solution for this integral, as in Equation 2.18b.

$$\phi \approx \frac{t + c_a/U}{t + 2c_a/U}, \quad (2.18a)$$

$$\begin{aligned} C_{L,wag} &\approx \pi (\alpha + w_{3/4}/U) + f_0 (f_1 + f_2 + f_3) \\ &= \frac{1}{2} C_{L,qs} + \pi\alpha + f_0 (f_1 + f_2 + f_3), \end{aligned} \quad (2.18b)$$

$$f_0 \equiv \frac{2\gamma}{(16Y^2 + (5 + 4\tau)^2)^2}, \quad (2.18c)$$

$$f_1 \equiv -(5 + 4\tau) (16Y^2 + (5 + 4\tau)^2), \quad (2.18d)$$

$$f_2 \equiv 64Y (5 + 4\tau) \left(-\arctan\left(\frac{3 - 4\tau}{4Y}\right) + \frac{\pi}{2} \text{sign}(Y) \right), \quad (2.18e)$$

$$f_3 \equiv -4 (16Y^2 - (5 + 4\tau)^2) \log\left(\frac{64}{16Y^2 + (3 - 4\tau)^2}\right), \quad (2.18f)$$

$$\tau \equiv t \frac{U}{c}, \quad (2.18g)$$

$$Y \equiv \frac{y_v}{c}, \quad (2.18h)$$

$$\gamma \equiv \frac{\Gamma_v}{Uc}. \quad (2.18i)$$

If the vortex is far enough away (that is, if $y_v \gg c_a$), then the changes are slow enough that $C_{L,wag}$ approaches the quasi-static approximation. The magnitude of the peaks in the lift are reduced by the Wagner function, yielding the empirical fits in Equation 2.19.

$$C_{L,ext1} \approx 2\pi\alpha + \left(\frac{2 + 5 \left(\frac{y_v}{c_a}\right)^{0.8}}{4 + 5 \left(\frac{y_v}{c_a}\right)^{0.8}} \right) \left(\frac{\Gamma_v}{2Uy_v} \right), \quad (2.19a)$$

$$C_{L,ext2} \approx 2\pi\alpha - \left(\frac{2 + \left(\frac{y_v}{c_a} - 1.4\right)}{4 + \left(\frac{y_v}{c_a} - 1.4\right)} \right) \left(\frac{\Gamma_v}{2Uy_v} \right), \quad (2.19b)$$

$$\begin{aligned} \Delta C_{L,ext} &= C_{L,ext2} - C_{L,ext1}, \\ &\approx - \left(1 + \frac{\frac{y_v}{c_a}}{\frac{y_v}{c_a} + 3} \right) \left(\frac{\Gamma_v}{2Uy_v} \right). \end{aligned} \quad (2.19c)$$

Here, $C_{L,ext1}$ is the magnitude of the first peak, $C_{L,ext2}$ is of the second, and $\Delta C_{L,ext}$ is the difference between the two. These fits are reasonable for $y_v > c_a$.

2.3 Extension of Tchieu-Leonard unsteady airfoil model

This section describes an extension of Tchieu and Leonard's [65] (TL) model of an unsteady airfoil. The new work, referred to as the Extended Tchieu-Leonard (E-TL) model adds to the existing work a point vortex that convects past the airfoil. A summary of the derivation is presented here, while the detailed derivation is in Appendix B.

2.3.1 Tchieu-Leonard unsteady airfoil model

As published, the TL model describes a method of efficiently simulating the lift and moment on a pitching and heaving airfoil as it sheds a wake. Rather than using the Wagner function as its wake model, the TL model sheds discrete vortices which move along the x-axis and change in circulation over time to conserve the circulation and impulse in the flow. In this model, a vortex is only shed when its rate of change of circulation changes sign. Compared to shedding a new vortex at each timestep, this significantly reduces the computational expense of the simulation.

In the TL model, the airfoil is approximated by a flat plate, with the flow around it computed through conformal mapping of potential flow. This allows for analytical computation of the vorticity distribution along the flat plate due to the angle of attack, the pitching rate of the plate, and external wake vortices along the x-axis. Both of these distributions have zero vorticity at the trailing edge of the plate, and so enforce the Kutta condition both separately and jointly. The lift, pitching moment, and quasi-steady bound circulation of the airfoil are computed from different mathematical moments of the total vorticity distribution.

2.3.2 Extended Tchieu-Leonard model

The addition of an external vortex requires a foray into conformal mapping. The initial potential flow is generated around a two-dimensional cylinder, which is then transformed into a flat plate. The angles and distances in this initial coordinate system are denoted by a subscript 0. Thus, the cylinder has diameter c_0 , while the flat plate has a chord length of c . The transformation of the cylinder's coordinates into the flat plate's is

$$z = z_0 + \frac{(c_0/2)^2}{z_0}. \quad (2.20)$$

The complex potential of the cylinder centered at the origin, with an external vortex of strength Γ_v at point $r_{0v}e^{i\theta_{0v}}$ is

$$F_{vortex} = \frac{\Gamma_v}{2\pi i} \left(\log(z_0 - r_{0v} e^{i\theta_{0v}}) - \log\left(z_0 - \frac{c_0^2}{4r_{0v}} e^{i\theta_{0v}}\right) \right) + \frac{\Gamma_{KC,vortex}}{2\pi i} \log(z_0). \quad (2.21)$$

To ensure that the Kutta condition is enforced, the potential must have

$$\Gamma_{KC,vortex} = \frac{\Gamma_v (r_{0v}^2 - (c_0/2)^2)}{(c_0/2)^2 + r_{0v}^2 - c_0 r_{0v} \cos(\theta_{0v})}. \quad (2.22)$$

The vorticity on the plate is Equation B.20, which is omitted here for brevity.

The n^{th} moment of vorticity is defined as

$$\mu_{vortex,n} = \int_{c/2}^{-c/2} \gamma_{vortex}(x) x^n dx. \quad (2.23)$$

The bound circulation due to the external vortex is the zeroth moment of vorticity, $\mu_{vortex,0}$:

$$\mu_{vortex,0} = \Gamma_{KC,vortex} - \Gamma_v. \quad (2.24)$$

Its contribution to the lift, L_v , is a function of the time-derivative of $\mu_{vortex,1}$:

$$\mu_{vortex,1} = -\Gamma_v \frac{c_0^2 \cos(\theta_{0v})}{2r_{0v}}, \quad (2.25)$$

$$\begin{aligned} L_v &= \rho \frac{d}{dt} (\mu_{vortex,1}), \\ &= \frac{c_0^2 \rho \Gamma_v}{2r_{0v}^2} \left(\cos(\theta_{0v}) \frac{dr_{0v}}{dt} + r_{0v} \sin(\theta_{0v}) \frac{d\theta_{0v}}{dt} \right). \end{aligned} \quad (2.26)$$

Unfortunately, θ_{0v} and r_{0v} are in terms of the original coordinate system, though the simulation is performed in the transformed coordinates. The necessary coordinate transformation and chain-rule computations for the derivatives can be performed in a few lines of code. To match the restrictions in the original TL model on motion of the wake vortices after they have been released, the external vortex is constrained to move at a constant y -height, and with the freestream speed.

Though this derivation described the effect of one external vortex, the linearity of potential flow makes it simple to include additional external vortices.

At long distances, this method resembles unsteady thin airfoil theory. Far from the body, r_{0v} and θ_{0v} approach r_v and θ_v , respectively. If the v subscripts are dropped from those coordinates, the L_v term, normalized into a coefficient, becomes identical to the result of the point vortex model in Equation 2.14. As before, its maximum lift is proportional to the inverse of the y -distance to the airfoil. In contrast, the lift due to the bound vorticity is proportional to the inverse of the square of that distance. This means that it is relatively negligible at large distances. This agreement between the E-TL and point vortex models provides a useful verification of the model.

2.4 Unsteady Panel Methods

This section describes the creation and use of an unsteady panel method (UPM) to model the gust generators and gust-wing interaction.

2.4.1 Background

The panel methods used in this thesis were inspired by the ideas from Anderson [2] and Katz and Plotkin [42]. The general approach of a two-dimensional panel method is to discretize the surface of a body into a series of line segments, and require that the velocity must be tangent to those panels at particular points. Different types of potential elements have been used in panel methods, including source and vortex panels. This implementation uses vortex panels whose circulations vary linearly across their length, and the non-penetration requirement is enforced at the center of each panel. To make the flow leave the trailing edge smoothly, the circulation at the trailing edge is zero, thus enforcing the Kutta Condition. In combination with a prescribed freestream velocity, as well as any other velocity perturbations outside the body, the non-penetration requirement leads to a linear set of equations that determine the vorticity along each panel. The restrictions on panel methods are similar to those of thin airfoil theory, since both are based on potential flow models. Thus, panel methods assume inviscid, attached flow that smoothly leaves the trailing edge of the body. This model neglects added mass effects, which were considered in Theodorsen's flutter model.

The previous summary describes the basics of both steady and unsteady panel methods. A few elaborations are required to extend this to unsteady flow. For example, the pressure around the body must be computed with the unsteady Bernoulli equation. More crucially, a wake model must be implemented. Here, the wake is modeled as a linear vortex panel extending from the back of the airfoil as well as a series of point vortices beyond that. This panel remains aligned with the airfoil,

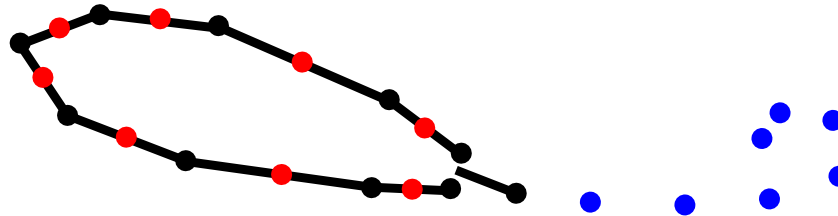


Figure 2.4: Schematic of the unsteady panel method. The black lines are the panels that define the body and beginning of the wake. The black circles represent the vertices where the vorticity needs to be solved for, which are the ends of the body's panels. The red circles are the control points where non-penetration is enforced. The blue dots are the point vortices in its wake.

but the wake vortices convect with their local velocity field. At each time step, a new wake element is created near the trailing edge of the airfoil. According to Kelvin's circulation theorem, the circulation in the flow must be conserved over time. Once a vortex is released, it does not decay, so the circulation of the new wake element is determined by the bound circulation of the airfoil, yielding a constant total circulation in the simulation over time. Since the wake influences the velocity at the non-penetration points of the panel method, these modifications are included in the aforementioned linear equations, yielding the strengths of the panels as well as of the new wake element at each time step. The singularity at the core of the point vortices is removed by using Rankine vortices with a core radius of 10^{-7} chord lengths. To more accurately compute the movement of the wake vortices, the wake's evolution is computed using a second-order Runge-Kutta method.

A schematic of the UPM is shown in Figure 2.4. This represents a simulation of an airfoil shedding its starting vortex, seven time steps into the simulation. The airfoil on the left is divided into eight linear panels, with the black points representing the ten vertices whose vorticity must be solved for, and the red points representing the control points where non-penetration is enforced. The trailing-edge vortex panel is shown with one vertex, as its other vertex is required to have zero vorticity. The blue dots behind the airfoil are its wake, discretized into point vortices.

2.4.2 Equations of the Vortex Panel Method

2.4.2.1 Vortex Panels

The vortex panels in use have linearly varying vorticity across their lengths. Figure 2.5 shows a vortex panel in its local x - y coordinate system. The left end has vorticity of γ_1 , and the right has γ_2 . Equation 2.27 describes the potential, Φ , at a relative

point (x, y) . The potential is constructed by assuming distributed infinitesimal vortices along the length of the panel, with strength $\gamma(s)$. The position on the panel of length L is parameterized as s .

$$\gamma(s) = \gamma_1 + (\gamma_2 - \gamma_1) \frac{s}{L}, \quad (2.27a)$$

$$\begin{aligned} d\Phi(s, x, y) &= \frac{\gamma(s)}{2\pi} \theta(s, x, y), \\ &= \frac{\gamma(s)}{2\pi} \arctan\left(\frac{y}{x-s}\right), \end{aligned} \quad (2.27b)$$

$$\Phi = \int_0^L d\Phi ds. \quad (2.27c)$$

The result of this integral, Equation 2.28, can be more compactly written with $\Delta\gamma$ as the difference in circulation at the ends, and Γ as the total circulation.

$$\Delta\gamma = \gamma_2 - \gamma_1, \quad (2.28a)$$

$$\Gamma = \frac{L(\gamma_1 + \gamma_2)}{2}, \quad (2.28b)$$

$$\begin{aligned} \Phi &= \frac{\Gamma}{2\pi} \arctan\left(\frac{x-L}{y}\right) - \frac{y\Delta\gamma}{4\pi} \\ &+ \frac{1}{4\pi L} \left(\Delta\gamma \left((L-x)x + y^2 \right) - 2x\Gamma \right) \left(\arctan\left(\frac{L-x}{y}\right) + \arctan\left(\frac{x}{y}\right) \right) \\ &+ \frac{y}{8\pi L} \left(\Delta\gamma(L-2x) - 2\Gamma \right) \left(\log\left((L-x)^2 + y^2 \right) - \log\left(x^2 + y^2 \right) \right). \end{aligned} \quad (2.28c)$$

As confirmation, if $\Delta\gamma = 0$ and L approaches zero as Γ is kept constant, then the point vortex potential is recovered. Care must be taken in using this potential to generate a velocity field, as the branch cuts necessary for the arctangent functions introduce discontinuities.

2.4.2.2 Determination of Panel Strengths

The vorticity at each of the vertices, γ , is determined by three sets of equations: the non-penetration of the flow at the midpoints of the panels, the Kutta Condition at the trailing edge, and the conservation of circulation over time. For a body discretized with N points, there are $N + 1$ total equations to solve, as the strength of the trailing wake panel must also be obtained.

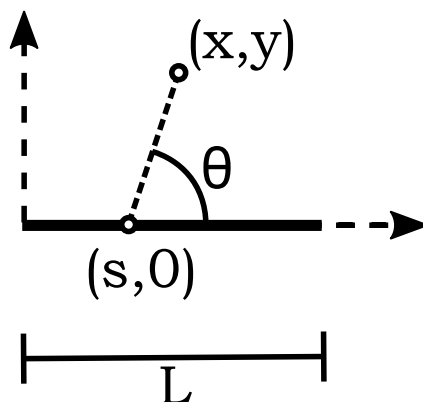


Figure 2.5: Diagram of a vortex panel in its local coordinate system.

A bit of nomenclature is necessary to explain the non-penetration equation in Equation 2.29. The velocity at the i^{th} panel's center caused by unit-strength vorticity from the j^{th} vertex is $\vec{u}_{vertex,j}(\vec{x}_{panel,i})$. The unit vector normal to the i^{th} panel is \hat{n}_i . The velocity of the i^{th} panel's midpoint due to the body's translation and rotation in the plane is $\vec{u}_{body}(\vec{x}_{panel,i})$. The velocity at the same point due to the vortices in the wake is $\vec{u}_{wake}(\vec{x}_{panel,i})$. Simply put, Equation 2.29 ensures that the total velocity from the vortex panels balances the velocity due to the freestream, body motion, and wake at the control points.

$$\sum_j \gamma_j \vec{u}_{vertex,j}(\vec{x}_{panel,i}) \cdot \hat{n}_i = - \left(\vec{U}_\infty + \vec{u}_{body}(\vec{x}_{panel,i}) + \vec{u}_{wake}(\vec{x}_{panel,i}) \right) \cdot \hat{n}_i. \quad (2.29)$$

The Kutta condition is a single simpler equation: the strengths at the two vertices of the trailing edge must sum to zero.

The final equation uses the lengths of the panels to compute the total circulation, and requires that it matches the total circulation at the previous time step.

Each of these equations are linear with the vorticity at each vertex, so the $(N_{pts} + 1)$ equations are assembled into a square matrix which is solved to find these strengths.

2.4.3 Panel Method Simulations

This section describes the parameters of the UPM simulations and displays their results. The first set of simulations examined the wake created by the pitching airfoil. The second studied the heaving plate and the vortical wake that it created. The third had a fixed airfoil, and considered the effect of a passing vortex on the

airfoil's forces and wake. These results are discussed and compared to the other models in section 2.5.

2.4.3.1 Pitching Airfoil

Panel method simulations of the pitching vortex generator were conducted with a NACA 0018 airfoil discretized into 30 panels, and a time step of 0.025 convective time units. The simulations started with the airfoil at $\alpha = \alpha_1 = 0$, and rotated about its quarter-chord point as in Equation 2.1e. These explored the parameter space of $1 \leq \alpha_2 \leq 15$ and $0.2 \leq t_{pitch}/t_c \leq 2$, to see the effect of different final angles and pitching times.

Images of the vortical wake behind the airfoil at its final angle are shown in Figure 2.6, where each wake vortex is drawn with the same diameter, and the color reflects its circulation: red is positive, white is zero, and blue is negative. In Figure 2.6a, the short pitching time resulted in a small number of point vortices of relatively high circulation. Figure 2.6b shows that slower pitching led to a shed vortex that is less spatially concentrated, and composed of many vortices. Comparison of the different pitching amplitudes reveals the expected result that a larger pitching angle results in stronger vortices.

2.4.3.2 Heaving Plate

Simulations of the heaving plate used 30 points to define the flat plate and a time step of $0.05 t_{cp}$. To match experiments, the plate had semicircular ends, and a thickness ratio of 1/8 or 1/16. The plate's motion followed the modified Eldredge equation (Equation 2.7) through the parameter space of $0.25 \leq T \leq 10$ and $0.1 \leq S \leq 1$, to see the effects of different heaving times and speeds.

Figure 2.7 shows snapshots of simulations performed with both plates over two heaving speeds, the parameters of which are listed in the figure. The plates heaved the same dimensional distance in each case. The black line on the left is the plate. Each wake vortex is drawn with the same diameter, and the color reflects its circulation: red is positive, white is zero, and blue is negative.

The impact of different heaving times is also seen. The faster motion, in the bottom of each pair of plots, shows that the vortices shed at the beginning and end of motion were still nearby. This shows that rapid heaving, or a short heaving distance, reduces

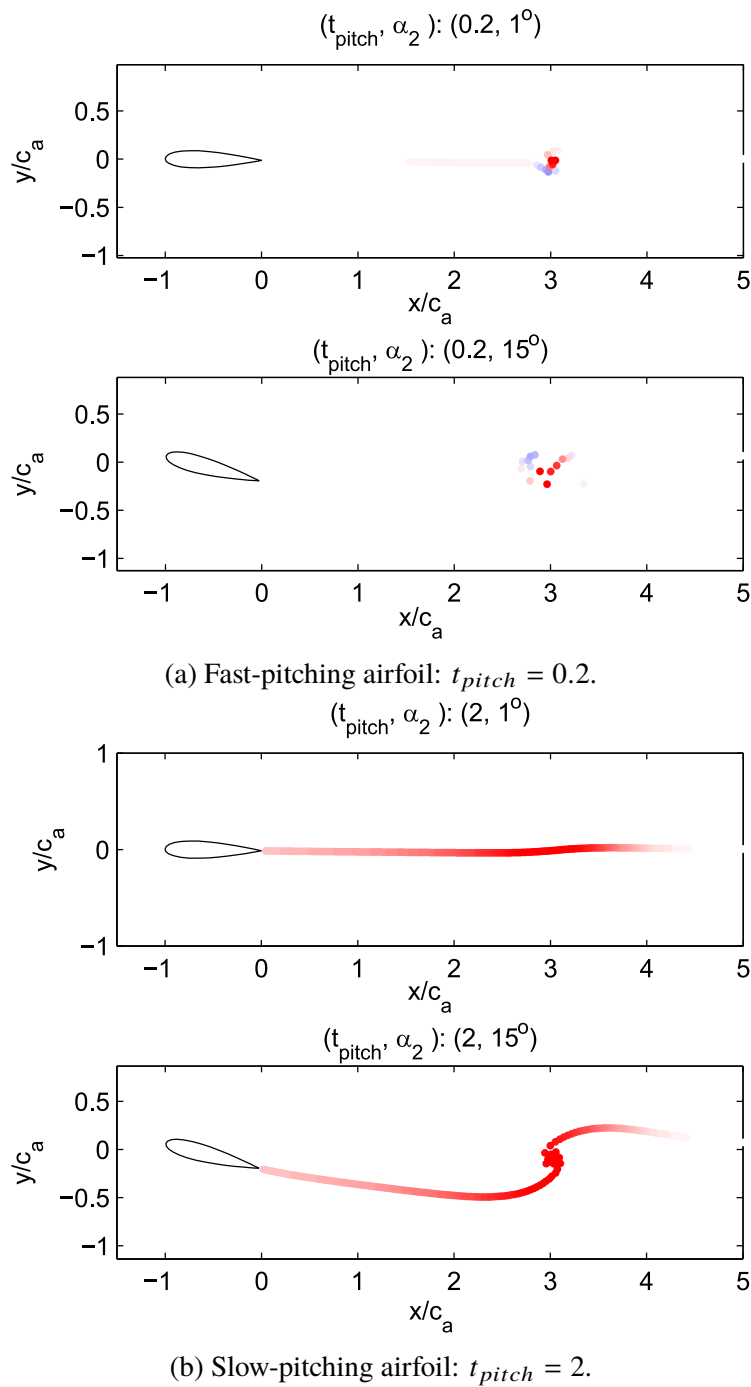


Figure 2.6: Simulated wakes of the pitching airfoil, $3t_c$ after pitching with different parameters. Distance is normalized by the airfoil's chord, and time by the convective time. The parameters of motion are in the title of each plot.

Model name	Acronym	Wake model?	Notes
Steady thin airfoil theory	S-TAT	No	No time-derivatives
Quasi-steady thin airfoil theory	QS-TAT	No	Time-derivatives on motion
Wagner thin airfoil theory	W-TAT	Yes	With Wagner function
Unsteady panel method	UPM	Yes	Wake moves in x-y
Tchieu-Leonard model	TL	Yes	Wake along x-axis
Extended Tchieu-Leonard	E-TL	Yes	TL with an external vortex

Table 2.1: List of aerodynamic models.

the isolation of the primary vortex. The faster heaving and longer plate both resulted in stronger shed vortices, visible as the extended regions of visible vortices.

Beyond the expected strength of the shed vortices, there was little effect of the different plate lengths. The simulations reported later in this chapter used a thickness ratio of 1/16.

2.4.3.3 Airfoil-Vortex Interaction

The airfoil-vortex interactions were simulated with a NACA 0018 airfoil with 30 panels, a time step of 0.05 convective time units, and either with or without a wake. The airfoil was at an angle of attack of 0° , 5° , or 10° . The vortical gust was initialized 7.5 chord lengths upstream of the airfoil's leading edge, its initial vertical position varied over $-2 \leq y_v/c_a \leq 2$, and its circulation over $-2.7 \leq \Gamma_v/(\pi c_a U/2) \leq 2.7$.

The paths of the simulated vortical gusts and the variation in C_L can be seen in Figure 2.12 are discussed in detail in the next section.

2.5 Comparison of Analytical Models and Simulations

This section examines the similarities and differences between the models developed from thin airfoil theory, the extended Tchieu-Leonard model, and the panel-method simulations. The different models, and their acronyms, are summarized in Table 2.1.

To compare the different models, the circulation of a shed 'vortex' was estimated from the change in bound circulation between $-t_c/2$ before to $t_c/2$ after the change in angle or direction of motion. This was done for each of the numerical and analytical models. These estimates were then normalized by the circulation estimates from unsteady thin airfoil theory: Equation 2.6 for the pitching airfoil, and Equation 2.13 for the heaving plate.

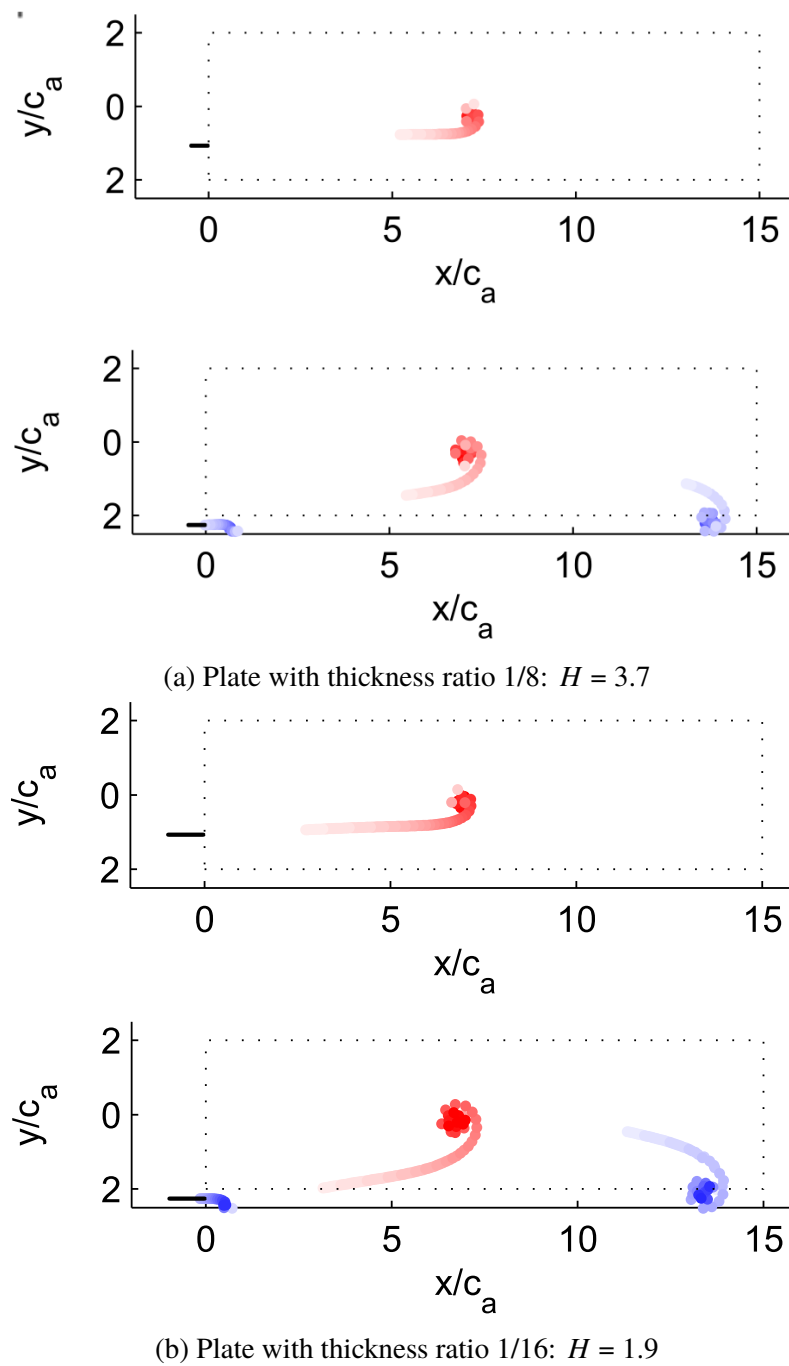


Figure 2.7: Simulated wakes from both lengths of heaving plates, $7.5t_{ca}$ after heaving with different parameters. The plate is drawn to-scale on the left side of each plot. Distance is normalized by the airfoil's chord, and time by the convective time. In each pair, the top plot has a heaving speed of $S = 0.093$, and the bottom plot has $S = 0.28$.

Model	Relative Execution Time
Analytic	1
Tchieu-Leonard	6.7
Wakeless UPM	460
Full UPM	6880

Table 2.2: Execution time for each model, normalized by that of the analytic equations.

To quantify the relative computational cost of each method, each method was timed while simulating, in MATLAB, a vortex passing an airfoil for 351 time steps. The results are shown in Table 2.2, where the most expensive method took thousands of times longer than the cheapest. For reference, the analytic equations were computed on a modern laptop in 13 ms.

2.5.1 Pitching Airfoil

The minimum and maximum parameters of the UPM simulations were used to compare the different models of the lift behavior of the pitching airfoil, as shown in Figure 2.8. The lift has been non-dimensionalized by the final lift. Six models are plotted: the steady thin airfoil theory, quasi-steady thin airfoil theory, the Wagner function, thin airfoil theory with the Wagner function, the Tchieu-Leonard model, and the unsteady panel method. In these plots, the simplified model of instantaneous pitching, Equation 2.4, is equivalent, once normalized, to the Wagner function. The rows display different pitching amplitudes: 1° in the top row, and 15° in the bottom row. The effects of different pitching speeds can be seen across the two columns: the right column performed the pitching motion ten times more slowly than the left column.

Only the UPM yielded different normalized results with different pitching amplitudes. This is expected, since each of the other models are linear with the angle of attack.

The greatest differences resulted from the different pitching times. Except for the Wagner function and S-TAT, each of the models predicted a peak in the lift for some sets of parameters. The magnitude of this peak dropped along with the pitching speed. All models except the S-TAT and QS-TAT displayed a slow approach to the final value of lift. Since these two lack wake models, this is expected behavior.

Of the unsteady models, the UPM estimates the smallest lift peak. With the fast pitching, it is the most similar to the Wagner function, which was derived to model

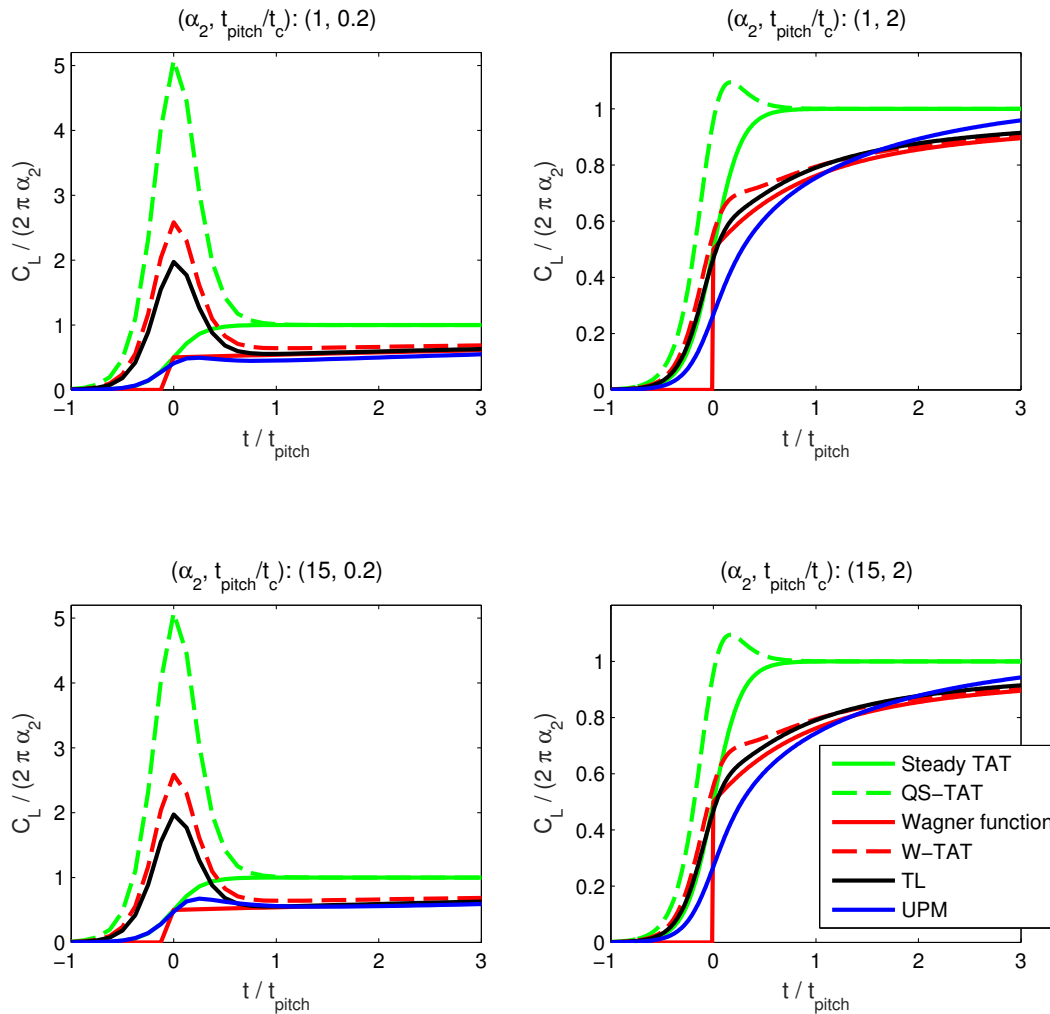


Figure 2.8: Estimated lift coefficients of the pitching airfoil, normalized by the thin airfoil theory estimate of the final lift. Time is normalized by the pitching time. The parameters of motion are in the title of each plot. Note the different scales on the left vs right frames.

a rapid change in angle of attack. With the slower speed, each of the wake-modeling methods are similar to the Wagner function. Here, the panel method appears to lag the other models.

The estimates of the shed vortex strength are seen in Figure 2.9 for the quasi-steady TAT, TAT with the Wagner function, unsteady panel method, and the Tchieu-Leonard model. When t_{pitch} was long, the change in circulation on the body was no longer concentrated around $t = 0$. Thus a long pitching time created a weak shear layer, rather than a compact vortex. Since the circulation of the vortex is only assumed to be shed within $t_c/2$ of pitching, this explains the drop-off in vortex

strength over long pitching times.

Other than the UPM, all of the models are linear with the change in angle of attack, and so have no variation along that axis, after normalization. The Wagner function assumes small angles, so it is unsurprising that there was greater disagreement with the UPM at high final angles of attack.

The final striking difference between the models is that the quasi-steady estimate is approximately twice as high as the unsteady TAT estimates. This is because it lacks a wake model, and so does not have the factor of one half introduced by the Wagner function or its analogs.

Overall, the estimated vortex circulations from the models with wakes generally agree with the simple unsteady TAT estimates.

2.5.2 Heaving Plate

The minimum and maximum parameters of the UPM simulations were used to compare the different models of the lift behavior of the heaving plate, as shown in Figure 2.10. The lift has been non-dimensionalized by the estimated lift of the steadily heaving plate, and time has been non-dimensionalized by the heaving time. The slow motion is on the top, and fast motion is on the bottom. The heaving time is one-quarter of the convection time on the left, and 40 times longer on the right.

As before, only the panel method resulted in different normalized forces for different heaving speeds. This is because the other models are linear with the heaving speed. The differences were small, however. At $S = 1$, the lift in the UPM increased slightly more quickly. This is because the plate was moving away from its wake more quickly than the Wagner function assumes.

The effects of different T were more substantial. When the plate heaved for a very short time, the acceleration of the plate strongly affected the lift. The QS-TAT model was essentially double the amplitude of the W-TAT, as the forces changed quickly. The TL model predicted strong peaks at the times of maximum acceleration. The UPM predicted very weak lift in this case. With larger T , the plate moved steadily for a time, and the forces approached their steady-state values with each model. Since it lacks a wake model, the QS-TAT model jumped to the estimated static lift. The W-TAT model had smoother transitions between the different phases of motion, and asymptotically approached the steady values over time. The TL model was very similar to the W-TAT model, except for the substantial lift peaks. These peaks reached the same non-dimensional amplitudes as in the $T = 0.25$ case, though with

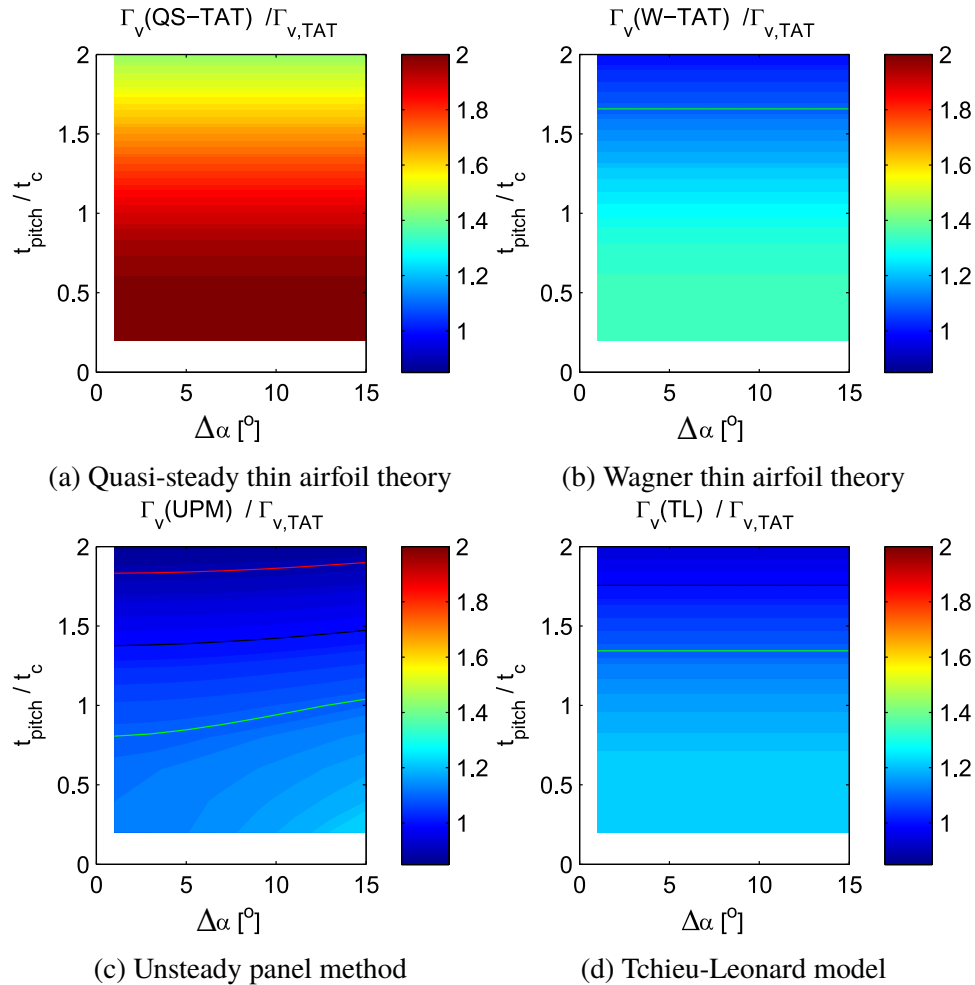


Figure 2.9: Comparison of estimated pitching gust circulations, normalized by the unsteady thin airfoil theory estimate. The red, black, and green lines are isocontours at 0.9, 1.0, and 1.1, respectively.

much shorter duration. Here, the UPM was similar to the W-TAT case, though with the aforementioned variations.

The estimates of the shed vortex strength are seen in Figure 2.11 for the quasi-steady TAT, TAT with the Wagner function, unsteady panel method, and Tchieu-Leonard model. The main outlier is the QS-TAT model, because it does not have a wake model. Without the moderating influence of the Wagner function, it changed circulation instantly, resulting in stronger vortices than unsteady TAT predicted.

All of the models, other than the UPM, are linear with the heaving speed, and so they have no variation in the normalized circulation along that axis. The exception, the UPM, predicts the circulation at high S to be larger than the TAT prediction.

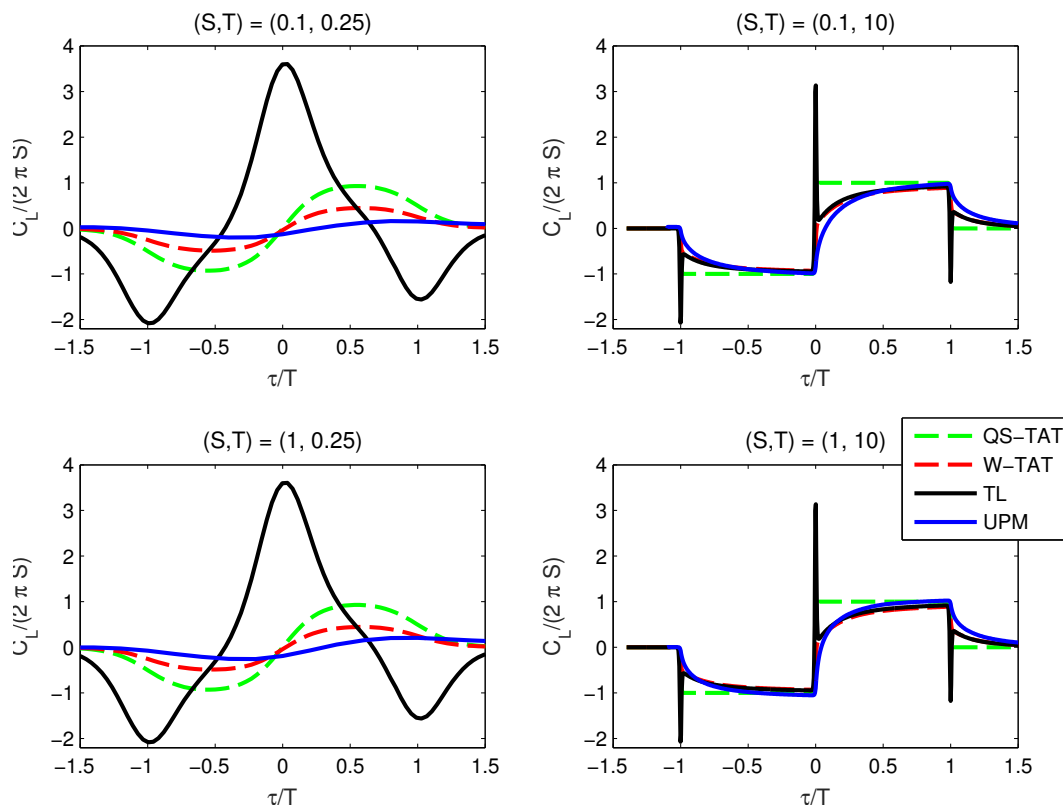


Figure 2.10: Lift coefficient of the simulated heaving plate. The C_L is normalized by the steady thin airfoil theory estimate of lift while heaving at speed SU , and time is normalized by the heaving and convective times.

This is likely because the effective speed of the steadily heaving plate is $U\sqrt{1+S^2}$, rather than U , so the bound vorticity should asymptote to a higher value.

As with the lift, the heaving time had a significant effect on the shed vorticity. When T was very small, the vortex could not reach its full strength due to interference from the vortices that were released at the start and end of the motion. Also, the net vorticity is zero, so very little vorticity was released during the simulation, due to the influence of the Wagner function. The strength of the shed primary vortex asymptotically approached a limit as T became longer, because the influence of those other vortices weakened as they traveled farther from the body.

2.5.3 Airfoil-Vortex Interaction

Two representative sets of results of the airfoil-vortex interaction are shown in Figure 2.12. In each pair of figures, the top frame shows C_L scaled by the peak magnitude estimated by TAT. The bottom frame shows the path of the simulated vortical gust.

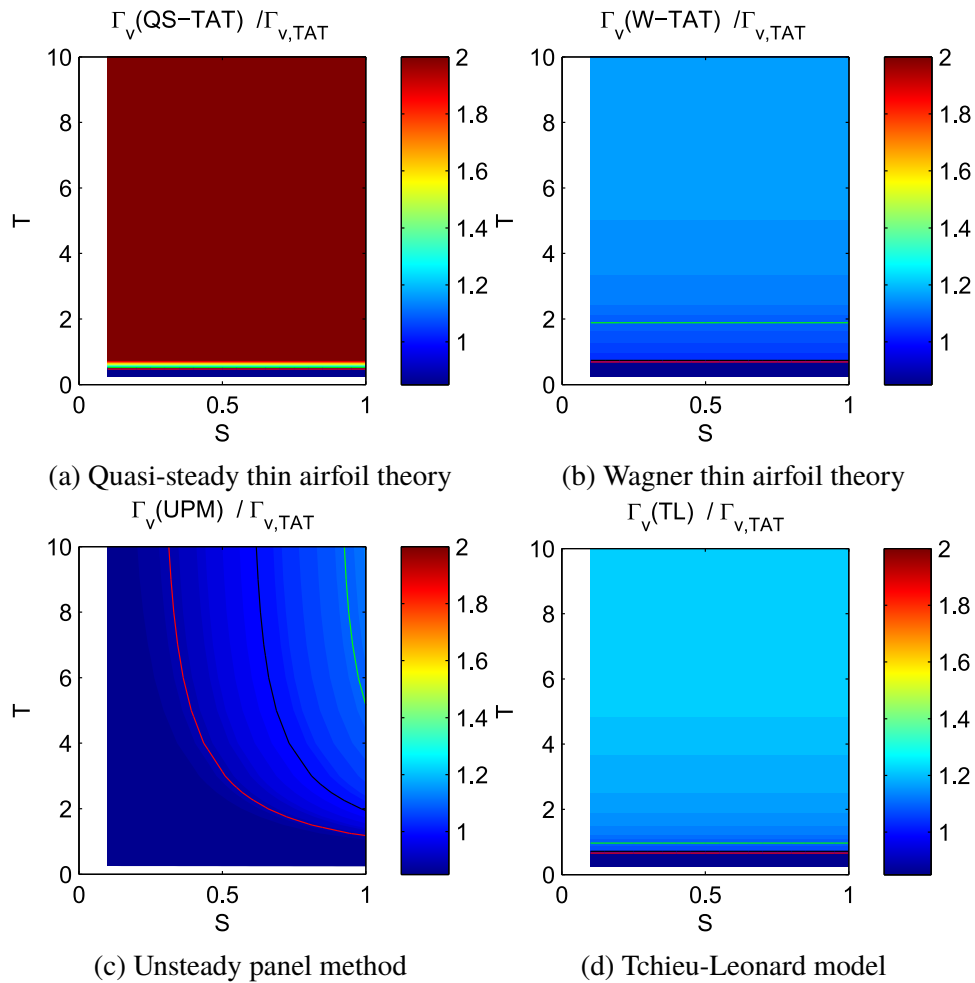


Figure 2.11: Comparison of estimated heaving gust circulations, normalized by the unsteady thin airfoil theory estimate. The red, black, and green lines are isocontours at 0.9, 1.0, and 1.1, respectively.

Only the UPM allowed for movement of the vortex in the y -direction. A larger array of comparisons can be seen in Figures C.1 - C.3.

Figure 2.12a is representative of simulations where the vortex began sufficiently far (in the y -direction) from the airfoil, and the incoming vortex was sufficiently weak. These conditions led to good agreement within the two main classes of models: those with, or without a wake. The wakeless UPM and QS-TAT models were nearly identical, since the vortex did not move much in the y -direction in the simulation. The UPM, W-TAT, and TL models were very similar in shape, though with a time delay between them. In other simulations, good agreement was seen at $\alpha = 0^\circ$, and slightly worse agreement in the $\alpha = 10^\circ$ cases. This is because the airfoil at a higher

angle deflected the path vortex more, reducing the effectiveness of the straight-path approximation.

In contrast to Figure 2.12a, Figure 2.12b shows where there is significant disagreement due to the strong vortex which closely approached the airfoil. The lift responses of the models with wakes have similar amplitudes, but the time delays between them are more pronounced, and the rates of change of lift are also different. Comparison between the wakeless UPM and the QS-TAT model also shows a substantial time lag, as well as a slight difference in shape. Part of the reason for the disagreement can be seen by examining the paths of the vortices. With the wakeless UPM, the vortex was permanently deflected downward. In the full UPM, the vortex interacted strongly with the wake, and was deflected upward. These paths no longer matched the assumption of an undeflected vortex, so the QS-TAT, W-TAT, and E-TL models are less appropriate to use under these conditions.

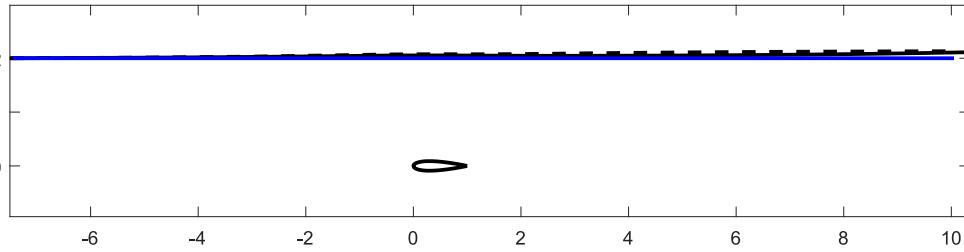
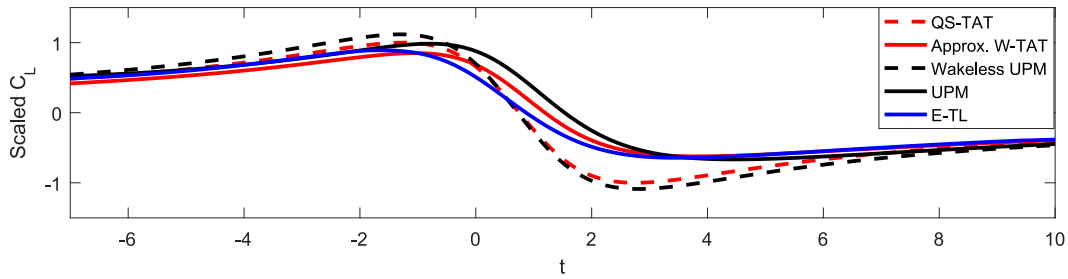
2.6 Summary

The simplest models in this thesis are the analytic models with (Equation 2.18) and without (Equation 2.15) the Wagner function. The next most complex is the Tchieu-Leonard unsteady airfoil model. The most complex are the panel methods, both with and without the wake model. This ranking of simplicity also reflects the computational costs of each method.

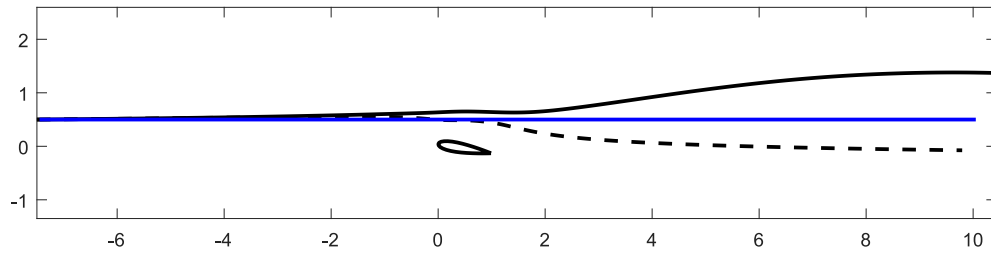
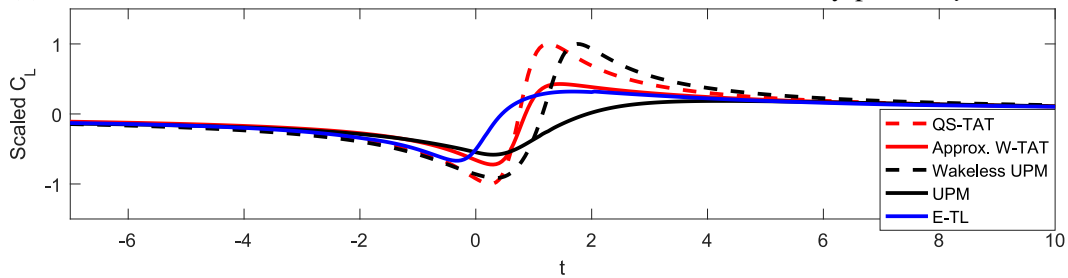
The simulations in this chapter confirm that the simple models with wakes can provide reasonable estimates of the circulation of an airfoil or flat plate undergoing motion or interacting with an external vortex, in comparison to more complex potential flow simulations. As a result, the theoretical estimates of the strength of the shed vortices were in agreement over a wide range of parameters, as long as a wake model was included.

With respect to an external vortex interacting with an airfoil, the different estimates differed significantly when the vortex was strong and near the airfoil. This is precisely the set of circumstances where potential flow simulations are expected to disagree with experiments, due to the lack of viscous effects. When the vortex was weak and far from the wing, the lift changed slowly enough that the methods with wake models yielded similar results. Each of those methods has a different model of the wake, however, and so they did not converge to identical results.

Since the results of the different models are fairly similar, the expense of the UPM is not justified when the vortex is far from the body. When it is closer, the physical



(a) The airfoil is at $\alpha = 0^\circ$, with a vortex of circulation $\Gamma_v = 2.7Uc_a$ and y-position $y_v = 2c_a$.



(b) The airfoil is at $\alpha = 10^\circ$, with a vortex of circulation $\Gamma_v = -2.7Uc_a$ and y-position $y_v = 0.5c_a$.

Figure 2.12: Select lift coefficients and vortex paths from the simulations. The top plot in each pair shows the normalized variation in C_L for the models using quasi-steady thin airfoil theory, approximate Wagner thin airfoil theory, wakeless UPM, full UPM, and the extended Tchieu-Leonard model. The bottom plot in each pair shows the paths of the simulated vortices as they pass the airfoil. The scaled C_L was computed by subtracting the static C_L , $C_{L,0}$, then normalizing by the estimated lift peak height: $(C_L - C_{L,0})/(\Gamma_v/(2Uy_v))$.

accuracy of each method is unknown. To resolve this ignorance, comparison with experiments follows in Chapters 4 and 5.

*Chapter 3***EXPERIMENTAL EQUIPMENT****3.1 Introduction**

This chapter describes the equipment used in Chapters 4 and 5. These experiments used force measurements and particle image velocimetry (PIV) to examine the generation of gusts and their interactions with a downstream airfoil. These included PIV around and downstream of the heaving plate, downstream of the pitching airfoil, and around a static airfoil set up downstream of these devices. Forces were measured on the downstream airfoil, particularly in response to the gust generators. The parameters and details of each experiment are described in Appendix A.

3.2 NOAH Water Tunnel

Experiments were performed in the NOAH water tunnel at Caltech. A representative schematic of PIV around an airfoil in this tunnel is shown in Figure 3.1. This is a recirculating free-surface water tunnel. The test section is 46 cm wide and 150 cm long, with the water 46 cm deep, and its walls and bottom are Plexiglas for visibility. Before entering a 4:1 contraction, the flow passes through two 7.6 cm-thick honeycomb panels and three fine mesh screens to reduce the turbulence in the flow. Rails on the top edges of the test section were used for mounting the static airfoil and free surface plate.

The calibration curve for the tunnel, determined using PIV, is shown in Figure 3.2, as well as the freestream turbulence level. The freestream turbulence was measured at less than 6% for each of the tested pump frequencies. Most experiments were conducted with a freestream speed of $U = 20$ cm/s.

The coordinate system in this thesis has x as the streamwise direction, y as the horizontal spanwise direction, and z as the vertical direction. The origin is located along the streamwise centerline of the test section.

3.3 Particle Image Velocimetry

PIV was used to measure the velocity field, in some of the experiments, around the tunnel's midline using a LaVision PIV system. Images were captured using one or two Photron Fastcam APS-RX CMOS cameras, with a resolution of 1024 x 1024

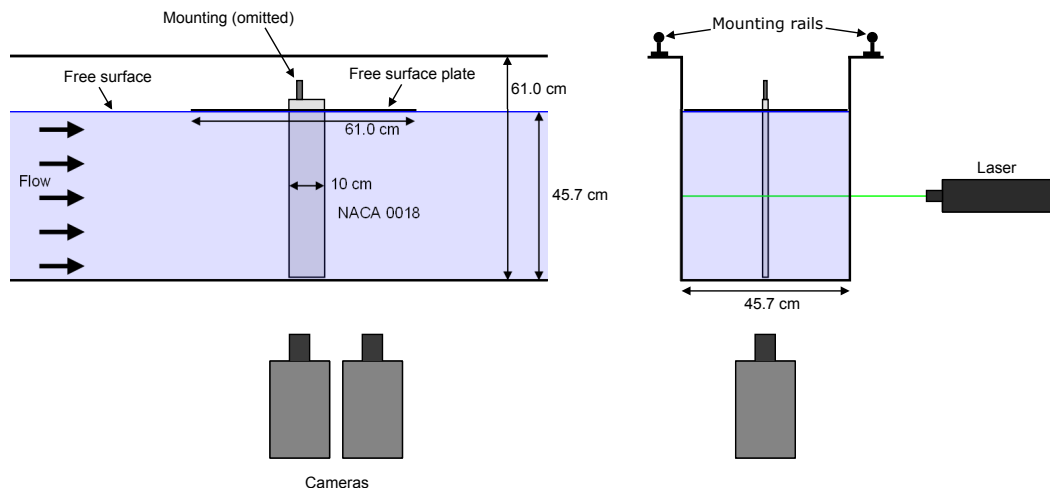


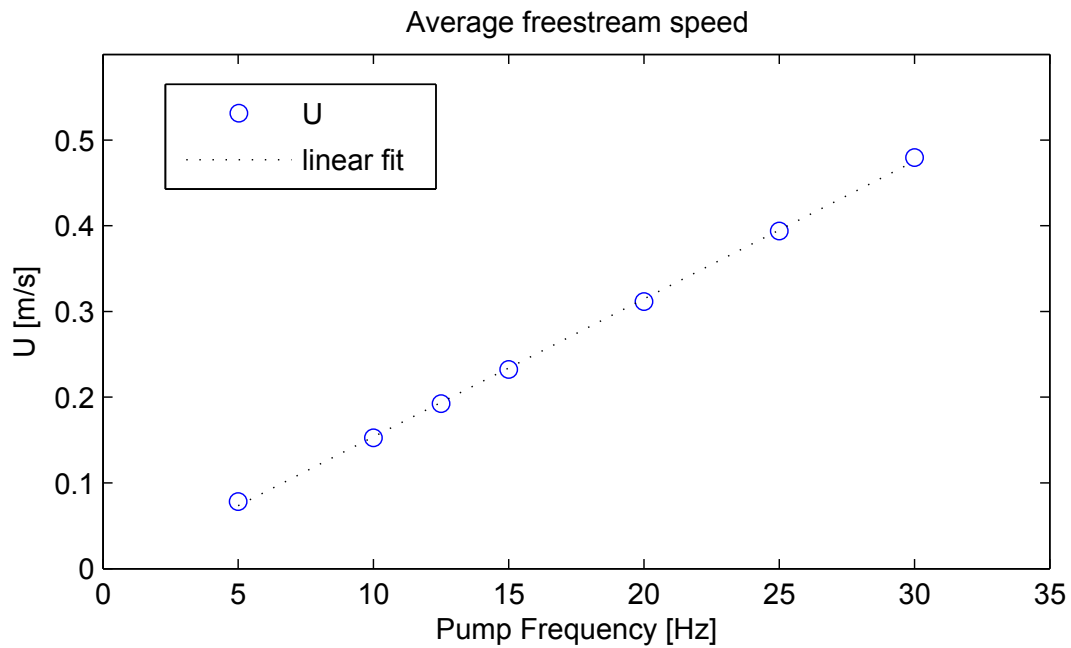
Figure 3.1: Diagram of the NOAH tunnel's test section. On the left is a side view, and the right shows a cross-section. PIV cameras were aligned to provide a larger streamwise field of view around the airfoil.

pixels. These captured 1024 or 2048 images in sequence. The frame rate and other details varied in each experiment and are detailed in Appendix A.

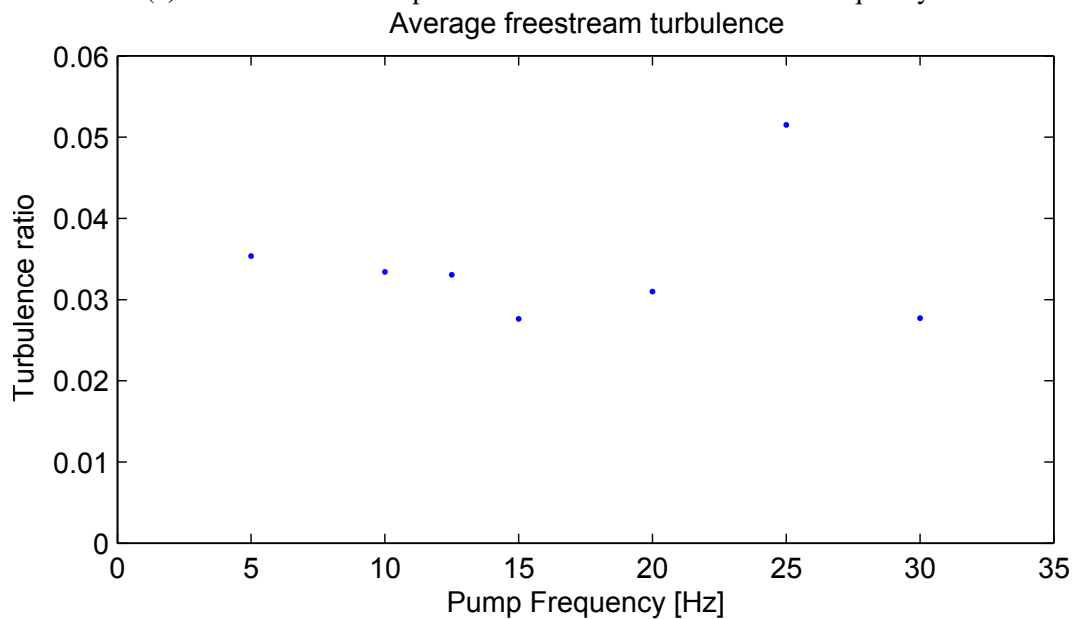
A 25 mJ DM20-527 Photonics YAG laser was used for illumination. The laser beam was expanded into a sheet, illuminating neutrally buoyant $10\ \mu\text{m}$ hollow glass beads in the tunnel. Depending on the experiment, a cylindrical or Powell lens was used to expand the beam. Except for the experiments examining the three-dimensionality of the flow, the beam was expanded into a sheet in the $x - y$ plane of the tunnel, at the z -midpoint of the test section. In those exceptions, the beam was expanded into a sheet in the $x - z$ plane, at the y -midpoint. LaVision DaVis 7 or 8 was used to compute velocity fields from the recorded images. Post-processing in MATLAB included median filters to remove spurious vectors. Details of the PIV processing are in Appendix A.

3.4 Static Airfoil

The tested wing had a 10 cm chord and 48.3 cm span, wetted to 46 cm, with the cross section of a NACA 0018 airfoil. This profile can be seen in Figure 3.3. It was 3D printed stereolithographically by Henning Product Development out of Watershed plastic, with a spatial resolution of $50\ \mu\text{m}$ per layer. To reduce its reflectivity in PIV experiments, the wing was lightly sanded, spray-painted black, and lightly sanded again. At the typical freestream speed of $U = 20\ \text{cm/s}$, this led to a Reynolds number of $Re_c = 20,000$.



(a) Tunnel freestream speed as a function of the dialed-in frequency.



(b) Freestream turbulence levels as a function of the dialed-in frequency.

Figure 3.2: Calibration and characterization of the NOAH tunnel. Frame *a* shows the mean velocity of the freestream as a function of the commanded pump frequency, and the linear fit. Frame *b* presents the turbulence intensity, calculated as the freestream-normalized RMS of the velocity fluctuations.



Figure 3.3: Cross-section of a NACA 0018 airfoil.

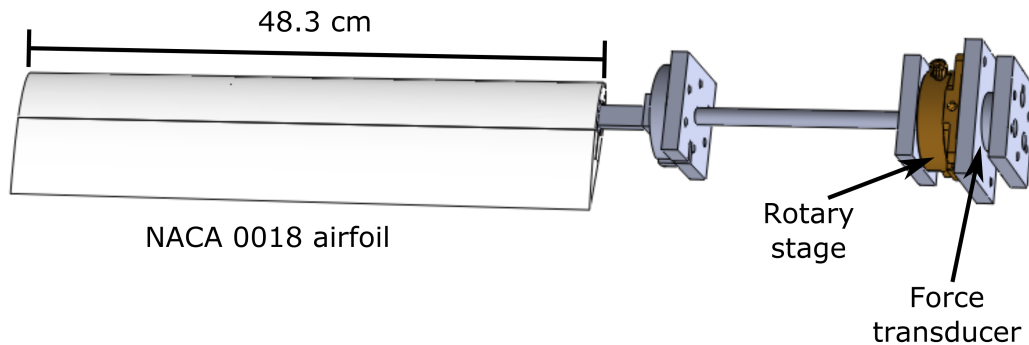


Figure 3.4: Diagram of the static wing's mount. Note the rotary stage and force transducer to the right. The plate on the far right was mounted to the support over the tunnel so that the wing hung downward.

The wing was suspended by a force transducer and rotary stage, allowing rotation about its quarter-chord point. An ATI Nano43 force transducer was used to measure the forces and torques on the airfoil over time. The Nano43 was calibrated to a range of ± 36 N of x-y force, and ± 0.5 Nm of torque. A Newport 481-A rotary stage was mounted between the force transducer and airfoil, allowing precise manual control of the airfoil's angle of attack. A diagram of the mounted wing is shown in Figure 3.4.

To reduce free-surface effects, the wing passed through, but did not touch, an acrylic free-surface plate with dimensions as shown in Figure 3.5. The wing fit inside the shown airfoil shape with 3 mm of clearance. The circular portion of this plate rotated in order to allow the airfoil to be tested at any angle of attack.

When appropriate, the airfoil was mounted 75 cm downstream from the gust generation system in order to measure the effects of the gusts. This distance of 7.5 chord lengths was chosen to reduce the short-range effects of the gust generators, such as local flow deflection by the pitching generator at its final angle of attack. Use of a significantly longer distance was infeasible due to the finite length of the test section.

3.5 Dynamic Airfoil

An additional airfoil was needed for experiments that used both a pitching gust generator and a downstream airfoil. For the dynamic pitching experiments, a NACA

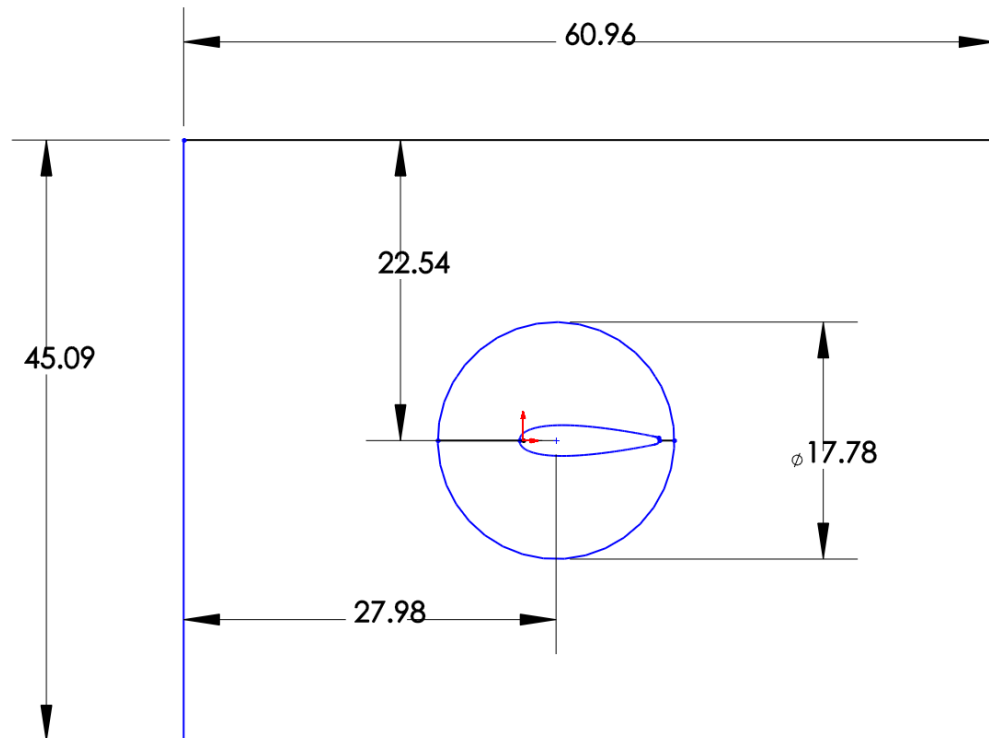


Figure 3.5: Diagram of the wing's free surface plate, which was 0.63 cm thick. Measurements are in centimeters. The circular portion allows for rotation of the airfoil, which passes through the airfoil-shaped hole at the center.

0018 airfoil with a 10 cm chord and 55 cm span, wetted to 46 cm, was used. Its axis of rotation was through its quarter-chord point. This airfoil was manufactured stereolithographically by Stratasys out of Somos Watershed XC 11122, with a minimum feature resolution of 25 microns. A schematic of this pitching airfoil's place in the NOAH tunnel is shown in Figure 3.6. In experiments with both airfoils, the distance between their quarter-chord points was 75 cm. The transverse distance from the airfoil's quarter-chord point to the midline is *yupstream*.

3.6 Heaving Plate Apparatus

In some experiments, the motion of the heaving plate was actuated with a LinTech ball screw with a diameter of 0.75" and lead of 0.5", driven by a NEMA 34-490 microstepping motor. This motion was measured using an Encoder Products Company rotary encoder mounted to the ball screw, with a resolution of 1000 lines per revolution. Two mechanisms were built, as shown in Figure 3.9a. The second iteration, Figure 3.9b, increased the mechanism's stiffness and accuracy. A

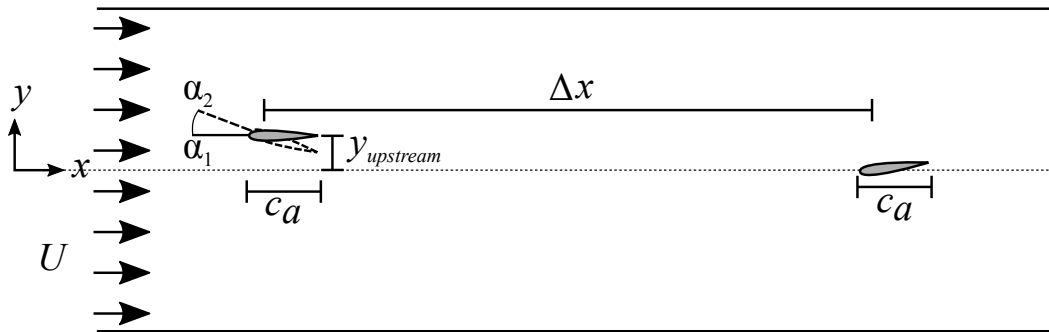


Figure 3.6: Diagram of the pitching airfoil system. The upper and lower lines are the sides of the water tunnel's test section. The dashed line is the midline. The axes shown are for definition of positive and negative directions. The initial and final angles of the pitching airfoil were α_1 and α_2 . The distance from the pitching airfoil to the tunnel's midline is $y_{upstream}$. The chord length of the airfoils was $c_a = 10$ cm. The distance to the test article was $\Delta x = 75$ cm.

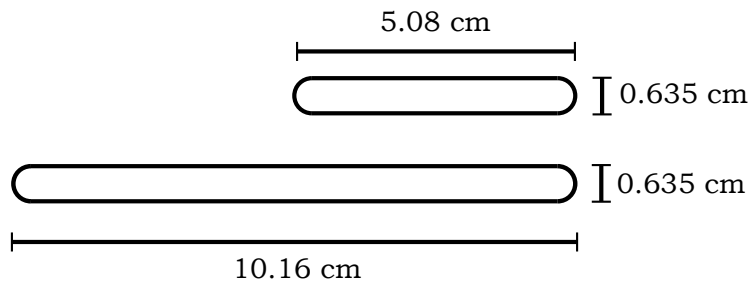


Figure 3.7: Cross-sections of the two heaving plates.

custom LabVIEW program was written to command the stepper motor, trigger the PIV system, measure the encoder position. LabVIEW interfaced with the devices through two NI PCIe-6321 data acquisition cards.

Two flat plates were machined from aluminum, with chord lengths of 5.08 cm and 10.16 cm. Both were 0.635 cm thick with semicircular leading and trailing edges, and extended in span above the waterline. The resulting thickness ratios of the plates were 1/8 and 1/16. Their cross sections can be seen in Figure 3.7. A schematic of the heaving plate's relative location in the NOAH tunnel is shown in Figure 3.8. When used, the heaving plate was mounted with its midline 75 cm upstream from the test article's quarter-chord. The y -position of the plate when it turns around is referred to as y_{peak} .

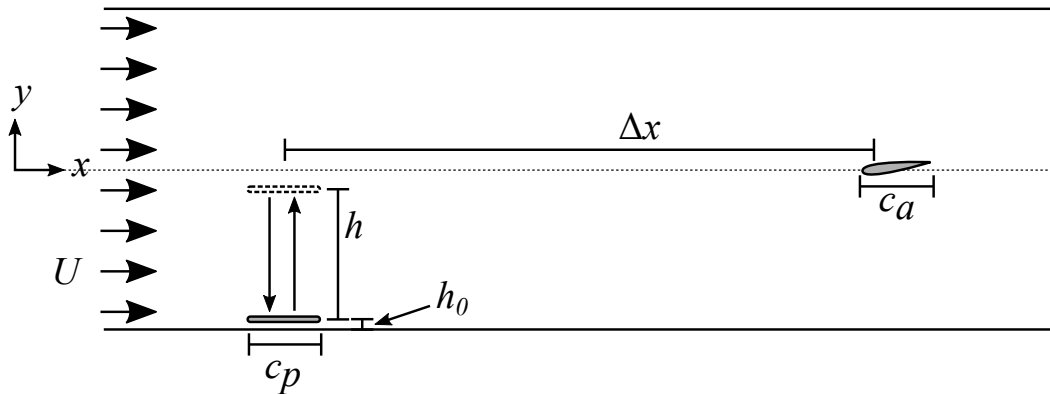


Figure 3.8: Diagram of the heaving plate system. The upper and lower lines are the sides of the water tunnel's test section. The axes shown are for definition of positive and negative directions. The heaving distance of the plate is h . Its initial distance from the wall is h_0 . The distance to the test article was $\Delta x = 75$ cm. The plate length is c_p .

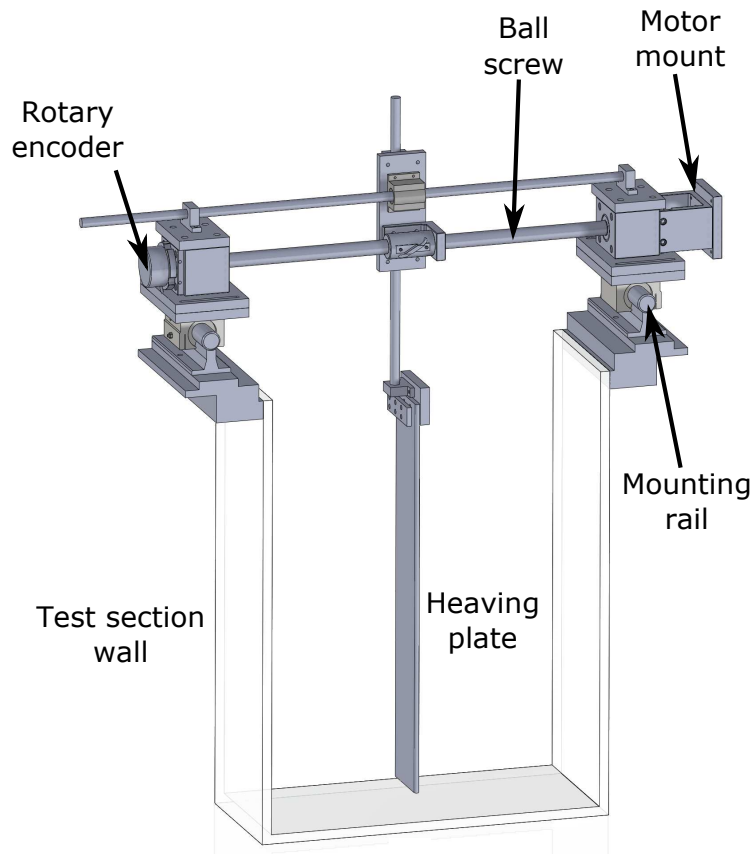
3.7 Gantry System

Some experiments used the NOAH tunnel's new gantry system, shown in Figure 3.10. This is a modification of a kit from CNC Router Parts, with a control system by IO Rodeo. The three linear axes were driven by NEMA 34 stepper motors with 6.8 N-m of holding torque. A NEMA 23 motor with 1.9 N-m of holding torque drove the angle of attack. The control system recorded the positions of the axes over time, as well as data from the force sensor on the airfoil. It also allowed precise triggering of the PIV system, ensuring synchronized force and PIV measurements.

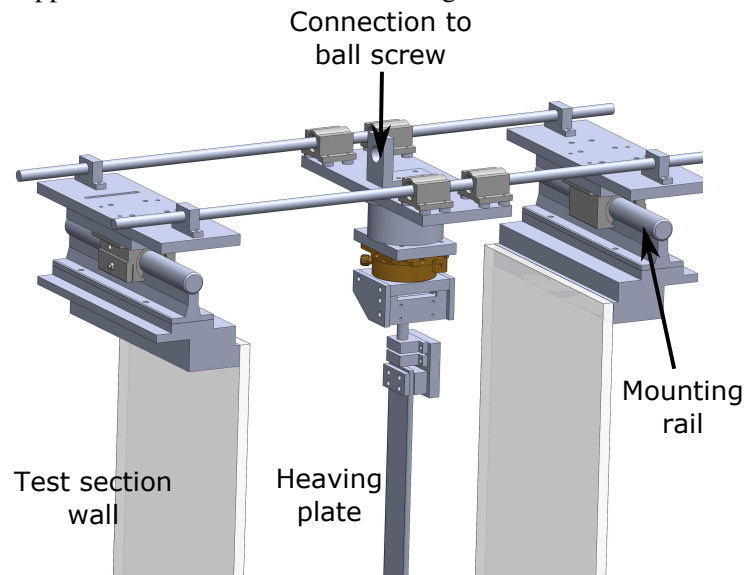
The gantry system was used to position and heave the flat plates, or to position and pitch the upstream gust-generating airfoil. No free surface plate was used around the upstream airfoil or flat plate, due to the difficulties posed by their motion.

3.8 Summary of Experiments

Several suites of experiments were performed. Broadly, the first sets used PIV to characterize the gusts generated by the heaving plates and pitching airfoil. Further experiments used PIV and force measurements to examine the interactions between the gusts and the downstream airfoil. Appendix A contains the details of each experiment. The number of repetitions of each experiment was chosen as a balance between the limited available time in the experimental facilities and a desire to explore a range of parameters of the generators while examining the repeatability of their effects. Chapters 4 and 5 address each experiment and its results.



(a) Model of the first mechanism for the heaving plate. The stepper motor is omitted from this diagram.



(b) Model of the second mechanism for the heaving plate. The ball screw, motor, and encoder are omitted from this diagram.

Figure 3.9: SolidWorks models of the two designs for actuation of the heaving plate. Both are mounted on rails on the NOAH tunnel.

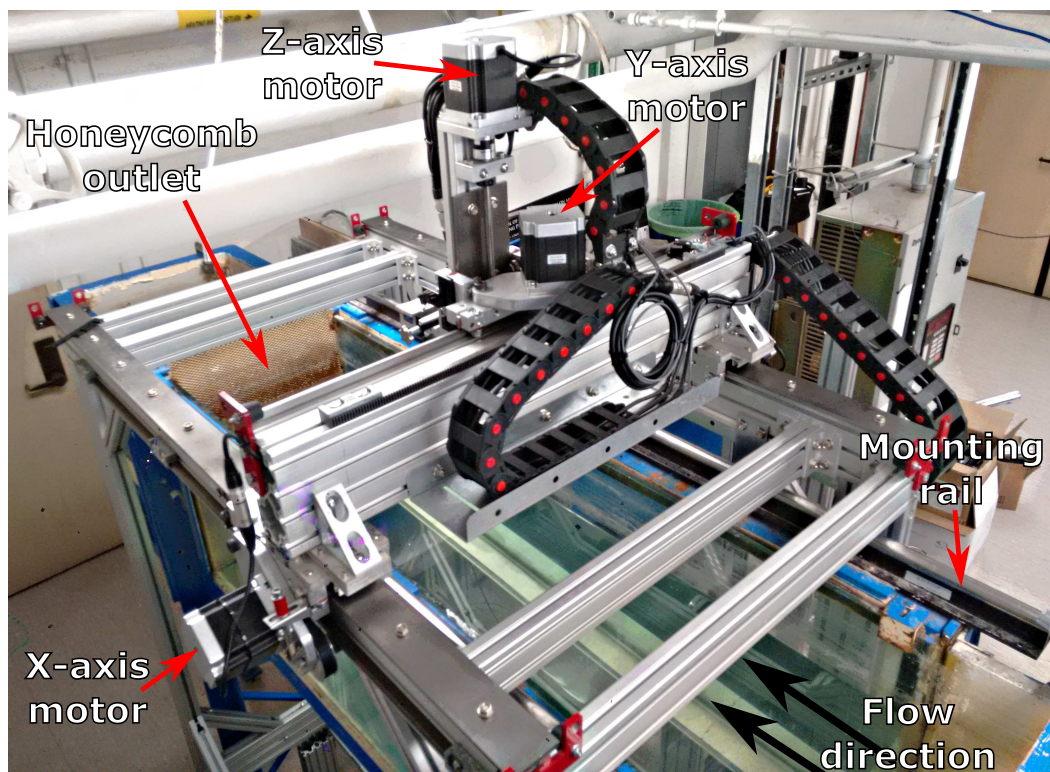


Figure 3.10: Image of the gantry system over the NOAH water tunnel test section. Downstream is toward the upper left of the image.

Chapter 4

GUST GENERATION

4.1 Introduction

This chapter describes¹ experiments performed with the heaving plate and pitching airfoil which aimed to characterize and compare the properties of each approach to vortical gust generation.

Previously, Chapter 2 analyzed these methods through the simplifying lens of potential flow theory, which neglects physically important effects like viscosity and three-dimensionality. The experiments in this chapter were performed in the water tunnel described in Chapter 3, and are described in detail in Appendix A.

After the experiments for each gust generator are presented, the results will be analyzed and discussed. Immediately preceding the summary of this chapter, the two gust generation methods will be directly compared.

4.2 Analysis Techniques

The analysis of these experiments relies heavily on two techniques: the visualization of the flow through ‘unwrapping,’ and the identification of vortices. This section describes these methods and how they were used.

4.2.1 Gust Unwrapping

Many of the flows observed in this thesis consist of flow structures convecting with the constant freestream velocity. This allows the flow to be unwrapped into a larger field of view, converting a time-varying two-dimensional measurement of part of the flow field into a single snapshot of the flow that encompasses the observed time span. This is illustrated in Figure 4.1. Individual frames, at the top of the figure, show only a portion of a structure, which is moving from left to right at speed U . At the bottom, these frames have been combined to show a view of the full structure.

More rigorously, for each velocity field at time t , the ‘initial’ position of that view is computed as $x' = x - tU$. The estimated structure is then assembled by averaging together each frame, interpolated onto its ‘initial’ position. With the freestream velocity subtracted, the result is a view of the convecting structure in its own frame.

¹Some of the work in this chapter was previously presented in an AIAA conference paper [34].

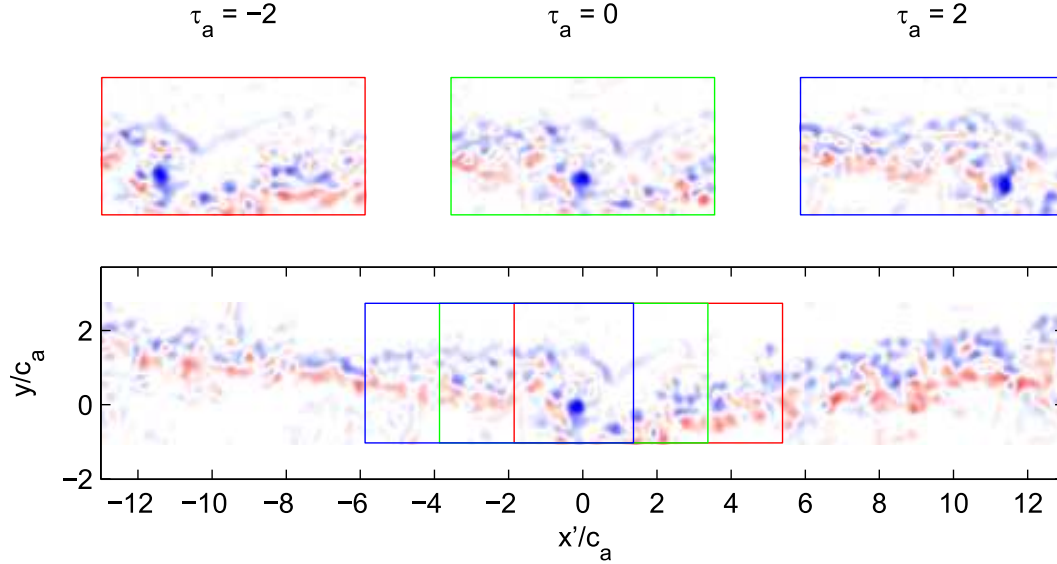


Figure 4.1: This shows a portion of the unwrapping process. Three snapshots of the vorticity field of a passing gust are shown. With the flow moving at constant speed from left to right, an unwrapped view of the convecting structure can be assembled from the snapshots as in the second plot. In practice, significantly more than three snapshots were used to unwrap the flow.

In this chapter, all of the spatial dimensions have been nondimensionalized by the airfoil's chord length, c_a , independent of the length of the gust-generating device. The unwrapped gusts present the nondimensionalized vorticity, u -velocity, or kinetic energy. The dimensionless kinetic energy of the unwrapped gusts is defined as $(u^2 + v^2)/U^2$, using the velocities in the frame of the convecting gust.

4.2.2 Vortex Identification

It is not simple to identify a vortex. The theoretical underpinnings of vortex identification are often based on local velocity gradients [9, 11, 37], which is troubling for experimentalists. The presence of noise in experimental measurements greatly reduces the efficacy of such methods, which motivated Michard and Graftieaux [28, 49] to develop a non-local method of vortex identification: the Γ_2 function. This is a Galilean invariant criterion that gives a measure of how circular the mean-subtracted flow is around a point. Equation 4.1 defines this function for two-dimensional flow.

$$\bar{u}(\mathbf{x}) = \frac{1}{A} \int_S u \, dS, \quad (4.1a)$$

$$\bar{v}(\mathbf{x}) = \frac{1}{A} \int_S v \, dS, \quad (4.1b)$$

$$\Gamma_2(\mathbf{x}) = \frac{1}{A} \int_S \frac{(v - \bar{v})x - (u - \bar{u})y}{\sqrt{x^2 + y^2} \sqrt{(u - \bar{u})^2 + (v - \bar{v})^2}} dS. \quad (4.1c)$$

The point around which the flow's circularity is evaluated is \mathbf{x} . The circular region of integration is S , its area is A , and the average velocity components in that region are denoted by an overline. If the mean-subtracted flow is perfectly circular around \mathbf{x} , then $\Gamma_2 = \pm 1$, depending on the direction of rotation. If the magnitude is greater than $2/\pi$, the region is declared vortical. In a simple flow, this is identical to saying that magnitude of the rotation is greater than that of the shear. Since the Γ_2 function subtracts the local average velocity, it is invariant to translating frames of reference.

Since the Γ_2 function integrates over a region, any weak noise is generally averaged out. Unfortunately, this leads to a free parameter: the radius of the integration region. The analyses that follow in the text use a range of integration radii, from 0.5 to 6 cm, which is 5% to 60% of the airfoil's chord length.

Once a vortical region has been identified, the vorticity within that area can be integrated to estimate the vortex's circulation. An additional concern with the Γ_2 criterion is that these approaches do not entirely capture the vorticity of ideal vortices. For example, when applied to a Lamb-Oseen vortex, the Γ_2 criterion estimates its circulation to be 72% of the true value.

The Γ_2 function provides an estimate of the location of the vortex's center: the point with the maximum magnitude of Γ_2 . The average radial and tangential velocity profiles of the vortex may then be computed by averaging those fields in annuli around the center.

In each set of experiments, the Γ_2 function was used to determine the circulation of the primary vortex in each frame where it was visible. This led to a distribution of values for each set of experimental parameters. The reported values in this chapter are the 25th, 50th, and 75th percentiles of these values, using the largest radius of integration. This displays both the median and variation in the measurements. This was necessary due to error in the computed velocity fields and variation of the flow over time.

This chapter also compares how well the theoretical values of the circulation match the experimental measurements. In later figures, the plotted values are the ratio between the unsteady thin airfoil theory's estimate and the median of the experimentally measured circulation, for the different radii of integration. Two fitting methods were

used. The curves labeled “LSQ” were determined by the least-squares division of the array of estimated values by the measured values. The “Mean of Ratio” curves are the average of the ratios for each experiment. If the experimental measurements match the theory, then these curves should be near unity.

The y -position of the vortex is reported in a similar fashion, using the distributions of identified vortex center locations. The reported x -velocity of the vortex was computed using a linear least-squares fit of the vortex’s x position over time.

4.3 Experimental Generation of Gusts via Pitching Airfoil

The standard method of producing a vortical gust has been to rapidly pitch an airfoil upstream of a test article. A diagram of the pitching airfoil in the NOAH tunnel is shown in Figure 3.6. This system has multiple parameters: the upstream airfoil’s y -position, $y_{upstream}$, and its initial and final angles of attack, α_1 and α_2 . The downstream airfoil is sketched in to represent its position in the experiments described in the next chapter. The distance from the upstream airfoil to the future test article, Δx , was 75 cm in each experiment, and its chord length, c_a , was 10 cm. Each of these experiments were performed at a chordwise Reynolds number, $Re_{c_a} = U c_a / \nu$, of 20,000.

As a baseline measurement of how much the airfoil disturbs the flow, PIV was recorded downstream of the static airfoil. PIV was then used to measure gusts created by rapidly pitching the airfoil from zero degrees to one of three final angles. Additionally, the three-dimensionality of one of these gusts was investigated using PIV in a spanwise plane.

4.3.1 Perturbation of Freestream

PIV measurements were taken downstream of the static airfoil, in order to examine its wake at two static angles of attack: 0° and -13° . The details of this experiment are in section A.2.4.

Figure 4.2 shows the unwrapped dimensionless kinetic energy of these wakes. The flow has traveled from left to right. These have been unwrapped to highlight the unsteadiness in the flow. The wake of the airfoil at 0° is significantly slower, thinner, and less energetic than that of the -13° airfoil. The most energetic portion of the thicker wake is also at a substantially lower y .

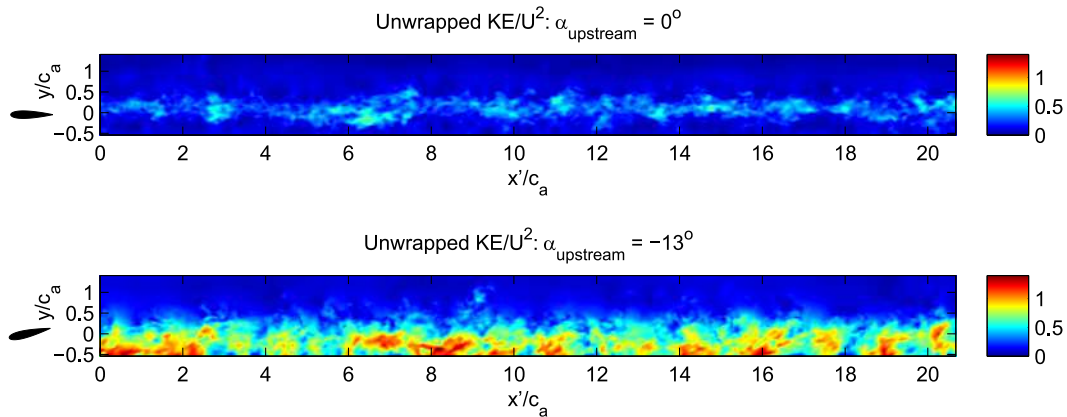


Figure 4.2: Unwrapped kinetic energy behind the static airfoil at two angles of attack: 0° and -13° . To the left are to-scale representations of the upstream airfoils at the two angles.

4.3.2 Characterization of Gusts

These experiments aimed to examine the gusts created by the pitching 10 cm airfoil. Of particular importance are the general structure of the gusts, and the properties of the vortices they contain. PIV measurements were taken 75 cm downstream of the airfoil, where a downstream airfoil would be in later experiments. The airfoil was rapidly pitched over a time of $1 t_c$ from 0° to a final angle of -5° , -10° , or -13° . This pitching time was near the minimum achievable with the current actuation method, and is compatible with strong shed vortices according to the numerical results shown in Figure 2.9. The details of this experiment are in section A.3.1.

The unwrapped vorticity that resulted from each set of parameters is shown in Figure 4.3. These vorticity fields are constructed from the median value of the vorticity across each set of parameters. Due to the non-dimensionalization used, x'/c_a is equivalent to $-t/t_c$ for the airfoil. Thus, the region to the right of $x' = 0$ is due to the airfoil before pitching, and to the left is after pitching.

The unwrapped gusts can be divided into two regions: the primary vortex that was shed when pitched, and the wake region outside that. In the -5° case, the primary vortex is difficult to find with the naked eye. In the other tests, the vortex is clearly visible as the concentration of vorticity at the center of the frame. After the pitching, $x' \lesssim 0$, the wake is more complicated and unsteady. For the -10° and -13° cases, there was an increase in the vortical activity in the wake around $8 t_c$ after the vortex. This level was similar to the wake of the static upstream airfoil at -13° . The post-pitching wake indefinitely continued to perturb the flow.

The primary vortices in the flow were identified using the Γ_2 criterion. Figure 4.4 shows the measured x-velocity and y-position of these vortices, determined from motion of the peak Γ_2 value, as functions of the Γ_2 radius of integration. This confirmed that the primary vortices travel with the freestream velocity. Figure 4.4b shows that the y-position of the vortices is fairly independent of the pitching angle, but varies more with the smaller pitching angle. The Γ_2 function did not successfully identify the vortex from the $\alpha_2 = -5^\circ$ experiments in many of the frames. As a result, there was significant uncertainty in the position and circulation of these vortices. Additional plots of the paths of the vortices can be seen in Figures C.5 and C.6.

The circulation of these primary vortices, normalized by the estimate from unsteady thin airfoil theory (Equation 2.6) is shown in Figure 4.5. The smaller pitching angle led to weaker vortices, beyond what theory predicted. The measured circulation varied significantly for the weaker vortices, partially due to the difficulty of identification. In contrast, the circulation of the strongest vortices agreed well with the theoretical value.

Figure 4.6 shows how well the measured circulation matches theory for a range of vortex identification radii. At the larger radii, the fit coefficient approached unity, suggesting that the circulation was well estimated by thin airfoil theory. The mismatch at small radii of integration is likely due to the vortex being larger than the integration region, such that not all of the vorticity was captured.

The average velocity profiles of the vortices, both radial and tangential, with the largest radius of integration, can be seen in Figure 4.7. The average radial velocity was effectively zero. The peak tangential velocity increased with the larger final angle of attack.

4.3.3 Three-dimensionality of Gusts

To examine the spanwise variation of the gusts, PIV was used to measure the flow in the $x - z$ plane: along the length of the vortex. The details of this experiment are in section A.3.3.

Figure 4.8 shows the unwrapped streamwise velocity of the gust created when the airfoil pitched from 0° to -13° . The expected position of the vortical gust is at $x' = 0$, where a region of reduced velocity is seen. There appears to be a linear region of higher velocity near $z = 0.25$, but this may be an artifact of joining the PIV frames. There are other variations in the freestream velocity beside the structure at $x' = 0$, but none as coherent as the vortical column.

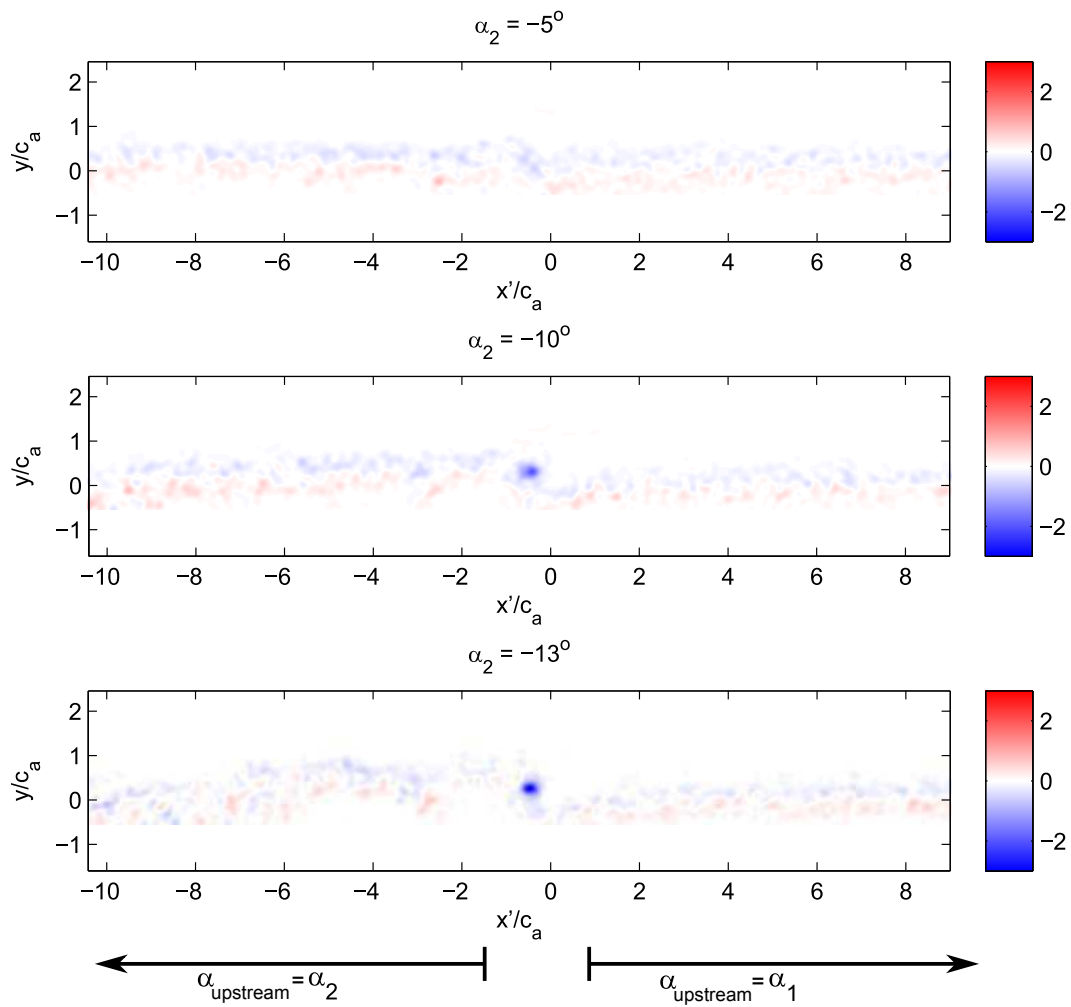
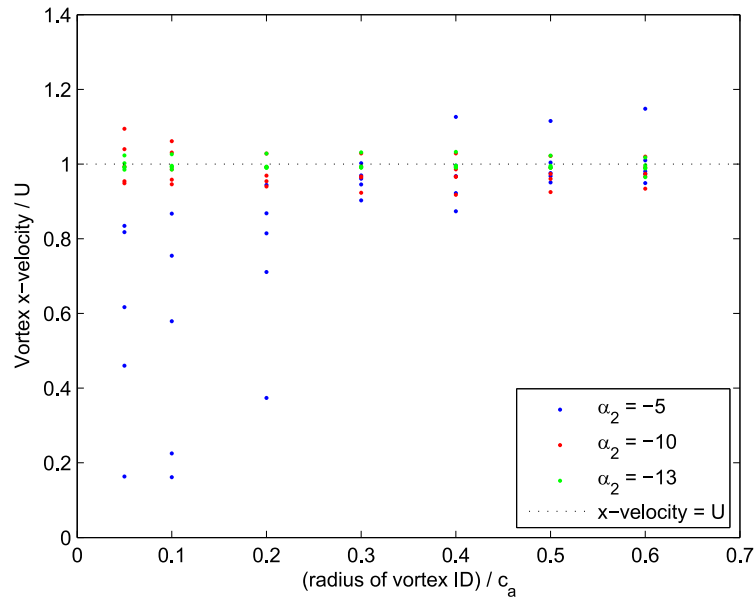


Figure 4.3: Unwrapped vorticity downstream of the airfoil after it pitched to -5° , -10° , or -13° . Vorticity has been normalized with the freestream velocity and airfoil chord length. The regions pertaining to the pre-pitching angle, α_1 , and post-pitching angle, α_2 , of the upstream airfoil are labeled at the bottom of the figure.



(a) Streamwise speed of the identified vortices.

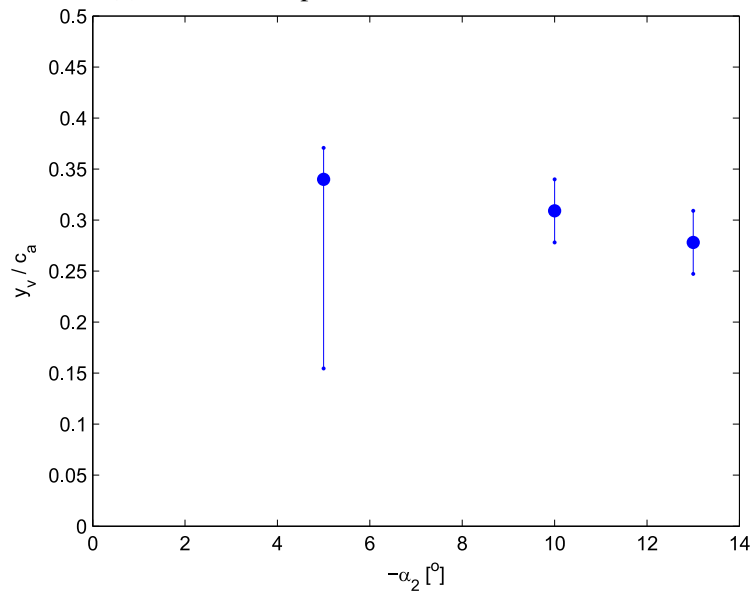
(b) y -position of the identified vortices. The large symbols are the median value of the position, and the whiskers are the 25th and 75th percentiles.

Figure 4.4: Speed and y -position of vortices created by the pitching airfoil, for a range of vortex identification radii. The lengths are normalized by the airfoil's length. Velocities are normalized by the freestream velocity.

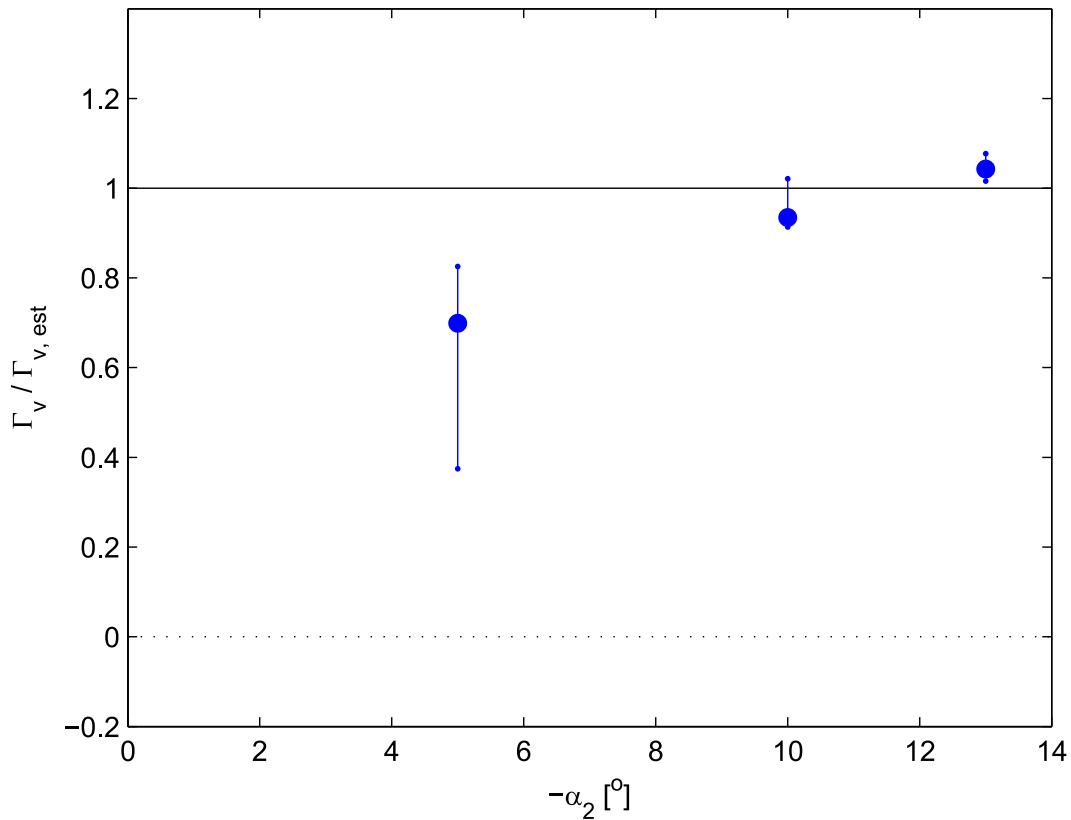


Figure 4.5: Normalized circulation of the primary vortices shed by the pitching airfoil, measured 75 cm downstream of the plate. The large symbols are the median value of the circulation, and the whiskers are the 25th and 75th percentiles.

4.3.4 Discussion

The streamlined profile of the static airfoil resulted in a weak wake being shed when the airfoil was at 0° and -5° , but a significantly slower and more unsteady wake at -13° . The airfoil was stalled at this point, resulting in an oscillating separated region and the thicker wake that accompanied that. This could be a problem when used as a gust generator, as the downstream test article would be continually influenced by the oncoming wake, particularly with the airfoil at -13° . The stark difference in the wakes before and after pitching suggests that the effect of the vortical gust on a test article may be difficult to separate from the change in the flow. Also, the flow around the test article may exhibit quite different behavior with these oncoming wakes, as compared to a less perturbed flow.

In Figure 4.3, an increase in the vorticity is seen about 8 convective time units after the vortex passed (that is, at $x' \approx -8$) for the two higher final angles of attack. This was likely a result of the flow around the airfoil adjusting to its new angle,

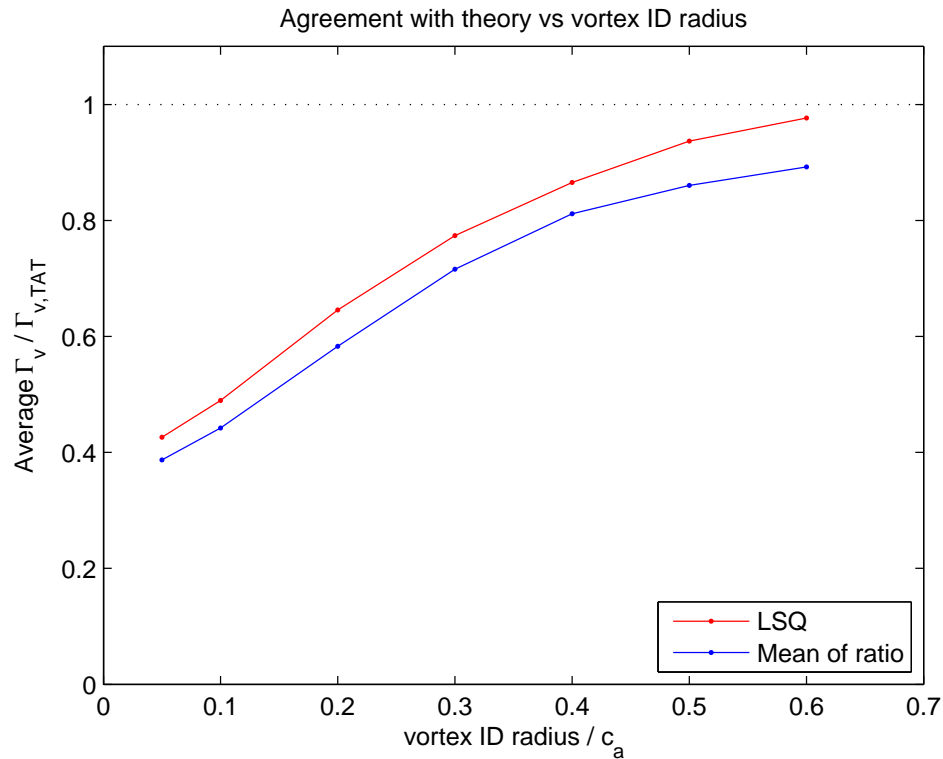


Figure 4.6: Scale factor for fitting the circulation of the pitching airfoil's primary vortices to the unsteady thin airfoil theory result, as a function of the vortex identification radius.

and beginning to shed the thicker and more unsteady wake characteristic of the stalled state. The wake thus has three portions: the initial wake before pitching, the transitional wake immediately after pitching, and the final wake due to the airfoil's new angle of attack. This complicated flow means more possible effects on a downstream test article.

A larger radius of integration tended to delimit a larger vortical area, so the circulation within increased. This was not an unbounded increase, as the fit seems to level off. The fit coefficient appears to approach unity, so the estimate from thin airfoil theory provides a good estimate of the measured value of the circulation. Unfortunately, the Γ_2 function was not always able to identify the weakest vortices, so their circulations are not precisely known. These were masked by the surrounding wake of the airfoil, and so were not easily identified.

In Figure 4.8, the PIV plane was not precisely in the plane of the vortex's midline. Since the vortex had negative circulation, the visible slower flow at $x' = 0$ means

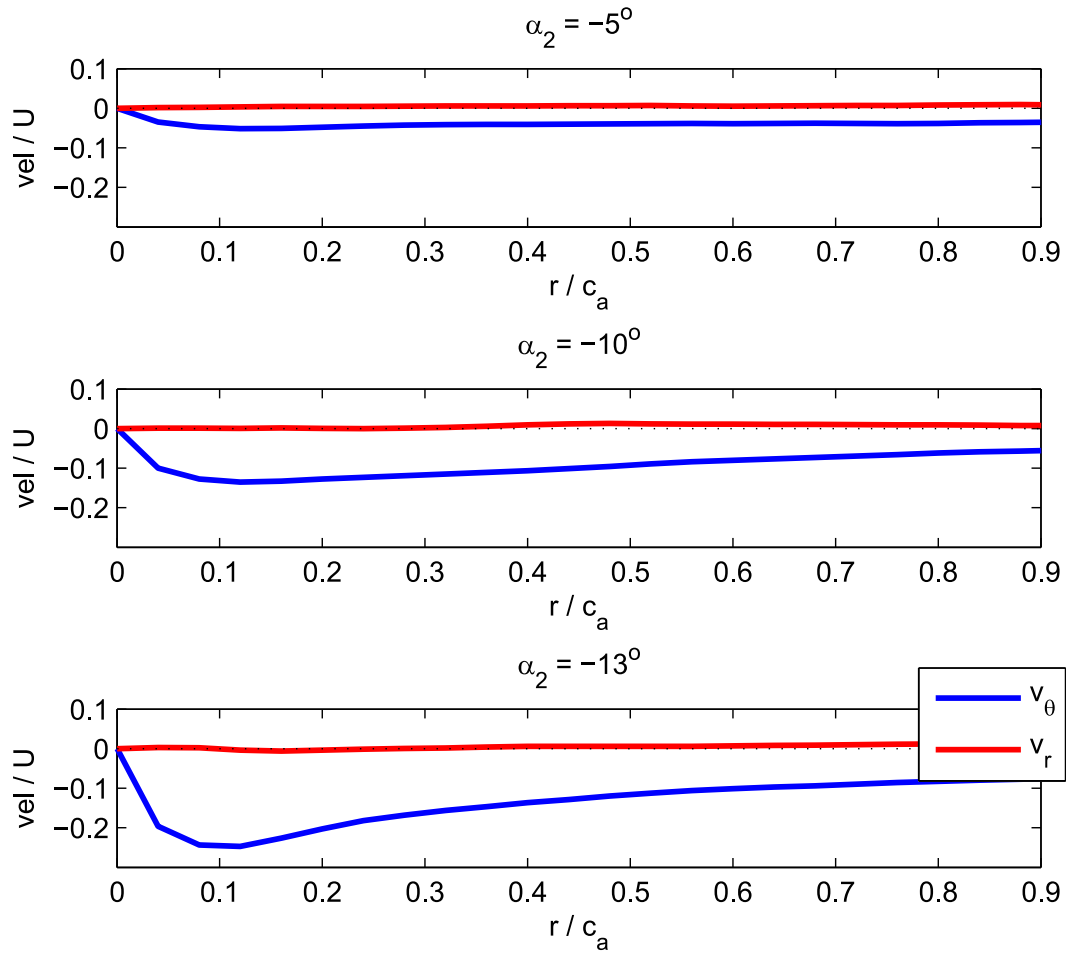


Figure 4.7: Velocity profiles of the vortices created by the pitching airfoil, normalized by the freestream velocity. The tangential and radial velocity profiles are v_θ and v_r , respectively.

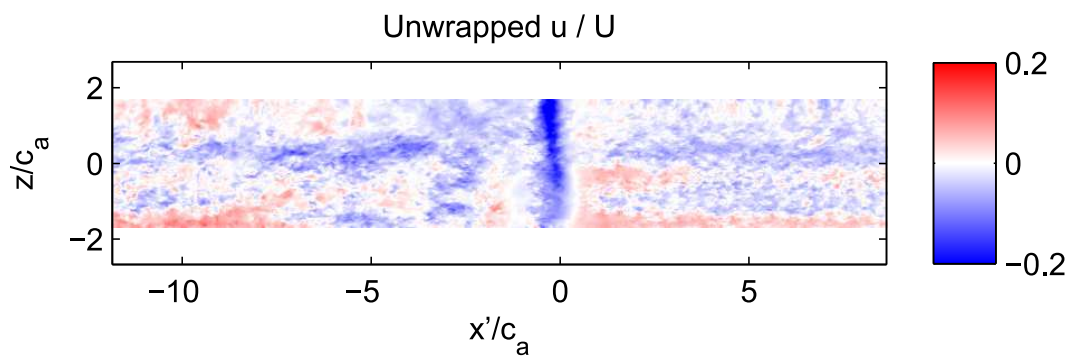


Figure 4.8: Unwrapped x -velocity downstream of the pitching airfoil, in the spanwise x - z plane.

that its core was farther from the camera than the PIV plane. There was some three-dimensionality to the flow, but the vortex was the dominant feature seen.

Overall, the pitching airfoil system was able to generate vortical gusts, the circulation of which were proportional to the theoretical estimates. The vortices convected with the freestream, and their y -positions were nearly independent of their circulations. The constant y -position of the airfoil resulted in a persistent wake, both before and after the desired vortical gust was created.

4.4 Experimental Generation of Gusts via Heaving Plate

A series of experiments were conducted to characterize the effects of the heaving plate, and its suitability for vortical gust generation. Figure 3.8 shows a diagram of the heaving plate in the NOAH tunnel. The downstream airfoil is sketched in to represent its position in the experiments described in the next chapter. Some parameters are necessary to describe the performance of this gust generator: the chord length of the plate, c_p , the initial distance from the wall, h_0 , and distance from the plate to the future test article, $\Delta x = 75$ cm. The inclusion of viscosity yields the Reynolds number of the static plate, $Re_{c_p} = Uc_p/\nu$. The plate changed directions over acceleration times of $t_{accel}/t_{cp} = 0.5 - 1.44$. These were near the minimum achievable by the actuators, and were consistent with strong vortices according to the unsteady potential models.

As a baseline, experiments first examined the effect on the freestream of a static plate near the edge of the tunnel. To isolate the response of the flow to the plate's motion, without the change in direction, a set of experiments measured the flow due to the plates moving from one side of the tunnel to the other at different speeds. Additionally, a range of chordwise Reynolds numbers, Re_{c_p} , and dimensionless heaving speeds, S , were tested with a plate that changed directions at the center of the tunnel, in order to see their influence. In-depth examination of the flow around the heaving plate for a range of S and heaving distances, H , was undertaken to characterize the vortex shedding process. Experiments downstream of the heaving plate measured the speed and circulation of the shed vortices over a range of S , H , and with both plate chord lengths. Furthermore, the three-dimensionality of the flow was measured using PIV along the length of the shed vortex.

4.4.1 Perturbation of Freestream

In order to measure whether the plates significantly changed the flow around the center of the tunnel, experiments were performed with each plate held statically near

the edge of the tunnel, with a freestream speed of $U = 20$ cm/s. This was tested with both lengths of heaving plates at separate times, and at either side of the tunnel. The parameters of this experiment are described in section A.4.5. Such potential perturbations of the freestream could be due to blockage effects or the wake of the plate.

Unwrapped views of the flow's kinetic energy 75 cm downstream of the plates, around the tunnel's centerline, can be seen in Figure 4.9. Comparison of the different flow fields showed that these tested parameters had negligible effects. Later experiments (section 5.3.1) repeated these tests, but included measurements of the forces on a downstream airfoil. The negligible change in the forces obviated the need for additional repetitions of this experiment. Overall, no significant change in the freestream was seen, using PIV or force measurements.

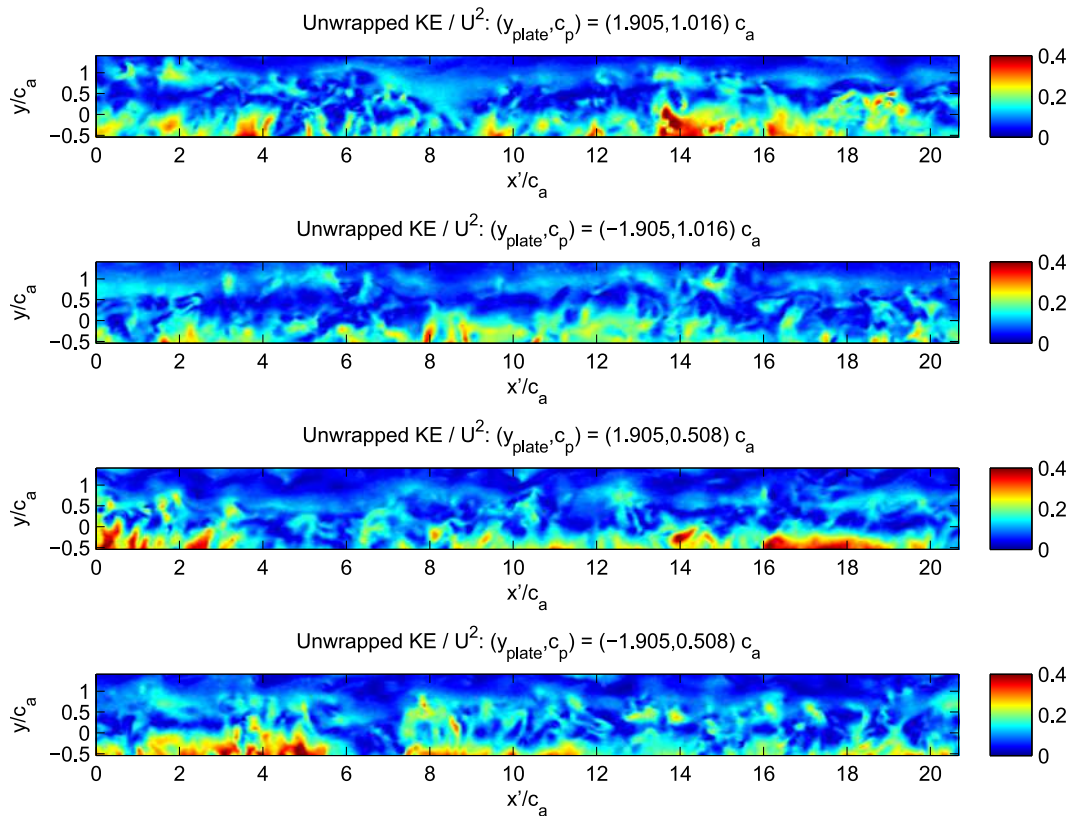


Figure 4.9: Unwrapped view of the kinetic energy around the center of the tunnel, downstream of the static plates which are in place near the walls. The first and third frames are at the $+y$ side of the tunnel, and the other two are at the $-y$ side. The first two frames used the 10 cm plate, where the others used the 5 cm plate. The plates are at $y_{plate} = \pm 1.9c_a$.

4.4.2 Passing Plate

Further experiments examined the effect of the plate moving from one side of the tunnel to the other without changing direction, with a freestream speed of $U = 20$ cm/s. This was intended to separate the effects of the beginning of motion from those of the change in direction. The parameters of this experiment are in section A.4.4. Figures 4.10 and 4.11 show the unwrapped passing wakes. Since the plate moved from $+y$ to $-y$, the wake appears to be a diagonal structure. In this frame, faster plates result in the structure appearing more vertical.

As the speed increased, the wakes became more energetic and convoluted. Using the longer plate also resulted in thicker and more unsteady wakes. The 10 cm plate's wake contained large vortical regions, and increasingly so at higher speeds.

4.4.3 Flow around the Heaving Plate

A detailed view of the flow around the heaving 10 cm plate was measured for a range of heaving distances and speeds, with constant $U = 20$ cm/s. The details of this experiment are in section A.4.2.

A simplified cartoon of the idealized flow around the heaving plate is shown in Figure 4.12. This is separated into two rows to highlight the different effects expected of the plate at different speeds. When the plate moves slowly, the flow remains attached to the plate. With faster motion, the flow around the plate should be separated, with a thick wake behind it. In both cases, the plate will be shedding wake vortices as it moves steadily. Once the plate changes directions, it sheds a primary vortex, which convects downstream as the plate returns toward its initial position. The regular vortex shedding then resumes after some time.

The behavior of the flow around the heaving plate can be divided into phases, as illustrated in Figure 4.13. The position of the plate over time is shown in Figure 4.13a, along with markers representing the position of the following panels. Figure 4.13b shows the wake behind the moving plate, immediately before the change in direction. Figure 4.13c shows the wake rolling up, and 4.13d shows the primary vortex (the red structure) after it has been released. Figure 4.13e shows a vortex that was released as the plate decelerated.

That example was at $S = 0.36$, but similar behaviors can be seen with different heaving speeds. In each case, the plate initially sat unmoving, and the flow around it was fully developed. Once the plate accelerated, the flow around the plate with the slowest S diverged significantly from the other cases. The flow remained attached

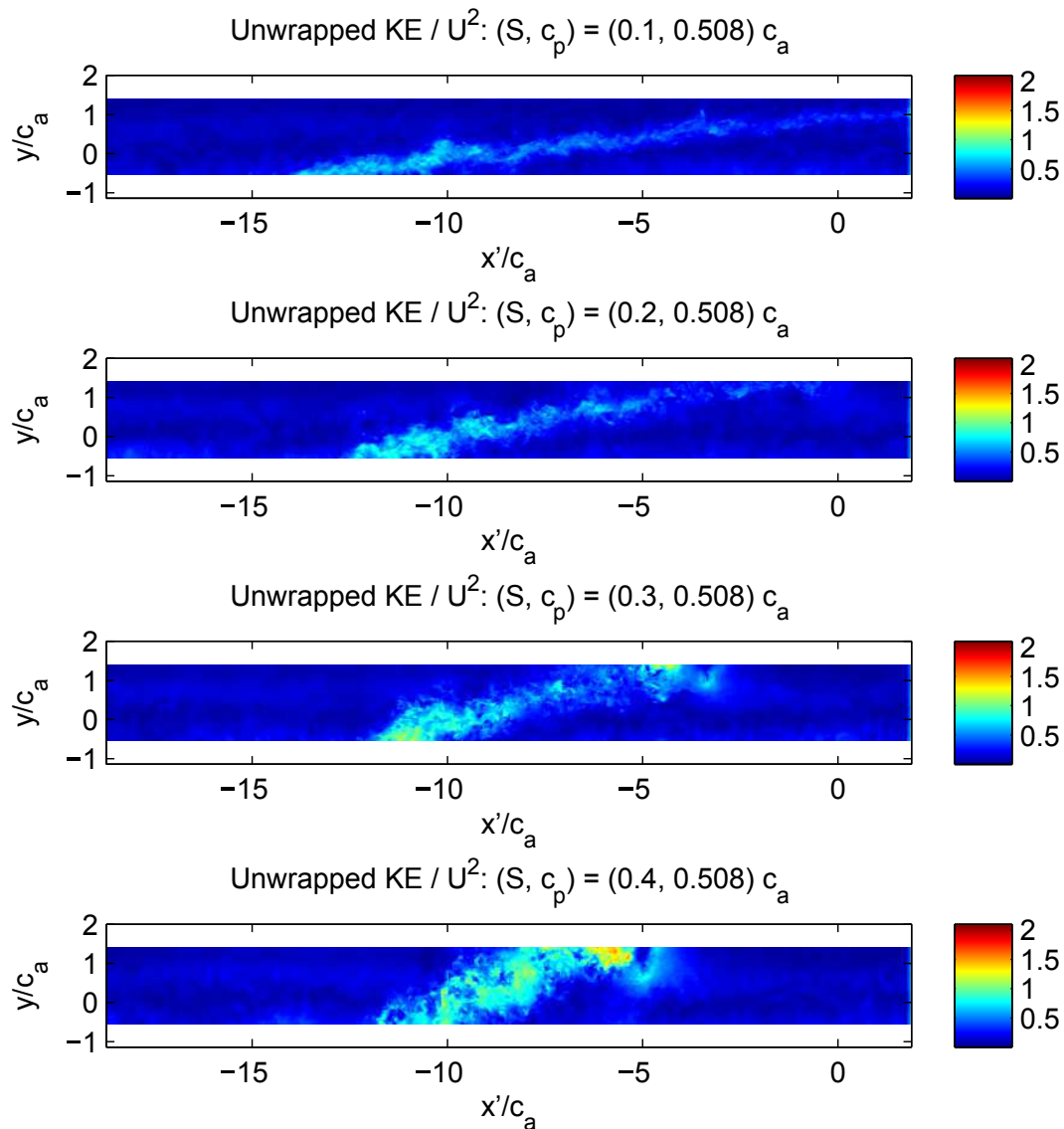


Figure 4.10: Unwrapped views of the normalized kinetic energy of the wake of the passing 5 cm plate. The value of S in each plot is in its title.

for that case, but a separated region developed in the others. In all cases, a starting vortex, with negative circulation, was shed as the flow developed. For the slowest S , regular von Kármán vortex shedding was seen throughout the motion, and modified only when the plate accelerated. At the peak of the motion, a stronger vortex of positive circulation was shed, and regular shedding resumed immediately. In the faster cases, as the plate moved upward, a separated region developed on the lower side of the plate, and von Kármán vortex shedding did not resume during the period of measurement. After the plate changed direction, this separated region rolled

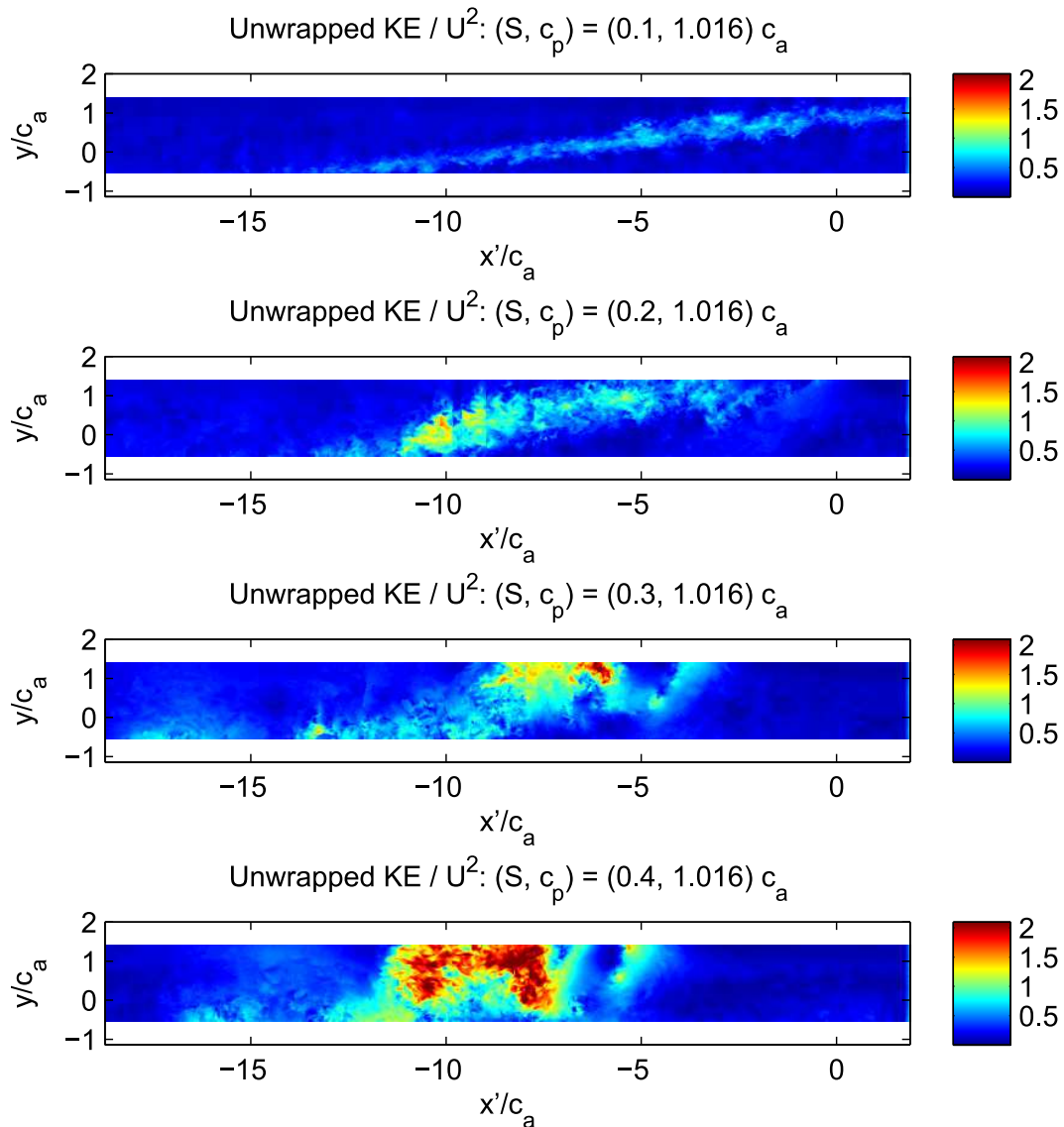


Figure 4.11: Unwrapped views of the normalized kinetic energy of the wake of the passing 10 cm plate. The value of S in each plot is in its title.

up and was shed as a primary vortex with positive circulation. On the upper side of the plate, a leading edge vortex was then seen to grow as the upper surface's separated region developed. When the plate decelerated to its initial position, negative circulation was again shed.

To measure the circulation of the shed vortex, Graftieaux's Γ_2 criterion was used immediately downstream of the plate to identify the primary vortex in each experiment. The circulation of each vortex, normalized by the estimate from thin airfoil theory (Equation 2.13), is plotted in Figure 4.14. The experiments with longer

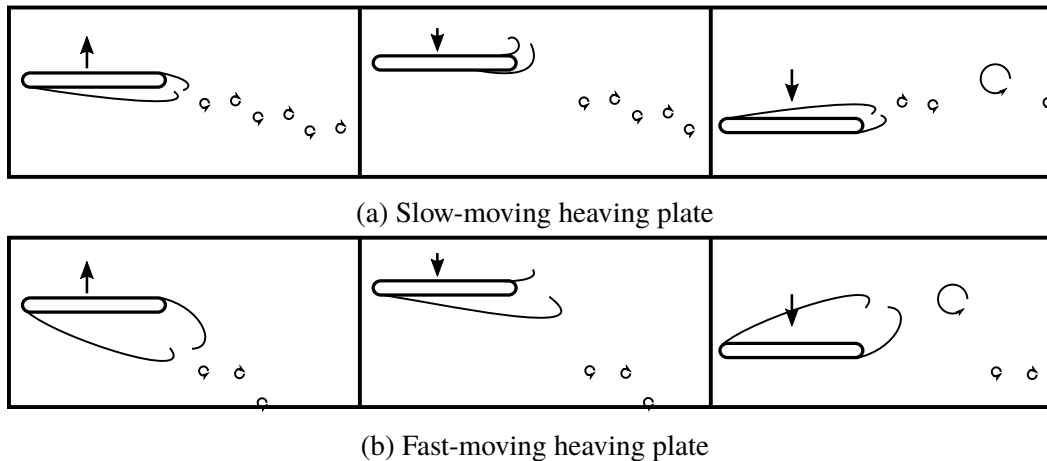


Figure 4.12: Sketches of the flow around the heaving plate. The top row is a slow-moving plate, with attached flow. The bottom row is a fast plate, which has separated flow. The three frames in each row represent, from left to right: the plate moving upward at constant speed, the plate immediately after changing direction, and the plate moving downward after having shed a vortex.

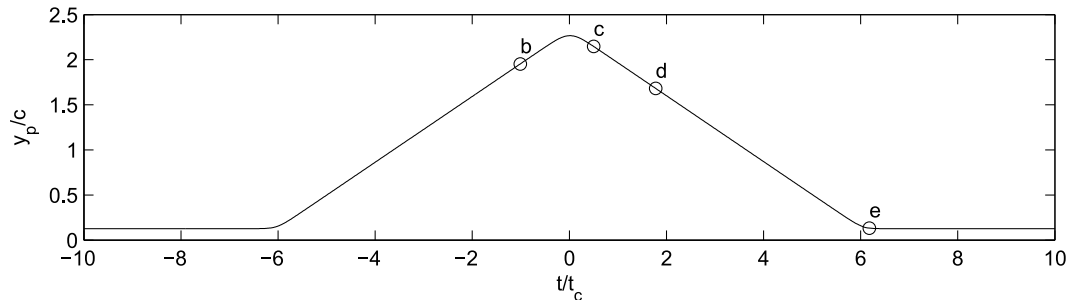
heaving times, T , more closely matched the estimates of thin airfoil theory. With the fastest plates, $S = 1.0$, there was a strong effect of the heaving time: as the plate moved farther, the gust's circulation approached the theoretical estimate.

Figure 4.15 shows how well the measured circulation matches theory for a range of vortex identification radii. The agreement increased initially with the vortex identification radius, but only to a point. The fit coefficient is significantly less than unity, demonstrating a mismatch with thin airfoil theory.

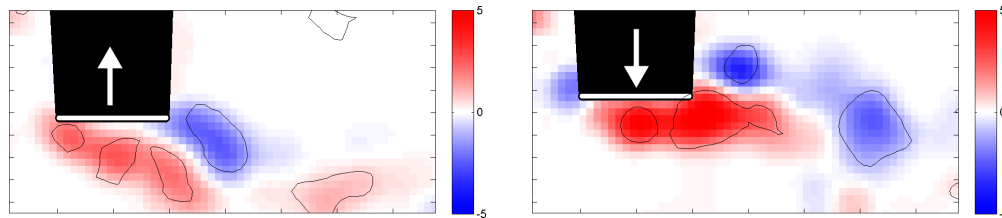
4.4.4 Effects of Re_c and S

Experiments were performed to examine the effect of different freestream speeds, U , and dimensionless heaving speeds, S , of the 10 cm plate. The plate was tested at freestream Reynolds numbers of 7,900, 13,500, and 19,500. The parameters of these experiments are detailed in section A.4.1.

Because the flow was illuminated from one side in this experiment, the plate cast a shadow over a region of the flow field. No PIV data was extracted from this dark region. As such, experiments with both directions of travel were performed, and their PIV fields were combined into a full view of the flow. Figure 4.16 shows snapshots of the vorticity around the plates shortly after the change in direction. At this point, the vorticity was rolling into a vortex before it detached from the plate

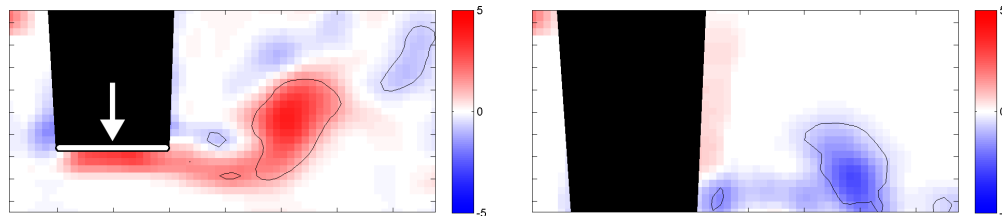


(a) The plate position over time. The times of the following vorticity fields are labeled on this plot.



(b) The plate is moving steadily upward, with a wake trailing behind.

(c) The plate has changed directions, and the wake is rolling up.



(d) The plate moves steadily downward, and the vortex continues to roll up.

(e) The plate has stopped moving, and has shed vorticity due to its deceleration and possible wall interactions.

Figure 4.13: Frame *a* shows the position of the heaving plate over time for experiments with $S = 0.36$ and $T = 5.9$, as well as the positions of the subsequent frames. Frames *b-e* show the vorticity field around the moving plate, averaged over five repetitions. The black contours delineate where the Γ_2 function identified vortices. The solid black region is the area in the shadow of the plate where PIV data is unavailable. The white arrow denotes the direction of the plate's motion. This figure reproduced from Hufstедler and McKeon [34].

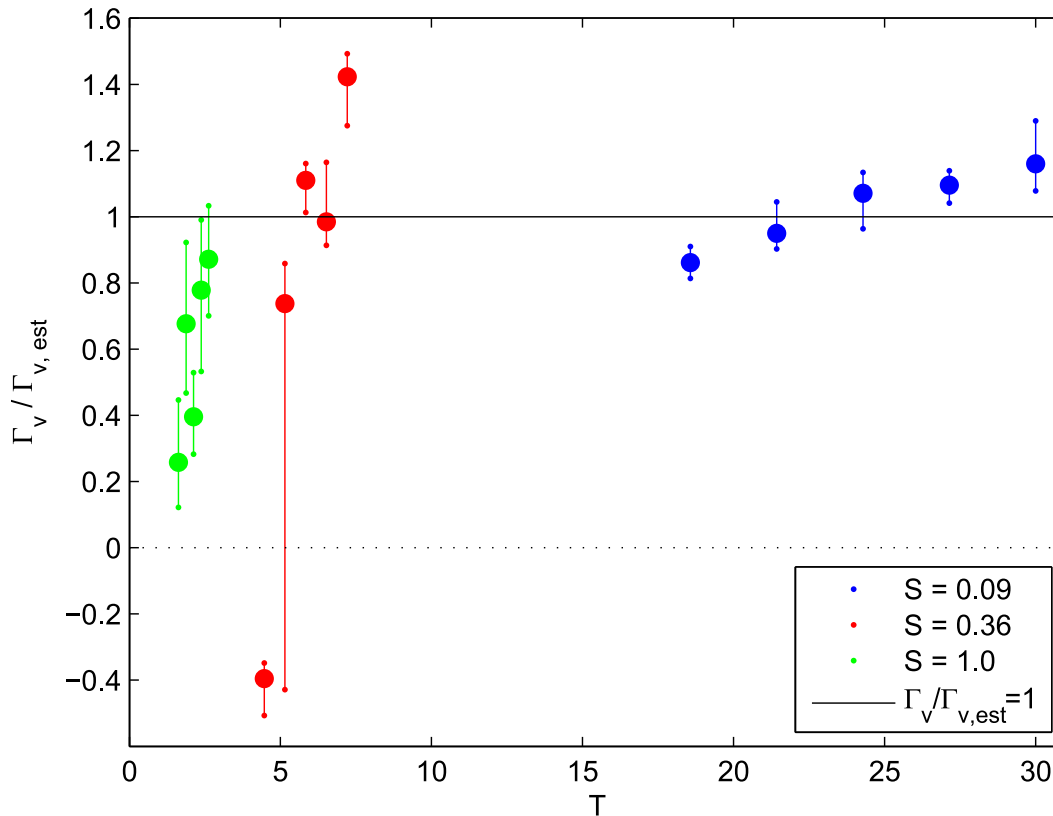


Figure 4.14: Normalized circulation of the primary vortices shed when the plate changed directions, measured immediately downstream of the plate. These were normalized by the thin airfoil theory estimate in Equation 2.13.

and traveled downstream. Over this range of parameters, variation of Re_{c_p} had a qualitatively minor effect on the flow around the plate, as compared to S . As S increased, the flow was increasingly disorganized, with a larger separated region on the plate which, when the plate changed direction, was shed as a large vortical region that then traveled downstream. Further snapshots of these developing flows are in Figure C.4.

4.4.5 Effects of c_p

PIV was used 75 cm downstream of the heaving plate to measure the effects of different plate lengths, c_p , as well as variation in S and H , on the properties of the gusts. The details of this experiment are in section A.4.3.

The unwrapped vorticity of a subset of the gusts, across the tested range of S , are shown in Figure 4.17. These consist of two portions: the primary vortex at the center, and the V-shaped wake region outside of it. This shape was due to the

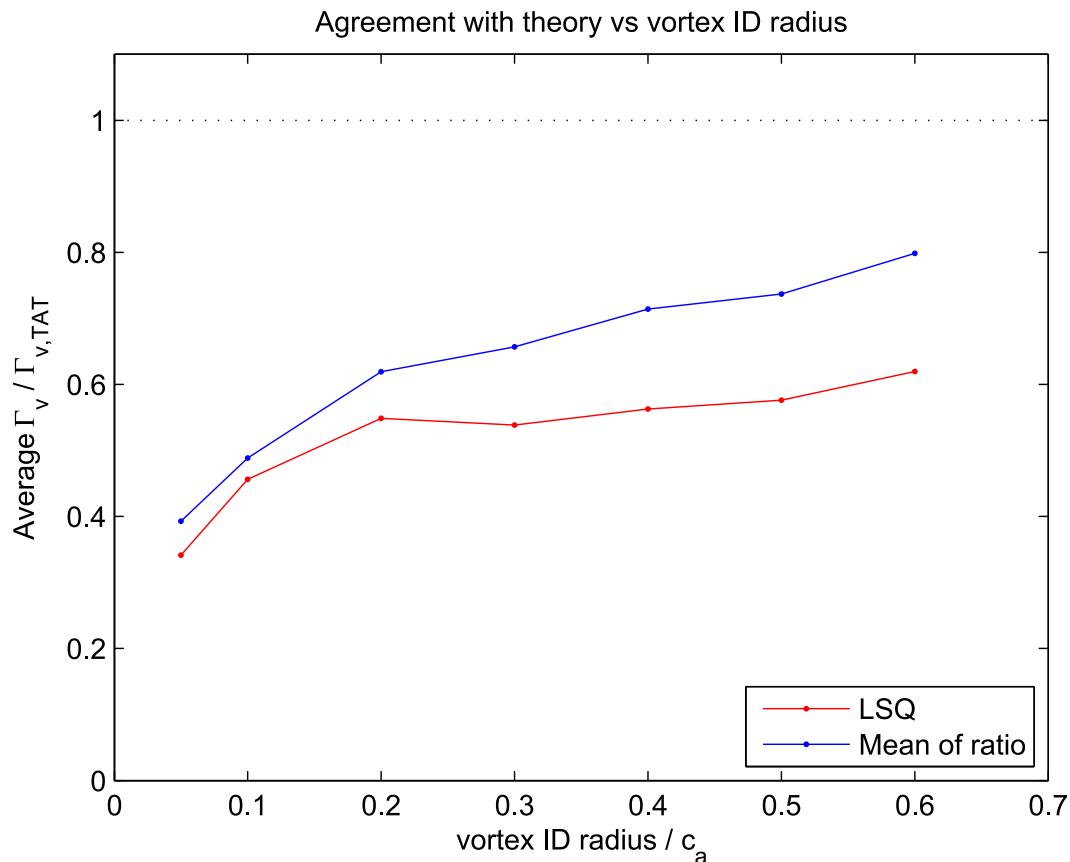


Figure 4.15: Scale factor for fitting the circulation of the primary vortices to the unsteady thin airfoil theory, measured immediately downstream of the plate.

path of the heaving plate as it advanced and withdrew. With either of the plates, increasing S led to larger and more energetic primary vortices, as well as more energy in the wake regions. Use of the longer plate resulted in more complicated flows, in both the wake and vortex regions.

The measured circulation of the primary vortices, normalized by the thin airfoil theory estimate (Equation 2.13), is plotted against their heaving time, T , in Figure 4.18. The slower plates, which traveled for longer times, tended to generate relatively stronger vortices, compared to the theoretical estimates. The shorter heaving time generally reduced the normalized strength of the vortices, but this was confounded by the heaving speed and plate length.

The fit between theory and experiments is shown in Figure 4.19, over the range of vortex identification radii. The agreement with theory increased as the vortex identification radius increased. The fit coefficient displays a good match between

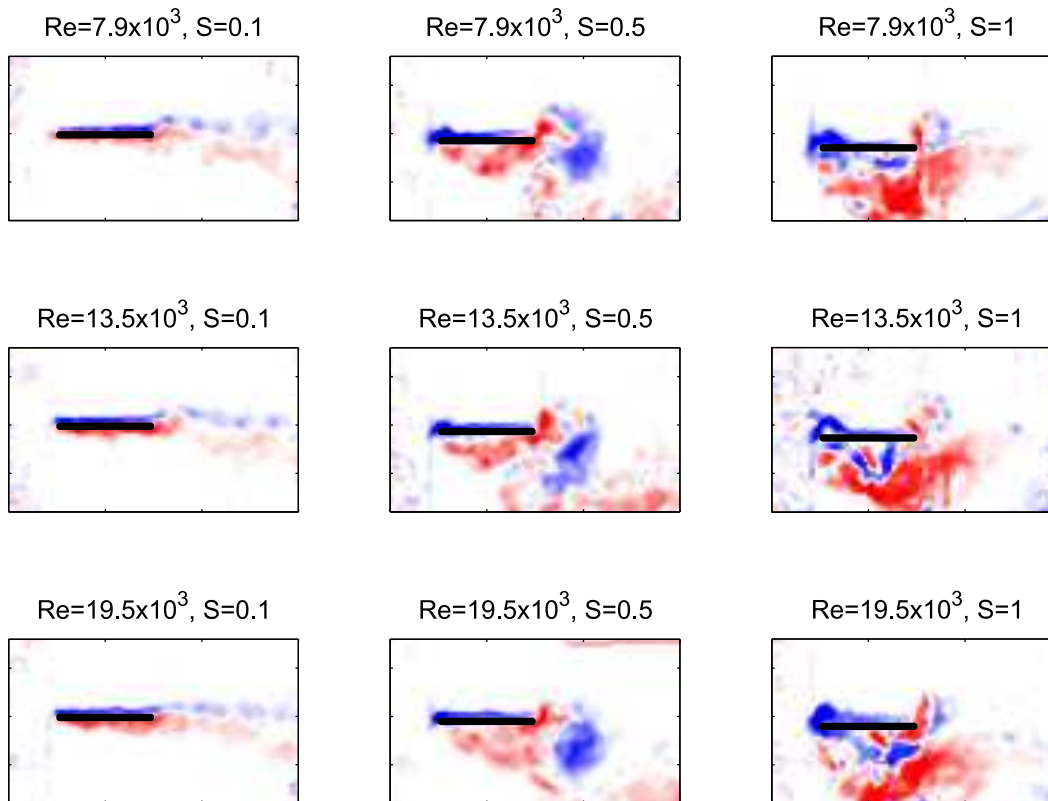


Figure 4.16: Vorticity around the plates at $0.25 t_c$ after the change in direction. The plate is currently moving downward. Each row is a different Re_c , and each column is a different S .

the theory and experiments, at the larger radii.

4.4.6 Effects of H and T

To examine the effects of H and T , further experiments measured PIV at the downstream location over a greater range of H and two heaving speeds, using the 5 cm plate. The details of this experiment are in Appendix A.4.6.

The positions and speeds of the identified vortices are shown in Figure 4.20. The x -velocity plot demonstrates that the vortices traveled with the freestream. The y -positions of the vortices track the positions where they were released, but with an offset.

The unwrapped vorticity of the gusts is shown in Figures 4.21 and 4.22. In each gust, the path of the plate can be seen as the diagonal wake on either side of the primary vortex. The slower motion in Figure 4.21 displays the averaging of the velocity fields as the shear-layer-like wake. The faster motion, Shown in figure 4.22,

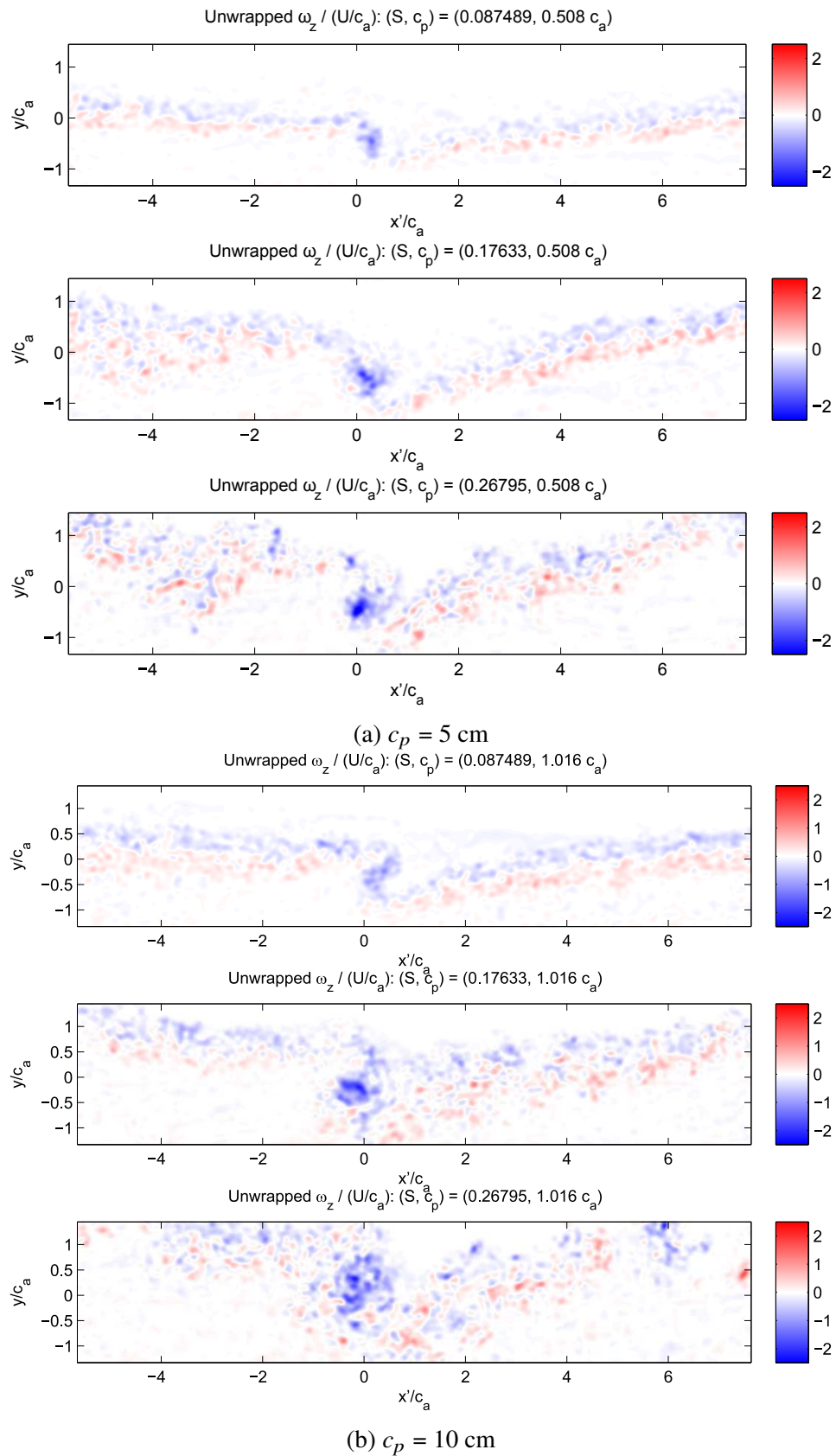


Figure 4.17: Unwrapped vorticity of the gusts 75 cm downstream of the heaving 5- and 10-cm plates. Each row is a different S : 0.09, 0.18, and 0.27.

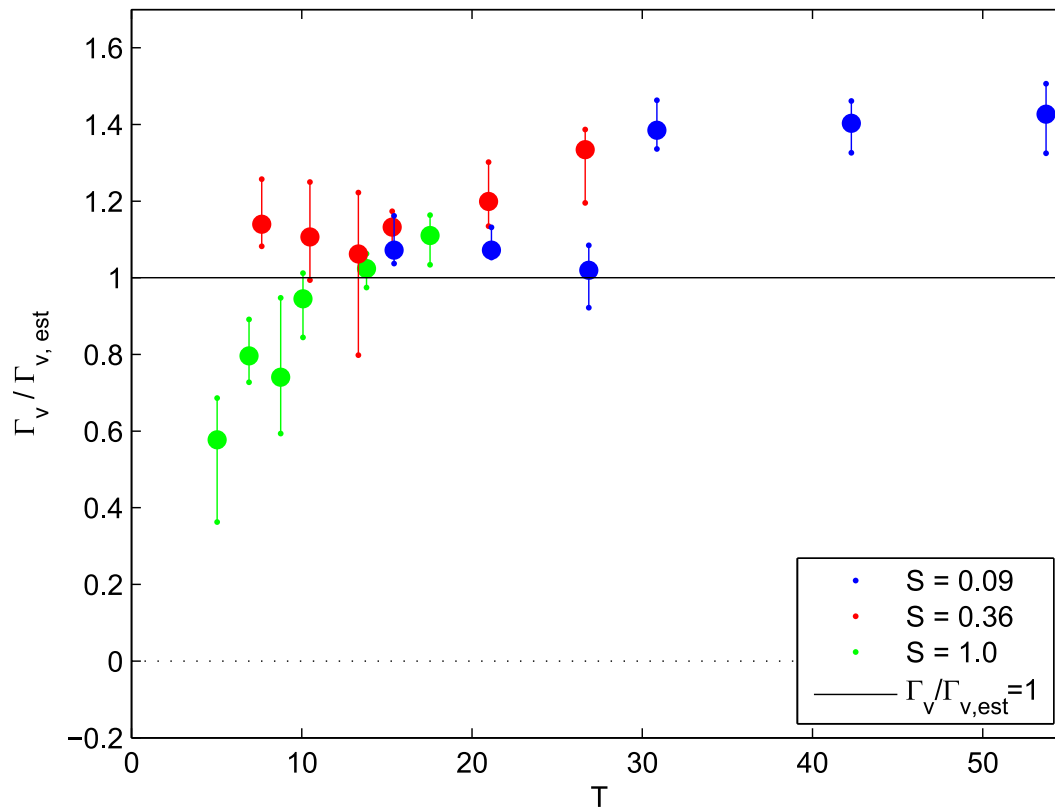


Figure 4.18: Circulation of the primary vortices shed when the 5 and 10 cm plates changed directions, measured 75 cm downstream of the plates. The large symbols are the median value of the circulation, and the whiskers are the 25th and 75th percentiles.

resulted in a more complicated flow, in both the vortex and wake regions. Here, additional structures created by the faster plate are visible at the upper edge of the field of view, both before and after the primary vortex.

The velocity profiles of the gusts are plotted in Figure 4.23. The radial velocity profiles are near zero, as would be expected in incompressible flow. The slower plates, in the left column, show consistent tangential velocity profiles: a peak in speed followed by a slow decrease. There was substantially more variability with the faster plate. These were larger vortices, and did not always demonstrate such a peak.

The normalized circulation of the primary vortices is shown in Figure 4.24, as a function of the plate's heaving time. As before, the vortices shed from the faster plate tend to be weaker than predicted. The two lowest values, at $T = 7$ and $T = 47.5$ are near the edges of the field of view, and so were not entirely visible. This resulted

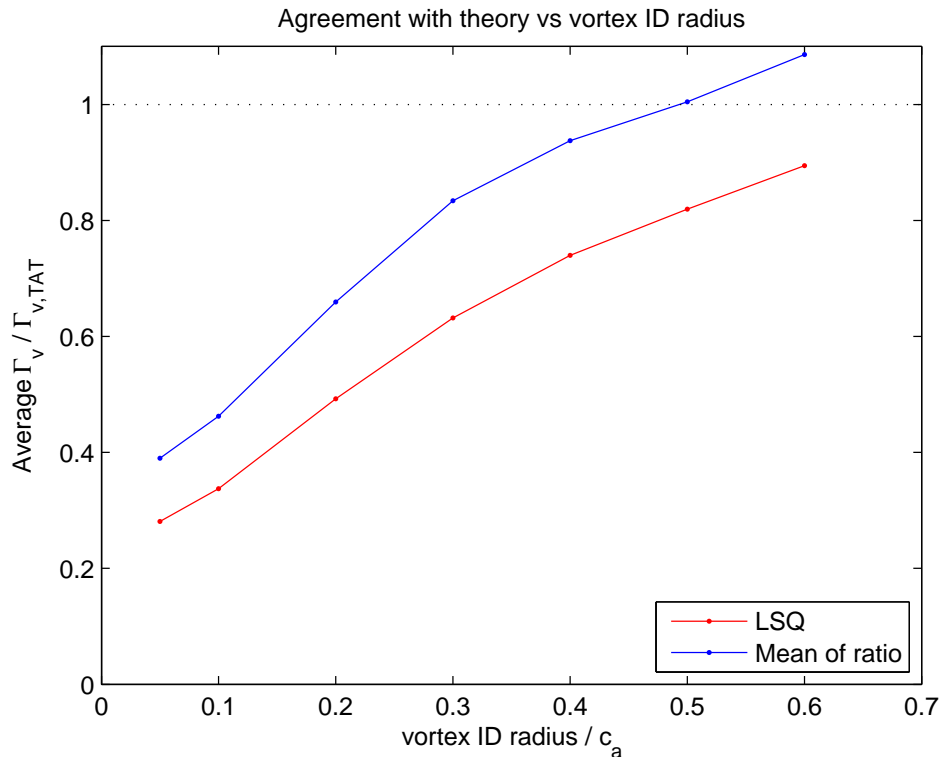


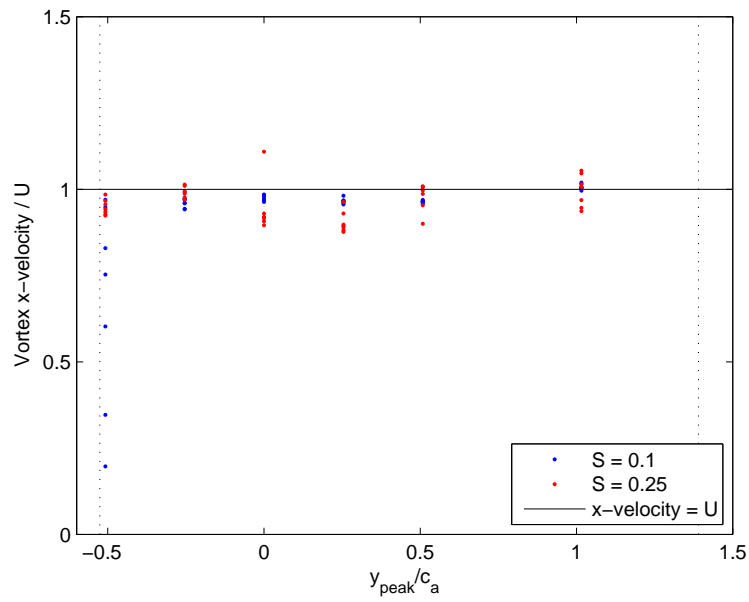
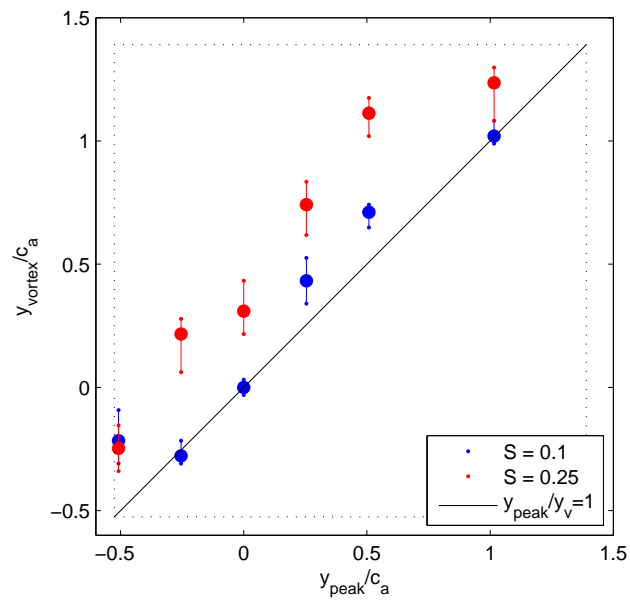
Figure 4.19: Scale factor for fitting the circulation of the primary vortices shed by the 5- and 10-cm plates to the unsteady thin airfoil theory, measured 75 cm downstream of the plates.

in inappropriately low estimates of their circulation.

Figure 4.25 shows how well the measured circulation matches theory for a range of vortex identification radii. As the radius of integration increased, the theoretical results appeared to accurately estimate those of the experiments.

4.4.7 Three-dimensionality of Gusts

The three-dimensionality of the gusts was examined using PIV along the span of the vortices. The details of this experiment are in section A.4.11. The unwrapped streamwise velocity of the gusts is shown in Figure 4.26. In both experiments with slower motion, there are spanwise structures near $x' = 0$, where the gust's arrival was expected. Using Figure 4.21 for comparison, the vortex itself appears to be the positive (red) structure at $x'/c_a = -2$. The fact that the flow was faster in this plane suggests that the core of the vortex was closer to the camera than the PIV plane. At the higher speed, there was more variability with z , especially with the longer plate. The shorter plate at $S = 0.25$ had a linear structure at $x'/c_a = -2$, which is

(a) x -velocity of the vortices(b) y -position of the vorticesFigure 4.20: Speed and y -position of vortices downstream of the heaving 5 cm plate.

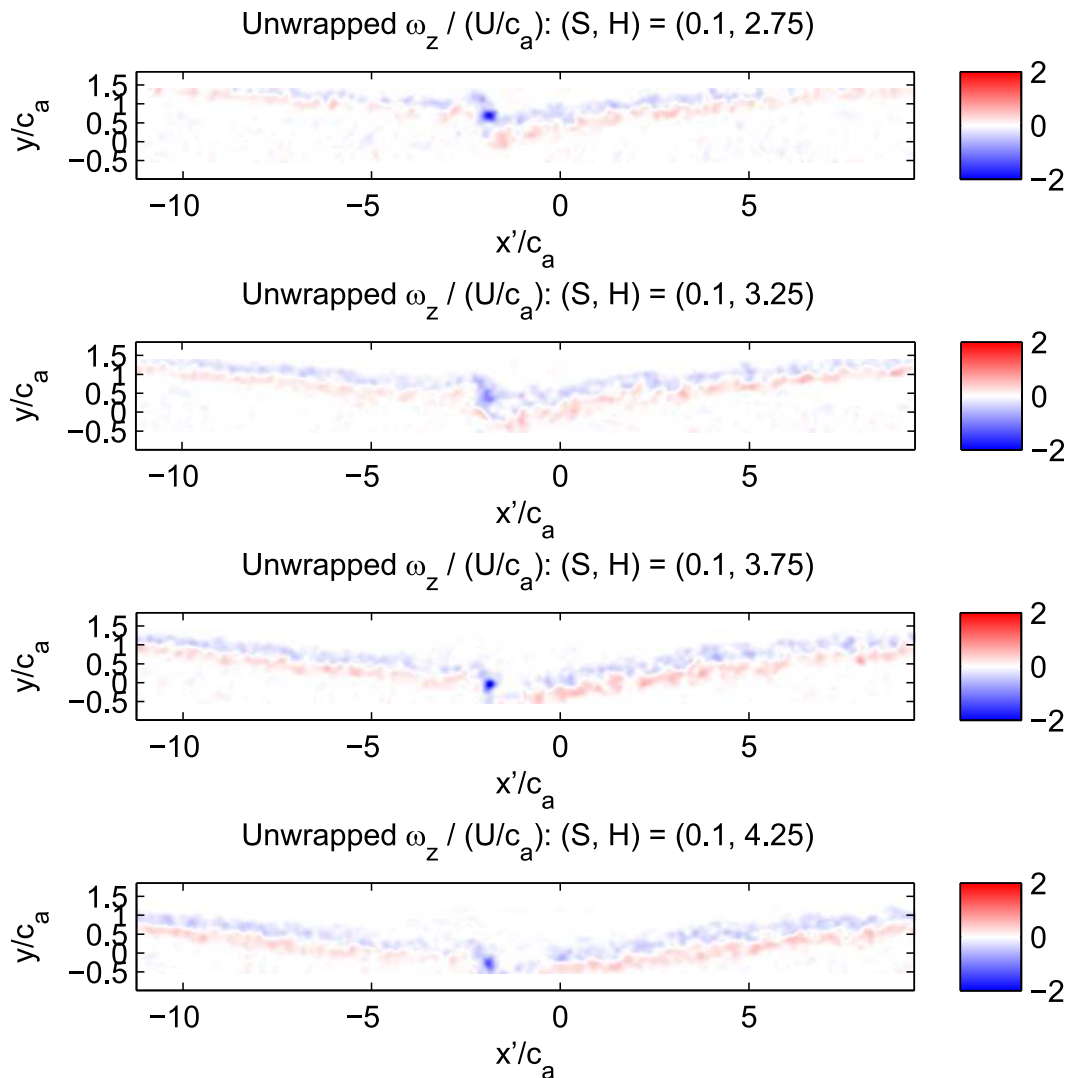


Figure 4.21: Unwrapped vorticity of the gusts downstream of the 5 cm plate heaving at $S = 0.1$.

suggestive of the vortex. The longer plate at that speed shows only a large region of reduced speed at that location.

4.4.8 Discussion

The heaving plate was able to generate vortical gusts that convected with the freestream, with circulations that were approximately proportional to the heaving speed and plate length.

The fact that the plate negligibly perturbed the freestream, when sitting statically near the edge of the tunnel, increases the utility of this system. Were the plate to

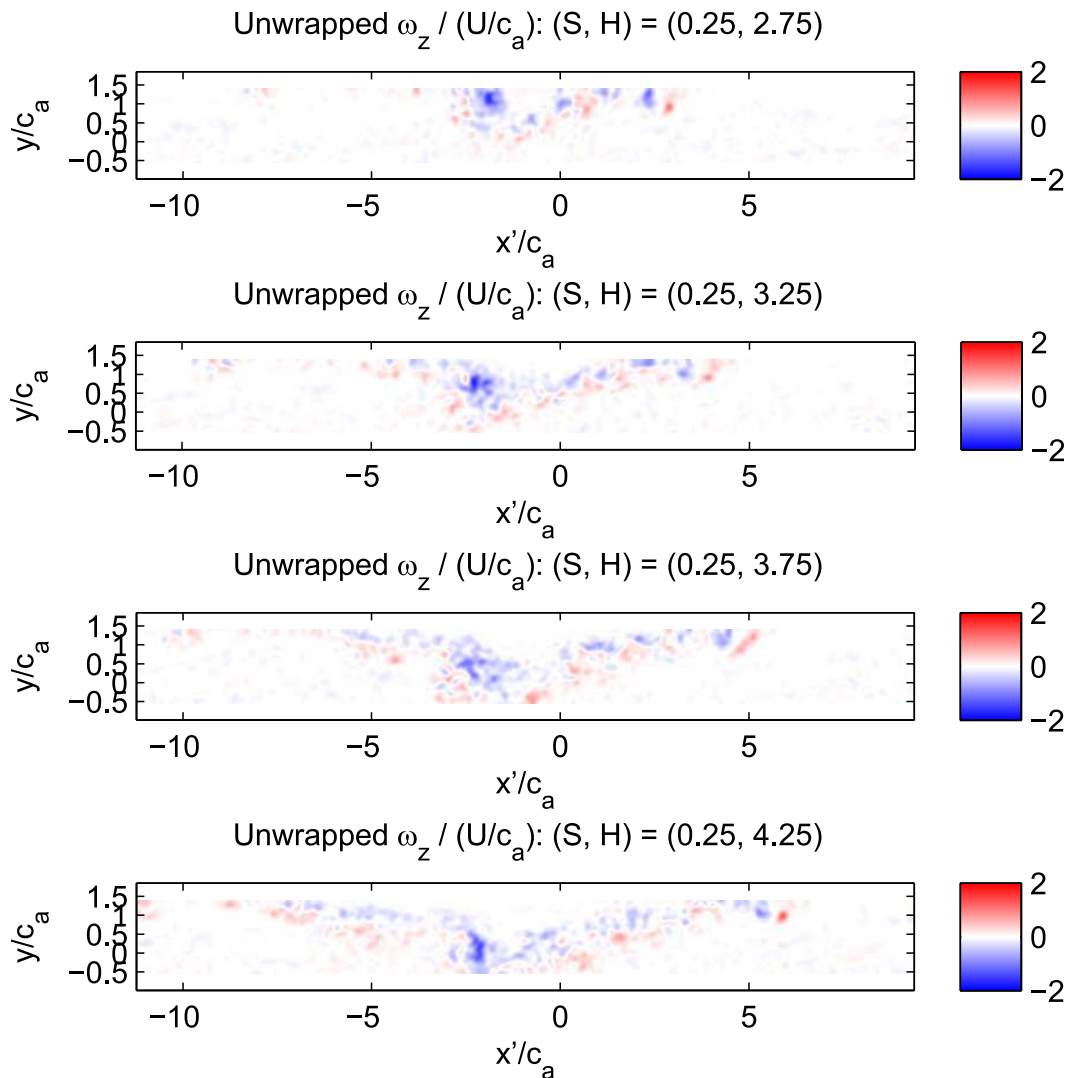


Figure 4.22: Unwrapped vorticity of the gusts downstream of the 5 cm plate heaving at $S = 0.25$.

introduce significant disturbances, it would change the flow around a downstream test article, with potential unwanted effects.

The circulation of the primary vortex was difficult to unambiguously measure, due to the properties of the Γ_2 criterion. As the size of the integration region increased, the measured circulations were closer to the theoretical values. Immediately behind the heaving plate, the strength of the shed vortices matched the theoretical estimates only for the slower heaving speeds. This trend continued through each experiment, where the faster S generally led to an over-prediction of the circulation.

The tangential velocity profiles of the shed vortices did not collapse into a simple

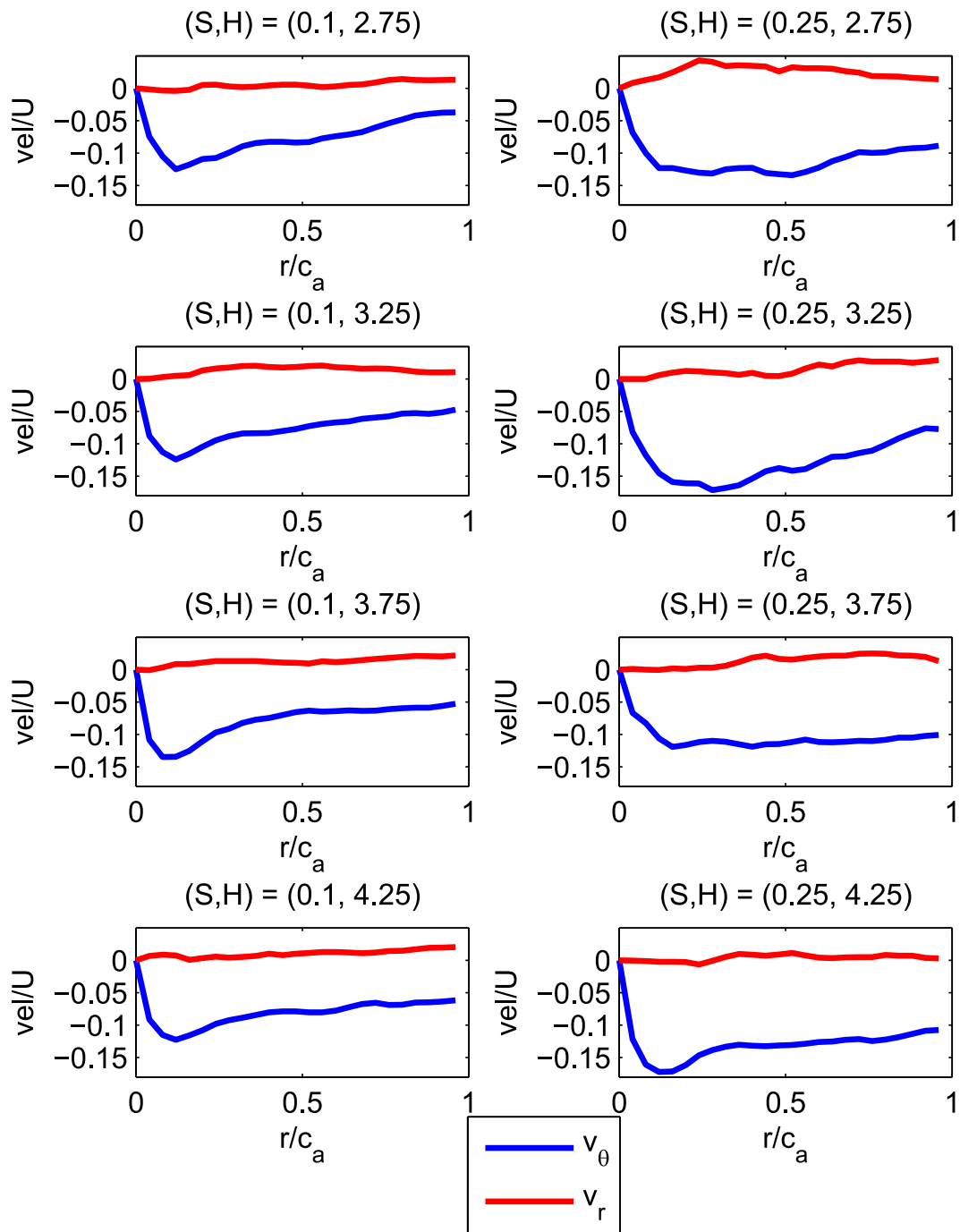


Figure 4.23: Velocity profiles of vortices downstream of the 5 cm plate. Each row of frames is a different heaving distance, and each column is a different speed. These values are in the titles.

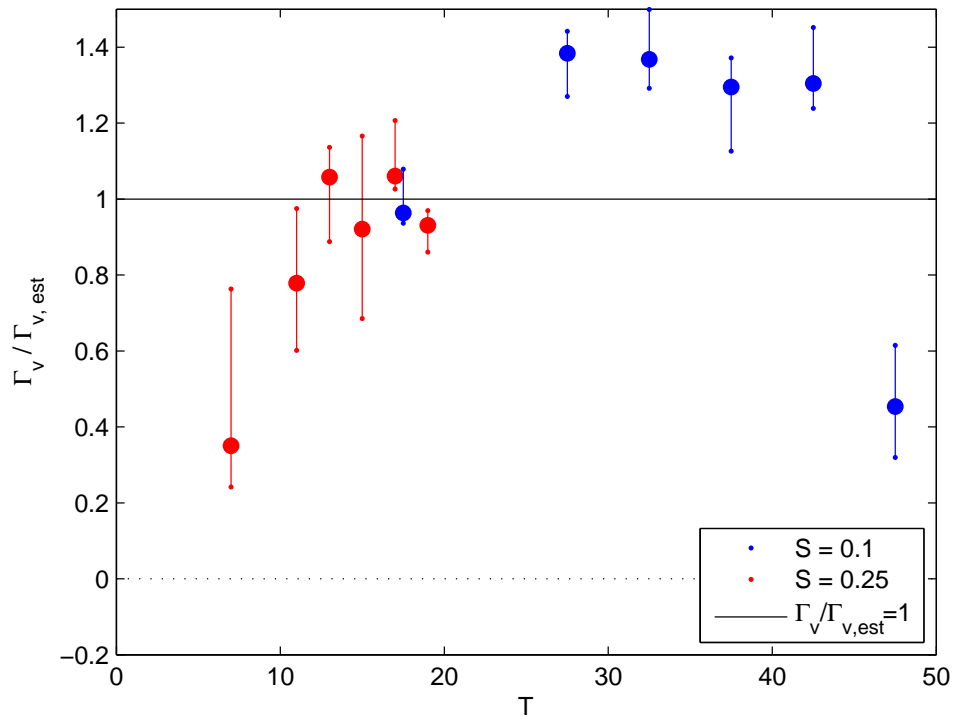


Figure 4.24: Circulation of the primary vortices shed when the plate changed directions, measured 75 cm downstream of the heaving 5 cm plate. The large symbols are the median value of the circulation, and the whiskers are the 25th and 75th percentiles.

curve when non-dimensionalized by the chord length and/or heaving speed. In general, they showed a velocity peak near the airfoil, which leveled off as distance increased.

The flow around the moving plates can be analyzed through the lens of the plate's effective angle of attack, $\alpha_{eff} = \arctan(S)$. For a flow that is insensitive to small changes in the Reynolds number, the flow around a plate that is moving at speed US transversely to a freestream of speed U should be identical to the flow around a plate at a freestream speed of $U_{eff} = U\sqrt{1+S^2}$ with angle of attack α_{eff} . For the experiments where $\alpha_{eff} \approx 5^\circ$ ($S \approx 0.09$), the flow remained attached to the plate throughout its motion, as would be expected with a static flat plate at that angle of attack. The separated flow behind the faster plates analogously supports this approach.

After S , the most influential parameter was T , the dimensionless heaving time.

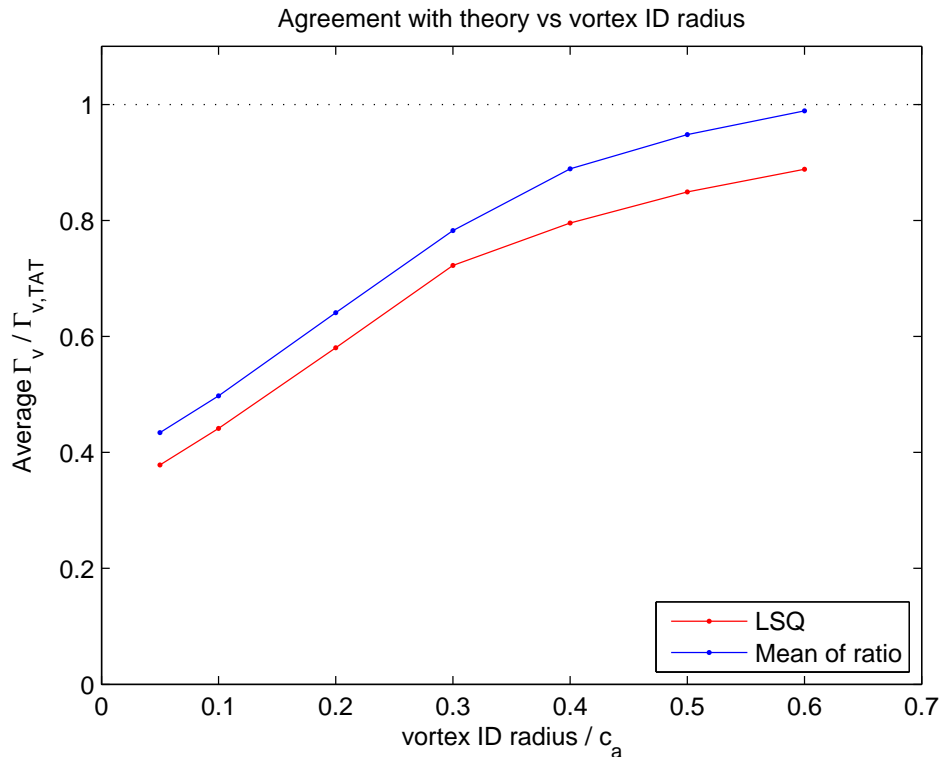


Figure 4.25: Scale factor for fitting the circulation of the primary vortices to the unsteady thin airfoil theory result, measured 75 cm downstream of the 5 cm plate.

When T was large, as was seen in experiments with low S , the flow around the plate had enough time to develop fully, and approach its final behavior. When T was too small, the flow did not have enough time to develop, resulting in too much interaction between the vortices due to starting, changing direction, and stopping. This starting vortex appears in Figure 4.22, on the upper right edge of the field of view. Since the heaving distance is $H = ST$, as the heaving distance increased, the primary vortex was farther from its starting vortex. The slower plate, in Figure 4.21, likely left its starting vortex far behind. The starting effects may also be seen in Figures 4.10 and 4.11, as the large vortical structures with the fastest moving plates. The longer plate at high speed also resulted in significant flow variation along the z direction. This may have been a starting effect, or a result of the flow not having long enough to develop.

The parameter space for the gust generator can be envisioned as a function of S and T , as in Figure 4.27. The symbols in this figure represent the experiments presented earlier in this chapter. The lower bounds of the useful parameters are based on flow

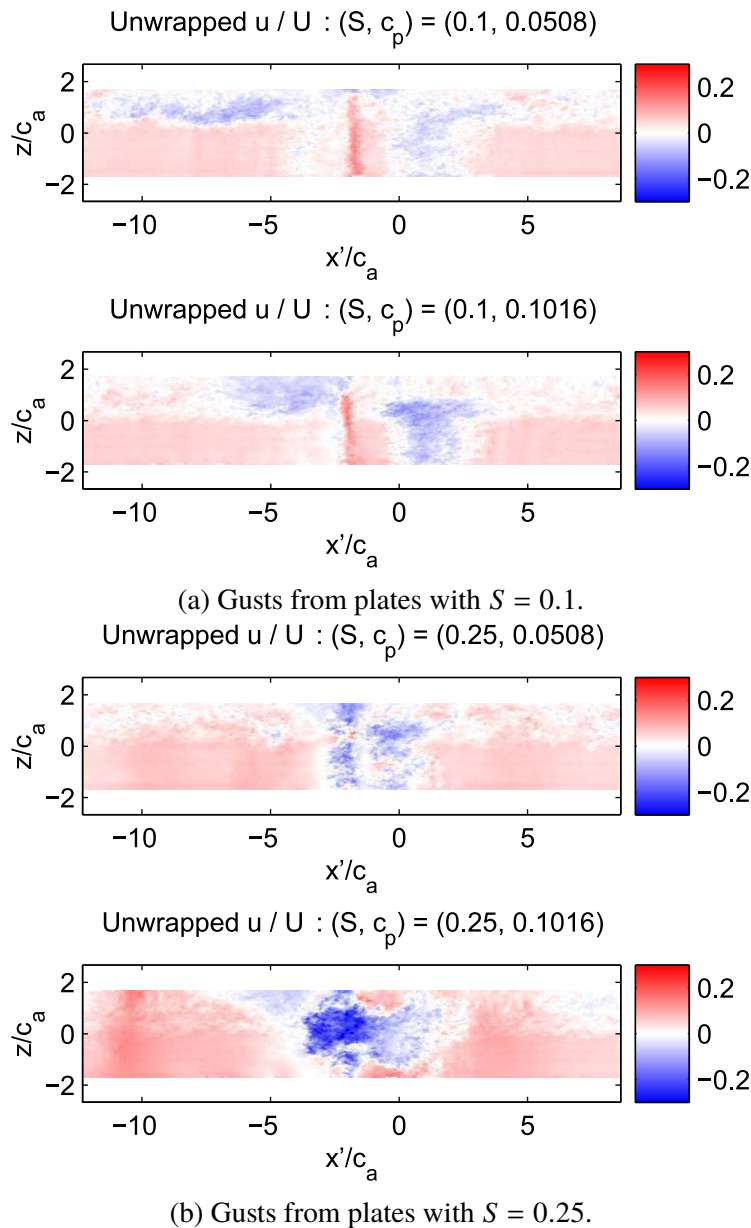


Figure 4.26: Unwrapped u -velocity downstream of the heaving plate, in the x - z plane. In each pair of figures, the top frame used the 5 cm plate, and bottom frame used the 10 cm plate.

physics, and the upper bounds by the experimental apparatus. If S is too small, the shed vortex will be overwhelmed by the von Kármán vortices that regularly shed from the plate. The maximum S is limited by the maximum acceleration achievable by the actuation system. Very high T is limited by the width of the tunnel, as well as the amount of time and storage space that can be dedicated to each experiment. According to the experiments in this section, as well as the earlier theoretical work,

the most useful vortices are created with high T . Unfortunately, that useful region where both T and S are large is unreachable due to the finite width of the test section. The two curved lines in the figure show the maximum bounds on T due to that physical limitation: the upper and lower curves refer to the use of the short and long plates in this tunnel, respectively. The shorter plate allows for higher T , but at the cost of weaker vortices.

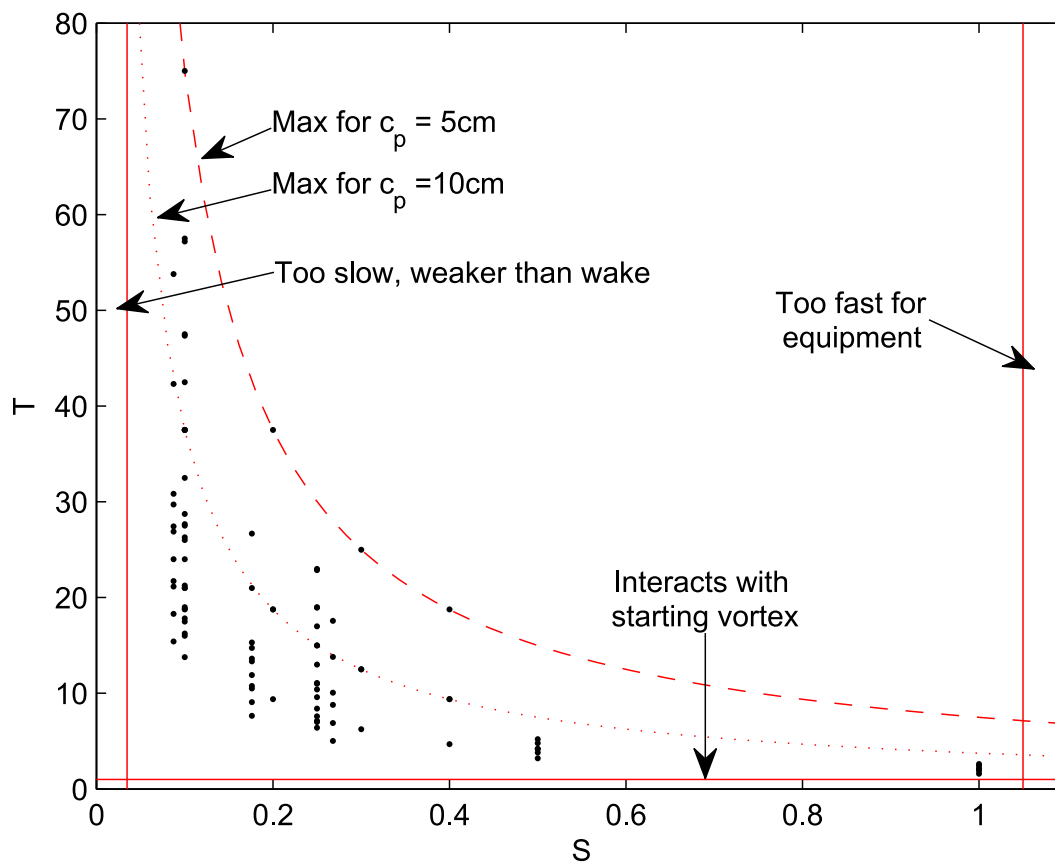


Figure 4.27: Parameter space of gust generator. The dots represent the conditions of performed experiments. The dashed (dotted) red line is the maximum achievable T with the 5.1 cm (10.2 cm) plate. The solid red lines are bounds on the speed and heaving time.

The flow around the heaving plate, after its change in direction, can be considered to pass through a range of behaviors on its way to emulating the flow around a static plate at α_{eff} . The stages of these behaviors are sketched in Figure 4.28. Time is on the vertical axis, so the different stages of flow evolution can be read by moving upward from a chosen α_{eff} . For example, a plate moving with $\alpha_{eff} = 20^\circ$ would have three main stages: the flow developing for a time around the plate until the leading edge vortex separates, the flow around the plate adjusts until it is

Plot label	Estimated $\Gamma_v \times 10^{-3}$ [1/s]	Equivalent α_2	Equivalent S
$S= 0.1$	1.6	-2.9°	0.1
$\alpha_2= -5.0^\circ$	2.7	-5.0°	0.17
$S= 0.25$	4.0	-7.3°	0.25
$\alpha_2= -10^\circ$	5.5	-10°	0.34
$\alpha_2= -13^\circ$	7.1	-13°	0.44

Table 4.1: Circulation of the vortices compared in Figure 4.29. The pitching airfoil has $c_a = 10$ cm, and the heaving plate has $c_p = 5$ cm.

shedding vortices regularly, and that shedding continues indefinitely as if the plate was statically held at α_{eff} . The kink at $\alpha_{eff}=10^\circ$ is related to the static stall for a plate near that angle, as shown in Figure 4.28b. The separated flow associated with stall means that the flow's response to perturbations is slower, and so it takes longer to reach its final state. The dashed lines show different timescales of the flow. The lower dashed line represents one convective time unit. This is effectively the minimum time for a disturbance in the boundary layer to pass the length of the plate. The next dashed line denotes the time needed for the plate, at that static angle, to complete one cycle of vortex shedding.

In sum, the heaving plate system can create useful vortical gusts under certain conditions. The fact that the plate does not perturb the freestream when not in use increases its utility.

4.5 Comparison of Gust Generation Methods

Figure 4.29 shows metrics of the different unwrapped gusts, measured 75 cm downstream of the generators. These have been averaged in the y -direction, yielding comparisons of the dimensionless streamwise velocity, transverse velocity, vorticity, kinetic energy, and enstrophy. The unwrapped pitching airfoil gusts used in this analysis can be seen in Figure 4.3. The relevant heaving plate gusts, generated with the 5 cm plate, can be seen in Figures 4.21 and 4.22. As baselines, the same quantities have been plotted for the static airfoils in the same position, as well as the unperturbed freestream. Since the circulations of the produced gusts were not identical, the circulations of these gusts, and their estimated equivalent S and α_2 values are shown in Table 4.1. These values were estimated using the theoretical values of the circulation of the shed vortex. For example, the circulation of the vortex created by the airfoil pitching to -5° is halfway between those of the heaving plate at $S=0.1$ and $S=0.25$.

The v velocity profile shows the expected increase then decrease in speed associated with a vortex. Comparison with the vorticity profile shows that there is indeed a vortical region there. The kinetic energy and enstrophy plots show the expected peaks at the vortex.

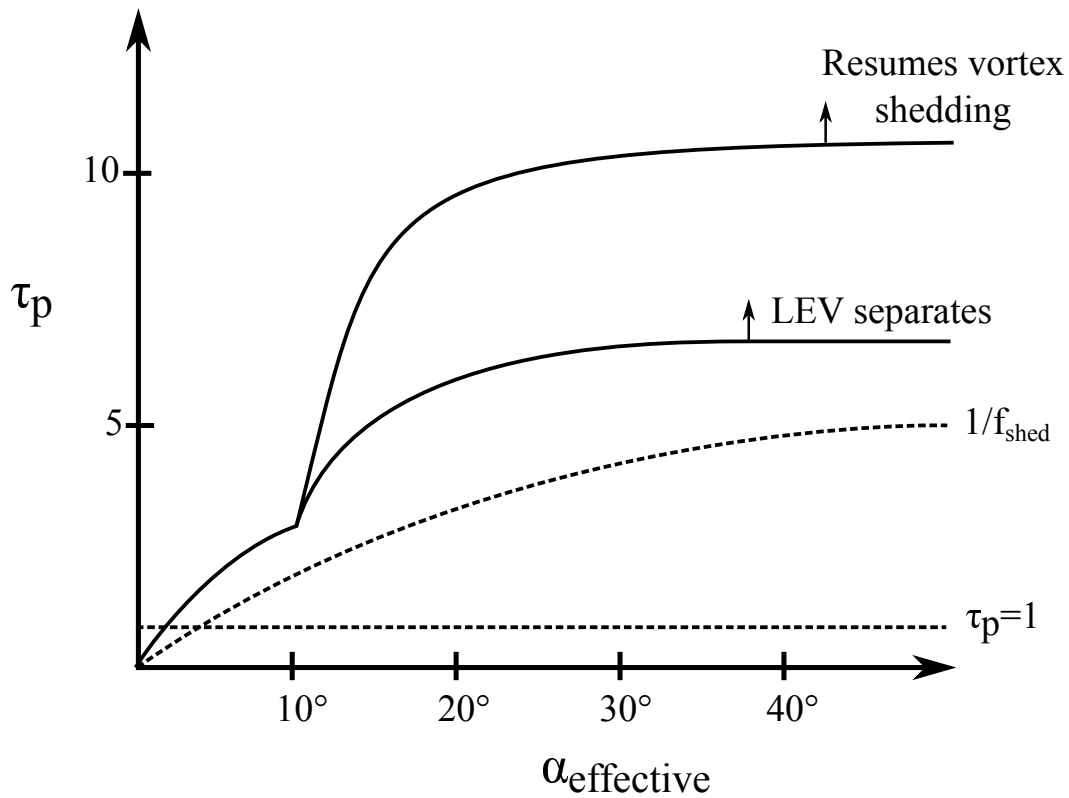
The vortex shed by the airfoil pitching to -5° is barely distinguishable from the background unsteadiness of the flow. Perhaps with a shorter airfoil, its wake would be weaker and the vortex would stand out more. The other vortices shed by the pitching airfoil are very spatially compact, compared to those of the heaving plate. This is particularly true for the $S = 0.25$ vortex, which is quite broad in both enstrophy and kinetic energy. The shown plots have not been scaled with respect to the chord lengths of the two devices. Doing so would double the relative width of the gusts from the heaving plate.

The wakes of the devices can be most readily compared in the kinetic energy plot. At $x'/c_a \lesssim -7$, the wake of the dynamic airfoil at -13° had reached the intensity of the static airfoil at the same angle. In contrast, the wake of the heaving plate left the field of view, and so was no longer disturbing the flow around the tunnel's midline.

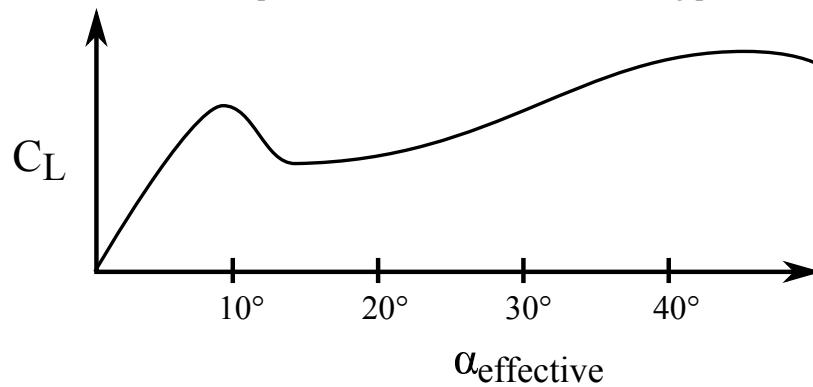
4.6 Summary

Both approaches to gust generation were able to create vortical gusts that convected downstream using only a single degree of actuation. The advantage of the heaving plate is that after it created its gust, it returned to the side of the tunnel, and no longer disturbed the test article. The heaving 5 cm plate has been shown to create a compact vortical gust, in comparison to the larger and less organized gusts from the longer plate. The pitching airfoil, in contrast, was effective in the creation of stronger and more compact vortices. It also required less power to pitch the airfoil, compared to the power needed to rapidly reverse the direction of the moving plate. The pitching airfoil had the downside, however, of remaining in place and continually disturbing the flow.

The two gust generation methods each have their benefits and drawbacks. Their use in the generation of gusts that interact with a test article is examined in the next chapter.



(a) Flow development timescales around the heaving plate.



(b) Approximate lift coefficient of the static plate.

Figure 4.28: The top plot is a sketch of the approximate development stages of the flow around the plate, as a function of the effective angle of attack. The travel time τ_p is the time after the change in direction. The lines delimit different stages of development around the heaving plate, such as losing the LEV and resuming regular vortex shedding. The bottom plot is a sketch of the static lift coefficient of the flat plate.

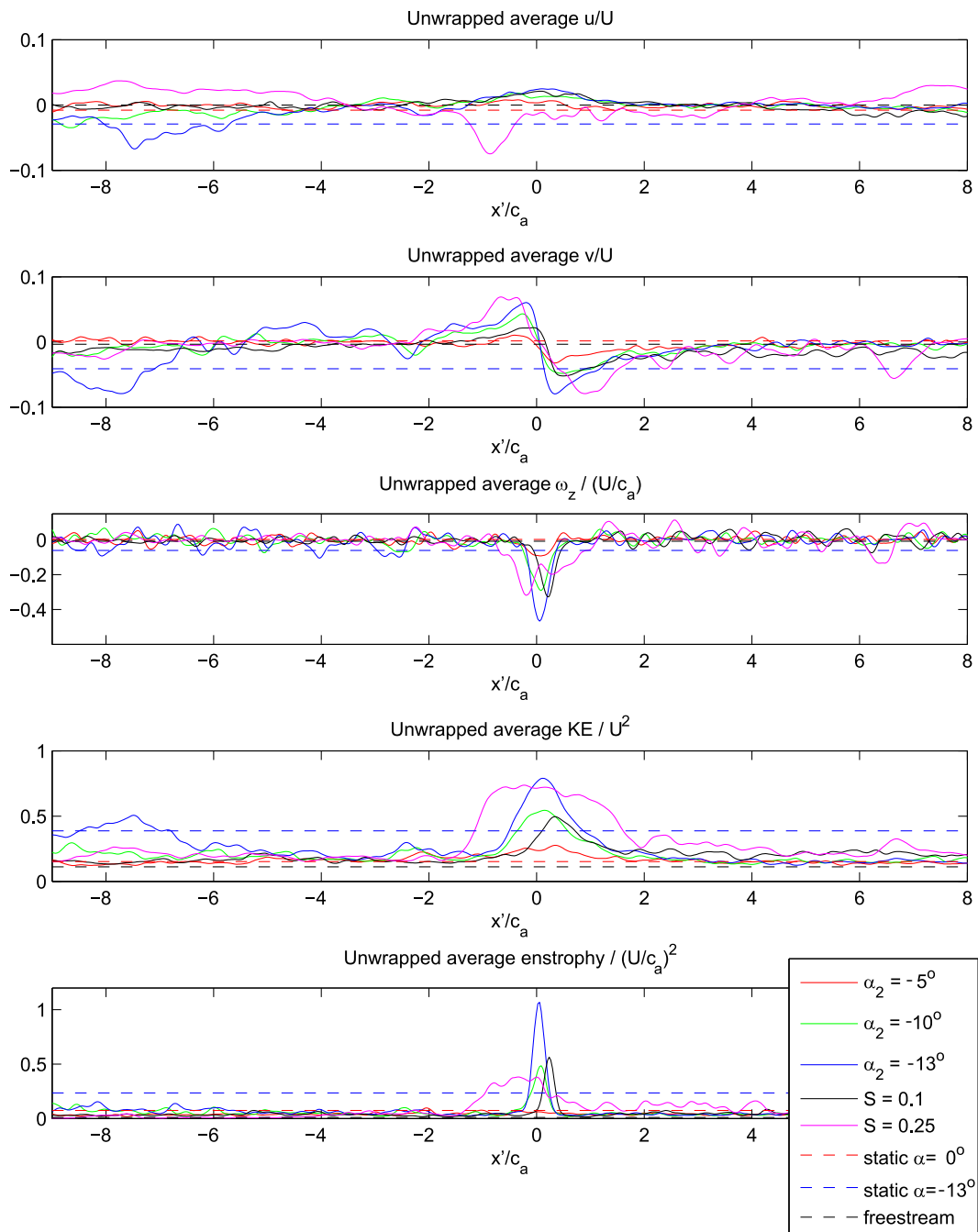


Figure 4.29: Average profiles of the gusts created with the 5-cm heaving plate and 10-cm pitching airfoil mechanisms. These are the y-average of the unwrapped gusts, for the normalized values of horizontal velocity, transverse velocity, vorticity, freestream-removed kinetic energy, and entropy.

*Chapter 5***GUST-WING INTERACTION****5.1 Introduction**

This chapter examines the response of an airfoil to gusts generated by the heaving and pitching devices which were described in the previous chapter. As a baseline for comparison, the forces on the downstream airfoil were measured both with and without the presence of the static gust generators. To examine the effect of the heaving plate's wake as opposed to the desired vortical gust, the effect of the heaving plate passing from one side of the tunnel to the other was also measured. With those baselines complete, a series of simultaneous PIV and force measurements were undertaken to examine the flow around, and forces on, the downstream airfoil in response to gusts from both devices. Additionally, the predictive abilities of the numerical and analytical models of the gust interaction will be examined. The chapter concludes with a comparison between the two gust-generating methods, and their effects on the test article.

5.2 Experimental Apparatus

Experiments were performed using either the ball screw apparatus or the gantry system to provide movement for the gust-generating plates or airfoil. The downstream airfoil was a NACA 0018 airfoil, mounted 75 cm downstream of the mounting point of the upstream device, in the center of the tunnel. This airfoil was tested at three angles of attack: 0° , 5° , 10° . The details of these devices are in Chapter 3.

The forces reported in this chapter have been low-pass filtered at 10 Hz to remove the effects of the tunnel's pump (operating at 12.5 Hz), and averaged over the different repetitions for each set of parameters. For comparison, the bluff-body shedding frequency corresponding to a body as thick as this airfoil at $\alpha = 0$ is roughly 2 Hz, much lower than the filter frequency. To properly compare results across each repetition of the experiments, the force oscillations due to vortex shedding were removed using a low-pass filter at 1.12 Hz. The magnitude of the force oscillations, at frequencies between 1.12 Hz and 10 Hz, is referred to as the 'force envelope.' These envelopes were calculated as the absolute value of the MATLAB-computed Hilbert transform of the oscillations in each of the different repetitions, averaged together. The results are relatively insensitive to changes in the low frequency filter

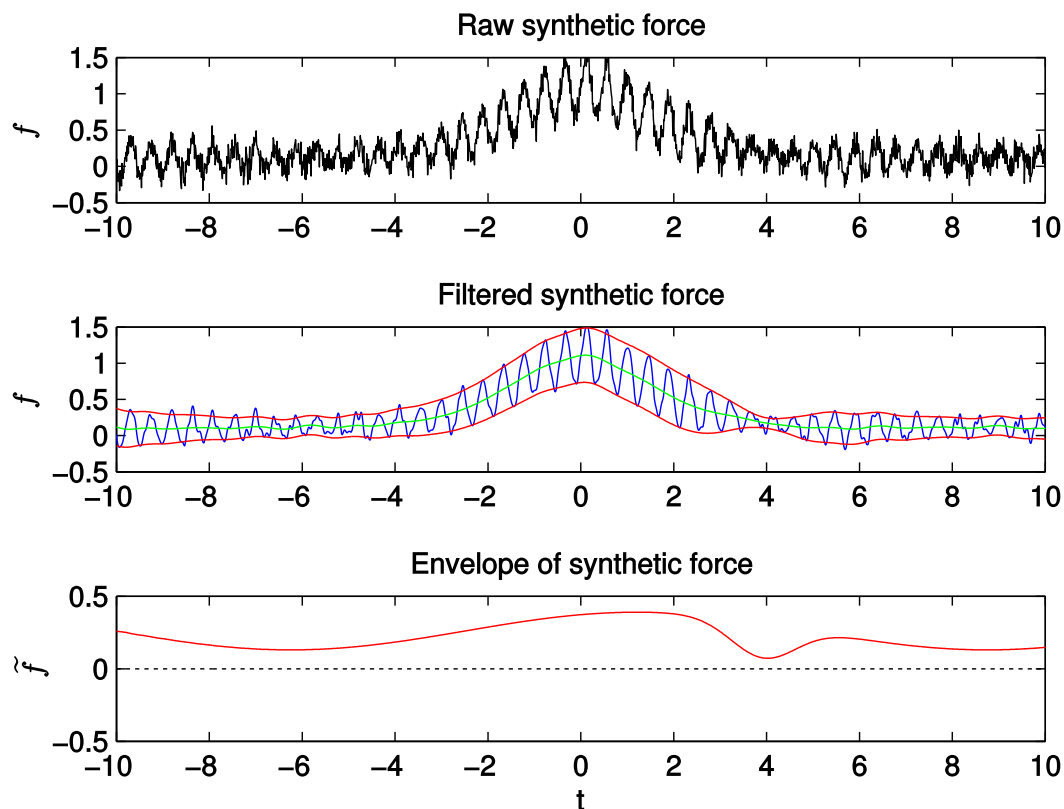


Figure 5.1: Demonstration of force filtering using synthetic data. The top plot is the ‘raw’ synthetic force data over time. The middle plot shows the noise-removed data in blue, the underlying low-frequency forces in green, and the envelope of the forces in red. The bottom plot shows the magnitude of the envelope over time. Note the different scale on this final plot.

in the range of 0.95 to 1.7 Hz, and to the high frequency filter in the range of 8 to 10.5 Hz. An example of this processing, applied to synthetic data, is shown in Figure 5.1. There, the ‘raw’ synthetic data is shown in the top plot, including regular oscillations and noise around low-frequency variation. The blue line in the second plot has filtered out the high-frequency noise. In green, only the low-frequency variation remains. The red lines are the bounding envelope around the regular oscillations. This envelope is shown in the bottom plot, with the low-frequency variation removed.

An additional issue with the forces is that the small magnitude of the drag force, D , on the downstream airfoil meant that its direct measurement was inaccurate. Alternatively, the estimated drag force, D_{est} , was computed by dividing the moment due to drag by the distance between the transducer and the mid-span of the wetted

airfoil. A similar process was used for the direct and indirect measurements of the lift: L and L_{est} , respectively. This chapter reports the indirectly measured drag forces. The directly measured results are included in Appendix C.3.

5.3 Baseline Forces

Ideally, a vortical gust generator would create a solitary vortex, with no other disturbance in the flow. As demonstrated in the previous chapter, the tested generation methods yielded gusts with both a vortex and a wake region. In some cases, the devices disturbed the flow even when they were not in motion.

The plates, when at rest near the walls, did not noticeably change the PIV-measured flow around the midline of the test section. It is possible, however, that their presence excited some weak flow behavior that would manifest as a change in the forces on a downstream airfoil. In contrast, the upstream airfoil continually shed its significant wake near the tunnel's midline. When the heaving plate moved across the tunnel without changing directions, it also generated a wake that traveled downstream, temporarily perturbing the flow around the midline. Each of these cases may translate to variation in the forces on a downstream airfoil.

This section aims to ascertain how these side-effects of the generators affect the forces on the test article, and so to better understand their suitability as vortical gust generators.

5.3.1 Static Gust Generators

Before and after the gust generators created their vortices, the generators sat statically, disturbing the flow to some degree. The tested positions of the static gust generators are shown in Figure 5.2. These experiments used the 5 cm plate at either side of the tunnel, or the upstream airfoil at the midline of the test section. These experiments are detailed in sections A.2.2, A.2.3, and A.2.5. For comparison, the unwrapped wakes of the upstream airfoil are shown in Figure 4.2.

The resulting average and standard deviations of the forces on the downstream airfoil, with and without the presence of the static gust generators, are plotted in Figure 5.3. Plots including the inaccurate directly measured drag coefficient can be seen in Figure C.7.

As a baseline, the unperturbed forces show that the lift on the airfoil was nearly symmetric around $\alpha = 0$, as would be expected with a zero-camber airfoil. Stall was seen at 10° , with a corresponding drop in lift and sharp increase in drag. The

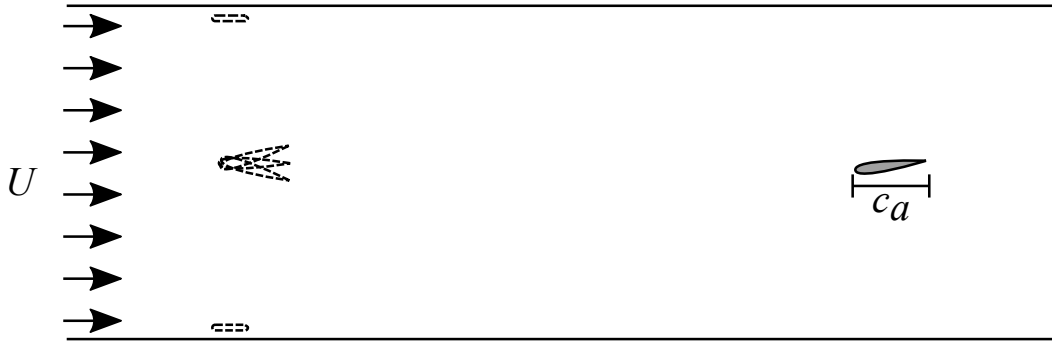


Figure 5.2: Diagram of the baseline force experiments. The dotted outlines refer to the different positions of the static gust generators, which were tested individually.

force oscillations due to vortex shedding are seen as the higher variability around $\alpha = \pm 5^\circ$, particularly with C_L and C_M . These oscillations were significantly reduced after stall.

The average lift and drag forces did not change significantly in the un-stalled region with any of the static devices, but the perturbations caused by the upstream airfoil pushed the stall angle higher. This modification of stall also manifested as a smaller increase in the drag, relative to the unperturbed flow. The presence of the upstream plates did not noticeably change the average forces on the test article.

Further differences are readily seen in the standard deviation of the forces, where the upstream airfoil reduced the unsteadiness of the forces on the downstream airfoil at moderate angles of attack, but increased them post-stall. There was also an effect of angle of attack, as the zero-angle upstream airfoil led to significantly less oscillation than the $\pm 13^\circ$ cases. Again, the plates on the sides of the tunnel did not significantly change the unsteadiness of the forces.

The mean forces are also represented as a drag polar in Figure 5.4. The corners in this plot correspond to the stall condition, where drag increased much more quickly than the lift. This view highlights the fact that the upstream airfoil yielded lower drag in the un-stalled portion, and a smoother transition to the post-stall regime.

5.3.2 Forces due to a passing plate

The heaving gust generator not only created a vortical gust, but a wake as well. To investigate the effect of this wake, the 5 cm plate was moved across the width of the tunnel at two constant speeds, $S = 0.1$ and $S = 0.25$, as detailed in Appendix A.4.7. The forces on the airfoil at three angles of attack are shown in Figure 5.5.

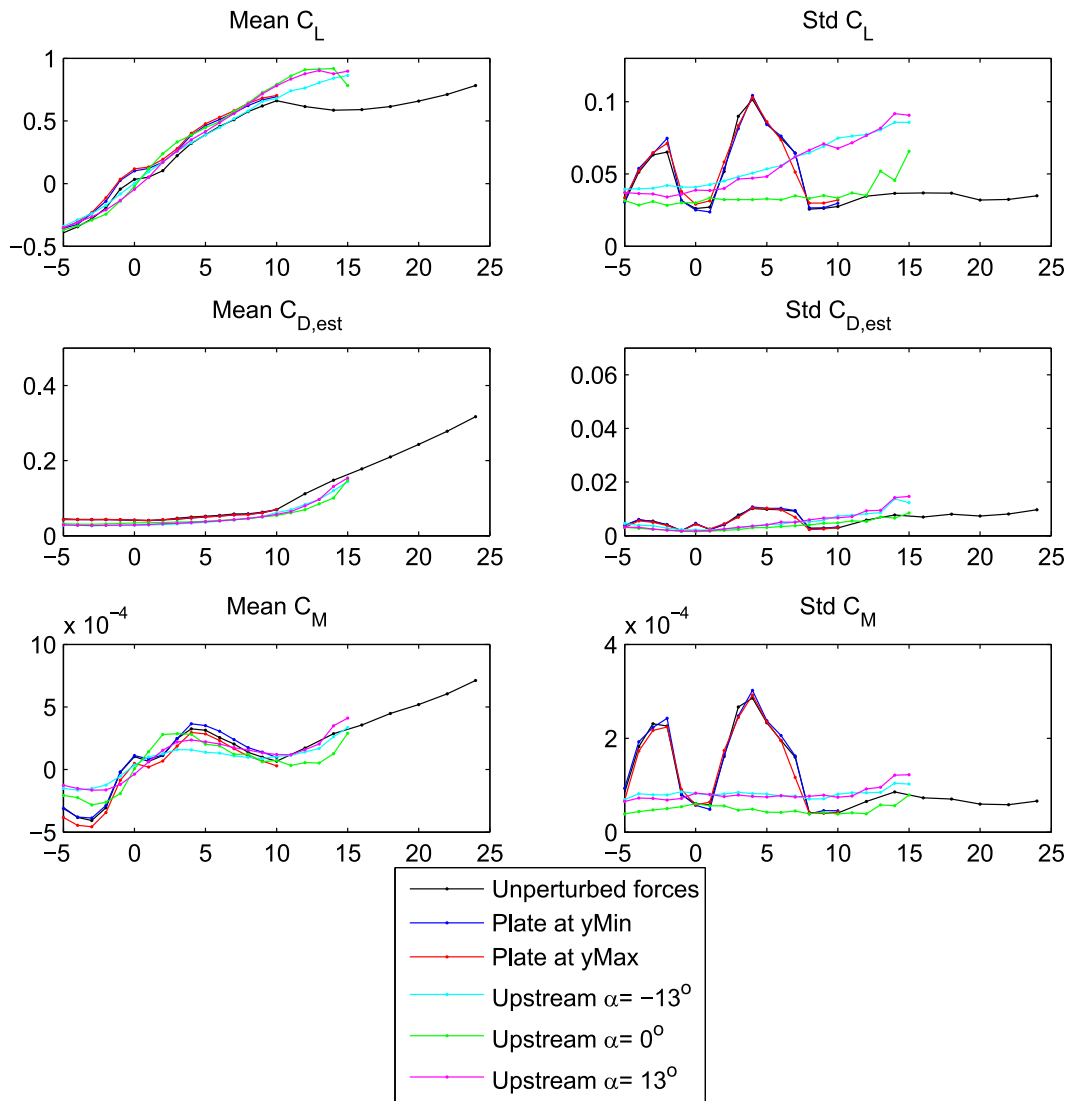


Figure 5.3: Average and standard deviations of forces on the airfoil: with an unperturbed freestream, or with the presence of the gust-generating plate or airfoil.

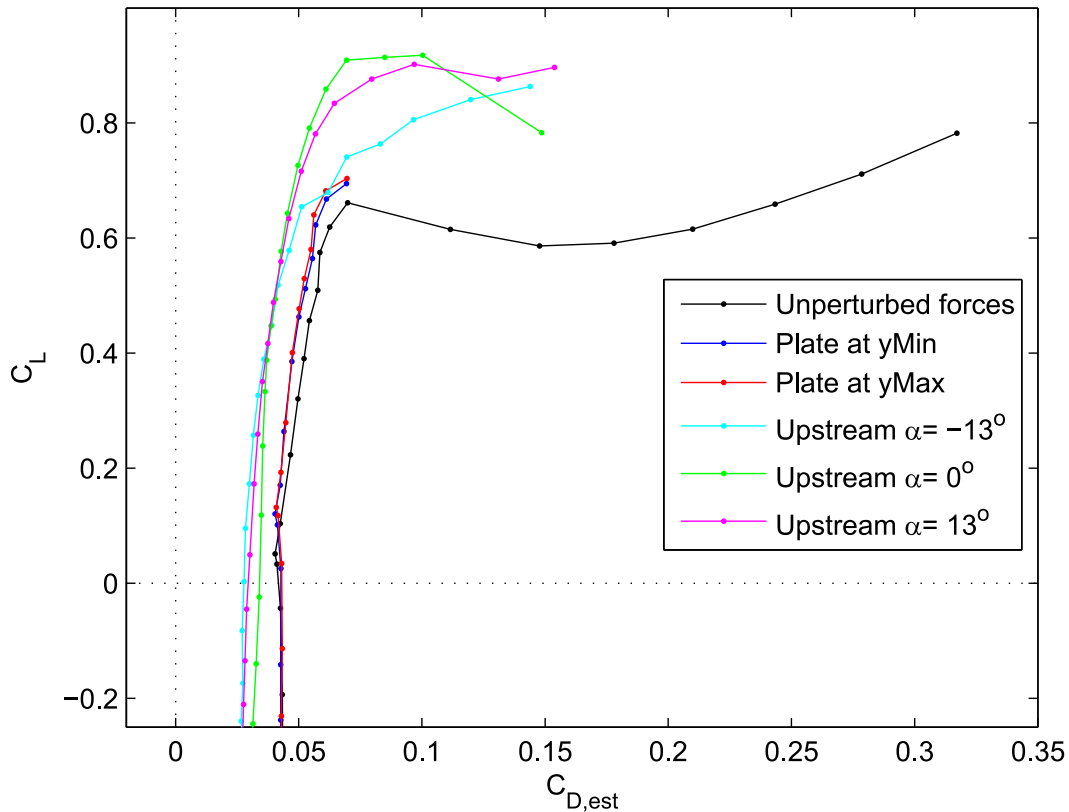


Figure 5.4: Drag polar of the average forces on the airfoil: with an unperturbed freestream, or with the presence of the gust-generating plate or airfoil.

These show the effects of the plate moving in the positive (+y) and negative (-y) directions. For comparison, Figure 4.10 shows the unwrapped wakes of the plate moving in the negative direction.

Across the parameter space, the drag had the most consistent response to the incoming wakes. It dropped relatively quickly, and returned to its average values over $5-10t_c$. The drag decreased more at the higher angles of attack. The plate moving at $S = 0.1$ resulted in a longer duration of the decrease and a smaller drop in drag, as compared to the $S = 0.25$ plate. The reduction in the low-pass filtered drag was substantial at both speeds, equivalent to a change of several degrees of α .

The response of the lift was not as simple. The change in the low-pass filtered lift was less substantial than the drop in drag, equivalent to a change of roughly two degrees of angle of attack with the faster plate.

The envelopes of the forces, a measure of their variation over time, are shown in Figure 5.6. The large variation in the steady-state forces at $\alpha = 5^\circ$, as compared to

the other angles, is due to von Kármán vortex shedding. In this case, the wake of the passing plate caused a drastic reduction in the force oscillations, which slowly returned to their steady-state values over roughly $10 t_c$. This behavior was not seen at $\alpha = 0^\circ$ or 10° .

5.3.3 Discussion

The upstream airfoil continually created significant perturbations in the flow, even when it was not being used to create vortical gusts. The plate temporarily disturbed the flow behind it, and only affected the test article if the plate went near the midline of the tunnel.

The static plates at the walls negligibly impacted the flow. The presence of a plate reduced the cross sectional area of the tunnel by 1.4% over a distance of about $0.5c_a$, while more than $7c_a$ ahead of the test article. The resulting blockage effect was minimal. The plate's wake likely merged into the boundary layers on the sides of the test section. These small effects did not modify the forces on the downstream airfoil at the midline of the tunnel.

The wake of the upstream airfoils had significant impacts on the test article. These perturbations disturbed the boundary layers on the downstream airfoil, potentially reducing the extent of separated flow. The lack of a developed region of separated flow could disrupt the regular shedding of vortices from the airfoil, and explain the reduction in unsteadiness of the forces around $\alpha = 5^\circ$ in Figure 5.3. This may also be the cause of lower drag on the airfoil. Around the unperturbed stall angle of $\alpha = 10^\circ$, the perturbations kept the flow attached to the airfoil, resulting in a higher stall angle.

Effectively, the presence of the upstream airfoil yielded a more unsteady freestream. The pitching airfoil, as tested, is thus inappropriate for experiments that require a very steady freestream. Perhaps if the airfoil were further from the midline, its wake would not interact with the test article as significantly. Unfortunately, this means that close interactions with its vortical gusts are impossible without compromising on the steadiness of the flow.

When the heaving plate moved across the tunnel, it disturbed the flow for a limited time, whereas the upstream airfoil continually perturbed the flow. The reduction in drag from the passing plate may have been due, in part, to the slower flow in the wake of the plate. The greater reduction in drag at higher angles of attack suggests that the oncoming wake caused the airfoil's separated region to be shed.

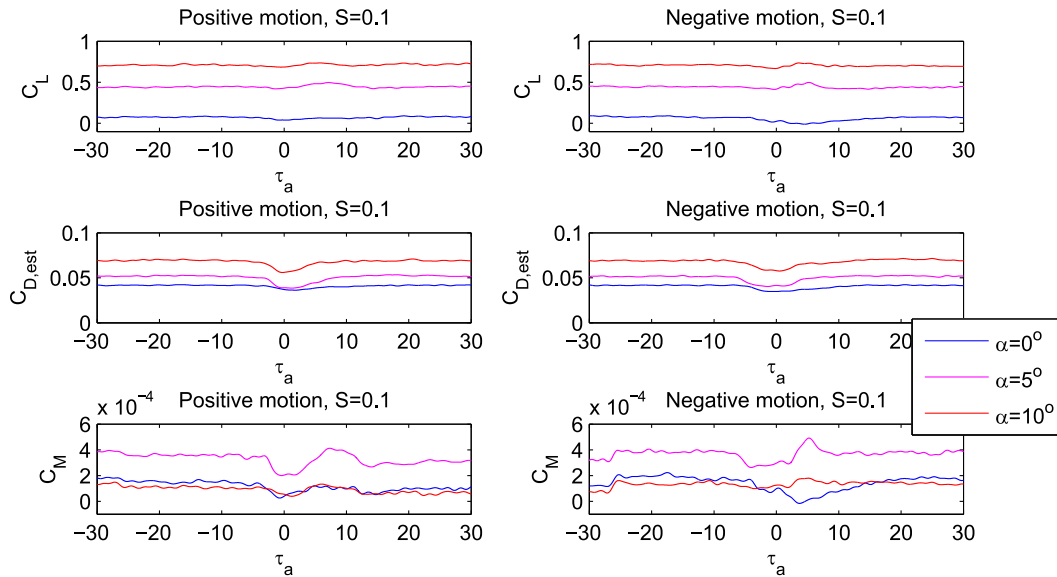
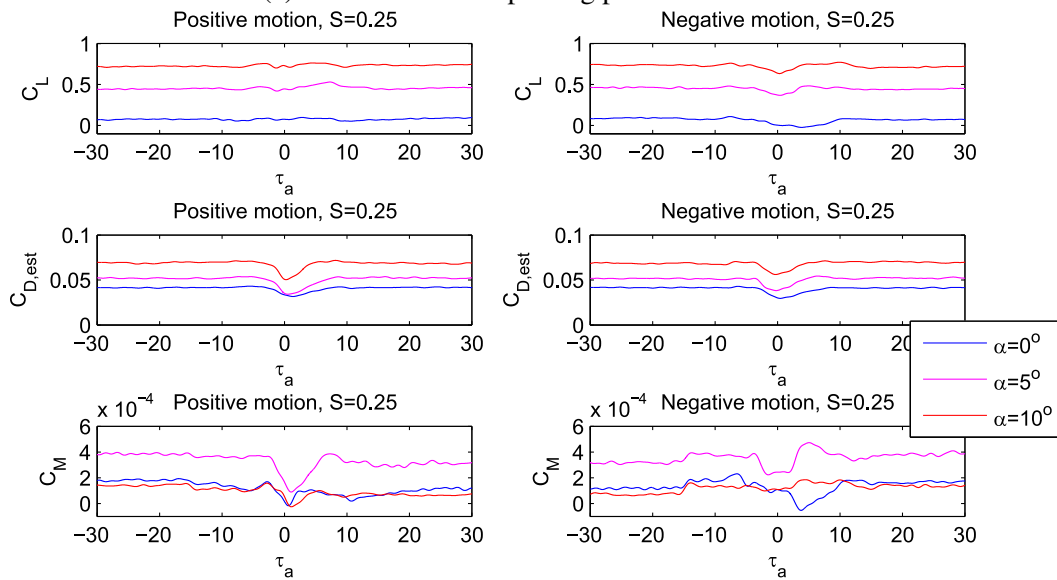
(a) Forces due to the passing plate with $S = 0.1$ (b) Forces due to the passing plate with $S = 0.25$

Figure 5.5: Forces due to the heaving plate moving from one side of the tunnel to the other at $S = 0.1$ and $S = 0.25$. ‘Positive motion’ means that the plate moved in the $+y$ direction. The downstream airfoil was at either 0° , 5° , or 10° . Time is shifted to have the estimated wake arrival time at $t = 0$, and scaled by the airfoil’s convective time unit.

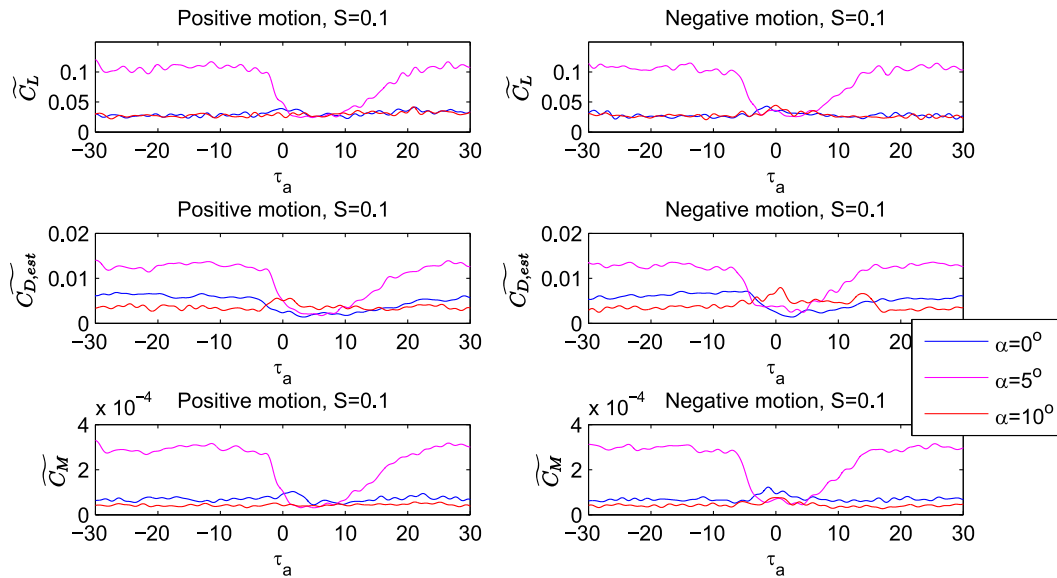
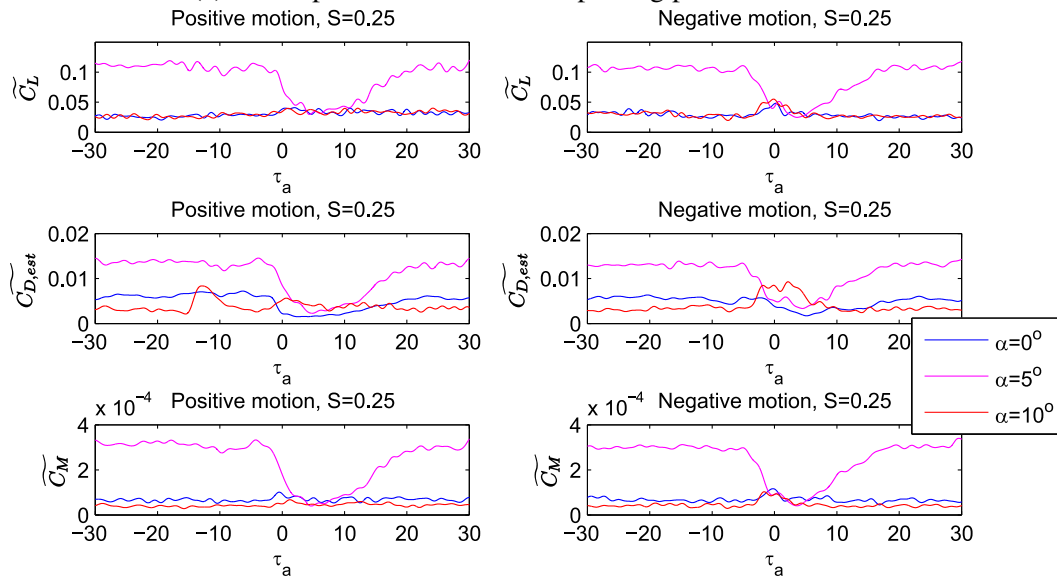
(a) Envelope of forces due to the passing plate with $S = 0.1$ (b) Envelope of forces due to the passing plate with $S = 0.25$

Figure 5.6: Envelope of forces due to the heaving plate moving from one side of the tunnel to the other at $S = 0.1$ and $S = 0.25$. Time is shifted to have the estimated wake arrival time at $t = 0$, and scaled by the airfoil's convective time unit.

The different durations of the decreases in drag with the different values of S may be simply explained by the fact that the faster plate disturbed the flow for less time. As before, if a steady freestream is required, this prohibits the use of the heaving plate in situations where it would pass in front of the test article.

Compared to the wake of the pitching airfoil, the effect of the heaving plate's wake appears less significant. This is primarily due to its transience. However, if significant unsteadiness in the freestream is acceptable, either method would be appropriate.

5.4 Interaction with Pitching Airfoil Gusts

The experiments in this section measured the response of the downstream airfoil to the effects of the pitching gust generator, using PIV and force measurements. The y -position of the upstream airfoil, its direction of pitching, and the angle of the downstream airfoil were varied as described in Appendix A.3.2. In each case, the upstream airfoil pitched from 0° to $\pm 13^\circ$. A schematic of the apparatus used in this set of experiments can be seen in Figure 3.6.

5.4.1 Experimental Results

An example of the results of one set of experiments is Figure 5.7. At the top are four snapshots of the vorticity field, where the primary vortex and wake from the gust generator are passing the airfoil. The Γ_2 criterion has been used to outline vortical regions in black. The second row is a plot of the experimental lift coefficients over time, with the temporal position of the vorticity snapshots denoted by circles. The red lines show the low-pass-filtered C_L from each repetition of the experiment. The black line is the average of those forces. The dashed blue lines show the average C_L envelope around the average C_L . The third plot shows the average C_L with the estimates from the different numerical models: quasi-steady thin airfoil theory (QS-TAT), Wagner thin airfoil theory (W-TAT), unsteady panel method (UPM), and the extended Tchieu-Leonard model (E-TL). Since the experimental lift curve of the airfoil was not predicted exactly by the numerical models, their lift curves were shifted slightly in C_L to match the experimentally measured steady value before the gust interaction. This was done to highlight the variation over time in response to the gust, rather than the constant difference in C_L . The final plot shows the upstream airfoil's angle of attack, as well as this angle translated in time by the travel time of the gust, indicating the expected arrival time of the vortex.

In the vorticity snapshots on Figure 5.7, the primary vortex is visible as the outlined

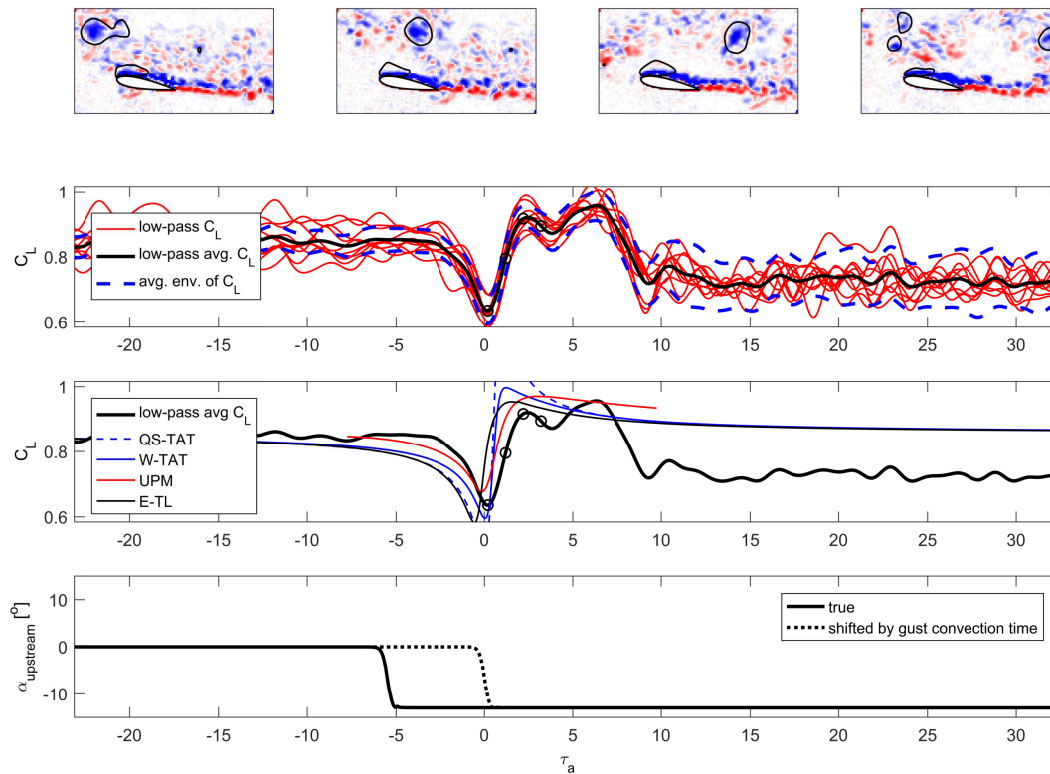


Figure 5.7: Gust from pitching airfoil interacting with the downstream airfoil: $y_{upstream} = 0.5c_a$, $\alpha_2 = -13^\circ$, $\alpha = 10^\circ$. The temporal position of the vorticity snapshots at the top are denoted by circles in the middle two plots. The second plot shows the low-pass filtered C_L across the different repetitions, the average of those, and the average C_L envelope. The third plot shows that average, as well as the estimates from numerical models. The bottom plot shows the angle of the upstream airfoil, as well as that angle shifted in time to compensate for the travel time of the gust.

strongly negative region about one chord-length above the airfoil. Across the four images, it traveled from just ahead of the airfoil to the downstream edge of the field of view. Also visible are complex, small-scale vortical structures around the vortex. These are associated with the wake of the upstream airfoil. Since this vortex had negative circulation, it deflected the wake near it correspondingly: the downstream portion moved downward, and the upstream portion moved upward. As shown in Figure 4.2, the wake of the upstream airfoil after pitching was thicker, slower, more unsteady, and shifted in y . Additionally, $5-10 t_c$ after the vortex reached the airfoil, an additional region of strong vorticity passed the airfoil. This was shed by the upstream airfoil after it released the primary vortex. Analogous phenomena were seen when the airfoil pitched to $+13^\circ$.

The y -position of the upstream airfoil had a significant impact on the flow around the test article. When the gust generator was closer to the y -axis than approximately $0.5c_a$, its wake significantly reduced the flow separation on the test article at $\alpha = 10^\circ$. The vortical gust in these cases also momentarily changed the vortex shedding on the plate. A vortex with positive circulation passing closely below the airfoil was significantly distorted, due to the matching sign of the lower boundary layer's vorticity. If this same vortex passed above the airfoil, it remained more coherent, and pulled some of the wake vorticity away as it continued on. Symmetrically, a negative vortex was distorted when it closely interacted with the upper surface, and so on. Since the suction surface of the test article at non-zero α was the upper surface, a negative vortex passing above slowed the flow even more, and sometimes caused additional flow separation.

The multiple force traces in Figure 5.7 are fairly representative of the greater set of experiments in one respect: the response to the vortical gust was very repeatable for each set of parameters. A comparison of the lift forces for each set of parameters is shown in Figure 5.8. In the appendix, Figures C.8 - C.10 display the moment and drag coefficients as well. The envelopes of these forces are in Figures C.11 - C.13. Since the wake of the upstream airfoil was different after pitching, the final forces on the test article sometimes differed significantly from the initial forces. This post-pitching change in the forces was most substantial for the airfoil at $\alpha=10^\circ$.

The variations in the low-pass filtered forces appear to coincide with three main factors: the incoming vortex, the strong perturbations that arrive 5-10 t_c after the vortex, and the change in the oncoming wake before and after the vortex. The transient effects from these factors are visible in the forces for around 10 t_c for $\alpha=0^\circ$, 10-20 t_c for $\alpha=5^\circ$, and 20-30 t_c for $\alpha=10^\circ$.

With regards to the vortex-associated forces, the low-pass filtered C_L curves broadly followed similar trends in each experiment. In response to a vortex with negative circulation, the lift initially dropped as the vortex approached the leading edge, then rebounded above the steady-state value as the vortex passed over the airfoil, and slowly approached its steady state value as the vortex traveled farther downstream. The opposite occurred in response to a vortex with positive circulation.

The change in the freestream caused by the upstream airfoil at its final angle of attack did not significantly change the forces in all the experiments, but such changes did occur. For example, the final lift and drag coefficients were substantially different from their initial values in the pair of tests with $\alpha=10^\circ$ and the upstream airfoil

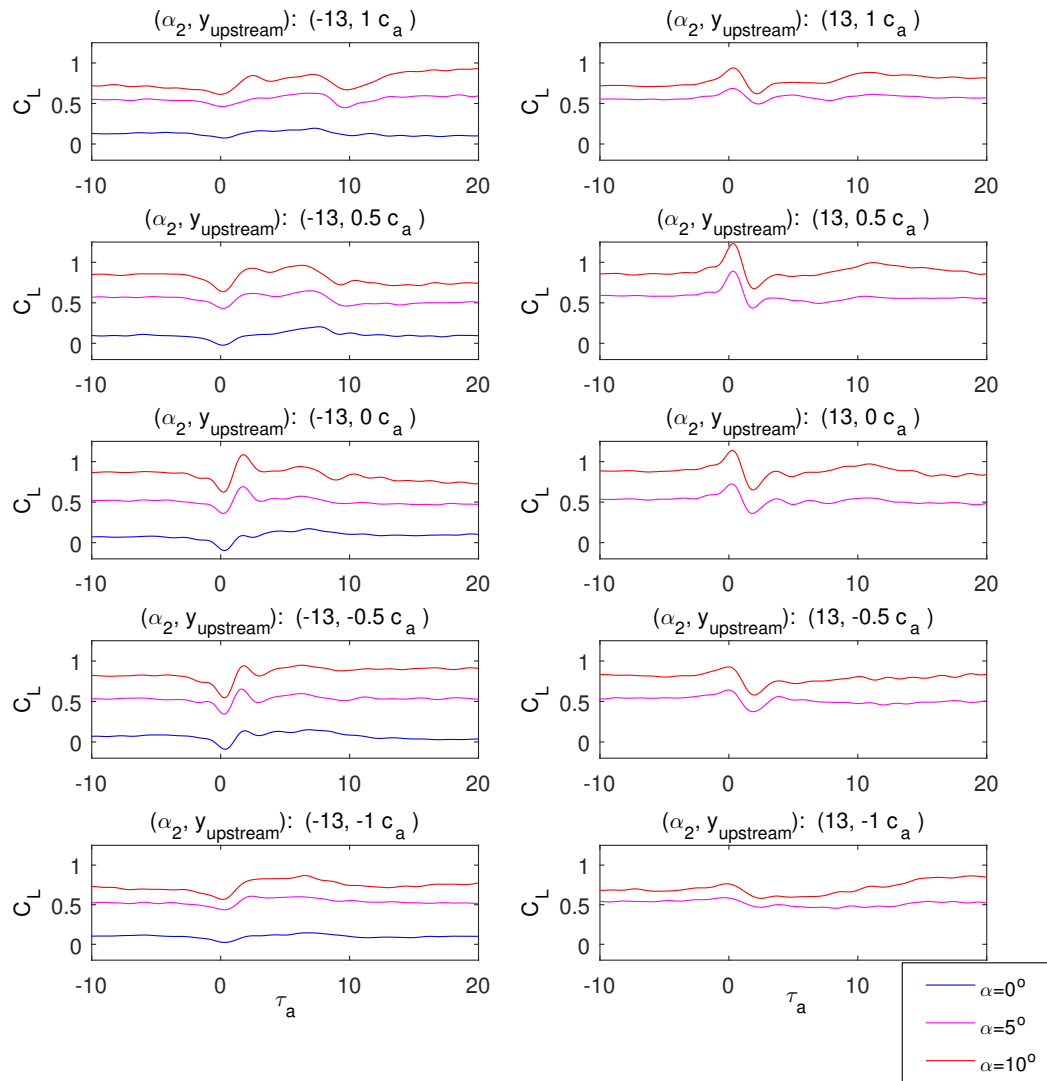


Figure 5.8: Low-pass filtered lift coefficients of the downstream airfoil in response to gusts from the pitching airfoil. Each panel contains force traces from a single release position and initial direction, but different airfoil angles of attack.

at $y_{upstream} = \pm 1c_a$, when its trailing edge pointed away from the midline. Some of the deviations occurred due to the wake impinging on only one side of the test article after pitching, rather than affecting both sides equally. The envelopes of the forces also displayed post-pitching changes, reflecting the impact of the new incoming wake. Particularly in the cases with $\alpha = 5^\circ$, the magnitude of the force oscillations dropped after the airfoil interacted with the thicker wake. The change in the shedding amplitude was rapid, occurring over approximately 2-5 t_c .

5.4.2 Comparison with Theory

To examine the accuracy of the numerical estimates, Figures 5.9 - 5.11 show the scaled lift coefficients of the airfoil's response to the different gusts, alongside the numerical estimates, for three angles of attack. The forces had their mean values subtracted, and the remainder was scaled by the C_L peak amplitude in Equation 2.16. Here, the vortex's y -distance from the airfoil was estimated as the y -position of the pitching airfoil's quarter-chord point. This scaling function is undefined when the airfoil was at $y_{upstream} = 0$, so those plots were instead scaled by the final angle of attack of the upstream airfoil, α_2 , and only have the UPM estimate. Figures 5.9, 5.10, and 5.11 show the results at α of 0° , 5° , and 10° , respectively.

Each of the numerical methods captured the general behavior of the lift: an initial peak when the vortex arrived, an overshoot of the mean, and a slow approach to a final value. None of the numerical results captured the detailed behavior after the overshoot. These models were also unable to capture the changes in the lift due to the upstream airfoil's final angle of attack, estimate of the drag on the airfoil, or estimate the oscillations due to vortex shedding.

All of the methods typically overestimated the lift peak. The UPM was the most accurate in modeling the rate of lift increase, as well as the magnitude and time of the lift peak. Even with $y_v = 0$, the UPM accurately modeled C_L until the vortex closely approached the airfoil, at which point the estimate diverged significantly from the physical result. The E-TL model predicted slightly stronger and earlier lift responses than the UPM, though not as strong as the QS-TAT model. The W-TAT model was intermediate between the results of the UPM and E-TL models.

5.4.3 Discussion

The gusts created by the pitching airfoil yielded repeatable changes in the forces on a downstream airfoil. These forces were attributable to three properties of the gust: the primary vortex, the vorticity shed from the upstream airfoil soon after pitching, and the difference between the initial and final states of the wake of the upstream airfoil.

The similarity between the experimental and numerical force traces in Figures 5.9-5.11 confirmed that the initial response to the gust was an inviscid effect of the oncoming vortex. After that, viscous effects dominated.

In some cases, particularly when $y_{upstream} = 0$, the vortices impacted and merged with the boundary layers on the airfoil. Surprisingly, this merging was not linked to

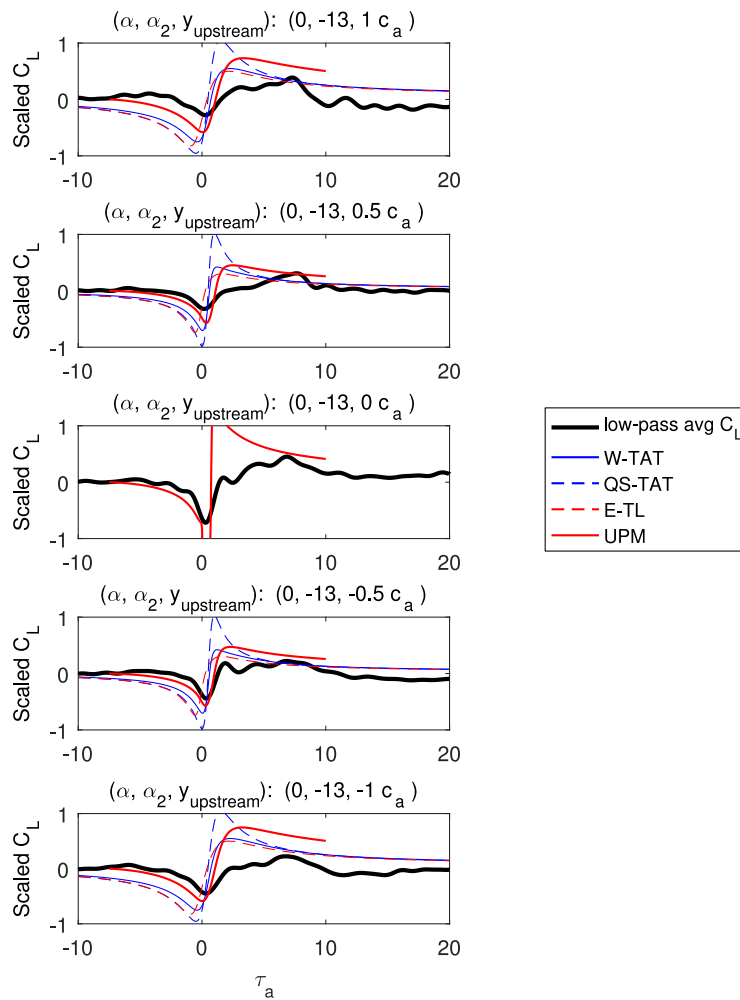


Figure 5.9: Mean-subtracted C_L due to gusts from the pitching airfoil impacting the test article at $\alpha = 0^\circ$, scaled by the quasi-steady estimate of the lift peak amplitude. For the $y_{upstream} = 0$ case, the lift is only scaled by α_2 . For comparison, the results of the different models are presented. Each row is a different $y_{upstream}$, as noted in the title of each panel.

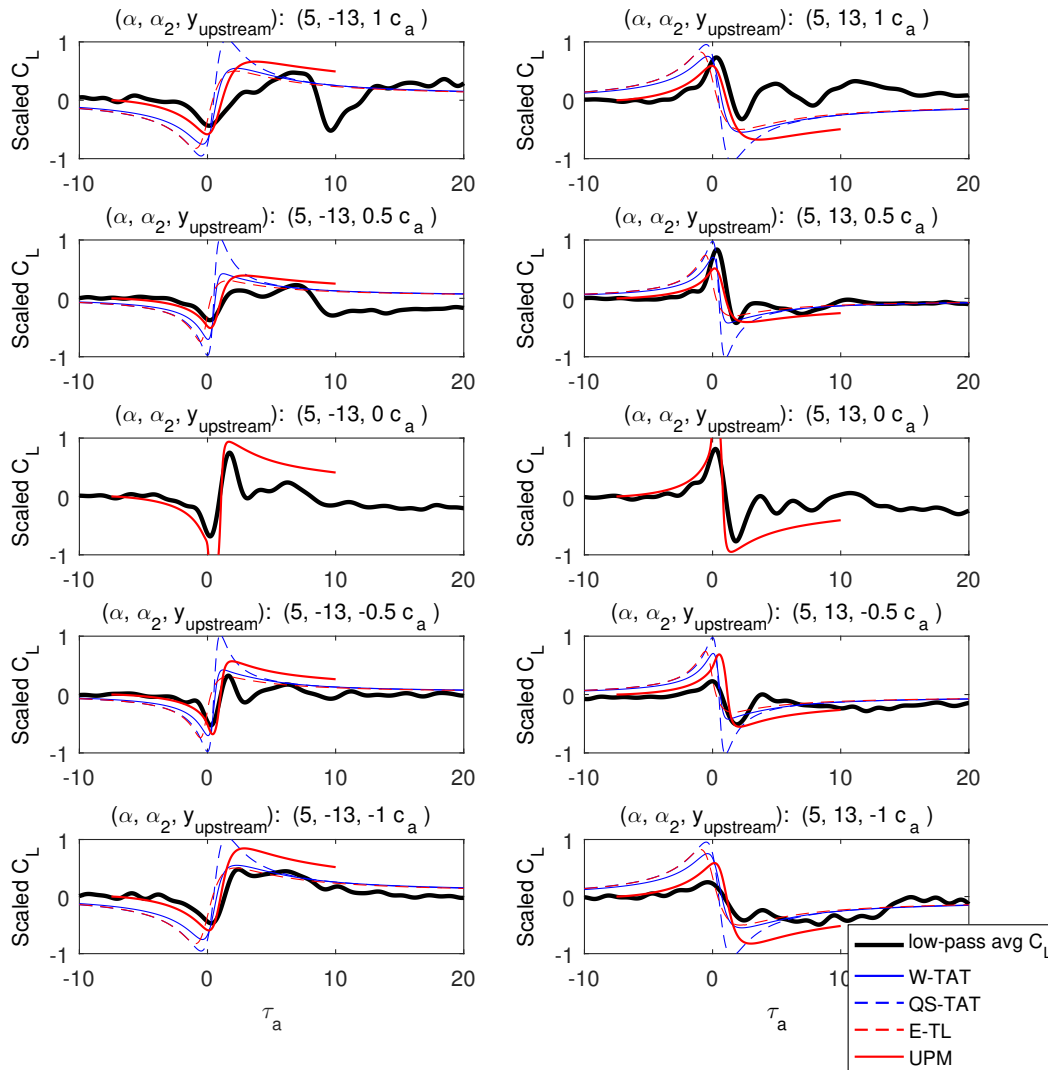


Figure 5.10: Mean-subtracted C_L due to gusts from the pitching airfoil impacting the test article at $\alpha = 5^\circ$, scaled by the quasi-steady estimate of the lift peak amplitude. For the $y_{upstream} = 0$ case, the lift is only scaled by α_2 . For comparison, the results of the different models are presented. Each row is a different $y_{upstream}$, and the columns are different pitching directions, as noted in the title of each panel.

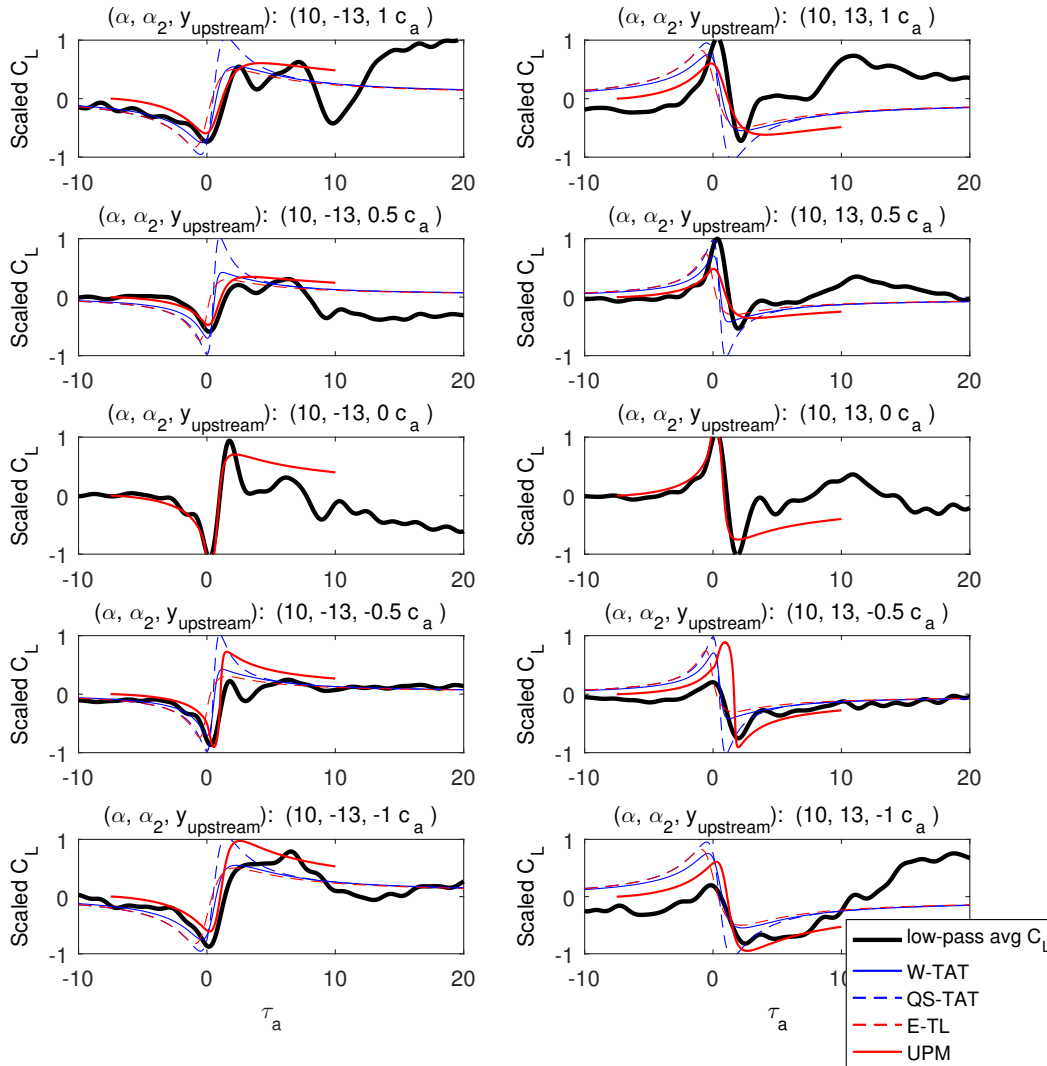


Figure 5.11: Mean-subtracted C_L due to gusts from the pitching airfoil impacting the test article at $\alpha = 10^\circ$, scaled by the quasi-steady estimate of the lift peak amplitude. For the $y_{\text{upstream}} = 0$ case, the lift is only scaled by α_2 . For comparison, the results of the different models are presented. Each row is a different y_{upstream} , and the columns are different pitching directions, as noted in the title of each panel.

any specific change in the forces. This appears to be because the perturbed boundary layers were quickly shed, and the released clump of higher vorticity continued to act as a vortex as it convected downstream.

The angle of attack of the downstream airfoil had a significant impact on the forces after the vortex passed, and the timescales associated with their changes. The airfoil at $\alpha=0^\circ$ could not support a significantly asymmetric flow, so any boundary layer disturbances were quickly shed, and so it recovered on a timescale comparable to the Wagner function. The asymmetric flow around the $\alpha=5^\circ$ airfoil responded more strongly to such disturbances, and required more time to shed the slightly separated flow on its suction side. The greater asymmetry, and incipiently stalled flow, of the airfoil at $\alpha=10^\circ$ led to more extreme reactions to perturbations, as well as a longer recovery time. In some cases, the large change in lift was due in part to the separated flow being ‘blown off’ by the incoming gust, temporarily reattaching the flow.

The aforementioned region of additional vorticity was likely due to the evolution of the flow around the upstream airfoil. After its rapid pitching, the airfoil was at an angle of -13° , so it was stalled in a static sense. This meant that the flow began to develop a large separated region. The development of the stalled flow is an unsteady process. On its way toward its final behavior, the airfoil shed much of the separated flow as a large region of strong vorticity. This became the strong disturbance that impacted the downstream airfoil. Were the airfoil pitched to a more moderate angle, it is likely that such a large vortical region would not have been shed. The impact of this additional vorticity was seen as a change in the lift on the downstream airfoil about 5-10 t_c after the passing of the vortex.

The difference in the upstream airfoil’s pre- and post-pitching wake resulted in permanent changes in the forces on the test article. Both the average value and magnitude of oscillation of those forces changed permanently. This was far from the ideal of a single transient interaction with a vortex. These permanent changes were due to multiple effects. In some cases, the thicker wake perturbed the flow around the downstream airfoil enough that the flow remained attached, resulting in increased lift and/or decreased drag. In others, the wake impacted only one side of the airfoil, causing an asymmetry in the pressure, and so a change in lift.

Each of the numerical and theoretical models with a wake adequately predicted the magnitude and temporal position of the initial lift peak. The models were unable to predict the later viscous effects. The lack of viscosity precludes prediction of the wake of the upstream airfoil. The simulations have no model of flow separation, and

so are incapable of modeling the creation of the additional shed vorticity, as well as the changes in the boundary layer of the downstream airfoil. The models should thus be compared only on their prediction of that initial lift peak.

The quasi-steady model, as well as the extended Tchieu-Leonard model, estimated faster changes in the forces than were observed. This is likely due to the fact that the QS-TAT model lacked the moderating effect of a wake model. Similarly, the E-TL model had not released a vortex since the beginning of the simulation, so the moderating effect was reduced due to the distance of the wake vortex. The unsteady panel method and the thin airfoil theory model with the Wagner function provided reasonable approximations of the initial peak in the lift. After that, viscosity, and the change in the flow due to the wake of the gust generator, made the estimates less accurate. For predictions of the initial change in forces due to the vortical gust, the W-TAT model appears to give fairly accurate estimates, with much lower computational costs than the panel method simulations.

Overall, the pitching airfoil was not a perfect gust generator. Though it was able to generate compact vortical gusts, its persistent presence upstream of the test article made it difficult to separate the effects of its wake from those of the vortex. Beyond the initial lift peak, it was difficult to attribute further effects solely to the passing vortex. This suggests that it is inappropriate to use for examining vortex-wing interactions when it is near the midline, as its unwanted effects would strongly affect the test article.

5.5 Interaction with heaving plate gusts

The experiments in this section measured the response of the downstream airfoil to the heaving gust generator using PIV and force measurements. The initial direction of travel, speed, and travel distance of the heaving plate, as well as the angle of attack of the downstream airfoil, were varied across these experiments, which are detailed in Appendices A.4.8 - A.4.10.

5.5.1 Experimental Results

A sample of the results can be seen in Figure 5.12, which is analogous to Figure 5.7, but with the heaving plate's position over time in the bottommost plot.

The PIV snapshots in Figure 5.7 show the outlined vortical gust above the airfoil, traveling from left to right. Since this vortex had negative circulation, the wake upstream of the vortex was deflected upward, and the downstream portion was

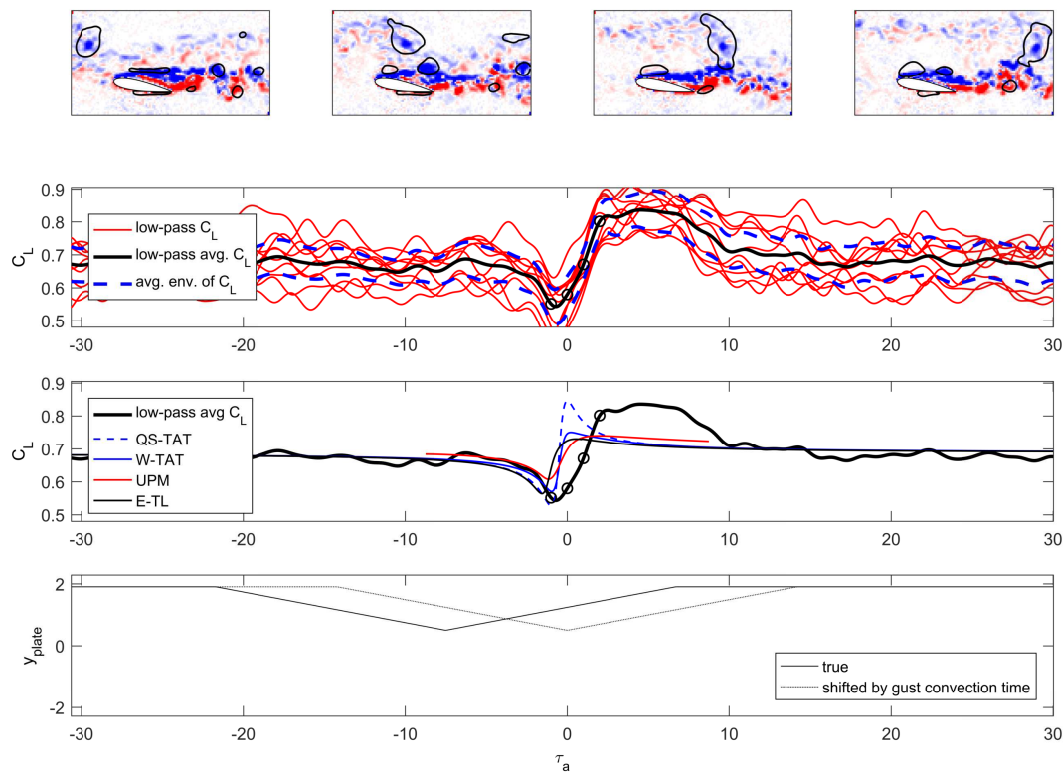


Figure 5.12: Gust from heaving plate interacting with the downstream airfoil: $y_{peak} = 0.5c_a$, negative initial motion, $\alpha = 10^\circ$. The temporal position of the vorticity snapshots at the top are denoted by circles in the middle two plots. The second plot shows the low-pass filtered C_L across the different repetitions, the average of those, and the average C_L envelope. The third plot shows that average, as well as the estimates from numerical models. The bottom plot shows the y -position of the upstream airfoil, as well as that position shifted in time to compensate for the travel time of the gust.

deflected downward. The wake of the heaving plate followed the y -position of the plate, and so was only visible in the PIV field of view for a limited amount of time. In experiments where the heaving plate passed the midline of the tunnel, the plate's wake passed the airfoil twice. These two factors, the vortical gust and the plate's wake, are associated with certain force responses. After the gust passed, the flow and forces returned to their initial state.

As with the gust from the pitching airfoil, the response of the forces to the gust from the heaving plate was very repeatable. This can be seen as the close overlap of the red lines in 5.7 when the vortex passed over the airfoil.

The lift forces in each experiment are plotted together in Figure 5.13. Figures C.14

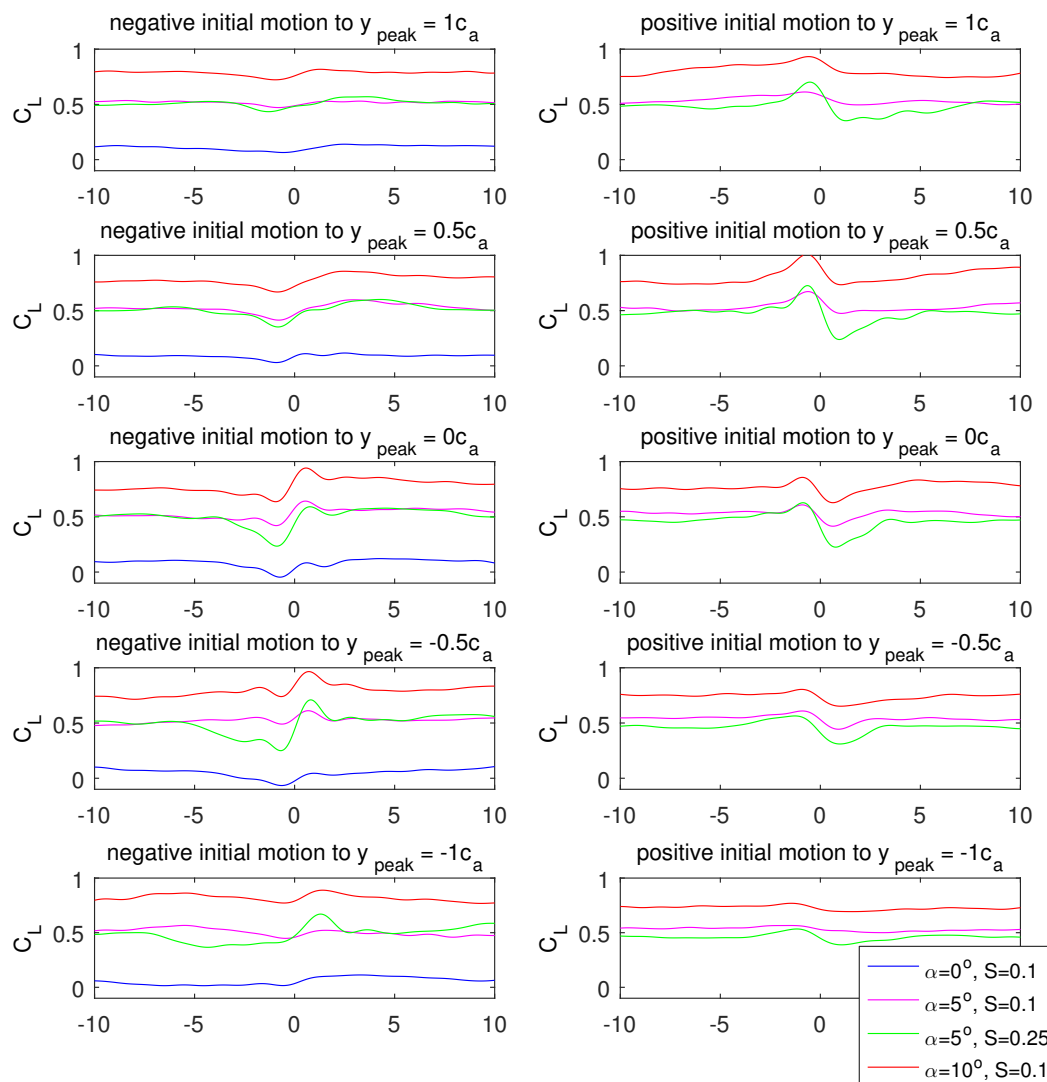


Figure 5.13: Lift coefficient due to gusts from the heaving plate interacting with the airfoil. Each panel contains force traces from a single release position and initial direction, but different airfoil angles of attack. The left column moved initially in the $-y$ direction, and the right in $+y$. Each row is a different y_{peak} .

- C.16 show the moment and drag histories as well. These show the evolution of the low-pass-filtered forces over time, with the gust passing the leading edge of the airfoil at $t = 0$. The left columns show the interaction with gusts generated by the plate initially moving in the $-y$ direction, which created a vortex with negative circulation when it changed direction, and vice-versa for the right column. The average envelopes of the forces are shown in Figures C.17 - C.19.

In response to an oncoming vortex with negative circulation, the lift coefficient

dipped, rose, and returned to the steady-state value. The opposite occurred with vortices of positive circulation.

The other factor in the variation of the forces was the wake of the plate. In the cases where the heaving plate passed the midline ($y_{peak} < 0$ for negative initial motion, or $y_{peak} > 0$ for positive initial motion), the lift deviated from its steady-state behavior earlier than the estimated vortex arrival time. These deviations were coincident with the arrival of the wake of the heaving plate.

The arrival of the wake is also visible in the force envelopes for $\alpha = 5^\circ$, which shrank in response to the perturbations. In the case of the negative initial motion at speed $S = 0.1$ to $y_{peak} = -c_a$, both interactions with the wake are seen, as well as recovery between those impacts. In contrast, positive initial motion to $y_{peak} = -c_a$ resulted in no noticeable changes to the force envelopes. When the flow around the airfoil was sufficiently perturbed, the envelopes returned to their original state over approximately $15 t_c$.

The airfoil's angle of attack also had an effect on the change in the forces. Early in the interaction, the changes in C_L were very similar across α , but they diverged after the first peak. At higher α the gusts led to larger and more lasting deviations in the forces. This recovery time was approximately 5-10 t_c for the lower angles, and 10-20 t_c for $\alpha = 10^\circ$. A comparison of lift traces in Figure 5.14 illustrates the variation of the recovery timescale with the angle of attack. In the cases where the plate passed the midline, the final passage of the wake set the beginning of this recovery time.

5.5.2 Comparison with Theory

To examine the accuracy of the numerical models, Figures 5.15 - 5.18 show the scaled lift coefficients of the airfoil, in response to the different gusts, for three angles of attack. The forces had their mean values subtracted, and the remainder was scaled by the C_L peak amplitude in Equation 2.16. Here, the y -position of the vortex was estimated as the peak position of the heaving plate. This function is undefined when the plate's peak was at $y = 0$, so those plots were instead scaled by the heaving speed of the plate alone. Figures 5.15, 5.16, and 5.18 show the results at α of 0° , 5° , and 10° with $S = 0.1$, and Figure 5.17 shows $\alpha = 5^\circ$ with $S = 0.25$.

When the heaving plate reached or passed the midline, none of the numerical models reliably provided accurate predictions of the lift on the airfoil, particularly at the higher angles of attack. In Figure 5.17, the numerical models typically overpredicted

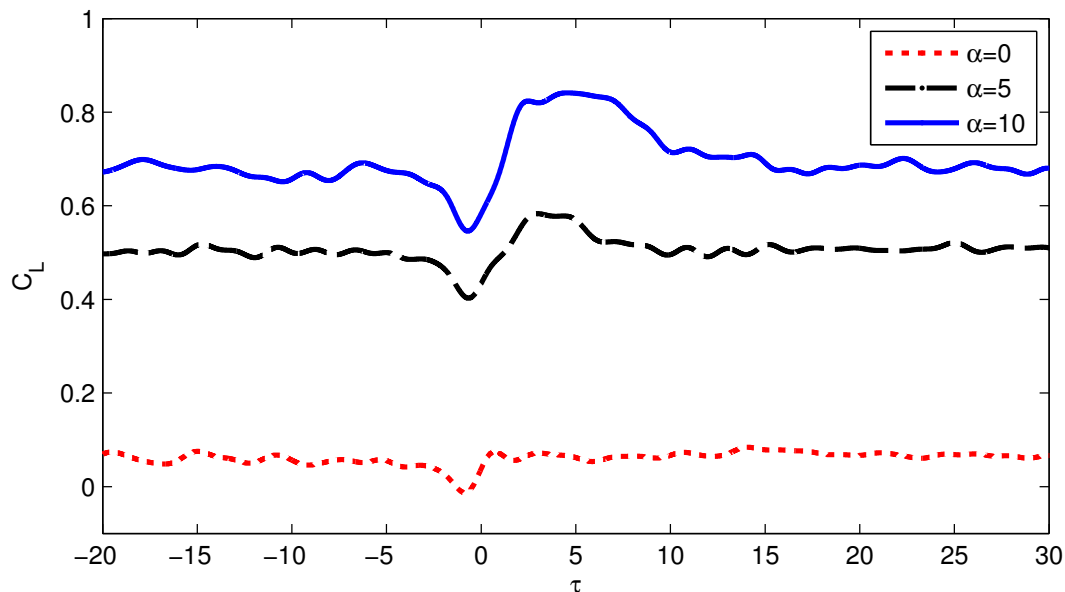


Figure 5.14: C_L due to gusts from the heaving plate moving at $S = 0.1$ to $y_{peak} = 0.5 c_a$, with the test article at different angles of attack. This shows the increasing recovery time along with increasing angle of attack.

the forces on the body due to the stronger gust.

In the cases where the wake did not pass the midline, the UPM and E-TL models performed well in the initial vortex interaction. The W-TAT model provided slightly less accurate predictions, and the QS-TAT model generally overpredicted the forces.

5.5.3 Discussion

The heaving plate successfully generated vortical gusts that interacted with the downstream airfoil, and resulted in repeatable forces. These forces were associated with two factors: the primary vortex and the wake of the plate.

When the plate did not pass the midline, the lift in the early vortex-wing interaction was adequately modeled by the estimates from the UPM or semi-analytic models. The quasi-steady method's inaccuracy was due to the fact that it lacks a wake model, and so it responded without the smoothing that the Wagner function provides. This suggests that the initial lift peak was an inviscid effect of the vortex, moderated by the wake of the airfoil.

In the experiments where the plate passed the tunnel's midline, its wake resulted in unwanted changes in the forces both before and after the vortical gust arrived. It reduced the amount of vortex shedding for the $\alpha = 5^\circ$ airfoil, increased the lift on

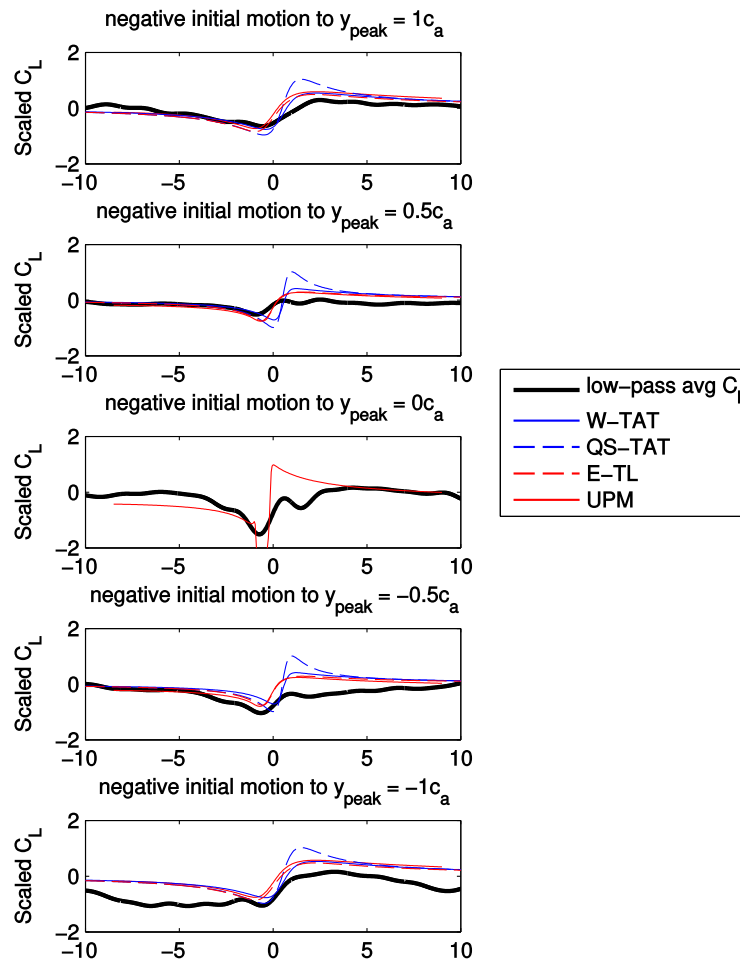


Figure 5.15: Mean-subtracted C_L due to gusts from the heaving plate moving at $S = 0.1$ impacting the test article at $\alpha = 0^\circ$, scaled by the quasi-steady estimate of the lift peak amplitude. For the $y_{upstream} = 0$ case, the lift is only scaled by S . For comparison, the results of the different models are presented. Each row is a different y_{peak} .

the $\alpha = 5^\circ$ and $\alpha = 10^\circ$ airfoils, and modified the lift on the $\alpha = 0^\circ$ airfoil. Though these effects were transient, they were significant.

The multiple timescales for the return of the flow to its original state suggest multiple causes. The rapid recovery of the forces for $\alpha = 0^\circ$ is consistent with the Wagner function. When the vortex and wake were far from the airfoil, the change in forces was similarly rapid, even at the higher angles of attack. This is because the flow was not grossly perturbed, and so could easily return to its initial state. When the gust strongly interacted with the airfoil at $\alpha = 10^\circ$, the flow reattached, and required additional time to re-develop its separated flow. Similarly, the $\alpha = 5^\circ$ airfoil needed

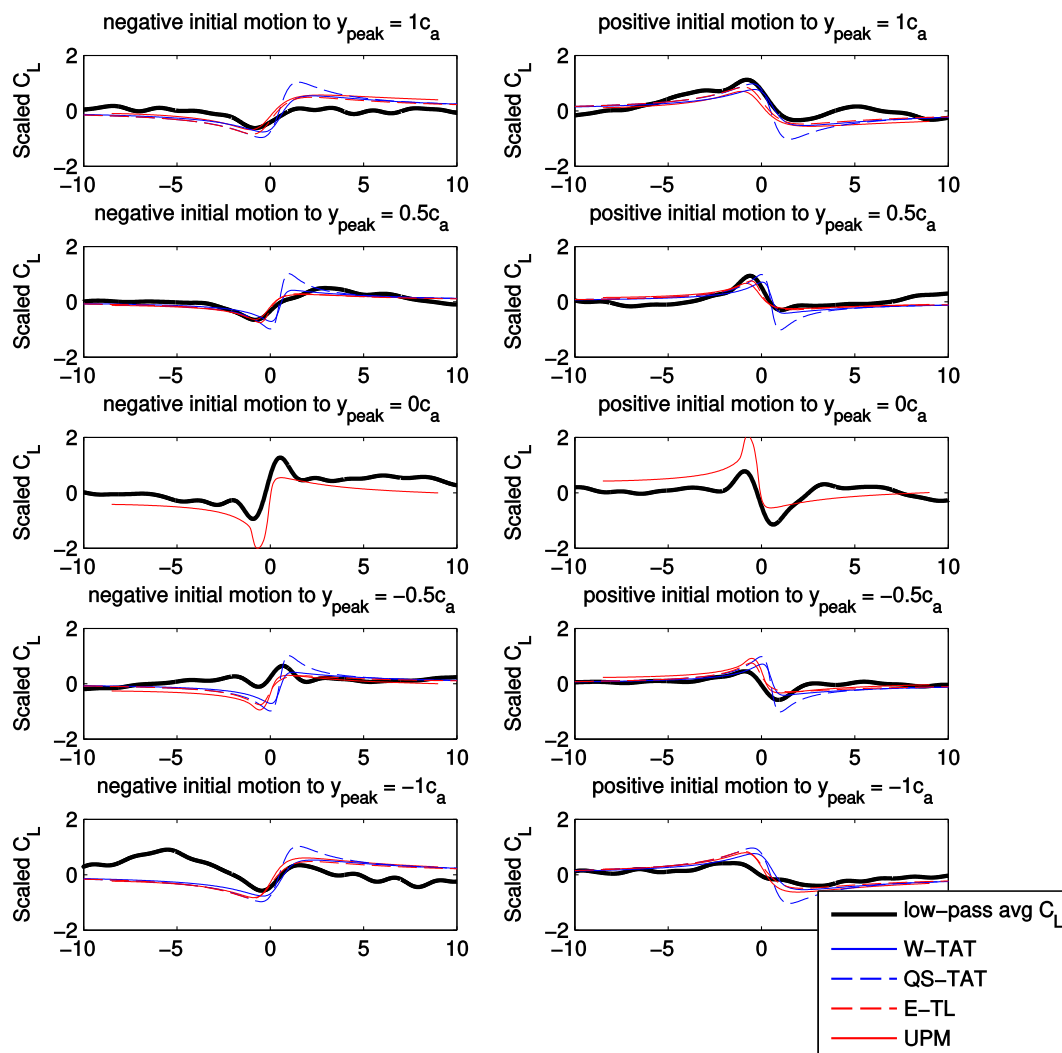


Figure 5.16: Mean-subtracted C_L due to gusts from the heaving plate moving at $S = 0.1$ impacting the test article at $\alpha = 5^\circ$, scaled by the quasi-steady estimate of the lift peak amplitude. For the $y_{upstream} = 0$ case, the lift is only scaled by S . For comparison, the results of the different models are presented. The left column moved initially in the $-y$ direction, and the right in $+y$. Each row is a different y_{peak} .

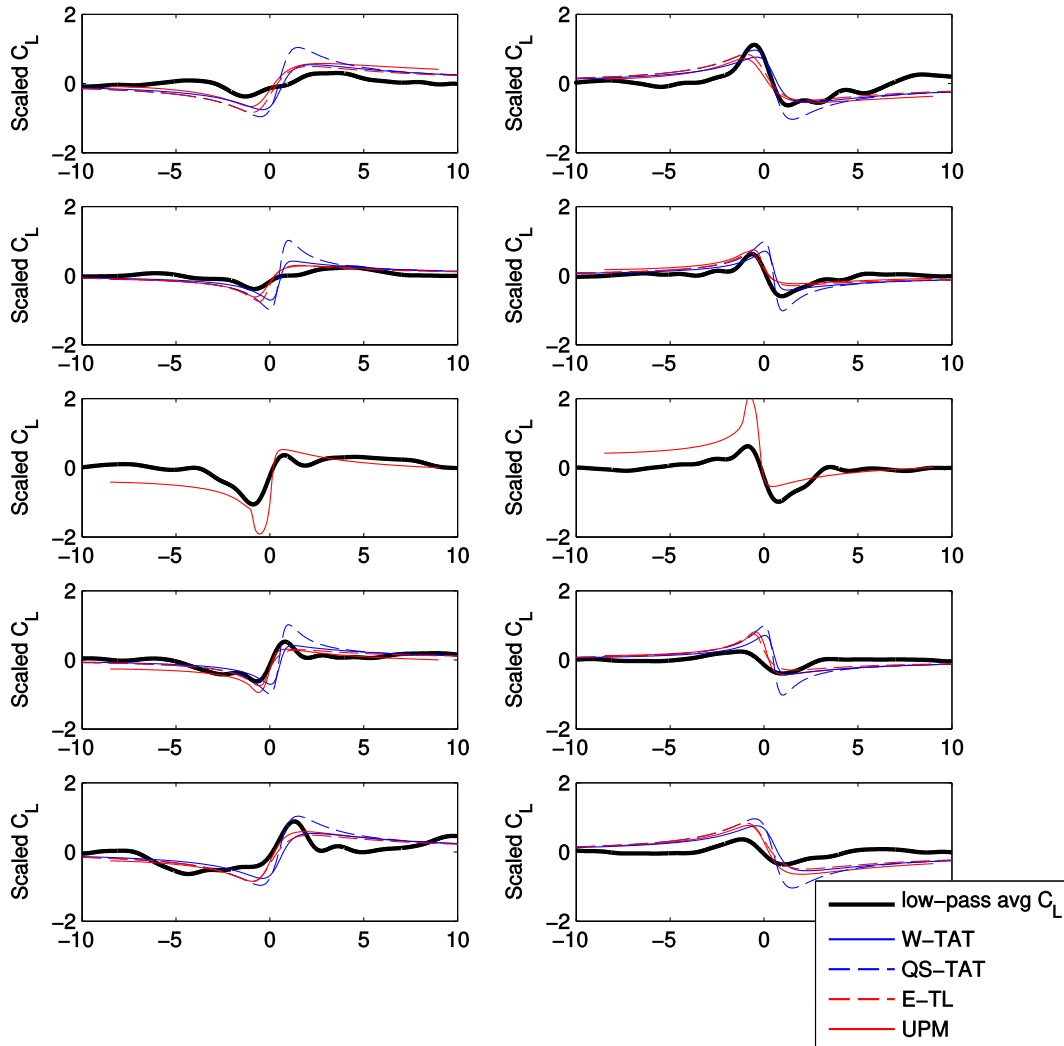


Figure 5.17: Mean-subtracted C_L due to gusts from the heaving plate moving at $S = 0.25$ impacting the test article at $\alpha = 5^\circ$, scaled by the quasi-steady estimate of the lift peak amplitude. For the $y_{upstream} = 0$ case, the lift is only scaled by S . For comparison, the results of the different models are presented. The left column moved initially in the $-y$ direction, and the right in $+y$. Each row is a different y_{peak} .

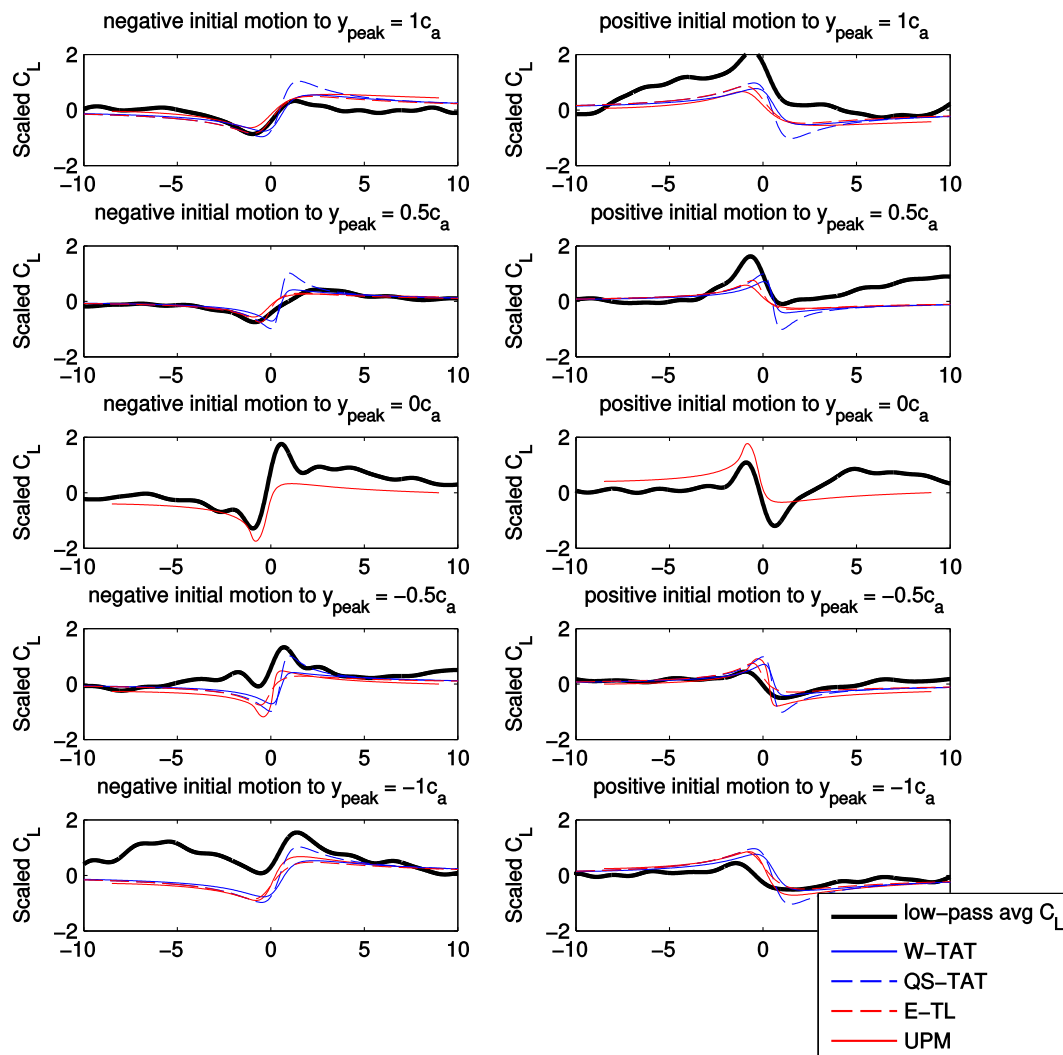


Figure 5.18: Mean-subtracted C_L due to gusts from the heaving plate moving at $S = 0.1$ impacting the test article at $\alpha = 10^\circ$, scaled by the quasi-steady estimate of the lift peak amplitude. For the $y_{upstream} = 0$ case, the lift is only scaled by S . For comparison, the results of the different models are presented. The left column moved initially in the $-y$ direction, and the right in $+y$. Each row is a different y_{peak} .

an intermediate amount of time to recover from strong perturbations. The recovery time of the vortex shedding was approximately $15 t_c$ for the $\alpha = 5^\circ$ airfoil. This appeared to be unrelated to the return to normalcy of the low-pass-filtered forces.

As with the pitching gust generator, the models were unable to properly predict the wake of the heaving plate, the spatial extent of the vortex, or the behavior of the boundary layers on the airfoil. The over-prediction of the lift in the $S = 0.25$ case is likely a result of two factors: the large size of the generated vortex and the difference between its predicted and true circulation. The larger vortex, and its associated structures, would result in a more drawn-out vortex interaction, as compared to the point-vortex used in the models. The over-prediction of the circulation simply resulted in larger estimated forces.

Since all of the numerical models lack viscosity, they were unable to account for the effects of the oncoming wake. Thus, they were inappropriate for modeling the cases where the plate passed the midline. This lack of viscosity also prevented predictions of the drag, which changed due to the velocity deficit in the wake of the plate, or due to the separated region on the airfoil being swept away by the gust. The different numerical models with wakes performed similarly, again confirming that the initial part of the vortex-wing interaction is an inviscid effect. The unsteady panel method and extended Tchieu-Leonard models were slightly more accurate than the model using the Wagner function in thin airfoil theory. The simplicity of the W-TAT model again recommends it, however, due to the relative expense of the other methods.

The heaving plate gust generator is imperfect. Although its wake only interacted with the test article for a finite time, and only when the plate reached the midline of tunnel, the resulting variations in the forces were of the same magnitude as those from the vortex interactions. This suggests that it is inappropriate to use for vortex generation when it would pass in front of the test article. Unfortunately, this constrains the polarity of the generated vortices to gusts with negative circulation above the airfoil, and positive circulation below it.

5.6 Summary

Superficially, the results of both gust generators are similar: they created vortical gusts and wakes which interacted with the downstream airfoil. Most cases demonstrated the expected change in lift associated with a vortex passing the airfoil: as a vortex with negative circulation approached, it induced an effective drop in the airfoil's angle of attack and reduced the lift, or an opposite effect was seen with

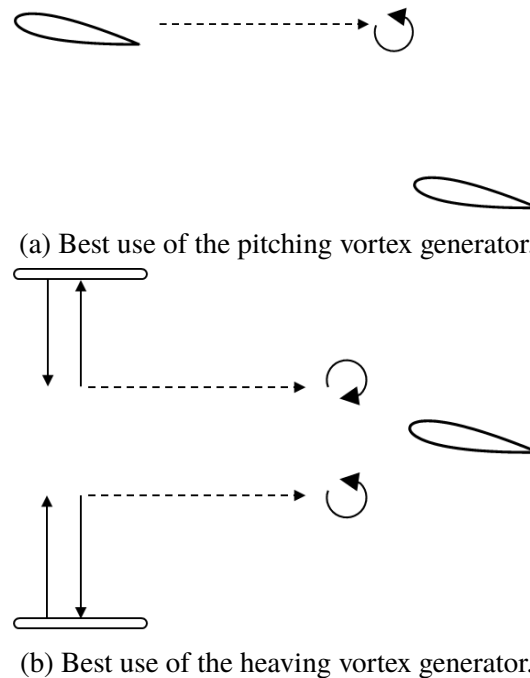


Figure 5.19: Suggestions for the best use of the investigated vortex generators: the pitching generator should be transversely far from the test article, and the heaving plate should not pass in front of the test article.

positive circulation. This is similar to the numerical results found by Golubev et al [26], though the lift oscillations were smoother in these experimental results.

The evolution of the vortex itself closely resembled the behaviors described by Rockwell [59]. When it was further than a chord length from the body, the vortex was relatively undisturbed. When it was closer, it was subjected to significant shear, and sometimes split into multiple vortical regions. The closest vortices directly interacted with the boundary layers of the airfoil. The asymmetry of the vortex's distortion, which was dependent on which side of the test article it passed, is similar to the results from Peng and Gregory [53].

The pitching airfoil created stronger and more compact vortices, but it also had a persistent wake. Additionally, its wake was significantly different before and after pitching. In some cases, this significantly altered the flow around the test article, permanently changing the average forces as well as disrupting the vortex shedding from the test article. As the flow around the upstream airfoil developed after pitching, a second burst of vorticity was released, which again modified the flow around the test article. To reduce these unwanted effects, the pitching vortex generator should

thus be limited to operation with a significant separation in y from the test article, as shown in Figure 5.19a.

The heaving plate also released a wake, which significantly interfered with the test article if the plate moved past the y -position of the test article. In contrast to the use of the pitching airfoil, the heaving plate's withdrawal to the edge of the tunnel meant that the flow around the test article returned to its previous state. Efforts to avoid the effects of its wake limit its usefulness to the creation of vortical gusts with negative circulation above the airfoil, or positive circulation below it. This is illustrated in Figure 5.19b.

With both systems, the wakes had significant effects when interacting with the test article. The perturbations in the wakes sometimes caused flow to reattach on the test article. In other instances, the perturbations modified the flow on one side of the airfoil, causing an asymmetry and resulting change in lift. The velocity deficit in the wake of the generators likely had an effect as well. It may have manifested as a decrease in drag, but the complexity of the interaction made attribution difficult. The evolution of these wakes was dependent on the streamwise distance between the generators and test article, but this distance was not varied in the current experiments.

Thus, each generation method has its benefits and drawbacks. The persistent wake of the airfoil permanently changed the flow around the test article, whereas the heaving plate's wake significantly disrupted the flow temporarily. The pitching airfoil could create vortices with either sense of rotation, while the heaving plate's wake limits it to one sense per side of the test article.

With both generators, the time needed for the low-pass-filtered forces on the test article to approach their final state was primarily dependent on the angle of attack of the test article. At low angles, the flow remained attached and the forces responded quickly, on timescales of $5-10 t_c$, which was consistent with the Wagner function. In contrast, at $\alpha = 10^\circ$, when the flow around the test article was significantly perturbed, the flow re-attached and its approach to its final state required approximately $20 t_c$. This is consistent with timescales reported in control of separated flows [12], and of flow development around impulsively started wings at high angles of attack [47]. In the case of separated flow control, this transient was associated with repeated oscillations of the bound circulation as vorticity was shed into the wake. Similarly, the timescales of the impulsively started wings are strongly related to the formation of a leading edge vortex, and repeated shedding of vorticity as the flow settled into a final separated state. Surprisingly, this long timescale has also been associated with

the reattachment of separated flow through the use of periodic perturbations [14].

The heaving plate was able to reveal one effect that was unobservable with the pitching generator: the reassertion of vortex shedding from the airfoil at $\alpha = 5^\circ$. This occurred on a timescale of roughly $15 t_c$.

The numerical methods with wake models provided reasonable estimates for the initial changes in lift, in the cases where the wakes were not overly intrusive. They did not properly capture the behavior after the initial vortex interaction, as the models did not include viscous effects like boundary layer evolution and separation. Although the UPM allowed the vortical gust to move freely, this was only significant when the vortex was close to the airfoil, which is when viscous effects would render any of these inviscid methods inaccurate. The quasi-steady method lacked models of the wake, and so it failed to capture the slower increase in the lift that this effect causes. The UPM and E-TL were slightly more accurate than the W-TAT method, but significantly more expensive to compute. Overall, the W-TAT model provided estimates that were appropriate for modeling the initial changes in lift due to vortex-gust interaction, with low computational costs.

Chapter 6

CONCLUSION

6.1 Summary

The research described in this thesis aimed to better understand the generation of vortical gusts and their effects on an airfoil. This consisted of three topics: numerical modeling, experimental generation of the gusts by pitching an airfoil or heaving a flat plate, and the interaction between these gusts and a fixed downstream airfoil.

Unsteady thin airfoil theory led to simple models of the circulation of vortices created by the gust generation methods. These found that the circulation is proportional to the product of the generator's chord length, the freestream velocity, and either the heaving speed or the change in angle of attack of the generator. Simulations of the gust generators, performed with an unsteady panel method or the extended Tchieu-Leonard model, showed good agreement with predictions of the simple analytical models. These models were also used to model the lift on an airfoil as a vortex convected past. When the vortex was weak and far from the body, all of the methods with models of the wake provided similar estimates. The unsteady panel method was the only model where the motion of the vortex was influenced by the airfoil and its wake. When the gust vortex was strong or near the body, it would no longer travel in a straight line in the panel method, breaking the assumptions of the analytic models. In this case, the results of the panel method would differ significantly from the simpler models.

Two physical methods of generating vortical gusts were built for use in a free-surface water tunnel: a pitching airfoil and a heaving plate. Both were actuated along single degrees of freedom. They were able to generate vortical gusts, but also had intrusive wakes. The pitching airfoil, since it remained in place upstream of the airfoil, continually released a wake behind it. The heaving plate moved to the edge of the tunnel, limiting the time that its wake influenced the flow around the test article. Compared to the vortical gusts from the heaving plate, those from the pitching airfoil were more spatially compact. Both methods were able to generate vortices whose circulations generally agreed with the predictions of unsteady thin airfoil theory.

These two devices were used to create disturbances that interacted with a downstream

airfoil. The lift on the airfoil generally followed the trends predicted by the simple thin airfoil theory models, unless the wakes of the generators interfered substantially. This limited the usefulness of both generators. In some cases, the pitching airfoil changed the flow around the test article to such an extent that the average forces were significantly different before and after pitching. If the pitching airfoil was near the midline of the tunnel, it also reduced the coherent vortex shedding from the test article when it was at moderate angles of attack. This limits its position to be far in the y -direction from the test article. The heaving gust generator was conceived to reduce the effect of the generator's wake on the test article, and was shown to not affect the test article when it was kept by the side of the tunnel. When the plate passed the midline, its wake impacted the test article twice, with significant effects on the flow and forces on the test article. Avoiding this interaction limited the polarity of the shed vortices: those with positive circulation below the airfoil, and negative above it.

The angle of attack of the airfoil had a significant impact on the time needed for the forces to transition from their perturbed levels to their final states. When the airfoil was at $\alpha = 0^\circ$, the forces approached their final state quickly, on a timescale of 5-10 t_c , which is similar to that of the Wagner function. When the airfoil was almost statically stalled at $\alpha = 10^\circ$, large perturbations from the gust could cause the flow to reattach, resulting in recovery timescales of up to 20 t_c . This is consistent with the timescales reported in control of separated flows [12] and rapidly accelerated plates [47].

The heaving plate yielded one result unavailable with the pitching plate: the timescale of resumption of vortex shedding from the airfoil at $\alpha = 5^\circ$, after a strong perturbation, was 15 t_c . The wake of the pitching gust generator had overwhelmed the development of the vortex shedding behavior in its experiments.

When the wakes did not significantly interfere with the test article the theoretical models provided reasonable estimates of the initial lift peak. After this peak, the simulations did not properly capture the evolution of the forces, as the simulations lacked models of the boundary layers and separated flow around the airfoil. The more complex models, the unsteady panel method and the extended Tchieu-Leonard model, did not provide substantially more accurate estimates of the lift than the simple point-vortex model with the Wagner function. The simplest model with a wake provided a useful balance between computational cost and physical relevance.

It is comforting to see that the simple models of unsteady thin airfoil theory provide

accurate models of the interaction between an airfoil and a vortical gust.

6.2 Future Work

The limitations of the two investigated gust generators suggest that a more complicated approach to gust generation could be useful. A combination of the two methods may combine the advantages of both, while eliminating most of their disadvantages. Since the simplest analytical models are based on linear thin airfoil theory, they can be additively combined. The combined motion will then be a mix of both pitching and heaving. At its simplest, consider an impulsive change in heaving velocity, $\Delta S = S_2 - S_1$, and angle of attack, $\Delta\alpha = \alpha_2 - \alpha_1$, at $t = 0$. In this case, consider S to be a signed velocity, so that positive values indicate motion in the $+y$ direction, and vice-versa. Thus the combination of Equations 2.6 and 2.13 yields

$$\Gamma_v = \frac{\pi}{2} U c (\Delta\alpha - \Delta S). \quad (6.1)$$

The previously analyzed heaving plate system had $S_1 = -S_2 = S$ and $\Delta\alpha = 0$. The pitching airfoil system had $S_1 = S_2 = 0$ and $\Delta\alpha = \alpha_2$. The combination of the two methods allows for a gust generator that advances and retracts to spare the test article its permanent influence, while being able to generate vortices of either polarity regardless of being above or below the test article. This simple analysis ignores any additional complications, such as the pitching location or any lead or lag between the motions, which may have an effect on the resulting gust. Further research could investigate optimal approaches to gust generation in this manner.

This research could also be used in conjunction with sensing and control schemes to reduce the effect of a vortical gust on a wing. Since the analytical methods provided a reasonable estimate of the initial response of the forces to a gust, this is a valid framework for advancement. For example, an approaching vortex with negative circulation could be countered by an increase in the wing's angle of attack, or a downward deflection of a trailing-edge flap. These are simplistic responses, but may merit further investigation.

These simple simulations were not able to fully capture the gust response. Further research may develop simple models that can capture the behavior of the reattaching and separating flows around the airfoils, as well as the vortex's interaction with the wake. These could yield better predictions of the forces, and thus be more useful

for future control schemes. Such models may require more detailed simulations to examine subtle phenomena in the airfoil's boundary layer.

BIBLIOGRAPHY

- [1] Federal Aviation Administration. Advisory circular 25.341-1: Dynamic gust loads. Technical report, Federal Aviation Administration, 2014.
- [2] JD Anderson Jr. *Fundamentals of Aerodynamics*. McGraw Hill Higher Education, New York, 4th edition, 2007.
- [3] YS Baik and LP Bernal. Experimental study of pitching and plunging airfoils at low Reynolds numbers. *Experiments in Fluids*, 53(6):1979–1992, 2012.
- [4] YS Baik, LP Bernal, K Granlund, and MV Ol. Unsteady force generation and vortex dynamics of pitching and plunging aerofoils. *Journal of Fluid Mechanics*, 709:37–68, 2012.
- [5] RMH Beckwith and H Babinsky. Impulsively started flat plate flow. *Journal of Aircraft*, 46(6):2186–2189, 2009.
- [6] V Brion, A Lepage, Y Amosse, D Soulevant, P Senecat, JC Abart, and P Pailart. Generation of vertical gusts in a transonic wind tunnel. *Experiments in Fluids*, 56(7):145, 2015.
- [7] S Brunton, C Rowley, and D Williams. Linear unsteady aerodynamic models from wind tunnel measurements. *41st AIAA Fluid Dynamics Conference and Exhibit*, (3581), 2011.
- [8] DA Buell. An experimental investigation of the velocity fluctuations behind oscillating vanes. Technical report, National Aeronautics and Space Administration, 1969.
- [9] P Chakraborty, S Balachandar, and RJ Adrian. On the relationships between local vortex identification schemes. *Journal of Fluid Mechanics*, 535:189–214, 2005.
- [10] J Choi. *Unsteady aerodynamics and optimal control of an airfoil at low Reynolds number*. PhD thesis, California Institute of Technology, 2016.
- [11] MS Chong, AE Perry, and BJ Cantwell. A general classification of three-dimensional flow fields. *Physics of Fluids A: Fluid Dynamics*, 2(5):765–777, 1990.

- [12] T Colonius and D Williams. Control of vortex shedding on two-and three-dimensional aerofoils. *Philosophical Transactions of the Royal Society A: Mathematical, Physical and Engineering Sciences*, 369, 2011.
- [13] JO Dabiri and M Gharib. The role of optimal vortex formation in biological fluid transport. *Proceedings of the Royal Society of London B: Biological Sciences*, 272(1572):1557–1560, 2005.
- [14] A Darabi and IJ Wygnanski. Active management of naturally separated flow over a solid surface. part 1. the forced reattachment process. *Journal of Fluid Mechanics*, 510:105–129, 2004.
- [15] P Donely. An experimental investigation of the normal acceleration of an airplane model in a gust. Technical Report 706, National Advisory Committee for Aeronautics, 1939.
- [16] P Donely. Summary of Information Relating to Gust Loads on Airplanes. Technical Report 997, National Advisory Committee for Aeronautics, 1950.
- [17] HL Dryden. A review of the statistical theory of turbulence. *Quarterly of Applied Mathematics*, 1(1):7–42, 1943.
- [18] R Dunne and BJ McKeon. Dynamic stall on a pitching and surging airfoil. *Experiments in Fluids*, 56(8):157, 2015.
- [19] J Eldredge, C Wang, and MV Ol. A computational study of a canonical pitch-up, pitch-down wing maneuver. *39th AIAA Fluid Dynamics Conference*, (3687), 2009.
- [20] J Etele. Overview of wind gust modelling with application to autonomous low-level UAV control. *Mechanical and Aerospace Engineering Department, Carleton University, Ottawa, Canada*, 2006.
- [21] F Falissard, A Lerat, and J Sidès. Computation of airfoil-vortex interaction using a vorticity-preserving scheme. *AIAA Journal*, 46(7):1614–1623, 2008.
- [22] YC Fung. *An introduction to the theory of aeroelasticity*. Courier Corporation, 2002.
- [23] IE Garrick. On some reciprocal relations in the theory of nonstationary flows. *NACA Annual Report*, 24, 1938.

- [24] V Golubev, T Hollenshade, L Nguyen, and M Visbal. High-accuracy low-Re simulations of airfoil-gust and airfoil-vortex interactions. *AIAA 40th Fluid Dynamics Conference and Exhibit*, (4868), 2010.
- [25] V Golubev, T Hollenshade, L Nguyen, and M Visbal. Parametric viscous analysis of gust interaction with SD7003 airfoil. *48th AIAA Aerospace Sciences Meeting Including the New Horizons Forum and Aerospace Exposition*, (928), 2010.
- [26] V Golubev, L Nguyen, and M Visbal. High-fidelity simulations of transitional airfoil interacting with upstream vortical structure. *49th AIAA Aerospace Sciences Meeting including the New Horizons Forum and Aerospace Exposition*, (394), 2011.
- [27] RE Gordnier and MR Visbal. Impact of a vortical gust on the aerodynamics of a finite aspect-ratio wing. *45th AIAA Fluid Dynamics Conference*, (3072), 2015.
- [28] L Graftieaux, M Michard, and N Grosjean. Combining PIV, POD and vortex identification algorithms for the study of unsteady turbulent swirling flows. *Measurement Science and Technology*, 12(9):1422, 2001.
- [29] K Granlund, B Monnier, MV Ol, and D Williams. Airfoil longitudinal gust response in separated vs. attached flows. *Physics of Fluids*, 26(2):027103, 2014.
- [30] KO Granlund, MV Ol, and LP Bernal. Unsteady pitching flat plates. *Journal of Fluid Mechanics*, 733:R5, 2013.
- [31] JM Greenberg. Airfoil in sinusoidal motion in a pulsating stream. Technical Report 1326, National Advisory Committee for Aeronautics, 1947.
- [32] D Hahn, P Scholz, and R Radespiel. Vortex generation in a low speed wind tunnel and vortex interactions with a high-lift airfoil. *30th AIAA Applied Aerodynamics Conference*, (3024), 2012.
- [33] SF Harding, GS Payne, and IG Bryden. Generating controllable velocity fluctuations using twin oscillating hydrofoils: experimental validation. *Journal of Fluid Mechanics*, 750:113–123, 2014.

- [34] EAL Hufstedler and BJ McKeon. Isolated gust generation for the investigation of airfoil-gust interaction. *46th AIAA Fluid Dynamics Conference*, (4257), 2016.
- [35] R Isaacs. Airfoil Theory for Flows of Variable Velocity. *Journal of the Aeronautical Sciences*, 12(1):113–117, 1945.
- [36] R Isaacs. Airfoil Theory for Rotary Wing Aircraft. *Journal of the Aeronautical Sciences*, 13(4):218–220, 1946.
- [37] J Jeong and F Hussain. On the identification of a vortex. *Journal of Fluid Mechanics*, 285:69–94, 1995.
- [38] AR Jones and H Babinsky. Unsteady lift generation on rotating wings at low Reynolds numbers. *Journal of Aircraft*, 47(3):1013–1021, 2010.
- [39] AR Jones, A Medina, H Spooner, and K Mulleners. Characterizing a burst leading-edge vortex on a rotating flat plate wing. *Experiments in Fluids*, 57(4):1–16, 2016.
- [40] RT Jones. Operational treatment of the nonuniform-lift theory in airplane dynamics. Technical Report 667, National Advisory Committee for Aeronautics, 1938.
- [41] IM Kalkhoran and DR Wilson. Experimental investigation of the parallel vortex-airfoil interaction at transonic speeds. *AIAA Journal*, 30(8):2087–2092, 1992.
- [42] J Katz and A Plotkin. *Low-speed aerodynamics: from wing theory to panel methods*. McGraw-Hill, New York, 1991.
- [43] W Kerstens, DR Williams, J Pfeiffer, R King, and T Colonius. Closed Loop Control of a Wing’s Lift for ‘Gust’ Suppression. *5th Flow Control Conference*, pages 1–11, June 2010.
- [44] S Klein, D Hoppmann, P Scholz, and R Radespiel. High-lift airfoil interacting with a vortical disturbance: wind-tunnel measurements. *AIAA Journal*, 53(6):1681–1692, 2014.
- [45] HG Küssner. Zusammenfassender Bericht über den instationären Auftrieb von Flügeln. *Luftfahrtforschung*, 13(12):410–424, 1936.

- [46] J Langelaan. Biologically inspired flight techniques for small and micro unmanned aerial vehicles. *AIAA guidance, navigation and control conference and exhibit*, (6511), 2008.
- [47] P Mancini, F Manar, K Granlund, MV Ol, and AR Jones. Unsteady aerodynamic characteristics of a translating rigid wing at low Reynolds number. *Physics of Fluids*, 27(12):123102, 2015.
- [48] A Medina and AR Jones. Leading-edge vortex burst on a low-aspect-ratio rotating flat plate. *Physical Review Fluids*, 1(4):044501, 2016.
- [49] M Michard, L Graftieaux, L Lollini, and N Grosjean. Identification of vortical structures by a non local criterion- application to PIV measurements and DNS-LES results of turbulent rotating flows. In *Symposium on Turbulent Shear Flows, 11 th, Grenoble, France*, pages 28–25, 1997.
- [50] R Morvant, KJ Badcock, and GN Barakos. Aerofoil-vortex interaction using the compressible vorticity confinement method. *AIAA Journal*, 43(1):63–75, 2005.
- [51] B Moulin and M Karpel. Gust loads alleviation using special control surfaces. *Journal of Aircraft*, 44(1):17–25, 2007.
- [52] C Patel, HT Lee, and I Kroo. Extracting energy from atmospheric turbulence with flight tests. *Technical Soaring*, 33(4):100–108, 2009.
- [53] D Peng and JW Gregory. Vortex dynamics during blade-vortex interactions. *Physics of Fluids*, 27(5):053104, 2015.
- [54] GM Perrotta and AR Jones. Transient aerodynamics of large transverse gusts and geometrically similar maneuvers. *54th AIAA Aerospace Sciences Meeting*, (2074), 2016.
- [55] C Pitt Ford and H Babinsky. Low Reynolds number experiments on an impulsively started flat plate at high incidence. *49th AIAA Aerospace Sciences Meeting including the New Horizons Forum and Aerospace Exposition*, (475), 2011.
- [56] C Pitt Ford and H Babinsky. Impulsively started flat plate circulation. *AIAA Journal*, 52(8):1800–1802, 2014.

- [57] CW Pitt Ford and H Babinsky. Lift and the leading edge vortex. *Journal of Fluid Mechanics*, 720, 2013.
- [58] D Rival, T Prangemeier, and C Tropea. The influence of airfoil kinematics on the formation of leading-edge vortices in bio-inspired flight. *Experiments in Fluids*, 46(5):823–833, 2009.
- [59] D Rockwell. Vortex-body interactions. *Annual Review of Fluid Mechanics*, 30(1):199–229, 1998.
- [60] T Schnipper, A Andersen, and T Bohr. Vortex wakes of a flapping foil. *Journal of Fluid Mechanics*, 633:411–423, 2009.
- [61] PR Spalart. Airplane trailing vortices. *Annual Review of Fluid Mechanics*, 30(1):107–138, 1998.
- [62] C Strangfeld, H Mueller-Vahl, D Greenblatt, C Nayeri, and CO Paschereit. Airfoil subjected to high-amplitude free-stream oscillations: theory and experiments. *7th AIAA Theoretical Fluid Mechanics Conference*, (2926), 2014.
- [63] J Straus, P Renzoni, and RE Mayle. Airfoil Pressure Measurements during a Blade Vortex Interaction and a Comparison with Theory. *AIAA Journal*, 28(2):222–228, 1990.
- [64] AA Tchieu. *The development of low-order models for the study of fluid-structure interaction*. PhD thesis, California Institute of Technology, 2011.
- [65] AA Tchieu and A Leonard. A discrete-vortex model for the arbitrary motion of a thin airfoil with fluidic control. *Journal of Fluids and Structures*, 27(5):680–693, 2011.
- [66] T Theodorsen. General theory of aerodynamic instability and the mechanism of flutter. *NACA Annual Report*, 20, 1935.
- [67] W Thomson. On vortex motion. *Transactions of the Royal Society of Edinburgh*, 25(01):217–260, 1868.
- [68] MS Triantafyllou, AH Techet, and FS Hover. Review of experimental work in biomimetic foils. *IEEE Journal of Oceanic Engineering*, 29(3):585–594, 2004.

- [69] HC Tsai and T Colonius. Coriolis effect on dynamic stall in a vertical axis wind turbine. *AIAA Journal*, 54(1):216–226, 2015.
- [70] T von Kármán. Progress in the statistical theory of turbulence. *Proceedings of the National Academy of Sciences*, 34(11):530–539, 1948.
- [71] T von Kármán and WR Sears. Airfoil theory for non-uniform motion. *Journal of the Aeronautical Sciences*, 5(10):379–390, 1938.
- [72] H Wagner. Über die Entstehung des dynamischen Auftriebes von Tragflügeln. *ZAMM-Journal of Applied Mathematics and Mechanics/Zeitschrift für Angewandte Mathematik und Mechanik*, 5(1):17–35, 1925.
- [73] D Williams, W Kerstens, J Pfeiffer, R King, and T Colonius. Unsteady lift suppression with a robust closed loop controller. In *Active Flow Control II*, pages 19–30. Springer, 2010.
- [74] D Williams, W Kerstens, and V Quach. Drag-power measurements of a plunging wing in an oscillating freestream. *41st AIAA Fluid Dynamics Conference and Exhibit*, (3255), 2011.
- [75] D Williams, V Quach, W Kerstens, S Buntain, G Tadmor, C Rowley, and Tim Colonius. Low Reynolds number wing response to an oscillating freestream with and without feed forward control. *47th AIAA Aerospace Sciences Meeting Including The New Horizons Forum and Aerospace Exposition*, (143), 2009.
- [76] HT Yu, LP Bernal, and MV Ol. Effects of planform geometry and pivot axis location on the aerodynamics of pitching low aspect ratio wings. *43rd AIAA Fluid Dynamics Conference*, (2992), 2013.

Appendix A

DESCRIPTIONS OF EXPERIMENTS

A.1 Introduction

This appendix details the parameters of the experiments presented in Chapters 4 and 5, which used the equipment described in Chapter 3. The sections refer to tables of parameters which are located at the end of this appendix.

The three groups of experiments are referred to as the static airfoil (SA), pitching gust generator (PGG), and heaving gust generator (HGG) experiments.

Unless otherwise indicated, the tunnel's pump frequency was 12.50 Hz, creating a freestream velocity of 0.2 m/s. This yielded a chordwise Reynolds number of 20,000 for the airfoils. When in use, the downstream airfoil was mounted with its quarter-chord point at the midline of the tunnel. All rotations of the airfoils were about their quarter-chord points. Each row of the tables in this appendix describes the parameters of an executed experiment. All plate motions, unless otherwise noted, followed the trajectory described in Equation 2.7. Unless otherwise noted, the PIV plane was parallel to the floor, recording data around the center of the test section.

A.2 Static Airfoil (SA) Experiments

The forces in these experiments were recorded through the gantry system, sampled at timesteps of 0.005 seconds.

In each applicable experiment in this section, the PIV system captured 2048 pairs of images at 200 Hz. A Powell lens was used to expand the laser beam into a sheet for PIV. Velocity fields were computed from the raw images using LaVision DaVis 8. This was accomplished for each set of images in three steps: mean subtraction, velocity computation, and vector merging. To remove the background illumination, the average intensity of the data over time was subtracted from each image. Velocity fields were then computed from each pair of mean-subtracted images with a multi-pass scheme. The first pass used square windows of 128 by 128 pixels, overlapping each by 50%. The second pass used 32 by 32 pixel circular windows with 50% overlap. These vector fields were then stitched together appropriately to show the total field of view. Spurious values of both velocity components were removed via

median filters at each spatial point over 10 time steps.

A.2.1 Experiment SA-1

This experiment measured the unperturbed flow around the airfoil using PIV and the force balance. Baseline force measurements were recorded with no flow, to both measure the amount of vibration in the room and to compensate for the displacement of the system's center of mass due to rotation. The experiments in moving water were repeated three times. See Table A.1.

A.2.2 Experiment SA-2

Force measurements were taken of the airfoil over a range of angles of attack: at one degree increments from -10° to 10° , inclusive, and in two degree increments from 12° to 24° , inclusive. To compensate for forces due to rotation of the test apparatus, the forces on the sensor with zero flow were measured at five degree increments from -10° to 25° , inclusive. Each experiment recorded the forces for 60 seconds.

A.2.3 Experiment SA-3

Forces on the airfoil were measured with the 5 cm plate 75 cm upstream, near the side of the tunnel. The plate was fixed at either ± 19.05 cm from the midline, which is 3.8 cm from the wall. The airfoil was at one degree increments of α from -5° to 10° , inclusive. To compensate for forces due to rotation of the test apparatus, the zeros of the force sensor (with the flow stopped) were measured at five degree increments from -10° to 25° , inclusive. The forces in these experiments were recorded for 60 seconds.

A.2.4 Experiment SA-4

This experiment measured PIV 75 cm downstream of the upstream airfoil, which was at 0° or -13° . Each experiment was performed twice.

A.2.5 Experiment SA-5

This experiment measured how the fixed upstream airfoil changed the static forces on the downstream wing. The forces were measured at one degree increments of α from -5° to 15° , and with the upstream airfoil at each of -13° , 0° , and 13° . To compensate for forces due to rotation of the test apparatus, the forces on the sensor with zero flow were measured at five degree increments from -5° to 15° , inclusive. Each experiment recorded the forces for 60 seconds.

A.3 Pitching Gust Generator (PGG) Experiments

The experiments in this section were performed with the gantry system shown in Figure 3.10. The trajectory of the gantry was specified, and PIV and forces were measured, at timesteps of 0.005 seconds. In experiments with airfoil motion, the pitching time was $t_{pitch}/t_c = 1$

In each applicable experiment, the PIV system captured 2048 pairs of images at 200 Hz. A Powell lens was used to expand the laser beam into a sheet for PIV. Velocity fields were computed from the raw images using LaVision DaVis 8. This was accomplished for each set of images in three steps: mean subtraction, velocity computation, and vector merging. To remove the background illumination, the average intensity of the data over time was subtracted from each image. Velocity fields were then computed from each pair of mean-subtracted images with a multi-pass scheme. The first pass used square windows of 128 by 128 pixels, overlapping each by 50%. The second pass used 32 by 32 pixel circular windows with 50% overlap. These vector fields were then stitched together appropriately to show the total field of view. Spurious values of both velocity components were removed via median filters at each spatial point over 10 time steps.

A.3.1 Experiment PGG-1

This experiment examined the gusts created by the pitching airfoil. PIV was measured 75 cm downstream of the airfoil, as it pitched from 0° to -5° , -10° , and -13° . Each experiment was repeated five times.

A.3.2 Experiment PGG-2

These experiments measured forces on and PIV around the downstream airfoil as it interacted with gusts created by the upstream airfoil pitching from 0° to -13° , with the pitching airfoil at different y-positions. The downstream airfoil was tested at 0° , 5° , and 10° . Experiments with simultaneous PIV and force measurement were repeated five times, and experiments with only force measurement were performed an additional five times. To compensate for forces due to rotation of the test apparatus, the forces on the sensor with zero flow were measured at each angle of attack. Each experiment recorded the forces for 60 seconds. The experimental parameters are listed in Table A.2.

A.3.3 Experiment PGG-3

These experiments examined the three-dimensionality of gusts created by the pitching airfoil. The airfoils pitched from 0° to -13° . The PIV plane was 75 cm downstream of the plates, in the $x - z$ (streamwise-vertical) plane at the midline ($y=0$) of the tunnel. This experiment was repeated five times.

A.4 Heaving Gust Generator (HGG) Experiments

Experiments HGG-1, HGG-2, and HGG-3 were conducted using the ball screw apparatus shown in Figure 3.9. In these, the acceleration time was 0.37 seconds. A cylindrical lens was used to expand the laser beam into a sheet for PIV. LaVision DaVis 7 was used to extract velocity fields from the raw images.

The rest of the experiments in this section were performed with the gantry system shown in Figure 3.10. The trajectory of the gantry was specified, and PIV and forces were measured, at timesteps of 0.005 seconds. Unless otherwise noted, in experiments with plate motion the acceleration time was $t_{accel} = t_{cp}/2$.

With the gantry system, the PIV system captured 2048 pairs of images at 200 Hz. A Powell lens was used to expand the laser beam into a sheet for PIV. Velocity fields were computed from the raw images using LaVision DaVis 8. This was accomplished for each set of images in three steps: mean subtraction, velocity computation, and vector merging. To remove the background illumination, the average intensity of the data over time was subtracted from each image. Velocity fields were then computed from each pair of mean-subtracted images with a multi-pass scheme. The first pass used square windows of 128 by 128 pixels, overlapping each by 50%. The second pass used 32 by 32 pixel circular windows with 50% overlap. These vector fields were then stitched together appropriately to show the total field of view. Spurious values of both velocity components were removed via median filters at each spatial point over 10 time steps. The other experiments used the gantry system shown in Figure 3.10. In these, a Powell lens was used to illuminate the flow for PIV.

A.4.1 Experiment HGG-1

This initial investigation of the heaving plate varied the freestream velocity U , the dimensionless heaving speed S , and the initial direction of travel in order to see their effects. The 10 cm plate was moved to the midline of the tunnel ($y = 0$) from an initial distance from the wall of 1.3 cm, which is a distance of $h = 21.6$ cm. The acceleration time was $0.72 t_{cp}$ with the fastest freestream. PIV was recorded around

the heaving plate at 250 Hz to capture 1024 images per camera. Velocity fields were extracted using two passes of 32 by 32 pixel windows with 50% overlap. The velocity fields from both cameras were then merged to provide the full field of view. This investigation used the apparatus shown in Figure 3.9a. The details are listed in Table A.3.

A.4.2 Experiment HGG-2

The effects of varying the heaving speed and distance were examined using PIV around the 10 cm heaving plate. The initial and final position of the plate was 1.3 cm from the wall. The plate acceleration time was $0.72 t_{cp}$. PIV measurements were taken at 250 Hz, capturing 1024 images per camera. The velocity fields were extracted using 2 passes of 32 by 32 pixel windows with 50% overlap. The velocity fields from both cameras were then merged to provide the larger field of view. As the plate was illuminated from one side, the average velocity fields from both directions of motion were combined to approximate the flow around both sides of the plate. This investigation used the apparatus shown in Figure 3.9a. Table A.4 provides the details of each experiment.

A.4.3 Experiment HGG-3

The ball screw apparatus was used to generate gusts that were measured using PIV at 75 cm downstream of the trailing edge of the plate, varying the heaving distance, speed, and using both plates. The initial and final position of the plate was 1.5 cm from the wall. PIV measurements were taken at 250 Hz, capturing 1024 images per camera. The velocity fields were extracted using 2 passes of 32 by 32 pixel windows with 75% overlap. The acceleration time was $0.72 t_{cp}$ for the 10 cm plate, and double that for the 5 cm plate. This investigation used the apparatus shown in Figure 3.9b. Table A.5 provides the details of each experiment.

A.4.4 Experiment HGG-4

This experiment examined the wake generated by the plates having moved across the width of the tunnel at different speeds. The plates followed half of the trajectory in Equation 2.7, but stopped after reaching the peak position at the opposite side of the tunnel. The plate was initially 3.8 cm from the edge of the tunnel and it moved to a symmetric position on the opposite side, yielding a total heaving distance of 38.1 cm. PIV was measured at 75 cm downstream of the heaving plate. The different combinations of plate length, heaving speed, and heaving distance are listed in Table

A.6.

A.4.5 Experiment HGG-5

These experiments examined the effect of the gust generating plates on the flow in the tunnel, using PIV, with the plate fixed 3.8 cm from the side of the tunnel. Both lengths of plates were used, and on either side of the tunnel. PIV was measured 75 cm downstream of the plates, around the midline of the tunnel.

A.4.6 Experiment HGG-6

These experiments characterized, using PIV, the vortical gusts created by the 5 cm heaving plate, for a range of heaving speeds and distances. The initial position of the plate was 3.8 cm from the edge of the tunnel. PIV was measured 75 cm downstream of the plate. The different heaving distances and speeds are listed in Table A.7.

A.4.7 Experiment HGG-7

These experiments measured forces on the downstream airfoil due to the 5 cm plate heaving from one side of the tunnel to the other, without returning. Different airfoil angles of attack, plate heaving speeds, and initial directions of motion were tested. These experiments followed half of the trajectory in Equation 2.7, stopping after reaching the peak position at the opposite side of the tunnel. The plate was initially 3.8 cm from the edge of the tunnel, and it moved to a symmetric position on the opposite side, yielding a total heaving distance of 38.1 cm. The experimental parameters are listed in Table A.8.

A.4.8 Experiment HGG-8

These experiments measured the forces on the downstream airfoil due to gusts from the 5 cm heaving plate for a range of heaving distances, both initial directions of motion, and multiple airfoil angles of attack. The dimensionless heaving speed, S , was fixed at 0.1. The parameters of each experiment are listed in Table A.9.

A.4.9 Experiment HGG-9

These experiments measured the forces on the downstream airfoil due to stronger gusts from the 5 cm heaving plate, for a range of heaving distances, both initial directions of motion, and multiple airfoil angles of attack. The dimensionless heaving speed, S , was fixed at 0.25. The experimental parameters are listed in Table A.10.

A.4.10 Experiment HGG-10

These experiments measured the forces on and PIV around the downstream airfoil, with gusts from the 5 cm heaving plate, for a range of heaving distances, both initial directions of motion, and multiple airfoil angles of attack. The dimensionless heaving speed, S , was fixed at 0.1. Simultaneous forces and PIV were recorded over five repetitions of each experiment. Forces alone were measured over five additional repetitions. The parameters of each experiment are listed in Table A.11.

A.4.11 Experiment HGG-11

These experiments examined the three-dimensionality of gusts created by the heaving plates. The initial position of the plate was $h_0 = 19.05$ cm from the midline of the tunnel, which was 3.8 cm from the edge. It changed directions at the midline of the tunnel, $y = 0$. Two heaving speeds were tested with both plates: $S = 0.1$ and $S = 0.25$. The PIV plane was 75 cm downstream of the plates, in the $x - z$ (streamwise-vertical) plane at the midline of the tunnel. Each experiment was repeated five times.

α [degree]	f_{pump} [Hz]	$N_{repetitions}$	PIV?
0	0.00	1	No
5	0.00	1	No
10	0.00	1	No
0	12.50	3	Yes
5	12.50	3	Yes
10	12.50	3	Yes

Table A.1: Parameters of Experiment SA-1.

α [°]	$\alpha_{upstream,final}$ [°]	$y_{upstream}$ [cm]
0	13	-10.0
0	13	-5.0
0	13	0.0
0	13	5.0
0	13	10.0
5	-13	-10.0
5	-13	-5.0
5	-13	0.0
5	-13	5.0
5	-13	10.0
5	13	-10.0
5	13	-5.0
5	13	0.0
5	13	5.0
5	13	10.0
10	-13	-10.0
10	-13	-5.0
10	-13	0.0
10	-13	5.0
10	-13	10.0
10	13	-10.0
10	13	-5.0
10	13	0.0
10	13	5.0
10	13	10.0

Table A.2: Parameters of Experiment PGG-2.

f_{pump} [Hz]	U [cm/s]	S
5.00	7.9	0.1
5.00	7.9	0.5
5.00	7.9	1.0
8.75	13.5	0.1
8.75	13.5	0.5
8.75	13.5	1.0
12.5	19.5	0.1
12.5	19.5	0.5
12.5	19.5	1.0

Table A.3: Experiment HGG-1. Parameters for exploring effects of Re and S . Experiments were performed for both initial directions of motion, and repeated twice.

S	h [cm]	y_{peak} [cm]
0.09	16.5	-5.08
0.36	16.5	-5.08
1.0	16.5	-5.08
0.09	19.1	-2.54
0.36	19.1	-2.54
1	19.1	-2.54
0.09	21.6	0.0
0.36	21.6	0.0
1.0	21.6	0.0
0.09	24.1	2.54
0.36	24.1	2.54
1.0	24.1	2.54
0.09	26.7	5.08
0.36	26.7	5.08
1.0	26.7	5.08

Table A.4: Experiment HGG-2. Parameters for exploring effects of S and H . Experiments were repeated three times.

S	h [cm]	y_{peak} [cm]
0.09	13.7	-7.62
0.18	13.7	-7.62
0.27	13.7	-7.62
0.09	18.8	-2.54
0.18	18.8	-2.54
0.27	18.8	-2.54
0.09	23.9	2.54
0.18	23.9	2.54
0.27	23.9	2.54

Table A.5: Experiment HGG-3. Parameters for exploring effects of S , H , and c_p . Experiments were repeated five times for each set of parameters, including use of both the 5 cm and 10 cm plates.

c_{plate} [cm]	S	H	T
5.08	0.1	7.5	75
5.08	0.2	7.5	37.5
5.08	0.3	7.5	25
5.08	0.4	7.5	18.75
10.16	0.1	3.75	37.5
10.16	0.2	3.75	18.75
10.16	0.3	3.75	12.5
10.16	0.4	3.75	9.375

Table A.6: Parameters of Experiment HGG-4. Each set of parameters was repeated five times.

S	H	T	y_{peak} [cm]
0.1	5.75	57.5	-10.16
0.1	4.75	47.5	-5.08
0.1	4.25	42.5	-2.54
0.1	3.75	37.5	0.0
0.1	3.25	32.5	2.54
0.1	2.75	27.5	5.08
0.1	1.75	17.5	10.16
0.25	5.75	23	10.16
0.25	4.75	19.0	-5.08
0.25	4.25	17.0	-2.54
0.25	3.75	15.0	0.0
0.25	3.25	13.0	2.54
0.25	2.75	11.0	5.08
0.25	1.75	7	10.16

Table A.7: Parameters of Experiment HGG-6. Each set of parameters was repeated five times.

α [°]	S	T	Direction
0	0.1	75	+
0	0.1	75	-
0	0.25	30	+
0	0.25	30	-
5	0.1	75	+
5	0.1	75	-
5	0.25	30	+
5	0.25	30	-
10	0.1	75	+
10	0.1	75	-
10	0.25	30	+
10	0.25	30	-

Table A.8: Parameters of Experiment HGG-7. ‘Direction’ refers to the initial direction of motion of the plate. Each set of parameters was repeated 10 times.

α [°]	T	H	y_{peak} [cm]	Direction
0	57.19	-5.72	-10.0	-
0	47.34	-4.73	-5.0	-
0	37.5	-3.75	0.0	-
0	27.66	-2.77	5.0	-
0	17.81	-1.78	10.0	-
5	17.81	1.78	-10.0	+
5	27.66	2.77	-5.0	+
5	37.5	3.75	0.0	+
5	47.34	4.73	5.0	+
5	57.19	5.72	10.0	+
5	57.19	-5.72	-10.0	-
5	47.34	-4.73	-5.0	-
5	37.5	-3.75	0.0	-
5	27.66	-2.77	5.0	-
5	17.81	-1.78	10.0	-
10	17.81	1.78	-10.0	+
10	27.66	2.77	-5.0	+
10	37.5	3.75	0.0	+
10	47.34	4.73	5.0	+
10	57.19	5.72	10.0	+
10	57.19	-5.72	-10.0	-
10	47.34	-4.73	-5.0	-
10	37.5	-3.75	0.0	-
10	27.66	-2.77	5.0	-
10	17.81	-1.78	10.0	-

Table A.9: Parameters of Experiment HGG-8. ‘Direction’ refers to the initial direction of motion of the plate. In all cases, $S=0.1$. Each set of parameters was repeated ten times.

α [°]	T	H	$y_{peak}[cm]$	Direction
5	17.81	1.78	-10.0	+
5	27.66	2.77	-5.0	+
5	37.5	3.75	0.0	+
5	47.34	4.73	5.0	+
5	57.19	5.72	10.0	+
5	57.19	-5.72	-10.0	-
5	47.34	-4.73	-5.0	-
5	37.5	-3.75	0.0	-
5	27.66	-2.77	5.0	-
5	17.81	-1.78	10.0	-

Table A.10: Parameters of Experiment HGG-9. ‘Direction’ refers to the initial direction of motion of the plate. In all cases, $S=0.25$. Each set of parameters was repeated ten times.

α [°]	T	H	y_{peak} [cm]	Direction
0	57.19	-29.05	-10.0	-
0	47.34	-24.05	-5.0	-
0	37.5	-19.05	0.0	-
0	27.66	-14.05	5.0	-
0	17.81	-9.05	10.0	-
5	17.81	9.05	-10.0	-
5	27.66	14.05	-5.0	-
5	37.5	19.05	0.0	-
5	47.34	24.05	5.0	-
5	57.19	29.05	10.0	-
5	57.19	-29.05	-10.0	+
5	47.34	-24.05	-5.0	+
5	37.5	-19.05	0.0	+
5	27.66	-14.05	5.0	+
5	17.81	-9.05	10.0	+
10	17.81	9.05	-10.0	-
10	27.66	14.05	-5.0	-
10	37.5	19.05	0.0	-
10	47.34	24.05	5.0	-
10	57.19	29.05	10.0	-
10	57.19	-29.05	-10.0	+
10	47.34	-24.05	-5.0	+
10	37.5	-19.05	0.0	+
10	27.66	-14.05	5.0	+
10	17.81	-9.05	10.0	+

Table A.11: Parameters of Experiment HGG-10. Simultaneous forces and PIV were recorded over five repetitions of each experiment. Forces alone were measured over five additional repetitions. In all cases, $S = 0.1$. ‘Direction’ refers to the initial direction of motion of the plate.

Appendix B

DERIVATION OF EXTENDED TCHIEU-LEONARD UNSTEADY AIRFOIL MODEL

B.1 Introduction

The Tcheiu-Leonard (TL) unsteady airfoil model allows for pitching and heaving a flat plate while it sheds vortices. Chapter 2.3 describes its use in this thesis. This appendix details the derivation of an extension that allows for the inclusion of an external vortex that convects past the airfoil. The appendix has three sections. The first describes the conformal mapping technique used in the derivation. The second details the derivation of the vorticity distribution on the plate. The third uses that distribution to modify the TL method's lift and pitching moment.

The vorticity distribution on the plate is composed of three distributions added together, which are due to the angle of attack, the rotation of the plate, and the wake vortices. Each of these distributions have zero circulation at the trailing edge, and so enforce the Kutta condition separately and in combination. The novel extension allows for a more general use of external vortices, rather than limiting them to the x -axis behind the trailing edge of the plate.

B.2 Conformal Mapping

Conformal mapping is used to transform complex potential flow around a cylinder to flow around a flat plate. In the untransformed frame, coordinates are denoted by a subscript 0. The transformed frame has no such subscript. A point in the untransformed frame is $z_0 = x_0 + iy_0 = r_0 e^{i\theta_0}$. In this frame, the aerodynamic body is a two-dimensional cylinder defined by its diameter c_0 as the circle $z_0 = c_0 e^{i\theta_0} / 2$. The complex potentials in this frame are denoted by F_0 , and the complex velocities by

$$W_0 = \frac{dF_0}{dz_0}. \quad (\text{B.1})$$

The coordinates of the transformed frame are $z = x + iy = r e^{i\theta}$. The transformation between these is

$$z = z_0 + \frac{(c_0/2)^2}{z_0}. \quad (\text{B.2})$$

This turns the cylinder of diameter c_0 to a plate of length $c = 2c_0$. The analysis also requires inverting that transformation, which is possible with

$$z_0 = \begin{cases} \frac{1}{2} \left(z + \sqrt{z^2 - c_0^2} \right), & -\pi/2 < \theta \leq \pi/2, \\ \frac{1}{2} \left(z - \sqrt{z^2 - c_0^2} \right), & \text{otherwise.} \end{cases} \quad (\text{B.3})$$

The complex velocity field around the flat plate can be computed as

$$W = \frac{dF_0}{dz_0} / \frac{dz}{dz_0}. \quad (\text{B.4})$$

The vorticity on the plate, $\gamma(x)$, is needed for computation of different moments used in the Tchieu-Leonard model. The vorticity on the plate is computed from the tangential velocity jump across it:

$$\gamma(x) = u(x, y = 0^-) - u(x, y = 0^+). \quad (\text{B.5})$$

B.3 Vorticity Distributions

B.3.1 Lifting Cylinder at Angle α

A cylinder of diameter c_0 , in a freestream with speed U and angle α has complex potential

$$F_{0,lift} = U \left(z_0 e^{-i\alpha} + \frac{c_0^2}{4z_0 e^{-i\alpha}} + \frac{\Gamma_{KC,lift}}{2\pi i} \log(z_0) \right). \quad (\text{B.6})$$

This has a streamline at $r_0 = c_0/2$, so there is no flow through the cylinder. To ensure zero flow at the trailing edge, the Kutta Condition, the cylinder has an additional internal circulation of

$$\Gamma_{KC,lift} = -2c_0\pi U \sin(\alpha). \quad (\text{B.7})$$

Once transformed into a flat plate, the velocity field is simply

$$W_{lift} = U e^{-i\alpha} \left(\frac{c_0 e^{2i\alpha} + 2z_0}{c_0 + 2z_0} \right). \quad (\text{B.8})$$

The circulation on the plate can be found by setting $z_0 = c_0 e^{i\theta_0}/2$, applying Equation B.5, and using $\theta_0 = \arccos\left(\frac{2x}{c}\right)$. This yields

$$\begin{aligned} \gamma_{lift} &= -2U \sin(\alpha) \tan\left(\frac{\theta_0}{2}\right), \\ &= -2U \sin(\alpha) \sqrt{\frac{c_0 - x}{c_0 + x}}. \end{aligned} \quad (\text{B.9})$$

The moments of the vorticity are computed as follows:

$$\begin{aligned}\mu_{lift,0} &= \int_{c/2}^{-c/2} \gamma(x) dx, \\ &= \Gamma_{KC,lift},\end{aligned}\tag{B.10}$$

$$\begin{aligned}\mu_{lift,1} &= \int_{c/2}^{-c/2} \gamma(x)x dx, \\ &= -\frac{c_0}{2}\Gamma_{KC,lift},\end{aligned}\tag{B.11}$$

$$\begin{aligned}\mu_{lift,2} &= \int_{c/2}^{-c/2} \gamma(x)x^2 dx. \\ &= \frac{c_0^2}{2}\Gamma_{KC,lift}.\end{aligned}\tag{B.12}$$

In Tchieu's model, the small-angle approximation was used to change $\sin(\alpha) \approx \alpha$. Also, the downwash due to heaving and pitching was included. As a result, the circulation in his model was

$$\Gamma_{KC,lift,Tchieu} = 2\pi c_0 (\dot{y}_{plate} - a\dot{\alpha} - U\alpha).\tag{B.13}$$

B.3.2 Rotating flat plate

For a flat rotating about its midpoint with angular velocity $\dot{\alpha}$, the circulation on the surface is

$$\gamma_{rotate}(x) = -2\dot{\alpha}\sqrt{\left(\frac{c_0}{2}\right)^2 - x^2}.\tag{B.14}$$

From this, the moments are

$$\begin{aligned}\mu_{rotate,0} &= \int_{c/2}^{-c/2} \gamma_{rotate}(x) dx, \\ &= -c_0^2\pi\dot{\alpha}, \\ &= \Gamma_{rotate},\end{aligned}\tag{B.15}$$

$$\begin{aligned}\mu_{rotate,1} &= \int_{c/2}^{-c/2} \gamma_{rotate}(x)x dx, \\ &= 0,\end{aligned}\tag{B.16}$$

$$\begin{aligned}\mu_{rotate,2} &= \int_{c/2}^{-c/2} \gamma_{rotate}(x)x^2 dx, \\ &= \frac{c_0^2}{4}\Gamma_{rotate}.\end{aligned}\tag{B.17}$$

B.3.3 External vortex

In Tchieu's analysis, the external vortices were in the wake, which restricted to lie on the half-line behind the plate. The following analysis describes the response of the plate to external vortices that are not restricted to the wake. The position of the external vortex is $z_{0v} = r_{0v}e^{i\theta_{0v}}$ in the original frame and z_v in the transformed coordinates. The vortex has circulation Γ_v . As this is an external vortex, $r_{0v} > c_0/2$.

The complex potential of a cylinder with an external vortex requires three parts: the external vortex, an image vortex within the cylinder, and a central vortex to enforce the Kutta condition. Together, these yield

$$F_{vortex} = \frac{\Gamma_v}{2\pi i} \left(\log(z_0 - r_{0v}e^{i\theta_{0v}}) - \log\left(z_0 - \frac{c_0^2}{4r_{0v}}e^{i\theta_{0v}}\right) \right) + \frac{\Gamma_{KC,vortex}}{2\pi i} \log(z_0),\tag{B.18}$$

with

$$\Gamma_{KC,vortex} = \frac{\Gamma_v(r_{0v}^2 - (c_0/2)^2)}{(c_0/2)^2 + r_{0v}^2 - c_0r_{0v}\cos(\theta_{0v})}.\tag{B.19}$$

The vorticity on the plate is

$$\gamma_{vortex}(\theta_0) = -\frac{f_1f_2}{f_3f_4},\tag{B.20}$$

using the following functions:

$$f_1 = 2\Gamma_v e^{\frac{1}{2}i(5\theta_0+4\theta_{0v})} \left(\frac{c_0}{2} - r_{0v}\right) r_{0v} \left(\frac{c_0}{2} + r_{0v}\right) \sin\left(\frac{\theta_0}{2}\right), \quad (\text{B.21a})$$

$$f_2 = -c_0 r_{0v} \cos(\theta_0) + \left(\frac{c_0^2}{2} + r_{0v}^2\right) \cos(\theta_{0v}) - c_0 r_{0v} \sin(\theta_{0v})^2, \quad (\text{B.21b})$$

$$f_3 = \left(1 + e^{i\theta_0}\right) \pi \left(-\frac{c_0}{2} e^{i\theta_{0v}} + e^{i\theta_0} r_{0v}\right) \left(\frac{c_0}{2} e^{i\theta_0} - e^{i\theta_{0v}} r_{0v}\right) \left(-\frac{c_0}{2} + e^{i(\theta_0+\theta_{0v})} r_{0v}\right), \quad (\text{B.21c})$$

$$f_4 = \left(\left(\frac{c_0}{2}\right)^2 + r_{0v}^2 - c_0 r_{0v} \cos(\theta_{0v})\right) \left(-r_{0v} + \frac{c_0}{2} \cos(\theta_0 + \theta_{0v}) + i \frac{c_0}{2} \sin(\theta_0 + \theta_{0v})\right). \quad (\text{B.21d})$$

The moments are more easily computed using the residue calculus in the complex plane. This requires the use of $W_{0,vortex}$, the complex velocity around the untransformed cylinder. The n^{th} moment is

$$\begin{aligned} \mu_{vortex,n} &= \int_{c/2}^{-c/2} \gamma_{vortex}(x) x^n dx, \\ &= \oint_{r_0=c_0/2} W_{0,vortex} \left(\frac{c}{2} \cos(\theta_0)\right)^2 dz_0. \end{aligned} \quad (\text{B.22})$$

Unfortunately, $\cos(\theta_0)$ is not usefully defined in this context. However, if the contour uses $c_0 = 2$, then $\cos(\theta_0) = (z_0 + 1/z_0)/2$ on that contour. The result can then be computed along that contour. The zeroth moment does not require such mathematical gymnastics, and is

$$\begin{aligned} \mu_{vortex,0} &= \int_{c/2}^{-c/2} \gamma_{vortex}(x) dx, \\ &= \Gamma_{KC,vortex} - \Gamma_v. \end{aligned} \quad (\text{B.23})$$

The first and second moments are computed with $c_0 = 2$ as:

$$\mu_{vortex,1} = -\Gamma_v \frac{2 \cos(\theta_{0v})}{r_{0v}}, \quad (\text{B.24})$$

$$\mu_{vortex,2} = 2\Gamma_{KC,vortex} - \frac{2\Gamma_v}{r_{0v}^2} \left(r_{0v}^2 + \cos(2\theta_{0v})\right). \quad (\text{B.25})$$

Via dimensional analysis and comparison to numerical integration, these can be amended to include variable c_0 :

$$\mu_{vortex,1} = -\Gamma_v \frac{c_0^2 \cos(\theta_{0v})}{2r_{0v}}, \quad (\text{B.26})$$

$$\mu_{vortex,2} = \frac{c_0^2}{2} \Gamma_{KC,vortex} - \frac{c_0^2 \Gamma_v}{2r_{0v}^2} \left(r_{0v}^2 + \left(\frac{c_0}{2} \right)^2 \cos(2\theta_{0v}) \right). \quad (\text{B.27})$$

B.3.3.1 Wake vortices

These relations simplify substantially when the vortices are forced to remain at $y = 0$ behind the trailing edge of the plate. Parameterizing the vortex's location in terms of x , we find:

$$\mu_{wake,0} = \Gamma_v \left(\sqrt{\frac{x_v + c_0}{x_v - c_0}} - 1 \right), \quad (\text{B.28})$$

$$\mu_{wake,1} = \Gamma_v \left(-x_v + \sqrt{x_v^2 - c_0^2} \right), \quad (\text{B.29})$$

$$\mu_{wake,2} = \Gamma_v \left(\left(x^2 - c_0 x + \frac{c_0^2}{2} \right) \sqrt{\frac{x_v + c_0}{x_v - c_0}} - x^2 \right). \quad (\text{B.30})$$

These recover Equations 2.6 and the relevant portion of Equation 2.20 in Tchieu's thesis.

B.4 Review and Extension of the TL model

Since potential theory is linear, this extension of the TL model requires the additive amendment of three terms: the bound circulation of the plate, the time-varying lift, and the time-varying pitching moment. The extended version of these terms is denoted by a subscript $()_{ext}$, and Tchieu's original values lack such a subscript.

B.4.1 Lift on plate

To compute the lift in the original model:

$$I_y = -\rho \left(\int_{-c/2}^{c/2} x \gamma(x) dx + \sum_{j=1}^N \Gamma_j x_j \right), \quad (\text{B.31})$$

$$L = -\frac{dI_y}{dt}. \quad (\text{B.32})$$

Combining our nomenclatures, Tchieu defines

$$\Gamma_0 = \mu_{lift,0} + \mu_{rotate,0}. \quad (\text{B.33})$$

Extending Tchieu's lift model with the general external vortices requires two changes: his Γ_0 must be amended to include the static circulation due to the passing vortex, and the y -impulse must include $\mu_{vortex,1}$. Updating Γ_0 is a simple matter:

$$\Gamma_{0,ext} = \Gamma_0 + \mu_{vortex,0}. \quad (\text{B.34})$$

The extended lift, L_{ext} , is found to have an additional term, L_v , from the modified impulse:

$$\begin{aligned} L_{ext} &= L + L_v, \\ &= L + \rho \frac{d}{dt} (\mu_{vortex,1}). \end{aligned} \quad (\text{B.35})$$

The vortex motion assumptions for the wake vortices are also applied to the general external vortex. These assumptions are that the vortex travels only in the $+x$ direction at speed U , and that its circulation does not change over time.

$$L_v = \frac{c_0^2 \rho \Gamma_v}{2r_{0v}^2} \left(\cos(\theta_{0v}) \frac{dr_{0v}}{dt} + r_{0v} \sin(\theta_{0v}) \frac{d\theta_{0v}}{dt} \right). \quad (\text{B.36})$$

Unfortunately, this equation uses the position of the vortex in terms of the original coordinate system, but the vortices move in the transformed coordinates. The time derivatives of the vortex's position can then be computed from Equation B.3, and the chain rule used to find the necessary derivatives. These do not lead to a simple result for L_v , but only require several lines of code to include them in the model.

B.4.2 Moment on plate

The pitching moment on the plate is also computed from the moments of vorticity.

$$\mathcal{A}(s) = -\frac{\rho}{2} \left(\int_{-c/2}^{c/2} (x+s)^2 \gamma(x) dx + \sum_{j=1}^N \Gamma_j (x_j + s)^2 \right), \quad (\text{B.37})$$

$$\begin{aligned}
M(a) &= -\frac{d\mathcal{A}(s)}{dt}, \\
&= \frac{\rho}{2} \frac{d}{dt} \left(\int_{-c/2}^{c/2} x^2 \gamma(x) dx + \sum_{j=1}^N \Gamma_j x_j^2 \right) + UI_y + aL.
\end{aligned} \tag{B.38}$$

This requires an additional term to Tchieu's Equation 2.25:

$$\begin{aligned}
M_{ext}(a) &= M + M_v, \\
&= M + \frac{\rho}{2} \frac{d}{dt} \left(\int_{-c/2}^{c/2} \left(x^2 - \frac{c^2}{8} \right) \gamma_{vortex}(x) dx \right) - \rho U \int_{-c/2}^{c/2} x \gamma_{vortex}(x) dx, \\
&= M + \frac{\rho}{2} \frac{d}{dt} \left(\mu_{vortex,2} - \frac{c^2}{8} \mu_{vortex,0} \right) - \rho U \mu_{vortex,1}.
\end{aligned} \tag{B.39}$$

Additionally, the L in Equation B.38 must be replaced with L_{ext} . The additional dimensionless moment is then

$$\begin{aligned}
C_{M,v} &= \frac{-2M_v}{\rho U^2 c^2}, \\
&= -\frac{\Gamma_v}{4U r_{0v}} \left(\cos(\theta_{0v}) + \frac{c_0^2}{4U} \left(\frac{\cos(2\theta_{0v})}{r_{0v}^2} \frac{dr_{0v}}{dt} + \frac{\sin(2\theta_{0v})}{r_{0v}} \frac{d\theta_{0v}}{dt} \right) \right).
\end{aligned} \tag{B.40}$$

The derivatives which were computed for the lift are also used here.

Appendix C

ADDITIONAL FIGURES

The following text describes the figures which are at the end of this appendix. These figures are intended to further support the earlier chapters.

C.1 Simulations

Figures C.1 - C.3 show the lift forces from the simulated vortex interaction over a range of parameters. Each row represents simulations with a different vortex strength, Γ_v . Each column used a different incoming vortex height, y_v . The red lines are the wakeless simulation, blue lines are the semi-analytic estimate that included the Wagner function, and black lines are the full simulation. The parenthetical numbers are $(\Gamma_v/(Uc), y_v/c)$ in each panel.

C.2 Heaving plate

Figure C.4 is a sequence of more snapshots of the heaving plate at varying S and Re_c , a subset of which was shown in Figure 4.16. These show the flow $0.1t_c$ before the change in direction, $0.25t_c$ after, and $1.0t_c$ after. This encompasses the release of the primary vortices.

Figures C.5 and C.6 show the position of the strongest identified vortices in each frame of the data, plotted against time. The first five rows represent the first through fifth repetitions of each experiment. The sixth row represents the result from the average flow field of those repetitions. Each column represents a different S . The size of each point is proportional to its absolute circulation. Red points represent positive circulation and blue, negative. The primary vortex is visible as the dominant blue diagonal in the center of most of the plots. Its absence from the slowest experiment means that the vortex was weak, compared to the surrounding flow, and not always identified.

C.3 Forces on static airfoil

Figure C.7 shows the full set of forces measured on the airfoil, in contrast to the subset in Figure 5.3.

C.4 Interaction with pitching airfoil gusts

Figures C.8-C.10 display the drag, lift, and moment coefficients from the airfoil-gust interactions due to the pitching airfoil, at different angles of attack. Time has been shifted such that the estimated gust impact is at $t = 0$. The envelopes of these forces are shown in Figures C.11 - C.13.

C.5 Interaction with heaving plate gusts

Figures C.14-C.16 display the drag, lift, and moment coefficients from the airfoil-gust interactions due to the heaving plate with $S = 0.1$, at different angles of attack. Time has been shifted such that the estimated gust impact is at $t = 0$. Experiments were performed at three angles of attack for $S = 0.1$, but only one for $S = 0.25$. The envelopes of these forces are shown in Figures C.17 - C.19.

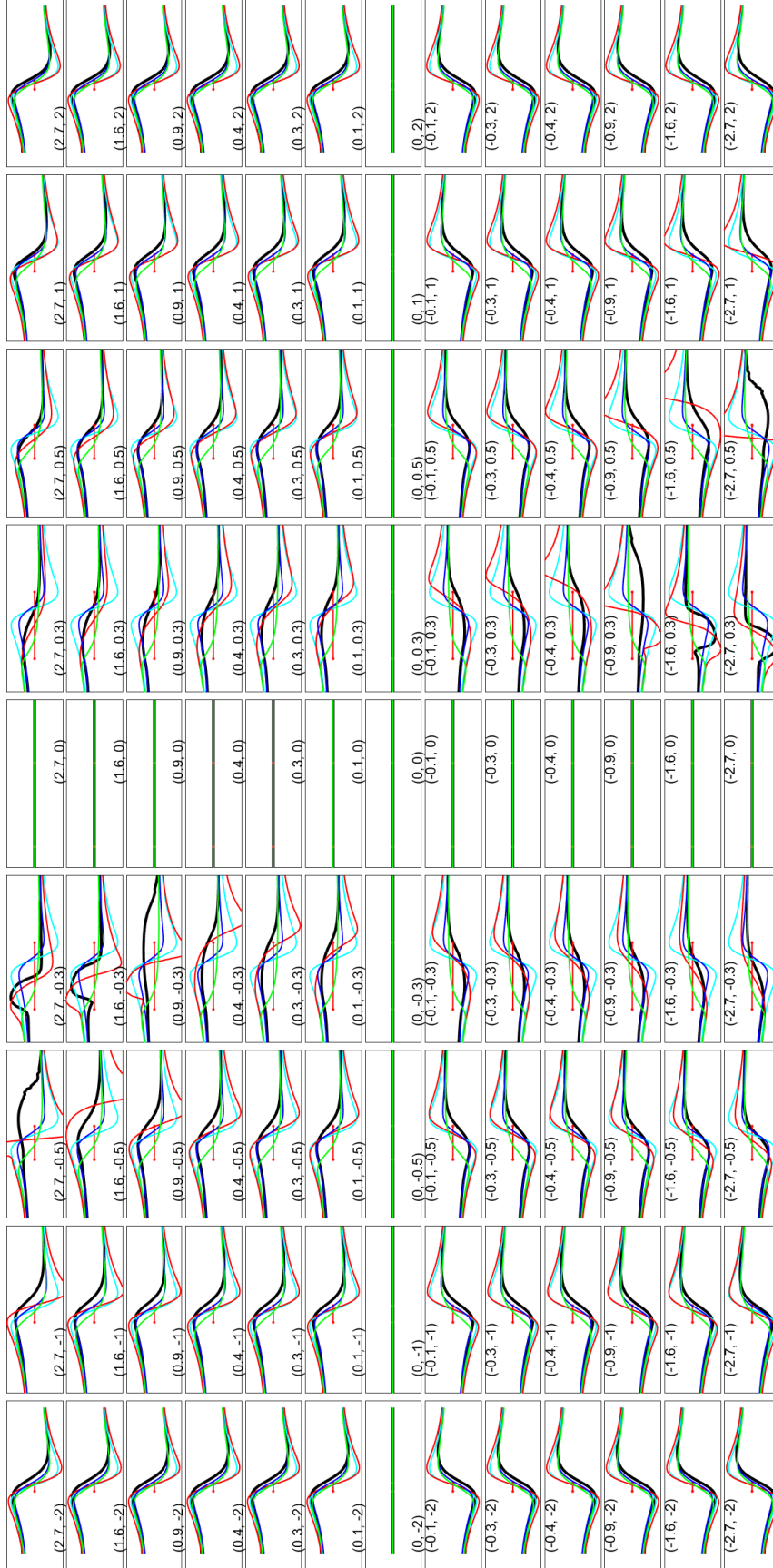


Figure C.1: Plots of the simulated variation in $C_L(t)$ for $\alpha = 0^\circ$, normalized by the magnitude of the steady thin airfoil theory peak $C_{L,0}$. The cyan line is the quasi-steady thin airfoil theory, blue is Wagner thin airfoil theory, red is the unsteady panel method, and black is the extended Tchieu-Leonard model. The numbers in each frame are $(\Gamma_v/(Uc), y_v/c)$

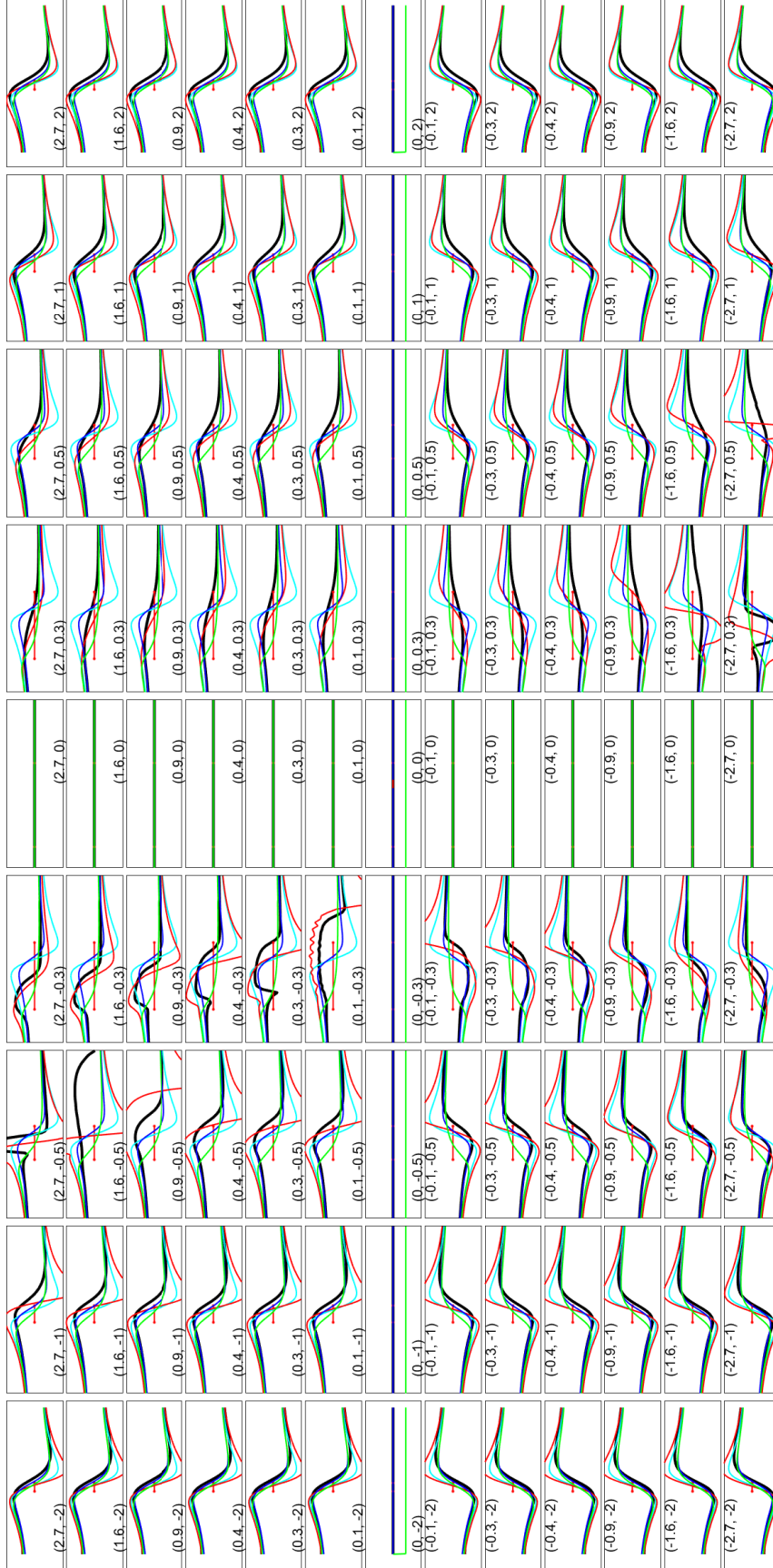


Figure C.2: Plots of the simulated variation in $C_L(t)$ for $\alpha = 5^\circ$, normalized by the magnitude of the steady thin airfoil theory peak $C_{L,0}$. The cyan line is the quasi-steady thin airfoil theory, blue is Wagner thin airfoil theory, red is the extended Tchieu-Leonard model, and black is the unsteady panel method. The numbers in each frame are $(\Gamma_v / (Uc), y_v / c)$

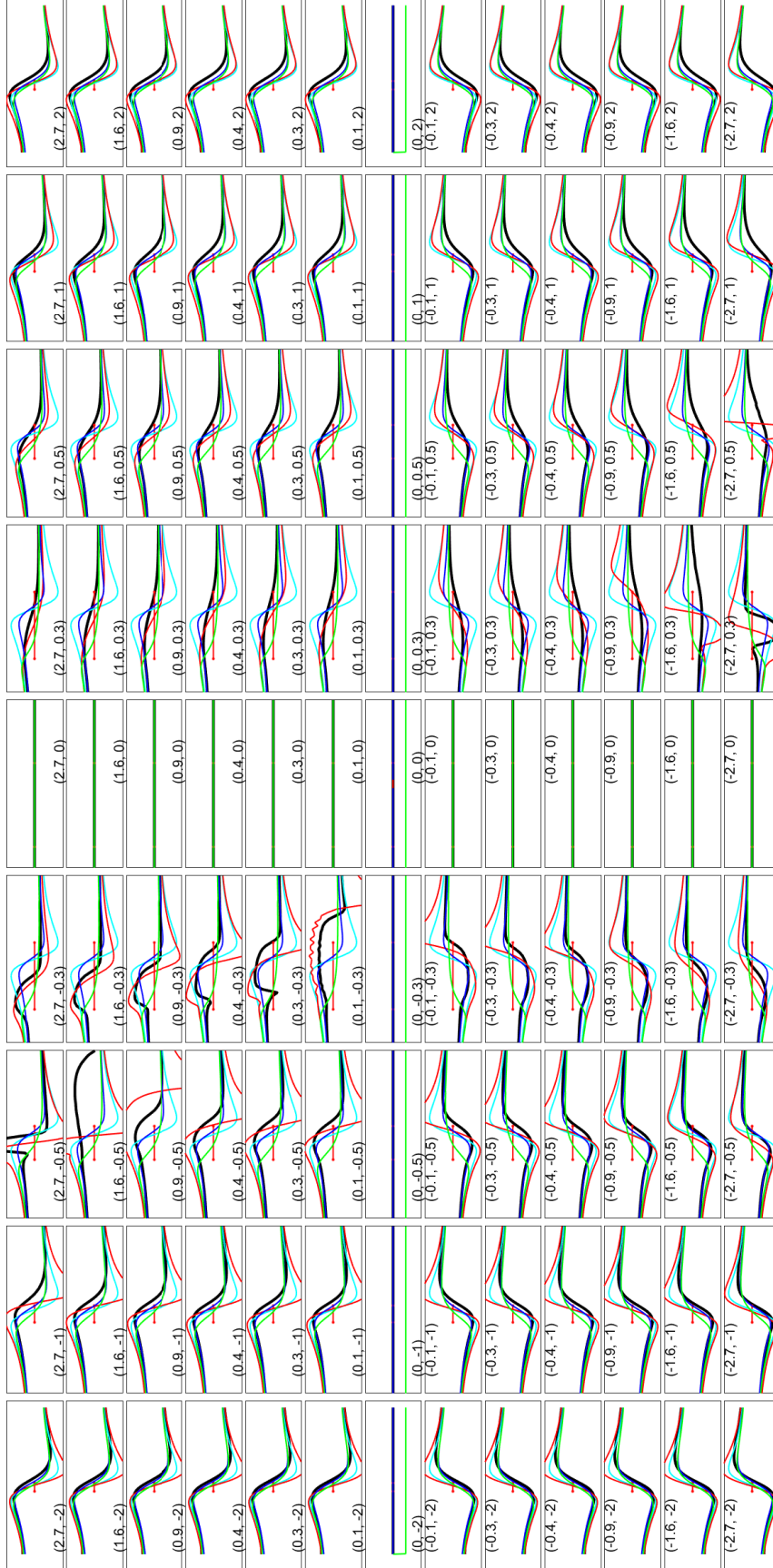
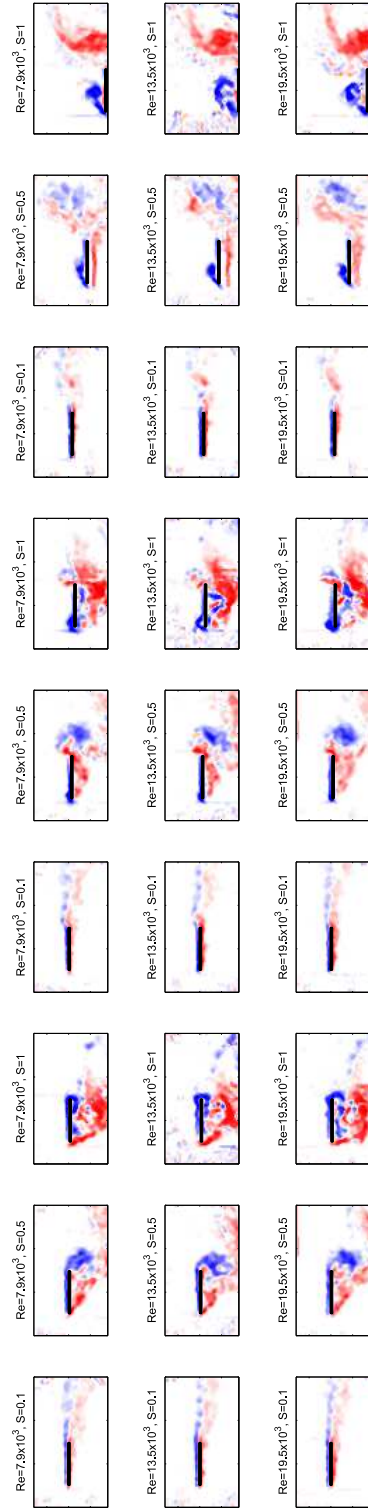


Figure C.3: Plots of the simulated variation in $C_L(t)$ for $\alpha = 10^\circ$, normalized by the magnitude of the steady thin airfoil theory peak C_L . The cyan line is the quasi-steady thin airfoil theory, blue is Wagner thin airfoil theory, red is the wakeless panel method, green is the extended Tchieu-Leonard model, and black is the steady thin airfoil theory. The numbers in each frame are $(\Gamma_v/(Uc), y_v/c)$



(a) Flow around the plates at $0.1 t_c$ before the change in direction. Plates are moving upward.

(b) Flow around the plates at $0.25 t_c$ after the change in direction. The wakes are rolling up.

(c) Flow around the plates at $1.0 t_c$ after the change in direction. The vortices are moving downstream.

Figure C.4: This sequence of figures shows the evolution of the flow around the plate when Re_c and S are varied.

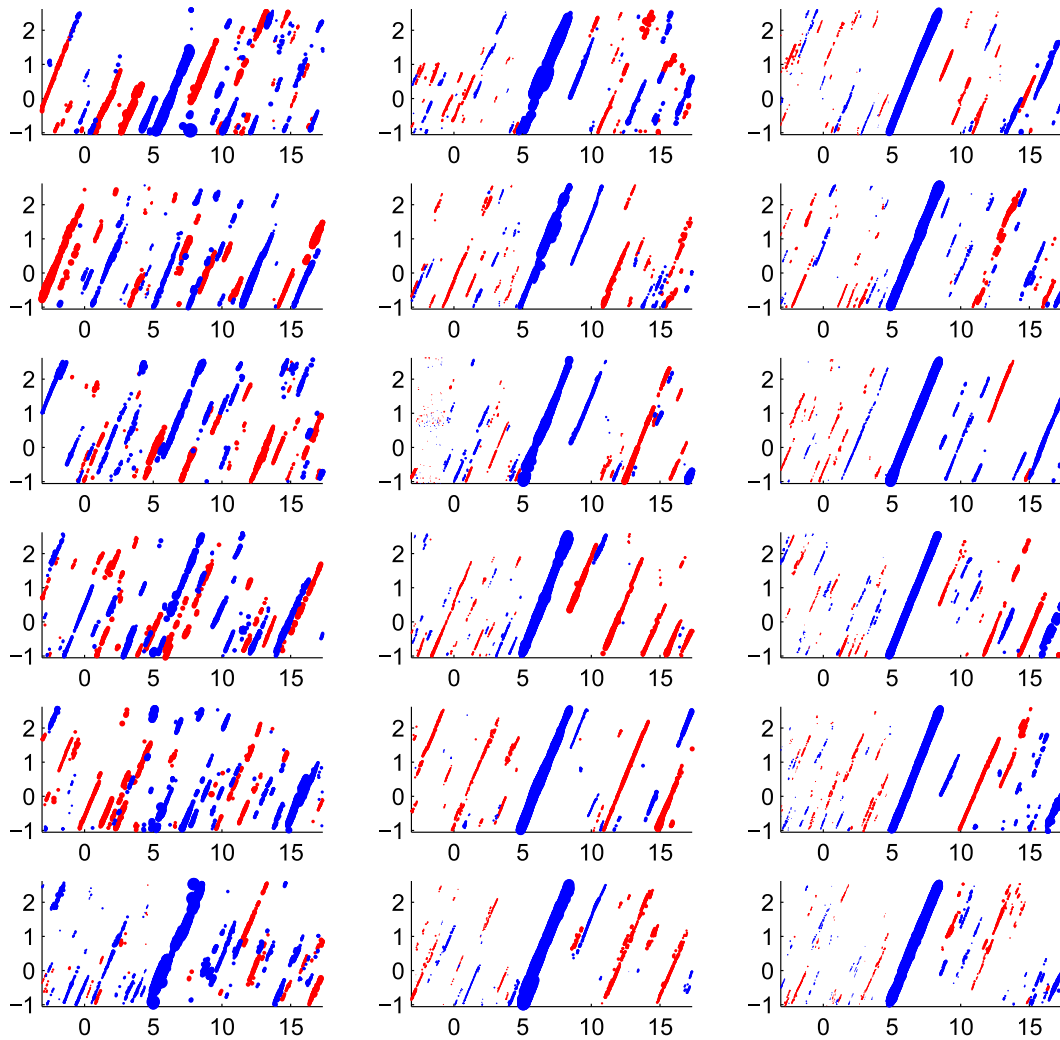


Figure C.5: Paths of vortices from the pitching airfoil: the x-axis is time, and y-axis is the x-position of the identified strongest vortex at that timestep. The columns are, from left to right, $S = -5^\circ, -10^\circ, -13^\circ$. The first five rows are individual repetitions of the experiment. The bottom row is from the average PIV field of those experiments.

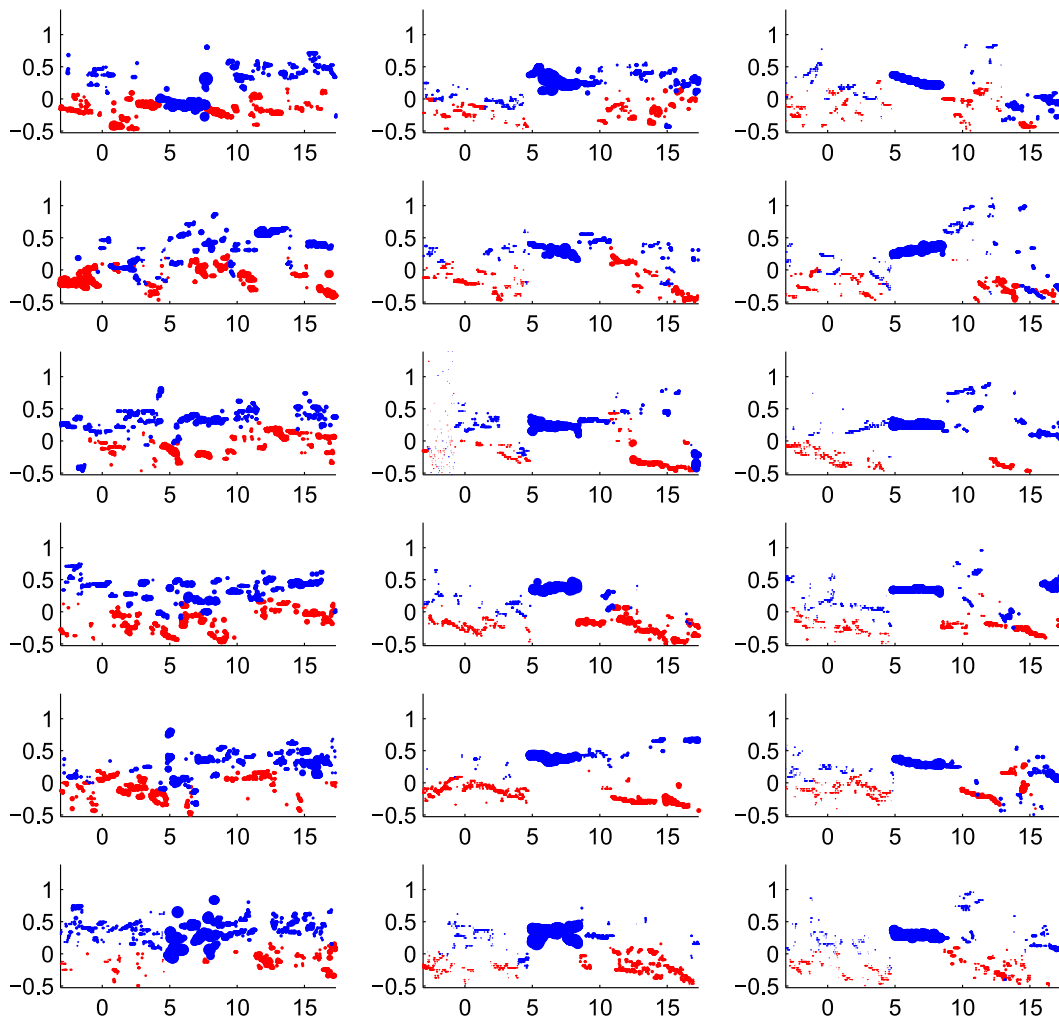


Figure C.6: Paths of vortices from the pitching airfoil: the x-axis is time, and y-axis is the y-position of the identified strongest vortex at that timestep. The columns are, from left to right, $S = -5^\circ, -10^\circ, -13^\circ$. The first five rows are individual repetitions of the experiment. The bottom row is from the average PIV field of those experiments.

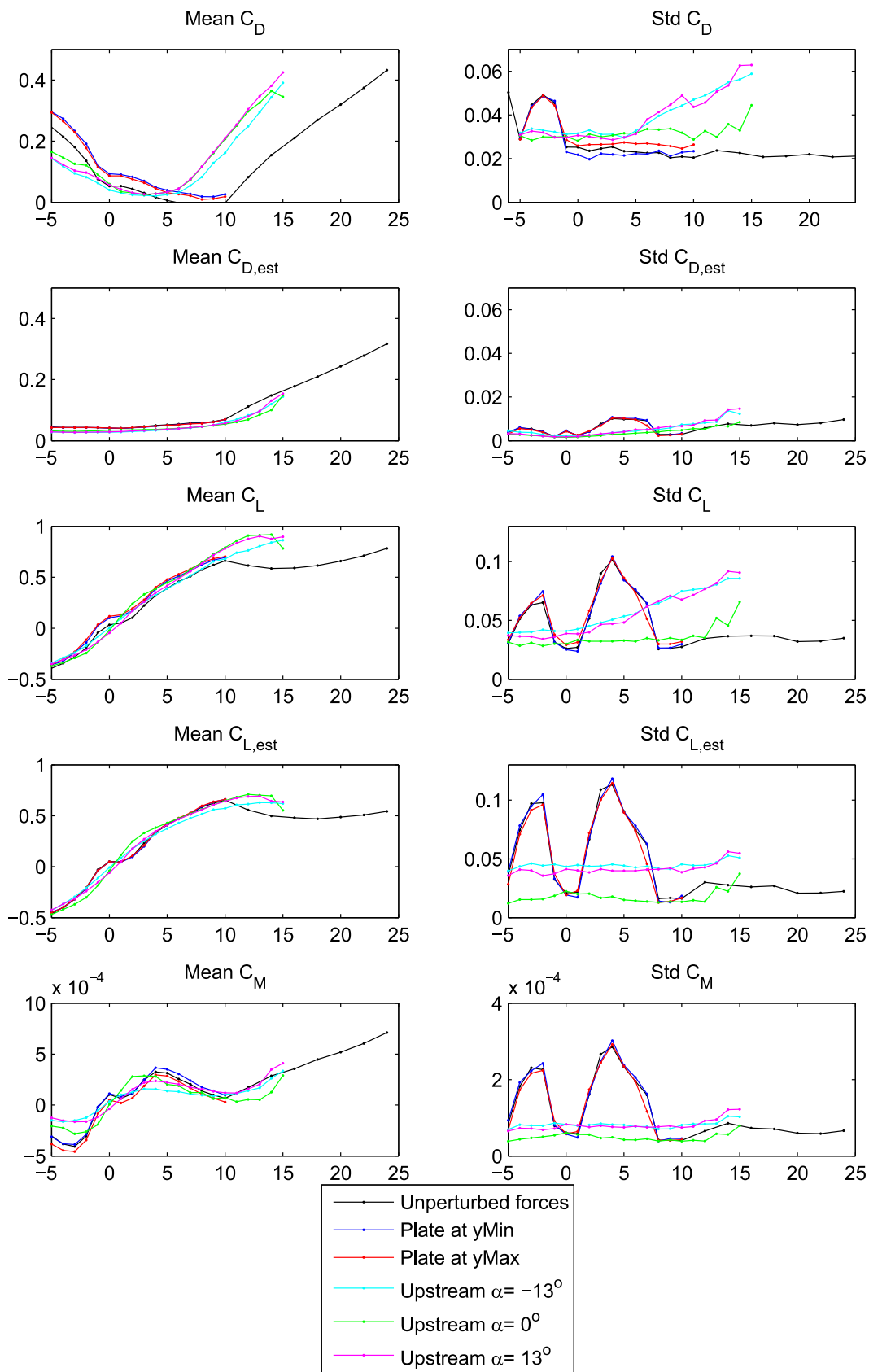


Figure C.7: Average and standard deviations of forces on the airfoil: with an unperturbed freestream, or with the presence of the gust-generating plate or airfoil.

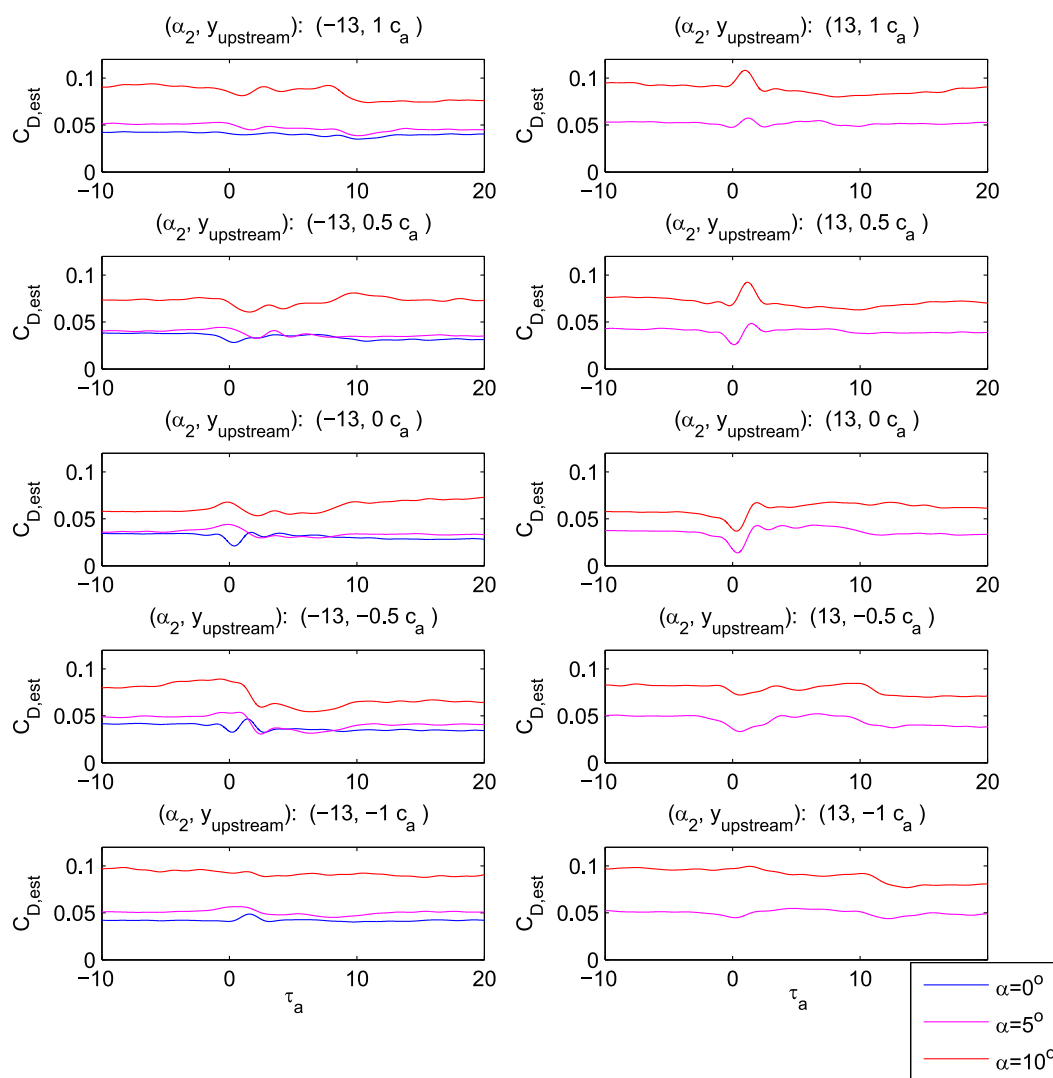


Figure C.8: Estimated drag coefficient due to gusts from the pitching airfoil interacting with the airfoil. Each frame contains force traces from a single release position and initial direction, but different airfoil angles of attack.

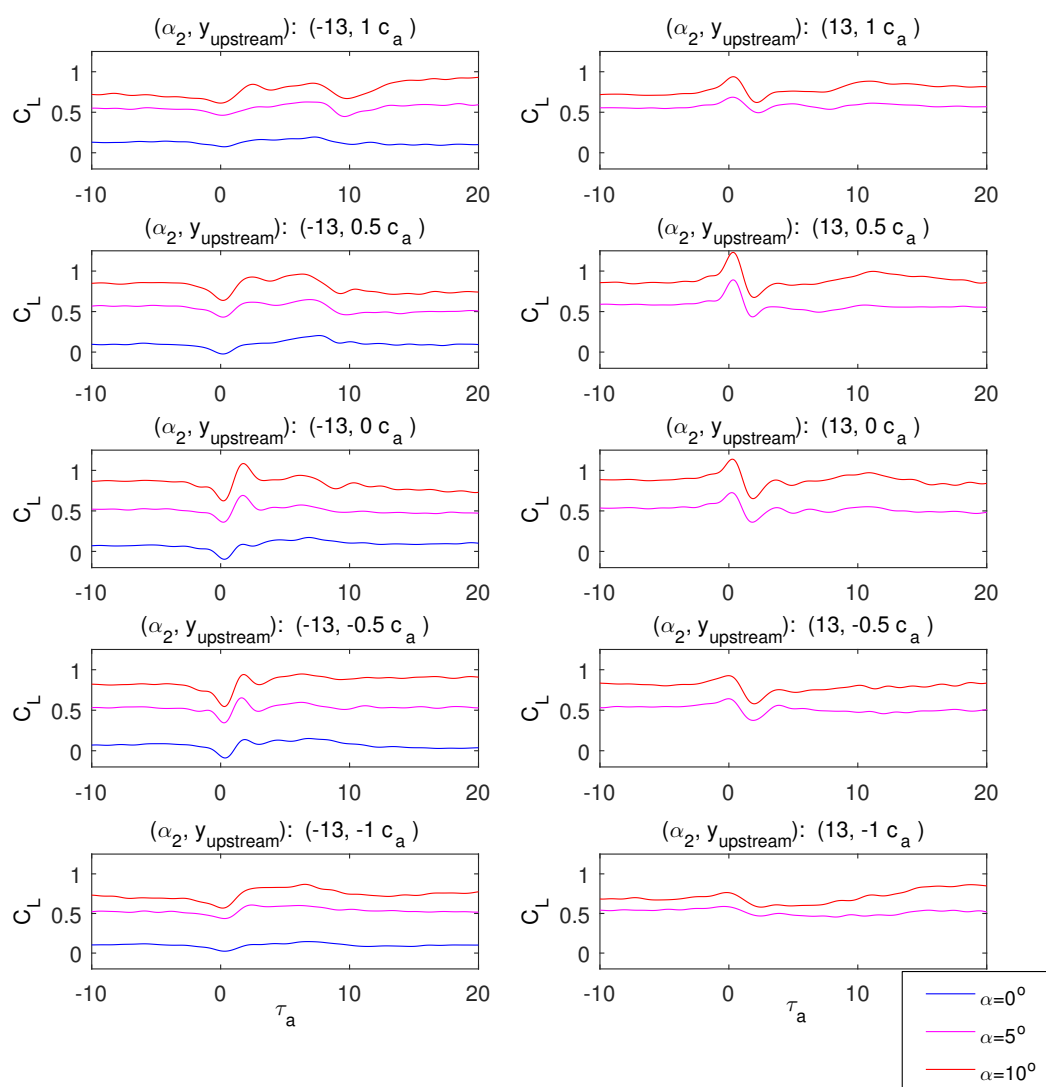


Figure C.9: Lift coefficient due to gusts from the pitching airfoil interacting with the airfoil. The dashed lines correspond to the simulations, and dotted lines denote the semi-analytic estimate. Each frame contains force traces from a single release position and initial direction, but different airfoil angles of attack.

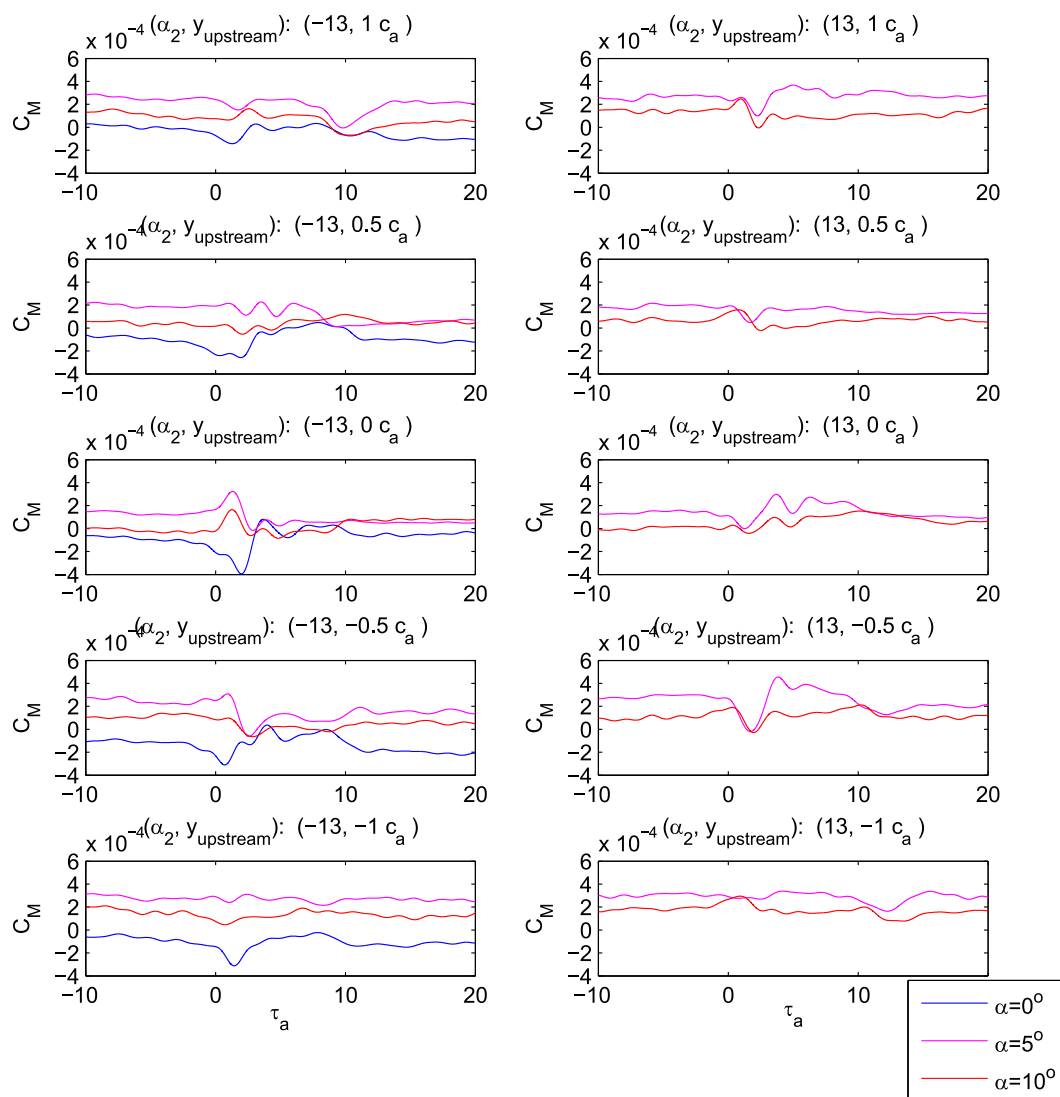


Figure C.10: Moment coefficient due to gusts from the pitching airfoil interacting with the airfoil. Each frame contains force traces from a single release position and initial direction, but different airfoil angles of attack.

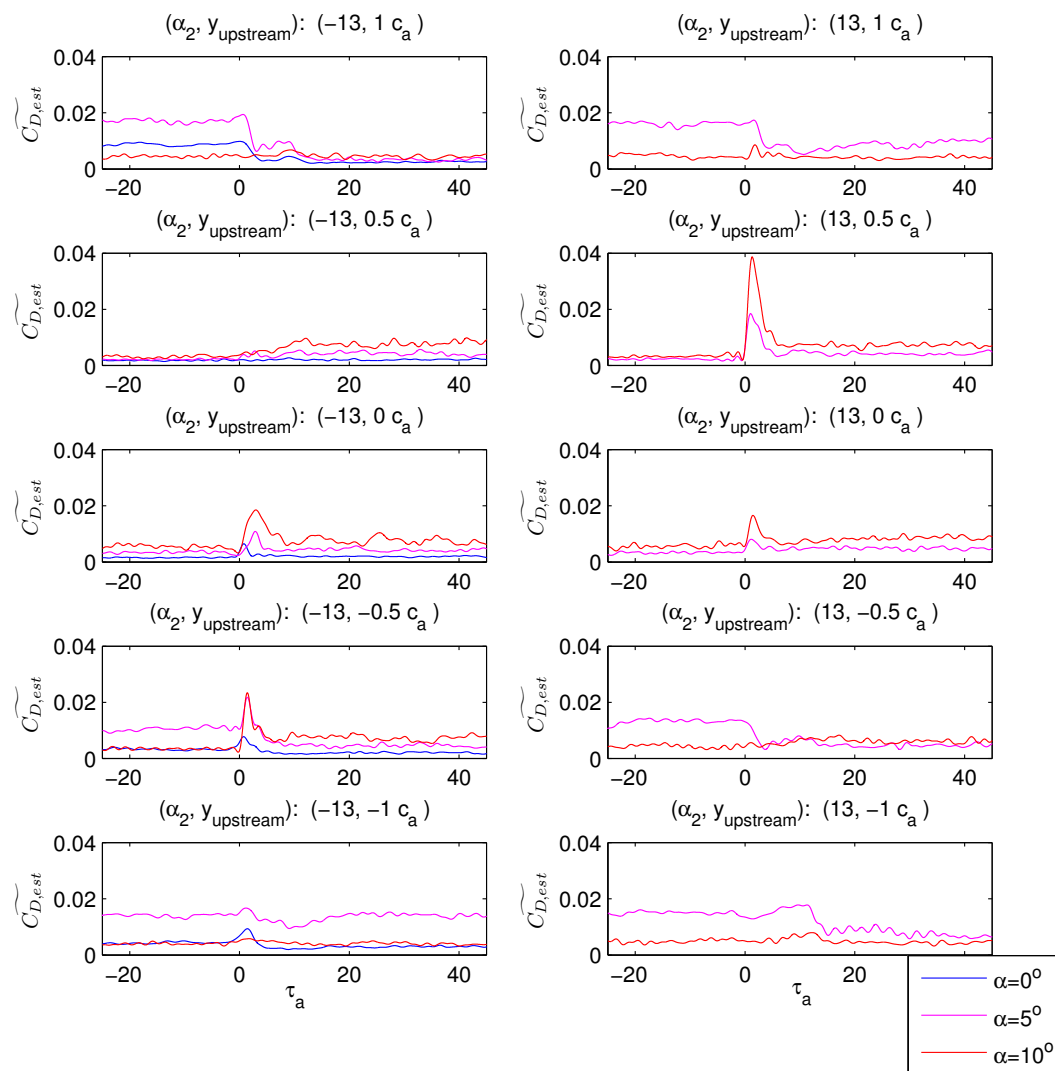


Figure C.11: Average envelope of the drag coefficient due to gusts from the pitching airfoil interacting with the airfoil. Each frame contains traces from a single release position and initial direction, but different airfoil angles of attack.

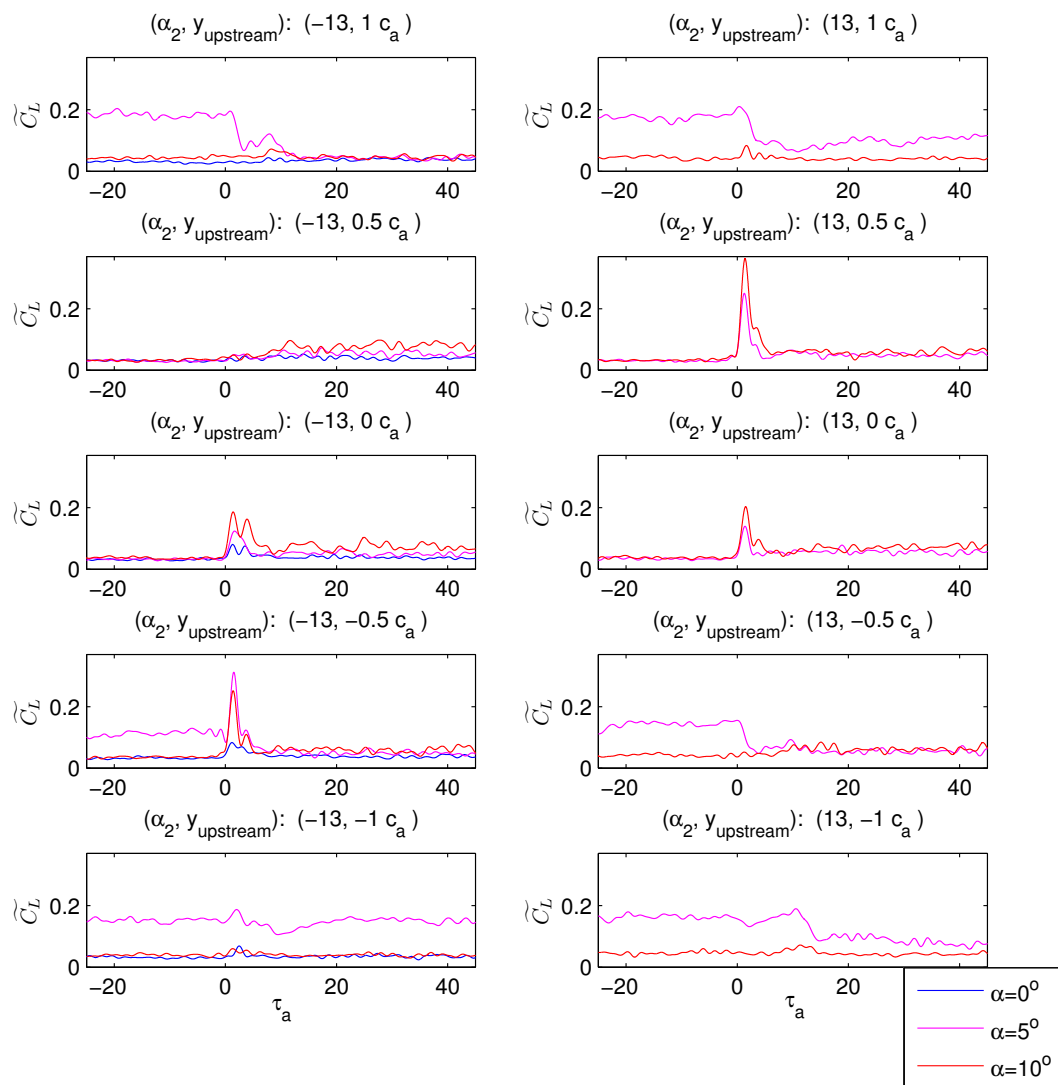


Figure C.12: Average envelope of the lift coefficient due to gusts from the pitching airfoil interacting with the airfoil. Each frame contains traces from a single release position and initial direction, but different airfoil angles of attack.

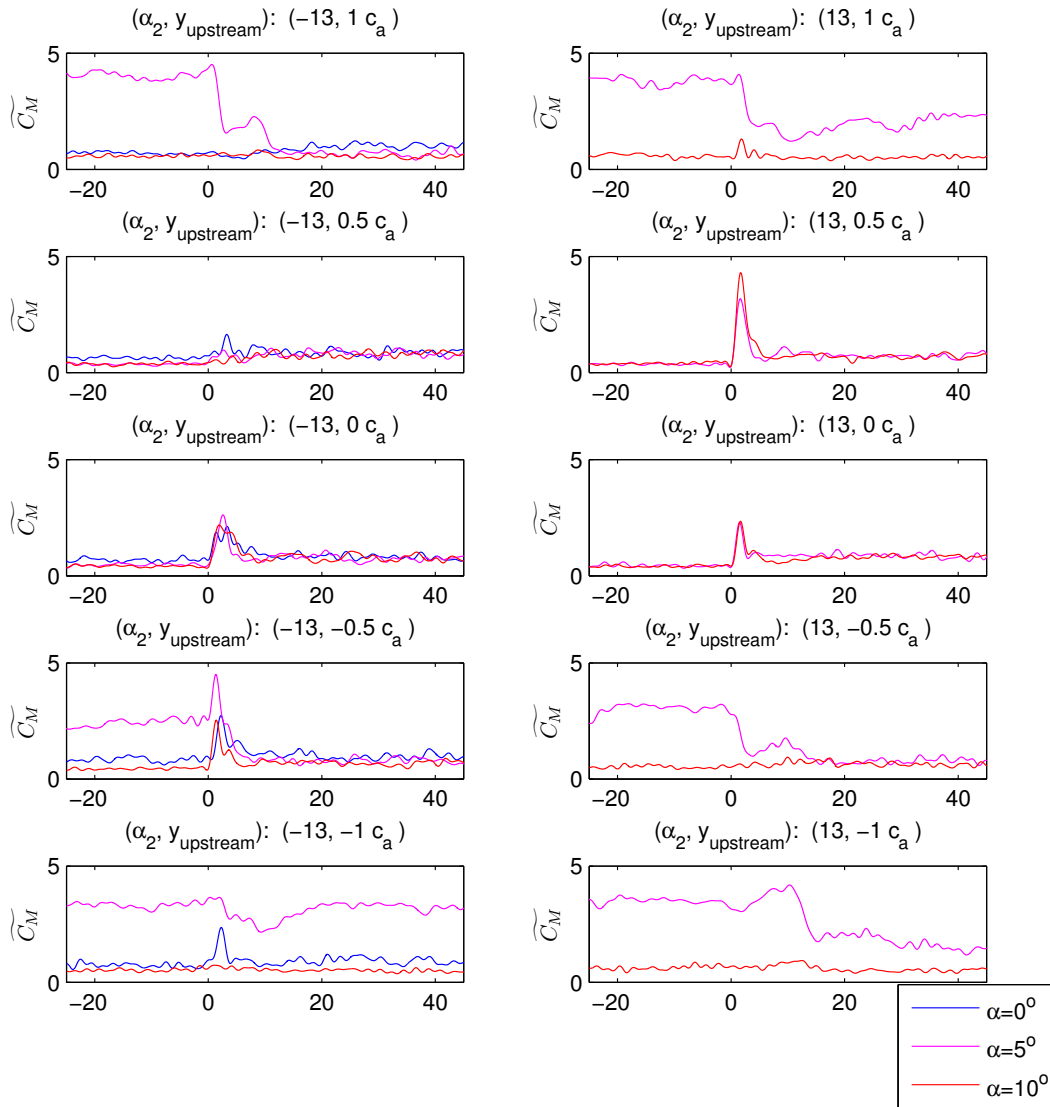


Figure C.13: Average envelope of the moment coefficient due to gusts from the pitching airfoil interacting with the airfoil. Each frame contains traces from a single release position and initial direction, but different airfoil angles of attack.

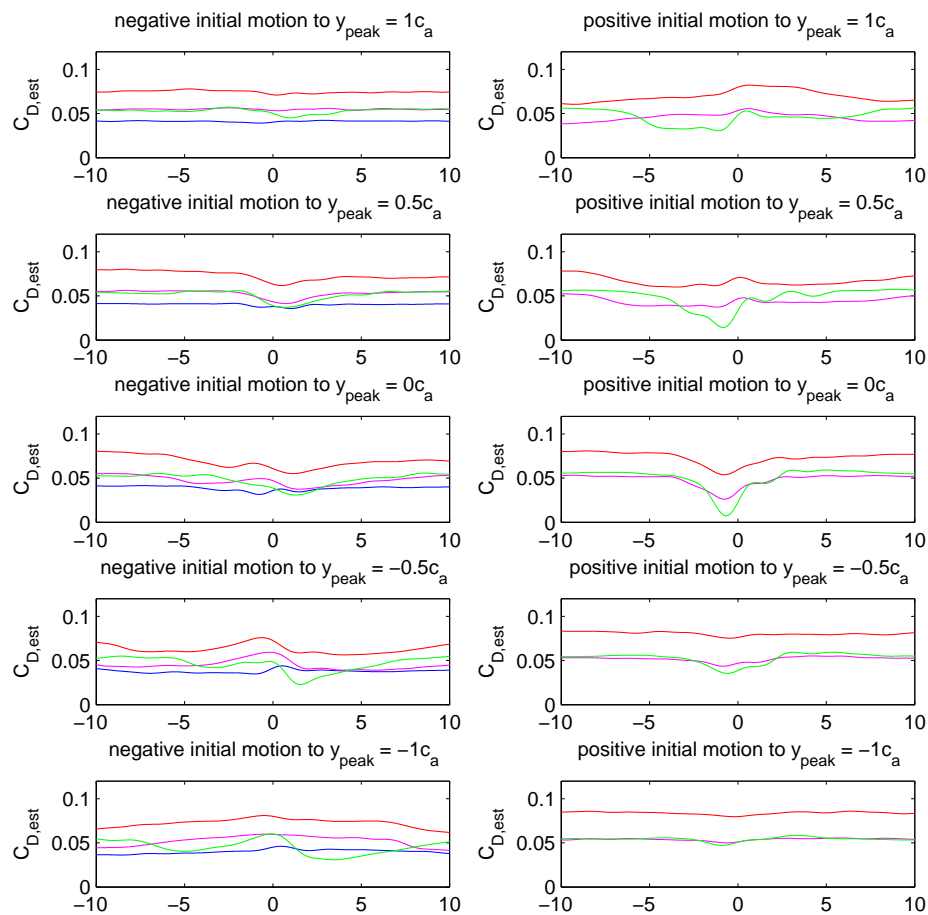


Figure C.14: Estimated drag coefficient due to gusts from the heaving plate interacting with the airfoil. Each frame contains force traces from a single release position and initial direction, but different airfoil angles of attack.

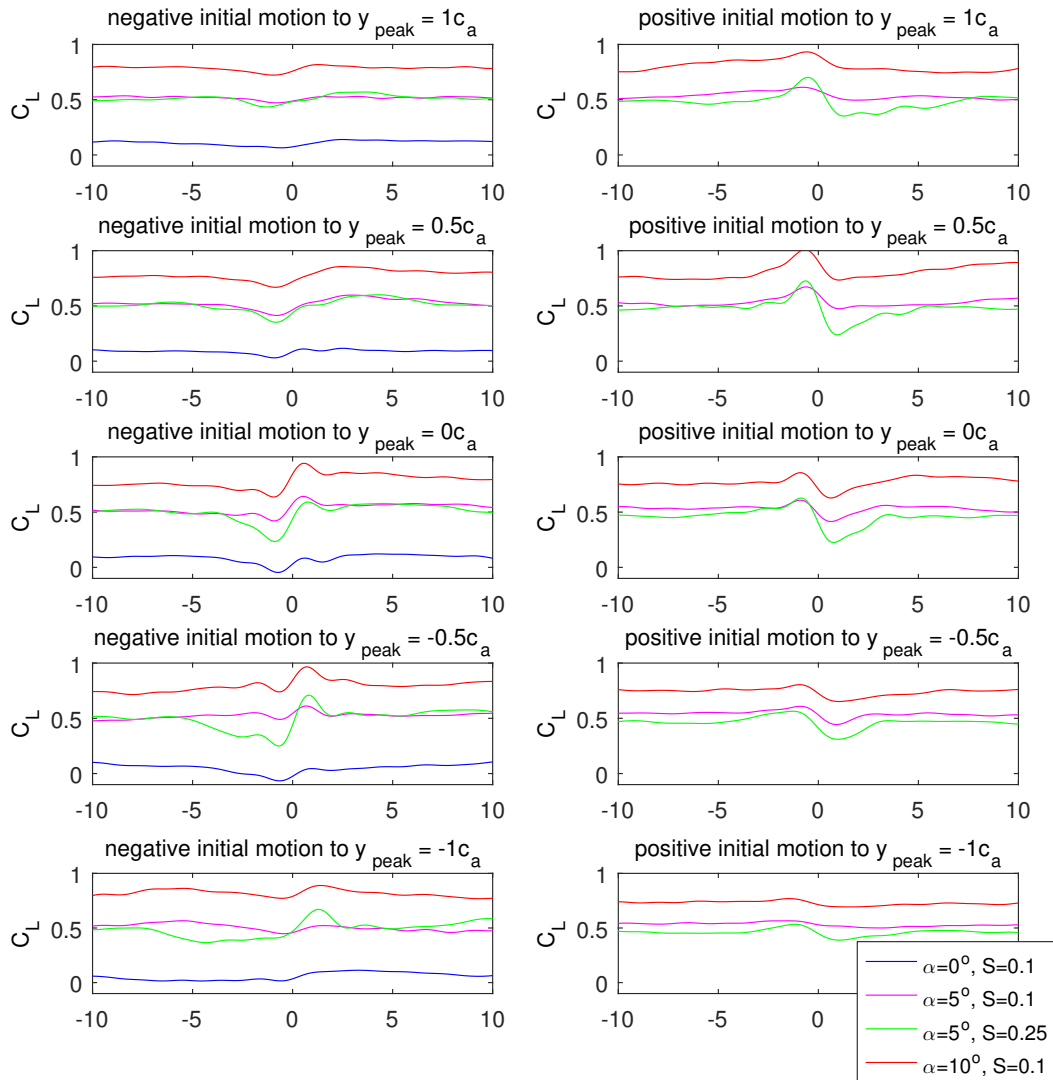


Figure C.15: Lift coefficient due to gusts from the heaving plate interacting with the airfoil. The dashed lines correspond to the simulations, and dotted lines denote the semi-analytic estimate. Each frame contains force traces from a single release position and initial direction, but different airfoil angles of attack.

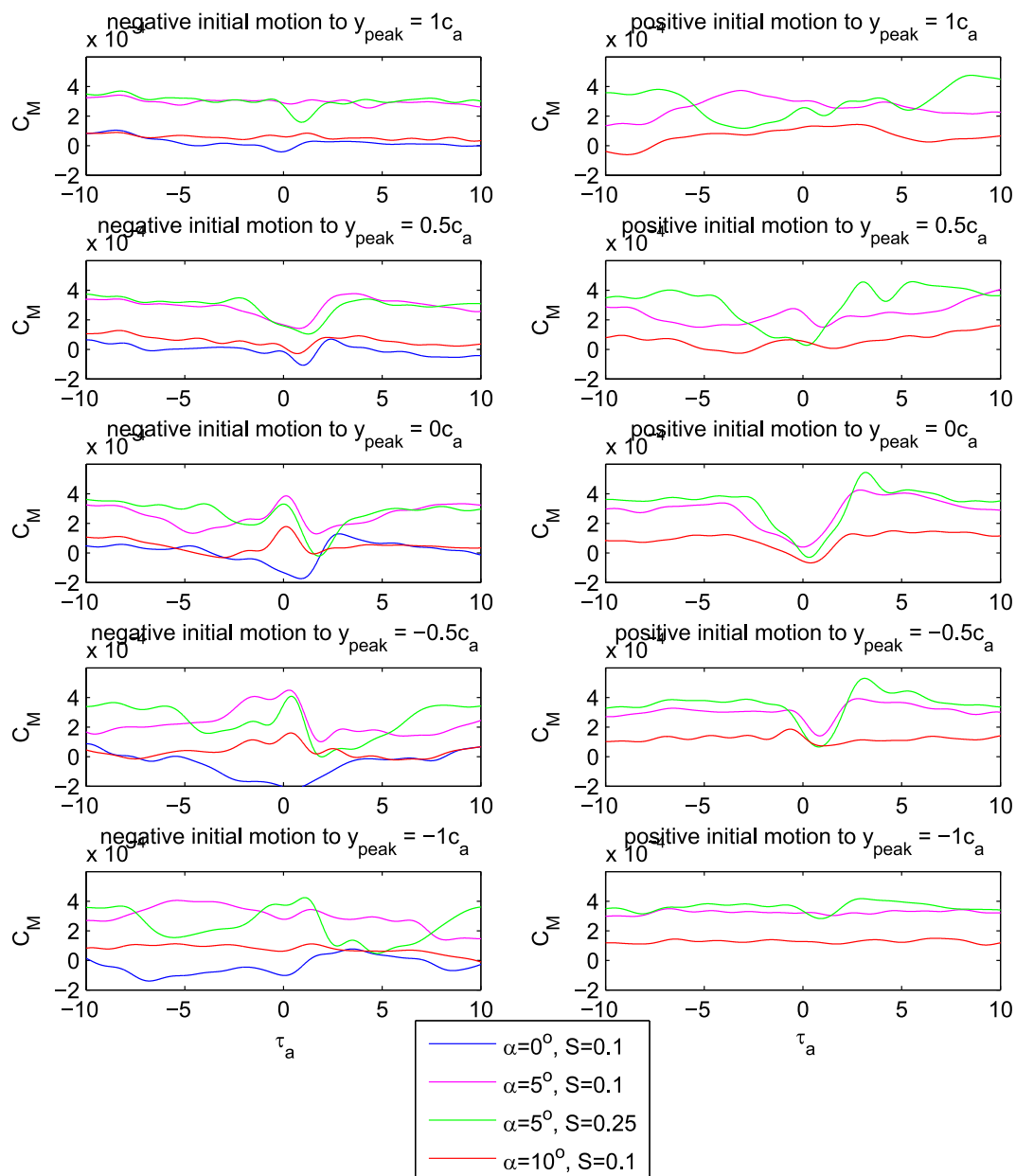


Figure C.16: Moment coefficient due to gusts from the heaving plate interacting with the airfoil. Each frame contains force traces from a single release position and initial direction, but different airfoil angles of attack.

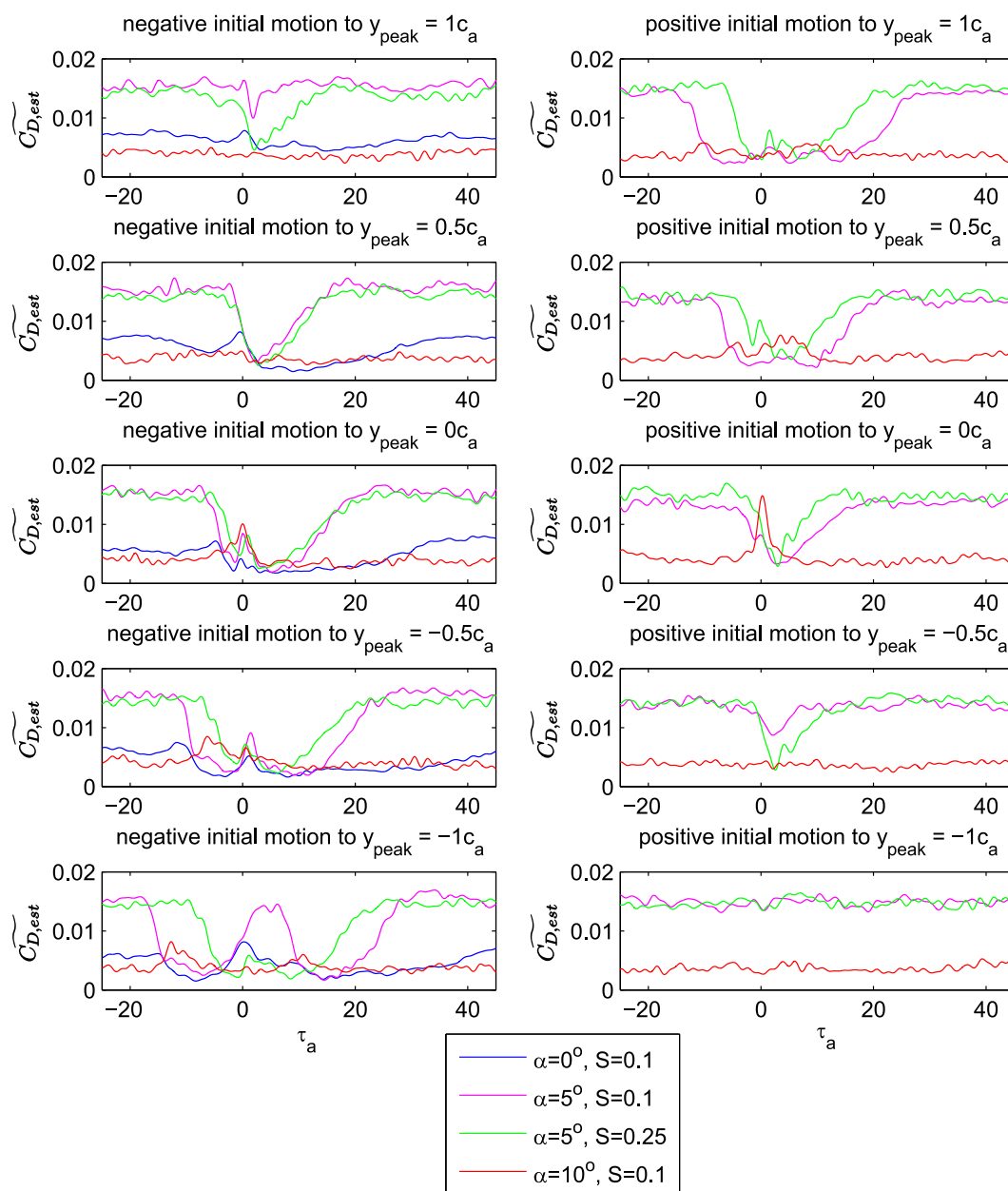


Figure C.17: Average envelope of the drag coefficient due to gusts from the heaving plate interacting with the airfoil. Each frame contains traces from a single release position and initial direction, but different airfoil angles of attack.

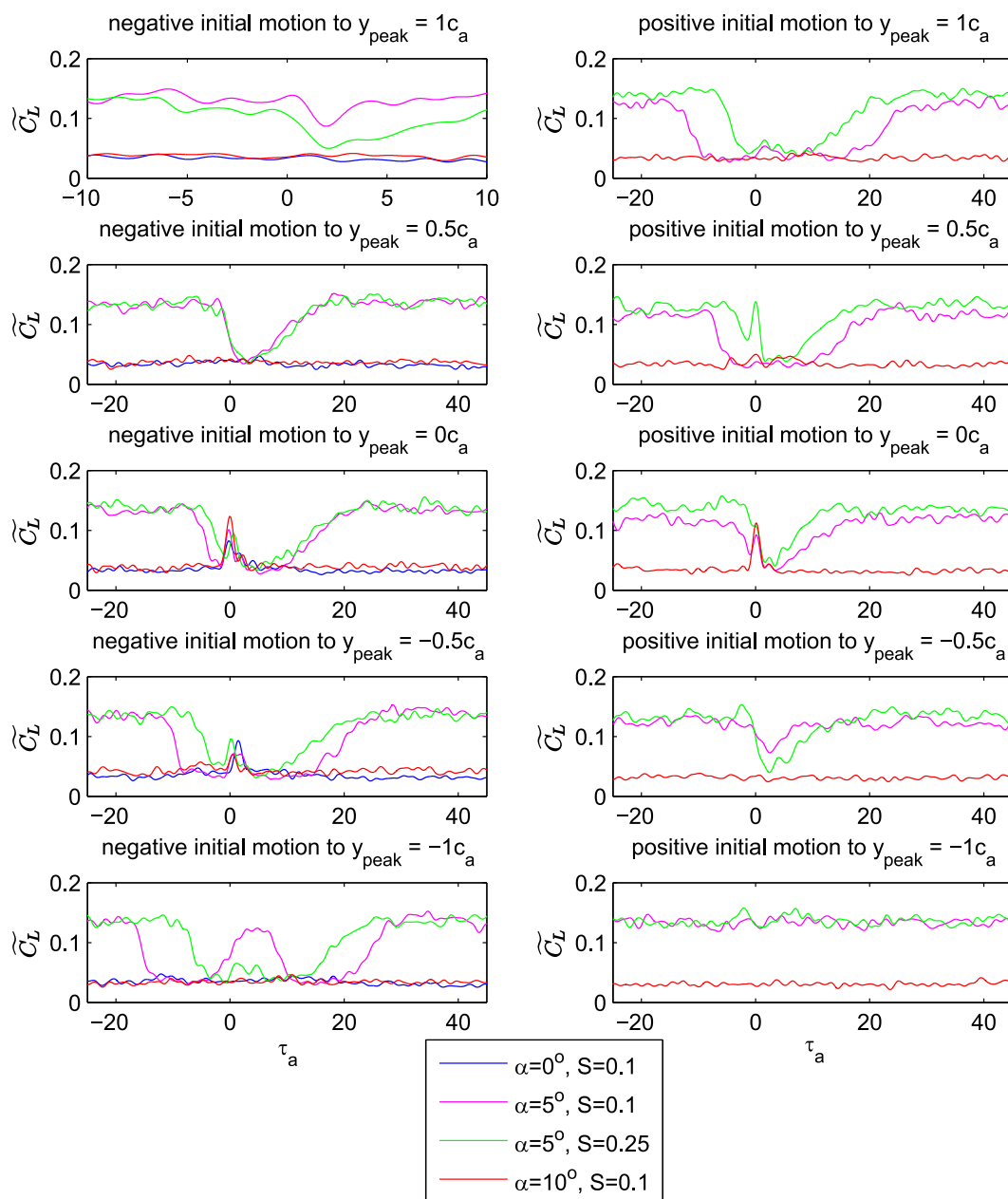


Figure C.18: Average envelope of the lift coefficient due to gusts from the heaving plate interacting with the airfoil. Each frame contains traces from a single release position and initial direction, but different airfoil angles of attack.

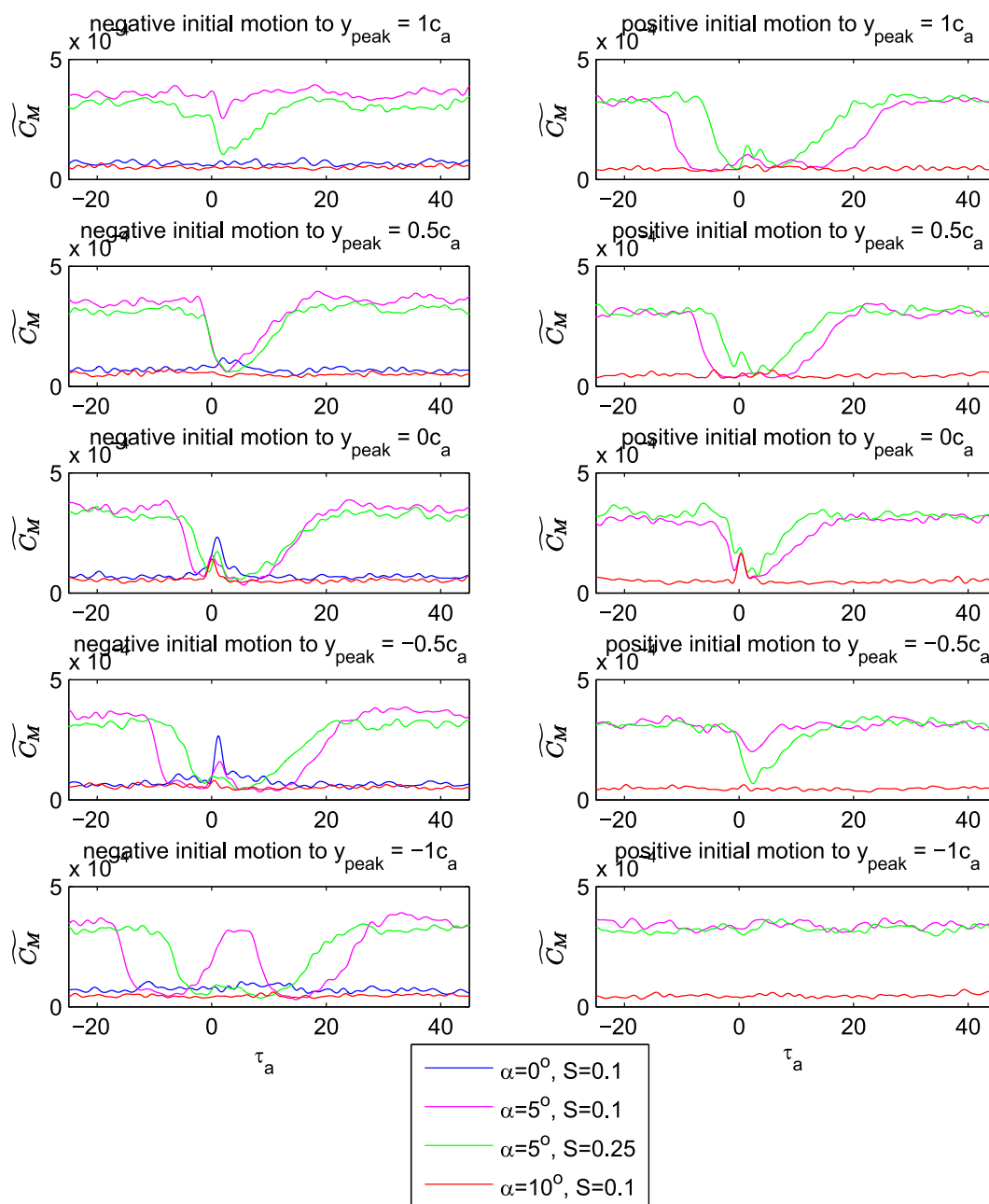


Figure C.19: Average envelope of the moment coefficient due to gusts from the heaving plate interacting with the airfoil. Each frame contains traces from a single release position and initial direction, but different airfoil angles of attack.